IPP-Report

Max-Planck-Institut für Plasmaphysik

Javier Rodrigo Pinzón Acosta

Modelling and Application of Doppler Reflectometry for Advanced Turbulence Studies on the ASDEX Upgrade Tokamak and the TJ-II Stellarator

IPP 2018-18
August 2018

FAKULTÄT FÜR PHYSIK
TECHNISCHE UNIVERSITÄT MÜNCHEN

Modelling and Application of Doppler Reflectometry for Advanced Turbulence Studies on the ASDEX Upgrade Tokamak and the TJ-II Stellarator

Javier Rodrigo Pinzón Acosta

Vollständiger Abdruck der von der Fakultät für Physik der Technischen Universität München zur Erlangung des akademischen Grades eines

Doktors der Naturwissenschaften

genehmigten Dissertation.

Vorsitzender:	Prof. Dr. Alejandro Ibarra
Prüfer der Dissertation:	1. Prof. Dr. Ulrich Stroth
	2. Prof. Dr. Lothar Oberauer
	3. Prof. Dr. Raul Sanchez
	4. Prof. Dr. Luis García Gonzalo

Die Dissertation wurde am 26.04.2018 bei der Technischen Universität München eingereicht und durch die Fakultät für Physik am 10.07.2018 angenommen.

DEPARTAMENTO DE FÍSICA
DOCTORADO EN PLASMAS Y FUSIÓN NUCLEAR

Modelling and Application of Doppler Reflectometry for Advanced Turbulence Studies on the ASDEX Upgrade Tokamak and the TJ-II Stellarator

Author: Javier Rodrigo Pinzón Acosta

Directors: Dr. Tim Happel
Dr. Teresa Estrada

Tutors: Prof. Dr. José Ramón Martín Solis (UC3M)
Prof. Dr. Ulrich Stroth (TUM)

Examination	Committee:	Signature
President:	Prof. Dr. Alejandro Ibarra	_____
Vocal 1:	Prof. Dr. Ulrich Stroth	_____
Vocal 2:	Prof. Dr. Lothar Oberauer	_____
Vocal 3:	Prof. Dr. Raul Sanchez	_____
Vocal 4:	Prof. Dr. Luis García	_____

Mark: Sobresaliente Cum Laude

Garching, 17th July 2018

Modelling and Application of Doppler Reflectometry for Advanced Turbulence Studies on the ASDEX Upgrade Tokamak and the TJ-II Stellarator

Author:	Javier Rodrigo Pinzón Acosta
Supervisors:	Prof. Dr. Ulrich Stroth
	Prof. Dr. José Ramón Martín Solis
Advisors:	Dr. Tim Happel
	Dr. Teresa Estrada
Submission Date:	26th April 2018

Fakultät für Physik, Technische Universität München

Doctorado en Plasmas y Fusión Nuclear, Universidad Carlos III de Madrid

Joint Doctoral Programme in Nuclear Fusion Science and Engineering (FUSION DC)

Siempre había sido un contemplativo que dolorosamente sufría la sensación del tiempo que pasa y que se lleva con él todo lo que querríamos eterno.

Ernesto Sabato, *Abaddón el exterminador*

Dein ist, Dein ja Dein, was du gesehnt!
Dein, was du geliebt, was du gestritten!
O glaube: Du wardst nicht umsonst geboren!
Hast nicht umsonst gelebt, gelitten!

Gustav Mahler, *Auferstehungssymphonie*

Abstract

The most advanced approach to make nuclear fusion an energy source available on earth is the confinement of high temperature plasmas with strong magnetic fields. This method is currently investigated in experimental devices such as tokamaks and stellarators, which use toroidal magnetic configurations designed to confine fusion plasma efficiently. However, turbulence contributes significantly to the transport of energy and particles, which results in a degradation of the confinement quality. Therefore, the understanding of the transport arising from turbulence and its suppression mechanisms may contribute to the improvement of the confinement and thus to the efficiency in present experiments and future fusion reactors. To this end, a careful experimental characterisation of the turbulence in fusion plasmas and its comparison with physical models is required, especially with results from gyrokinetic simulations. They can predict turbulence characteristics in detail, such as spectral properties, shape of turbulent structures and driving micro-instabilities.

Doppler reflectometry is one of the diagnostic techniques used for turbulence investigations in fusion plasmas. Based on the backscattering of a probing electromagnetic wave off density fluctuations, it provides local measurements of their velocity ($u_\perp$) perpendicular to the magnetic field and of the perpendicular wavenumber ($k_\perp$) spectrum of the density turbulence. In addition, the radial correlation technique uses two Doppler reflectometer channels for providing information on the radial structure of the turbulence, in particular an estimate of its radial correlation length (L_r). However, the complexity of the wave propagation and of the scattering process involved induces a non-trivial diagnostic response, which has to be considered for a proper interpretation of experimental measurements. In this thesis the Doppler reflectometry technique is thoroughly investigated analytically, numerically and experimentally. The advanced understanding obtained is then applied to turbulence studies which have been performed in both the ASDEX Upgrade tokamak and the TJ-II stellarator.

The wave propagation and scattering relevant for Doppler reflectometry are investigated using a linear analytical model (Born approximation), a physical optics model and two-dimensional full-wave simulations. This allows for a detailed study of both the linear and non-linear diagnostic responses. In particular, a new regime with an enhanced backscattering response to the fluctuation level is found and characterized for the first time. In connection, its impact on the $k_\perp$ spectra measurement is examined. Moreover the diagnostic response to Gaussian, flat and Kolmogorov-type spectra is studied in a broad $k_\perp$ and turbulence level range. The radial correlation technique is also investigated in detail. A new analysis method is developed, which gives a measurement of the mean tilt angle of the turbulent structures. This is a relevant quantity predicted by theories and gyrokinetic simulations, which can provide information on the turbulence interaction with plasma flows and the type of dominant micro-instabilities. The method is based on the analysis of the time delay of the cross-correlation function of the Doppler reflectometer signals. It is found that diagnostic effects may impact the measurements of L_r and the tilt angle. Corresponding correction factors are derived and applied.

A detailed characterization of L-mode plasmas using Doppler reflectometry is performed in both the ASDEX Upgrade tokamak and the TJ-II stellarator. Wavenumber spectra, $u_\perp$ profiles and L_r are measured simultaneously. The experimental data is analysed based on the modelling results, and the diagnostic effects on the measurements are investigated. Furthermore, the experimental observations are linked to the theory of turbulence regulation by sheared flows and to different types of micro-instabilities.

The experimental time delays of the cross-correlation are studied using the developed analysis techniques. The mean tilt angle of the turbulent structures is measured in the confined region of the ASDEX Upgrade tokamak and the TJ-II stellarator for the first time. The effect of the temporal decorrelation of the turbulence on the tilt angle measurement is investigated experimentally. In the ASDEX Upgrade tokamak, a change of the tilt angle has been measured between phases with either dominant ion or dominant electron heating. This change is consistent with a transition from a dominant ion-temperature gradient to a dominant trapped-electron mode driven turbulence. The tilt angle measured in the TJ-II stellarator is in qualitative agreement with results from linear gyrokinetic simulations. Moreover, a radial variation of the tilt angle consistent with expectations of the $u_\perp$ shear has been observed.

The profound study of Doppler reflectometry performed in this thesis has highlighted relevant diagnostic properties and effects, allowing for a more accurate and complete characterization of the turbulence. In particular, the finding of the enhanced power response regime has contributed to a better understanding of the measured $k_\perp$ spectra, and the tilt angle measurement method has provided a new element for experimental investigations and comparisons with simulations and theories. These innovative methods make advanced studies with Doppler reflectometry possible, which may contribute substantially to a better understanding of the turbulence in fusion plasmas.

Zusammenfassung

Die fortgeschrittenste Methode, um Kernfusion zu einer Energiequelle auf der Erde zu machen, besteht im Einschluss von Hochtemperaturplasmen durch starke magnetische Felder. Zur Zeit wird diese Methode in experimentellen Anlagen wie Tokamaks und Stellaratoren untersucht. Solche Maschinen werden für einen effizienten Plasmaeinschluss konzipiert. Trotzdem ist Turbulenz für einen großen Teil des Energie- und Teilchentransportes verantwortlich, was zu einer Verschlechterung des Plasmaeinschlusses beiträgt. Deswegen könnte das Verständnis der Transportprozesse und ihrer Unterdrückung zur Verbesserung des Energieeinschlusses und damit der Effizienz derzeitiger Experimente und zukünftiger Reaktoren führen. Aus diesem Grund ist eine detaillierte experimentelle Charakterisierung der Turbulenz in Fusionsplasmen und ein Vergleich der Messungen mit physikalischen Modellen erforderlich. Besonders wichtig sind Vergleiche mit gyrokinetischen Simulationen, welche bestimmte Turbulenzattribute wie spektrale Eigenschaften, Form der Turbulenzstrukturen sowie die antreibende Mikroinstabilitäten, vorhersagen.

Doppler-Reflektometrie ist eine der Diagnostiken, die für Turbulenzuntersuchungen verwendet werden. Dabei wird eine von außerhalb des Plasmas eingestrahlte Welle, die an Dichtefluktuationen gestreut wird, genutzt. Dies ermöglicht die lokale Messung der Geschwindigkeit der Dichtefluktuationen ($u_\perp$) senkrecht zum Magnetfeld und des Wellenzahlspektrums $P(k_\perp)$ der Dichteturbulenz. Zusätzlich werden bei der radialen Korrelationstechnik zwei Doppler-Reflektometriekanäle verwendet, um Information über die radiale Struktur der Turbulenz zu erhalten, z.B. die radiale Korrelationslänge (L_r). Für eine korrekte Interpretation der experimentellen Messungen muss jedoch eine nichttriviale Antwortfunktion der Diagnostik, die durch die komplexen Wellenausbreitungs- und Streuprozesse verursacht wird, berücksichtigt werden. In der vorliegenden Arbeit werden die für die Doppler-Reflektometrie relevanten Prozesse analytisch, numerisch und experimentell untersucht. Das gewonnene Wissen wird später für detaillierte Studien der Turbulenz am Tokamak ASDEX Upgrade und am Stellarator TJ-II angewendet.

Die Wellenausbreitung und -streuung, wird mit einem analytischen linearen Modell (Born-Näherung), einem Wellenoptik-Modell und zweidimensionalen Full-wave-Simulationen untersucht. Dies ermöglicht eine detaillierte Überprüfung der linearen und nichtlinearen Diagnostikantwort. Ein Diagnostikregime, in dem die Signalintensität überproportional stark mit der Turbulenzamplitude wächst, wird zum ersten Mal entdeckt und charakterisiert. Zudem wird seine Auswirkung auf die Messung der $k_\perp$-Spektren analysiert. Weiterhin wird die Antwortfunktion für Gaußsche-, flache und Kolmogorov-artige Spektren in einem breiten Bereich von Wellenzahlen und Turbulenzamplituden untersucht. Die radiale Korrelationstechnik wird ebenfalls modelliert. Eine neue Analysemethode wird entwickelt, die eine Messung des Neigungswinkels der Turbulenzstrukturen ermöglicht. Der Neigungswinkel ist eine Größe, die durch Theorien und gyrokinetische Simulationen vorhergesagt wird, und der Informationen über die Turbulenzwechselwirkung mit der Plasmaströmung und über die dominanten Mikroinstabilitäten liefern kann. Die Methode nutzt die Zeitverzögerungen der Kreuzkorrelationsfunktion der Doppler-Reflektometriesignale. Es würde herausgefunden, dass Diagnostikeffekte eine Wirkung

auf L_r- und Neigungswinkel-Messungen haben können. Deswegen werden Korrekturfaktoren abgeleitet und verwendet.

Eine detaillierte Charakterisierung von Plasmen mittels Doppler-Reflektometrie wird am Tokamak ASDEX Upgrade und am Stellarator TJ-II durchgeführt. Wellenzahlspektren, $u_\perp$ und L_r werden gleichzeitig untersucht. Basierend auf Modellierungen werden die experimentellen Daten analysiert und die Diagnostikeffekte untersucht. Die experimentellen Beobachtungen werden mit der Turbulenzregulation durch Scherströmungen und verschiedene Mikroinstabilitäten in Verbindung gebracht.

Die experimentellen Zeitverzögerungen der Kreuzkorrelation werden mit der entwickelten Analysetechnik untersucht. Dadurch wird zum ersten Mal der Neigungswinkel der Turbulenzstrukturen im Einschlussbereich des Tokamaks ASDEX Upgrade und des Stellarators TJ-II gemessen. Der Effekt der zeitlichen Dekorrelation der Turbulenz auf die Messung des Neigungswinkels wird experimentell untersucht. An ASDEX Upgrade wird eine Änderung des Neigungswinkels gemessen, die konsistent mit einem Übergang von dominanter ionengradientgetriebener Turbulenz zu dominanter Turbulenz durch gefangene Elektronen ist, abhängig von Plasma-Phasen mit dominanter Ionen- oder dominanter Elektronen-Heizung. Der Neigungswinkel der Strukturen am Stellarator TJ-II steht in qualitativer Übereinstimmung mit Ergebnissen linearer gyrokinetischer Simulationen. Darüber hinaus wird eine radiale Variation der Neigung gemessen, die mit Erwartungen der $u_\perp$-Verscherung übereinstimmen.

Die detaillierte Untersuchung der Doppler-Reflektometrie, die in dieser Arbeit vorgestellt wurde, hat Eigenschaften der Diagnostik aufgezeigt, die eine genauere und vollständigere Charakterisierung der Turbulenz erlauben. Besonders hervorzuheben sind das neu entdeckte Diagnostik-Regime, welches zu einer Verbesserung des Verständnisses der gemessenen Spektren geführt hat, und die Methode zur Messung des Neigungswinkels, welche einen bisher unzugänglichen Vergleichsparameter zu Simulationen und Theorien geliefert hat. Diese innovative Methoden ermöglichen fortgeschrittene Studien, die wesentlich zu einem besseren Verständnis der Turbulenz in Fusionsplasmen beitragen können.

Resumen

Uno de los métodos para hacer de la fusión nuclear una fuente de energía disponible sobre la faz de la tierra, consiste en el confinamiento por medio de campos magnéticos de plasmas a altas temperaturas. Este método se investiga actualmente en dispositivos experimentales como los tokamaks y stellarators, que cuentan con configuraciones magnéticas especialmente diseñadas para confinar eficientemente los plasmas de fusión. Sin embargo la turbulencia contribuye significativamente al transporte de partículas y energía, lo que conlleva a una reducción del confinamiento en los experimentos. Por esta razón, es necesario entender los procesos de transporte causados por la turbulencia y su supresión, para mejorar el confinamiento y la eficiencia en los experimentos actuales y en los futuros reactores. Una de las piezas claves para lograr un mejor entendimiento de tales procesos es la caracterización experimental detallada de la turbulencia y su comparación con modelos físicos. Especialmente con simulaciones giro-cinéticas que predicen características especificas de la turbulencia, tales como sus propiedades espectrales, la forma de sus estructuras y las micro inestabilidades que le proveen energía.

La reflectometría Doppler es un diagnóstico empleado para investigar la turbulencia en los plasmas de fusión. Esta técnica considera una onda electromagnética que tras ser lanzada al plasma es dispersada por las fluctuaciones de densidad, permitiendo medir la velocidad ($u_\perp$) perpendicular al campo magnético y el espectro en número de onda perpendicular ($k_\perp$) de la turbulencia de densidad. Adicionalmente, la técnica de correlación radial utiliza dos canales de reflectometría Doppler para obtener información sobre la estructura radial de la turbulencia, en particular sobre su longitud de correlación radial (L_r). Sin embargo, la complejidad de la propagación de la onda y de los procesos de dispersión inducen una respuesta no trivial del diagnostico que debe ser tenida en cuenta para interpretar correctamente los datos experimentales. En esta tesis la reflectometría Doppler se ha investigado analítica, numérica y experimentalmente en profundidad. El conocimiento obtenido se ha aplicado a estudios detallados de la turbulencia en el tokamak ASDEX Upgrade y el stellarator TJ-II.

La propagación de ondas y los procesos de dispersión relevantes para la reflectometría Doppler se han investigado utilizando un modelo lineal analítico (aproximación de Born), un modelo de óptica física y simulaciones de onda completa en dos dimensiones. Esto ha permitido estudiar en detalle las respuestas lineal y no lineal del diagnóstico. En particular, un nuevo régimen con una respuesta que sobrestima el nivel de turbulencia se ha descubierto y caracterizado por primera vez; además se ha investigado su efecto en las mediciones del espectro en $k_\perp$. Así mismo, se ha estudiado la respuesta del diagnóstico a espectros gaussianos, planos y tipo Kolmogorov en un amplio rango de $k_\perp$ y niveles de turbulencia. La técnica de correlación radial también se ha investigado en detalle, y se ha propuesto un nuevo método de análisis que permite medir el ángulo de inclinación de las estructuras de la turbulencia. Esta es una magnitud importante predicha por teorías y simulaciones giro-cinéticas, y que provee información sobre la interacción de la turbulencia con los flujos del plasma y los tipos de micro inestabilidades. El método se basa en el estudio de los retrasos temporales de la función de correlación de las señales de reflectometría. Se ha mostrado que los efectos instrumentales del diagnostico pueden

tener un impacto en las mediciones de L_r y del ángulo de inclinación, por ende factores de corrección han sido deducidos y aplicados.

Se ha caracterizado en detalle la turbulencia en plasmas modo L del tokamak ASDEX Upgrade y del stellarator TJ-II. Se han medido simultáneamente los espectros en $k_\perp$, perfiles de $u_\perp$ y L_r. Los datos experimentales se han analizado basándose en los resultados del modelado y se han investigado los efectos instrumentales del diagnóstico en las mediciones. Además, las observaciones experimentales se han podido relacionar con el mecanismo de regulación de la turbulencia por gradientes en la velocidad del plasma y los diferentes tipos de micro inestabilidades.

Los retrasos temporales de la función de correlación experimental se han investigado utilizando la técnica de análisis desarrollada. Por primera vez, se ha medido el ángulo de inclinación de las estructuras de la turbulencia en la región de confinamiento del tokamak ASDEX Upgrade y del stellarator TJ-II. El efecto de la decorrelación temporal de la turbulencia en el método de medición también se ha investigado experimentalmente. En el tokamak ASDEX Upgrade, se ha medido un cambio del ángulo de inclinación entre fases con calentamiento dominante de iones y electrones. Este cambio es consistente con una transición de un régimen de turbulencia dominado por gradiente de temperatura iónica a uno dominado por modo de electrones atrapados. El ángulo de inclinación medido en el stellarator TJ-II coincide cualitativamente con resultados de simulaciones giro-cinéticas. Además, se ha observado una variación radial del ángulo de inclinación que es consistente con la dirección del gradiente de $u_\perp$.

El estudio detallado de la reflectometria Doppler presentado en esta tesis ha revelado propiedades y efectos del diagnostico, cuyo conocimiento permite una caracterización más precisa y completa de la turbulencia. Vale la pena destacar: el descubrimiento del nuevo régimen de respuesta del diagnóstico, que permite entender mejor las mediciones de espectros en $k_\perp$; el método de medida del ángulo de inclinación, que provee un nuevo elemento para investigaciones experimentales y comparaciones con simulaciones y teorías. Estos métodos innovadores hacen posible investigaciones avanzadas con la reflectometría Doppler, que pueden contribuir significativamente al entendimiento de la turbulencia en los plasmas de fusión.

Contents

Chapter 1

Introduction

Plasma is the fourth state of matter and the most common in the universe. It is the state where nuclear fusion occurs naturally in the stars; the high temperatures and densities allow the atomic nuclei to overcome the repulsive Coulomb potential and to fuse into heavier nuclei. This process releases large amounts of energy and is the energy source of the stars. In the last 70 year, large efforts have been made in order to develop nuclear fusion as an energy source available on earth [1, 2]. The limited availability of fossil fuels and the environmental damage associated with their use make the search for new energy sources urgent [3, 4]. Nuclear fusion is one candidate for a next generation power supply for the growing energy consumption of the humanity.

Because of the large cross-section, the reaction between deuterium (D) and tritium (T) is the best suited for controlled nuclear fusion on earth. They fuse producing a helium (He) nucleus and a neutron (n) according to

$$\mathrm{D} + \mathrm{T} \rightarrow {}^{4}\mathrm{He}\,(3.5\,\mathrm{MeV}) + \mathrm{n}\,(14.1\,\mathrm{MeV}). \tag{1.1}$$

This exothermic reaction releases a large amount of energy (17.6 MeV) compared to chemical reactions, with typical energies of the order of several eV.

The use of this processes as an energy source requires to confine the nuclear fuel (D and T) in a specific volume and heat it to temperatures in the order of the keV, at which the fusion reactions are highly probable. At such high temperatures the fuel atoms are fully ionized and form a plasma. Moreover the amount of energy produced by the fusion reactions has to be larger than the energy lost during the processes of heating and confining the plasma. This leads to the Lawson criterion [5]

$$nT\tau_E > 3 \cdot 10^{21}\,\mathrm{keV\,s/m^3}, \tag{1.2}$$

where n and T are the particle density and the temperature of the plasma, respectively. τ_E is the energy confinement time, which is the characteristic time after which the energy of the plasma is lost to the surrounding environment. Hence the task is to find methods to effectively confine the so-called fusion plasmas. Although several methods have been proposed [1, 6], the most developed approach is the so-called magnetic confinement nuclear fusion.

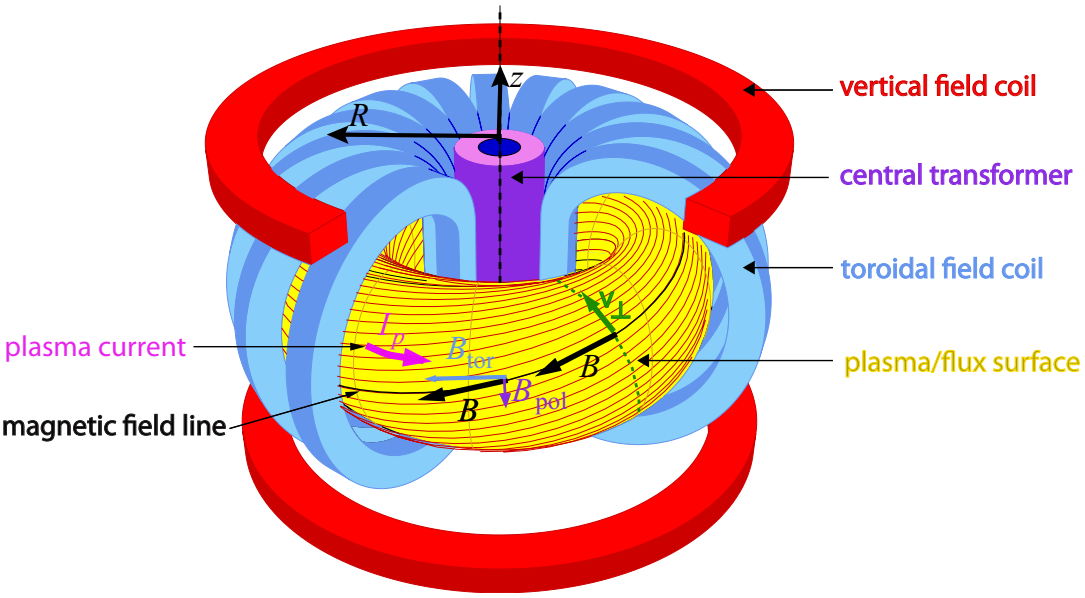

FIGURE 1.1: Schematic of a tokamak. The toroidal and vertical field coils, central transformer and plasma current I_p are indicated. The toroidal B_{tor}, poloidal B_{pol} and total $\mathbf{B}$ magnetic field are indicated. The resulting helical magnetic field line is depicted. Refer to the text for more details.

1.1 Magnetic confinement for nuclear fusion

Magnetic confinement is based on the principle that charged particles follow magnetic field lines circulating around them in the so-called *gyro-motion*. Hence charged particles constitutive of fusion plasmas can be confined with strong magnetic fields. Through history of magnetic confinement, different magnetic configurations have been investigated in several experimental devices [1, 2, 7]. Nowadays, the devices with the best performance are tokamaks and stellarators. In this section, basic properties and definitions of magnetic confinement are presented for the tokamak case. The magnetic configuration of stellarators will be discussed in Sec. 3.2.

Tokamaks are toroidally symmetric as schematically depicted in Fig. 1.1. The magnetic field $\mathbf{B}$ has toroidal, B_{tor}, and a poloidal, B_{pol}, components. The resulting magnetic field lines are helically twisted. The toroidal field is produced by external coils. The poloidal field is produced by a toroidal plasma current I_p, which is inductively driven by a central transformer. Vertical field coils are used for stability purposes. R is the distance to the symmetry axis and z the coordinate along it.

The magnetic field lines form nested magnetic flux surfaces, as the yellow one depicted in Fig. 1.1. The fast motion of particles along the magnetic field lines, named the *parallel* direction, makes the plasma parameters (as density and temperature) nearly uniform on the flux surfaces. On the contrary, along the *radial* (r) direction defined as perpendicular to the flux surface, plasma parameters may vary giving rise to gradients.

Electrons and ions in the plasma can be described as fluids. Due to the gyro-motion and collective effects, the fluids move with a velocity $\mathbf{v}_\perp$ on the flux surface and *perpendicularly* to the magnetic field. The propagation along the so-called *perpendicular*

direction is indicated in Fig. 1.1. The perpendicular fluid velocity consists of a combination of the $E \times B$ drift velocity $\mathbf{v}_{E\times B}$ and diamagnetic velocity $\mathbf{v}_{\mathrm{dia},j}$,

$$\mathbf{v}_{\perp,j} = \frac{\mathbf{E}\times\mathbf{B}}{B^2} - \frac{\nabla p_j \times \mathbf{B}}{n_j q_j B^2} = \mathbf{v}_{E\times B} + \mathbf{v}_{\mathrm{dia},j}, \tag{1.3}$$

where the sub-index j refers to electrons and ions. n_j is the particle density, $p_j = n_j T_j$ is the pressure with T_j the temperature, and q_j is the electric charge. $\mathbf{E}$ is the radial electric field, which is defined by the plasma potential ϕ through $\mathbf{E} = -\nabla\phi$. The electron density n_e is usually refer to as the plasma density n.

No motion across the flux surfaces is expected neither from the particle motion along the magnetic field lines nor from the perpendicular fluid velocity $\mathbf{v}_\perp$ However, different phenomena in the plasma produce an outward radial transport of energy and particles, which leads to a degradation of the confinement quality i.e. to a reduction of τ_E. The radial transport is at some extend produced by Coulomb collisions between the particles which lead to diffusion across the flux surfaces, this type of transport is called neoclassical [8]. Nevertheless, this contribution cannot account completely for the observed transport in fusion plasmas.

1.2 Turbulent transport

It has been found that fluctuations or turbulence in the plasma parameters may contribute significantly to radial transport [9, 10]. Turbulence in fusion plasma is triggered by micro-instabilities, which are driven by gradients of density and temperature. The irregular behaviour of the plasma generates turbulent eddies or structures with a finite radial size. They connect different flux surfaces contributing to radial transport. This contribution, called turbulent transport, is dominant for some operation regimes, e.g. the low confinement mode (L-mode) in tokamaks. The understanding of turbulence and its associated transport is an important task for improving the performance of magnetic confinement nuclear fusion devices.

A large progress has been made in the last years towards the modelling of turbulence in fusion plasmas [11]. The development of codes and the increase of computer power have made the simulation of the turbulence possible [12]. The comparison of detailed fluctuation measurements with theory and simulations is fundamental for the validation of simulation codes and for the understanding of the turbulence dynamics [13]. However from the experimental point of view, more detailed fluctuation measurements are required for comparison of specific features.

1.3 Doppler reflectometry

Doppler reflectometry is one of the diagnostic techniques used for fluctuation measurements in fusion plasmas [14]. It uses the backscattering of an injected microwave beam from density fluctuations at the so-called cutoff layer. This diagnostic provides local-

ized measurements of the perpendicular velocity ($u_\perp$) of the density fluctuations, and perpendicular wavenumber ($k_\perp$) resolved fluctuation level. Furthermore, the so-called radial correlation Doppler reflectometry uses two probing beams measuring at radially displaced positions. It allows to investigated the radial structures of the density fluctuations, in particular the radial correlation length L_r [15].

Doppler reflectometry and radial correlation Doppler reflectometry are techniques well suited for the characterization of the density fluctuations. Together, they can provide information on the structure of the turbulence on the radial-perpendicular plane. Nevertheless, the complexity of the wave propagation and the scattering processes in plasma introduce a non-trivial diagnostic response. Accordingly, diagnostic effects have been observed in experiments [16, 17], simulations [18, 19] and theory [20, 21]. Such effects have to be further investigated and need to be accounted for in the experimental data analysis in order to provide a more accurate and complete characterization of the turbulence.

1.4 Scope of this thesis

The aim of this thesis is two-fold. On the one hand, the Doppler reflectometry diagnostic, i.e. the wave propagation and scattering processes involved are investigated with a physical optics model, two-dimensional full-wave simulations, and in Born approximation. The impact of diagnostic effects on the measurements, and the characterization of the turbulence using correlation measurements are studied in detail. A new analysis technique able to provide information on the mean tilt angle of the turbulent structures on the radial-perpendicular plane is developed. This is a measurement of the turbulence anisotropy relevant for investigations of the turbulent dynamics.

On the other hand, Doppler reflectometry is applied in the ASDEX Upgrade tokamak and the TJ-II stellarator for turbulence characterisations. The fluctuation level, radial correlation length L_r, and propagation velocity $u_\perp$ of the density fluctuations are simultaneously investigated. The experimental data are interpreted based on the modelling results and the influence of diagnostic effects on the measurements are discussed. The tilt angle of the turbulent structures is measured in the core region of both devices for the first time. This new measurements are compared with results from gyrokinetic simulations.

The thesis is organized as follows: The fist four chapters are of introductory character. Chapter 2 gives an overview of the turbulence in fusion plasmas and the aspects to be considered in this work. Chapter 3 introduces the experimental devices, the ASDEX Upgrade tokamak and the TJ-II stellarator, as well as the heating systems and diagnostics relevant for this thesis. In chapter 4 the Doppler reflectometry technique is presented in detail. The modelling of the diagnostic is presented in chapters 5–7: Chapter 5 introduces the modelling tools which are applied in chapters 6 and 7 to the power response and correlation measurements, respectively. The experimental characterization of the turbulence in both devices is presented in chapter 8. In chapter 9 the tilt angle measurement is used to investigated different turbulence regimes in the ASDEX Upgrade tokamak. Finally, in chapter 10 the conclusions and an outlook are given.

Chapter 2

Turbulence in fusion plasmas

The turbulence is an inherent process in nature characterized by stochastic fluctuations of the quantities describing physical systems. Turbulence is nowadays an active research field with relevance in several physical systems, among them magnetic confinement nuclear fusion devices, where turbulent transport degrades the energy confinement time [9, 10]. In this chapter, general aspects of turbulence are introduced for the neutral fluid case. Then, the properties of the turbulence in fusion plasmas to be investigated in this thesis are discussed.

2.1 Neutral fluid case and spectral properties of the turbulence

Neutral fluids offer a classical example of turbulence. In incompressible fluids, described by the Navier-Stockes equation, the Reynolds number Re is the parameter governing the flow regime [22]. Re is defined as the ratio between the inertial and the viscous forces in a fluid. For $Re \ll 1$, viscosity dominates and homogenises the fluid velocity, obtaining a laminar flow as depicted in Fig. 2.1a. On the contrary, for $Re \gg 1$ the inertial forces dominate and give rise to a turbulent flow characterized by turbulent eddies or structures as depicted in Fig. 2.1b.

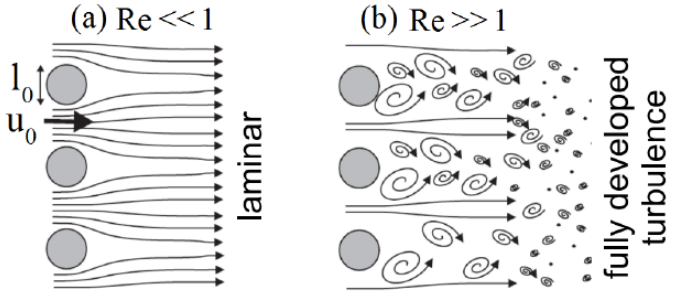

FIGURE 2.1: Artistic representation of (a) laminar and (b) turbulent flows in neutral fluids for different Reynolds numbers Re. Turbulent structures or eddies are indicated in (b). Adapted from Ref. [22].

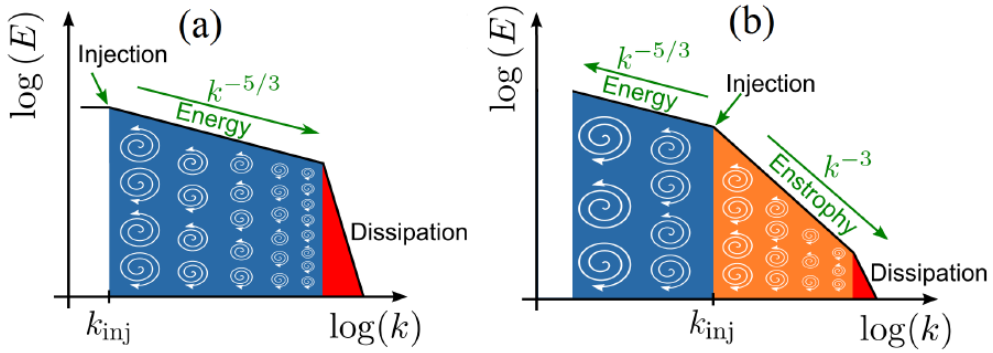

FIGURE 2.2: (a) Kolmogorov k spectrum for a 3D fluid turbulence. The energy with a spectral index $-5/3$ is indicated. (b) k-spectrum for 2D fluid turbulence. Energy and enstrophy cascades with spectral indices of -3 and $-5/3$ are indicated. The eddy size are schematically depicted (adapted from Ref. [26])

In the turbulent flow case, energy is injected into the system at the scale l_0. Then, the inertial forces allows a non-linear energy transfer to other length scales, which lead to the production of eddies or structures of multiple sizes. This so-called energy cascade, redistributes the energy over a wide range of length scales described by the wavenumber k, which is the inverse of the structure size. The energy distribution across different scales is described by the wavenumber (k) spectrum of the turbulence.

In the case of isotropic three-dimensional (3D) fluid turbulence, the energy distribution is described by the Kolmogorov k spectrum [23]. The spectral energy per wavenumber follows a power law $E(k) \sim k^{\nu}$, with a spectral index $\nu = -5/3$ in the so-called inertial range. This scaling is obtained by considering non-linear energy transfer from the injection scale $k_{\mathrm{inj}} \sim l_0^{-1}$ towards smaller scales or equivalently larger k. Above the inertial range, the viscosity dominates and the energy is dissipated. The Kolmogorov spectrum is depicted in Fig. 2.2a. The energy cascade from the injection scale towards smaller scales is indicated, and the eddy size is schematically depicted.

The situation is different for isotropic 2D fluids. In this case, the dimensional constraint makes the enstrophy an invariant [24, 25]. Thus two cascades are produced. An inverse energy cascade towards large scales characterized by a spectral index of $-5/3$, and a direct enstrophy cascade towards smaller structures with a spectral index of -3. The k spectrum for the 2D case is depicted in Fig. 2.2b, the energy and enstrophy cascades are indicated.

The k spectrum gives a statistical characterization of the turbulence, which provides information on the non-linear energy transfer processes and the energy injection scale. The turbulence in fusion plasmas can be also characterized in terms of the k spectra, however, deviations from the two cases described before are to expected because of the complexity of fusion plasmas as discussed next.

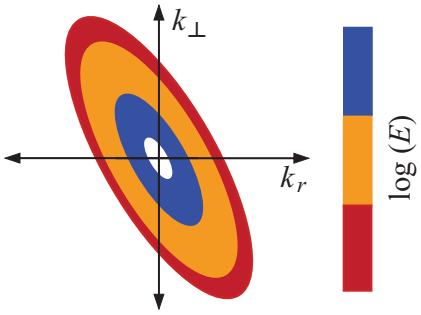

FIGURE 2.3: Schematic 2D spectrum as a function of radial (k_r) and perpendicular ($k_\perp$) wavenumbers. Elongation and tilt indicate the anisotropy of the turbulence in the radial-perpendicular plane.

2.2 Characterization of turbulence in fusion plasmas

The turbulence in fusion plasmas is more complex than the neutral fluid case. Among other reasons, the complexity arises because of different reasons: (i) Electrons and ions in plasma imply the presence of two fluids interacting between each other and with electromagnetic fields. (ii) Fluctuations (indicated with δ) of multiple quantities are involved: δn, δT_i, δT_e, $\delta\phi$, δB. (iii) Different micro-instabilities may lead to multiple energy injection scales which may overlap with the dissipation range [27]. (iv) The fast motion of particles along the strong magnetic field smooths out fluctuations in the parallel direction, hence the turbulence can be rather described as 2D in the radial-perpendicular plane. Even in this plane, isotropy is not expected because of the radial gradients of the plasma parameters [28, 29].

Because of the anisotropy, the k spectrum has to be specified by the radial (k_r) and perpendicular ($k_\perp$) wavenumbers. A schematic 2D wavenumber spectrum is depicted in Fig. 2.3 in the $(k_r, k_\perp)$-plane. The elongation and tilt of the spectrum manifest the anisotropy of the turbulence. For instance, the energy distribution of the density fluctuations over the wavenumber can be written as

$$E(k_r, k_\perp) \sim |h(k_r, k_\perp)|^2 \delta n_{\mathrm{rms}}^2, \tag{2.1}$$

where $|h(k_r, k_\perp)|^2$ is the 2D wavenumber spectrum and δn_{rms} is the density *fluctuation* or *turbulence level*. Measurements of the 2D k spectrum would provide detailed information on the properties of the turbulence in the radial-perpendicular plane. Nevertheless, such an experimental characterization is challenging.

Fluctuation diagnostics such as Doppler reflectometry provide perpendicular wavenumber ($k_\perp$) resolved measurements of the fluctuation level. Hence it is useful to define the $k_\perp$ spectrum $|h_\perp(k_\perp)|^2$ of the fluctuations along the perpendicular direction,

$$E(k_\perp) \sim |h_\perp(k_\perp)|^2 \delta n_{\mathrm{rms}}^2, \tag{2.2}$$

The relationship between the 2D k spectrum and the $k_\perp$ spectrum will be discussed in detail in Ch. 6.

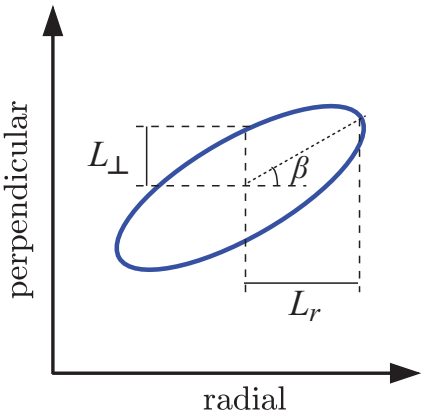

FIGURE 2.4: Schematic representation of an average turbulent structure on the radial-perpendicular plane. The size along radial (L_r) and perpendicular ($L_\perp$) directions are indicated. The tilt angle β with respect to the radial direction is depicted.

The experimentally measured $k_\perp$ spectra are typically Kolmogorov-like [16, 17, 30, 31, 31, 32], although the spectral indices differ from the cases discussed in Sec. 2.1. In the low $k_\perp$ range, spectral indices in the range -1.5 to -3.5 have been measured, which is closed to fluid predictions. Whereas in the large $k_\perp$ range, more pronounced spectral indices have been observed from -6 to -9 [16, 17, 30, 31]. The regions with different spectral indices are separated at $k_\perp \rho_i \sim 1$ where $\rho_i = \sqrt{m_i T_i}/eB$ is the ion Larmor radius (m_i is the ion mass). This is a characteristic length scale for micro-instabilities. Kolmogorov-type wavenumber spectra have been also found in simulations. The spectral indices are in the same range as the experimental measurements [17, 28], moreover they depend on specific plasma conditions and the dominant micro-instabilities. Furthermore, differences of the spectra along the radial and the perpendicular directions have been found, as an evidence of the anisotropy of the turbulence [28].

The correlation properties of the turbulence provide also a statistical characterization in space and time. The correlation length indicates the distance within which the fluctuations are correlated. This is equivalent to the average size of the turbulent structures or eddies. In Fig. 2.4 an average turbulent structure is schematically shown in the radial-perpendicular plane. The radial (L_r) and perpendicular ($L_\perp$) correlation lengths define the average structure size. Note that the structure can be elongated ($L_r \neq L_\perp$) and tilted by an angle β with respect to the radial direction. The average tilt angle highlights the turbulence anisotropy on the radial-perpendicular plane.

The intrinsic dynamics of the turbulence leads to the generation and destruction of structures. The decorrelation time of the turbulence τ_d indicates the time after which the fluctuations decorrelate, or equivalently the mean life time of the structures.

2.3 Interaction with plasma flows

The turbulence propagates is the perpendicular direction with a velocity,

$$u_\perp = v_{E\times B} + v_{\text{ph}} \tag{2.3}$$

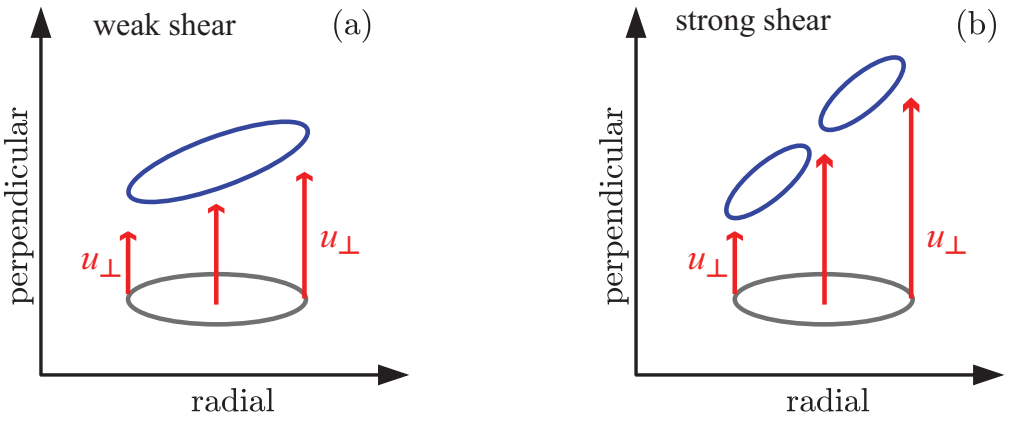

FIGURE 2.5: Schematic representation of the effect of sheared $u_\perp$ on turbulent structures. (a) A weak shear stretches and tilts the structure, while (b) a strong shear turns the structure apart.

where $v_{E\times B}$ is defined as in Eq. 1.3 and v_{ph} is the phase velocity. Eq. 2.3 implies that turbulence is advected by the $E \times B$ flow and has an intrinsic velocity v_{ph} in the plasma frame.

The dynamics of turbulence and plasma flows is strongly coupled [33]. One of the mechanisms relevant for this interplay is the turbulence regulation by sheared flows. The mechanism is schematically shown in Fig. 2.5 on the radial perpendicular plane, where one turbulent structure (in grey) propagates in a region with a $u_\perp$ gradient. In the case of a weak velocity shear (a), the structure is tilted and stretched by the sheared flow. In the case of strong shear (b), the structure is strongly deformed and is torn apart, which implies a reduction of the turbulence level and the radial correlation length. This turbulence suppression by sheared flows has been proposed as the mechanism responsible of the turbulence reduction and confinement improvement observed in the high confinement mode (H-mode) in tokamaks [34].

The interplay between turbulence and flows occurs also in the opposite direction, hence turbulence can excite flows by the Reynolds stress mechanism [33, 35, 36]. Self-organization of the turbulence may produce radially localized band-like flow patterns, named zonal flows [37]. Furthermore, it has been found that the residual stress observed in momentum transport is accounted for by contributions of turbulence with a finite tilt angle β through the Reynolds stress [36, 38, 39]

The previous mechanisms reveal that the tilt angle of the turbulent structures is a relevant element for investigating the interaction between turbulence and plasma flows. Moreover, it is a quantity predicted by theories and simulations which could be compared with experimental measurements. Nevertheless tilt angle measurements are challenging, especially in the confined region of fusion plasmas. One of the major contributions of this thesis is the development of a new method for measuring the mean tilt angle of the turbulent structures in the confined region.

2.4 Turbulence drive and micro-instabilities

The turbulence in fusion plasmas is triggered by micro-instabilities. The radial gradients of the plasma parameters provide the energy that drives micro-instabilities on the mm scale. Once micro-instabilities have been exited, non-linear processes redistribute the energy on a broad range of scales. As a results turbulence develops.

Micro-instabilities are characterized by their drive, length scale and phase velocity v_{ph}. The drive is given in terms of the normalized gradients $\nabla n/n$, $\nabla T_e/T_e$ and $\nabla T_i/T_i$. The length scale is specified by $k_\perp$ and typically normalized to the ion Larmor radius ρ_i, which is one relevant scale for micro-instabilities.

The main micro-instabilities and types of turbulence relevant for fusion plasmas are listed below:

- *Ion temperature gradient (ITG) mode*: This instability is driven by $\nabla T_i/T_i$ and stabilized by $\nabla n/n$. This mode propagates in the ion diamagnetic direction and its scale is $k_\perp \rho_i \lesssim 1$ [40].

- *Electron temperature gradient (ETG) mode*: This instability is driven by $\nabla T_e/T_e$ and stabilized by $\nabla n/n$. This mode propagates in the electron diamagnetic direction and its scale is $k_\perp \rho_i \gg 1$ [41].

- *Trapped electron mode (TEM)*: This instability is produced by electrons in trapped orbits and hence driven by $\nabla T_e/T_e$ and $\nabla n/n$. It is stabilized by collisions which lead to de-trapping of electrons. This mode propagates in the electron diamagnetic direction and has a typical size of $k_\perp \rho_i \lesssim 1$ [42].

- *Electromagnetic drift-wave (EDW)*: In the plasma edge, for $(\nabla n/n) \gtrsim (\nabla T_{i,e}/T_{i,e})$ the turbulence is of electromagnetic character. The typical scale for this type of turbulence is $k_\perp \rho_i \lesssim 1$ and the propagation velocity is in the electron diamagnetic direction [43, 44, 45].

2.5 Gyrokinetic simulations

The accurate modelling and prediction of turbulence in fusion plasmas a is complex task. Nowadays, the *gyrokinetic theory* is the most accurate framework for describing turbulence in magnetized plasmas. It performs a dynamical reduction of the system based on dynamical invariants related to the gyro-motion of the particles.

The gyrokinetic theory has been implemented in several codes specialized for several experimental devices [12, 41, 46, 47, 48]. Gyrokinetic simulations have provided a better understanding of the core turbulence in fusion plasmas. Recently, gyrokinetic simulations have been also applied to astrophysical plasmas [49, 50]. In this thesis, results from the gyrokinetic codes GENE [41] and GKW [46] for the ASDEX Upgrade tokamak, and from EUTERPE [47, 48] for the TJ-II stellarator are discussed.

Chapter 3

Experimental devices

In this chapter the two experimental devices used in this thesis are introduced; the ASDEX Upgrade tokamak (AUG) and the TJ-II stellarator. The relevant heating systems and diagnostic are also presented.

3.1 ASDEX Upgrade tokamak

The **A**xial **S**ymmetric **D**ivertor **EX**periment ASDEX Upgrade (AUG) is the tokamak in operation since 1990 at IPP in Garching, Germany [51]. The tokamak concept has been already introduced in Ch. 1.1. In addition to the toroidal and vertical field coils depicted in Fig. 1.1, AUG has further coils for shaping and fast stabilization of the plasma, as well as for the formation of the X-point characteristic of the divertor configuration. AUG has a major radius of $R_0 = 1.65$ m defined as the distance from the axis of symmetry to the center of the plasma or the magnetic axis. The cross-section of the plasma is D-shaped with a minor horizontal radius of 0.5 m and a minor vertical radius of 0.8 m. The toroidal magnetic field decays with R following $B_{\mathrm{tor}}(R) = B_0 R_0/R$. B_0 is the field on the magnetic axis which can vary between 1.0 and 3.1 T.

In Fig. 3.1, the poloidal cross-section of AUG is shown for two configurations that will be discussed next. The flux surfaces are depicted by solid and dashed lines. The solid grey lines represent closed flux surfaces where the plasma is confined. The dashed lines represent open flux surfaces containing magnetic field lines touching the walls of the machine. In this so-called scrape-off layer, particles follow the magnetic field lines until reaching the wall, therefore the plasma is not confined in this region. The separatrix (indicated with red) is the last closed flux surfaces separating the confined and the unconfined regions.

In the divertor configuration, the separatrix forms an X-point as depicted in Fig. 3.1. The divertor configuration moves the plasma-wall interaction far from the confined region, minimizing the influx of impurities into the plasma and focusing the heat load onto specially designed divertor targets. The flexibility of AUG allows to produce the X-point below the plasma as depicted in (a) and above as depicted in (b). The two configurations are called lower and upper single null (LSN and USN), respectively.

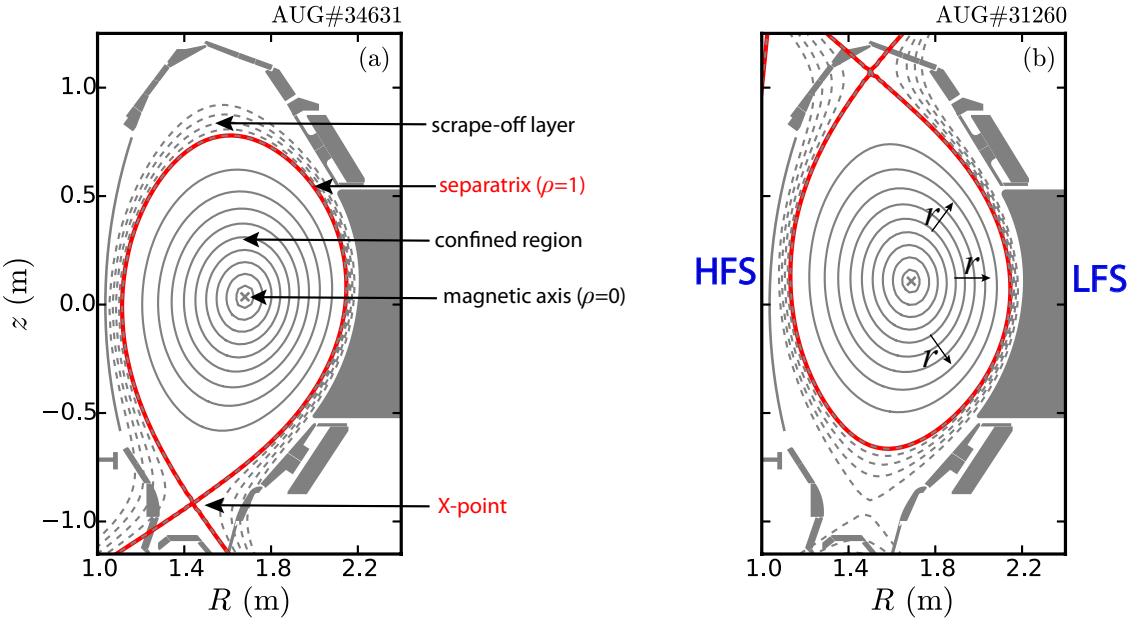

FIGURE 3.1: Poloidal cross-section of the ASDEX Upgrade tokamak. Flux surfaces are depicted by solid and dashed lines for the (a) upper and (b) lower single null configurations. Refer to the text for more details.

The flux surfaces are labelled with ρ (poloidal) defined as

$$\rho = \sqrt{\frac{\Psi - \Psi_a}{\Psi_s - \Psi_a}} \tag{3.1}$$

where Ψ is the poloidal magnetic flux and the sub-indices a and s stand for the magnetic axis and the separatrix. Hence $\rho = 0$ at the magnetic axis and 1 at the separatrix. ρ specifies the radial position in the plasma and its gradient ($\nabla\rho$) defines the radial r direction as indicated in Fig. 3.1b.

Because of the $1/R$ dependence of the toroidal magnetic field, the left hand side of the plasma is referred to as the high field side (HFS), whereas the right hand side is the low field side (LFS). Both are indicated in Fig. 3.1b.

3.2 TJ-II stellarator

TJ-II is a 4-periodic flexible heliac type stellarator [52]. It has been in operation since 1997 at CIEMAT in Madrid, Spain. Differently to the tokamak where the poloidal magnetic filed is achieved with a plasma current, in stellarators the helical magnetic field is completely produced by external coils. In TJ-II, the magnetic field is generated by the coil system depicted in Fig. 3.2a. It is composed by 32 toroidal field coils, 4 vertical field coils, one circular coil and one helical coil. The plasma circulates four times around the circular and helical coils as depicted in the figure. The circular coil with radius $R_0 = 1.5$ m defines the major axis. The average minor radius of the plasma is at the most 0.2 m depending on the magnetic configuration to be discussed next.

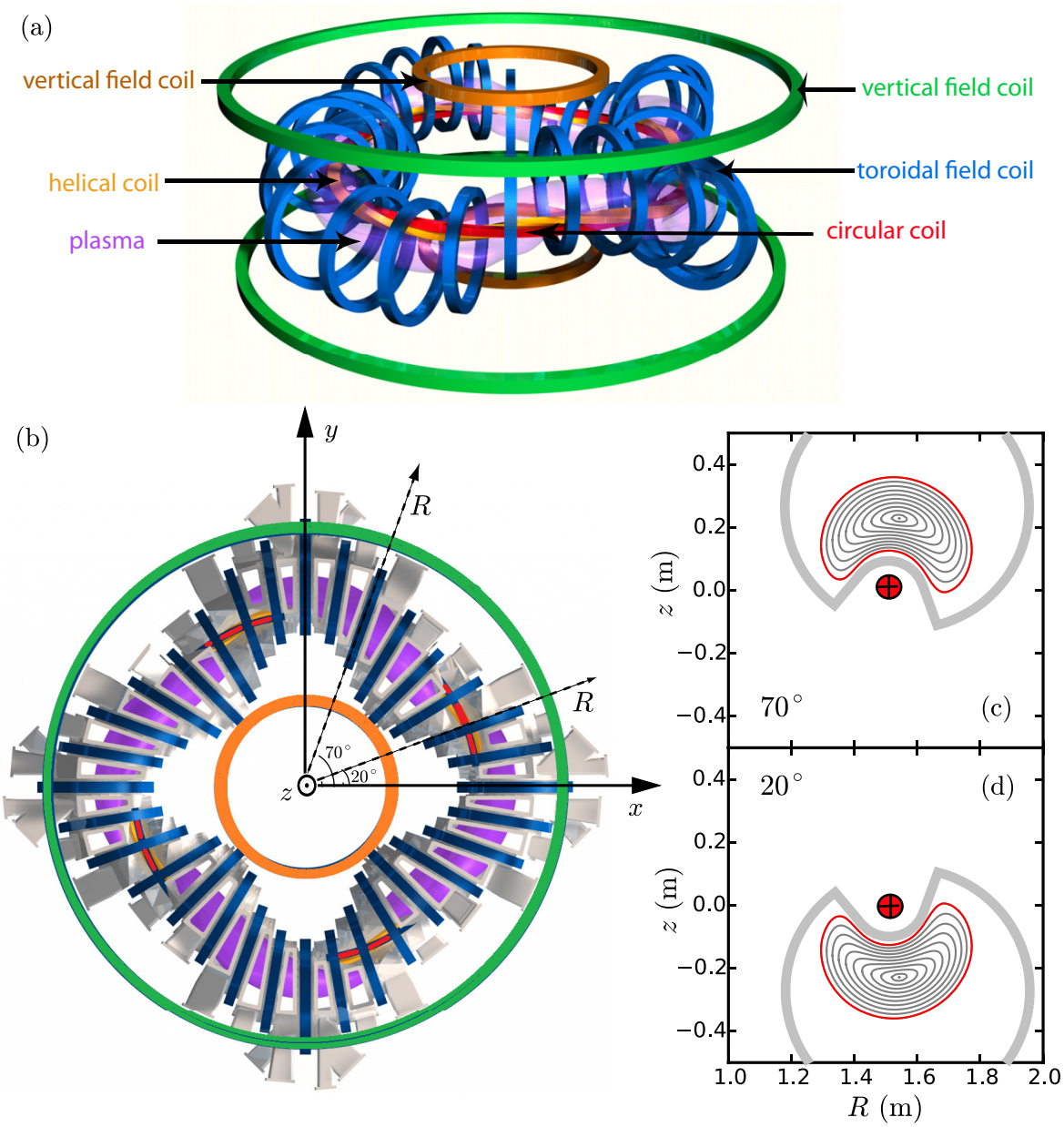

FIGURE 3.2: Schematic of the TJ-II coil system including the plasma; (a) 3D view and (b) top view indicating cartesian coordinates and R at two toroidal angles. Poloidal cross-section the toroidal angles (c) 70° and (d) 20°. Flux surfaces, vessel (light grey) and the circular coil (red $\oplus$) are depicted. Refer to the text for more details.

The periodicity of the machine is evident in the top view in Fig. 3.2b. In addition to the coils and plasma, elements of the vessel have been also included. The Cartesian coordinates (x, y, z) are indicated, moreover the coordinate R is indicated for the toroidal angles 20 and 70°. Note that at these positions, the plasma is either above or below the circular and helical coils.

The currents in the coils can be adjusted, which provides TJ-II with a high flexibility of the magnetic configuration. Several configurations characterized by a different plasma volume and rotational transform can be achieved. The magnetic field on the magnetic axis is about 1 T. The magnetic configuration investigated in this work is the standard one (labelled 100_44_64).

In TJ-II, neither the plasma nor the flux surfaces are toroidally symmetric. The poloidal cross-section of TJ-II at two toroidal angles is shown in Figs. 3.2c and d. Closed flux surfaces are depicted by grey lines and the separatrix by a red line. The vessel and the circular coil are also shown. The flux surfaces are bean-shaped. Furthermore as a consequence of the plasma winding around the circular coil, the flux surfaces appear above and below it in (c) and (d), respectively. The flux surfaces are labelled with ρ as discussed in the previous section for AUG, with $\rho = 0$ at the magnetic axis and $\rho = 1$ at the separatrix.

3.3 Heating systems

Plasmas have to be heated in order to achieve fusion relevant temperatures in the keV range. In the tokamak case, the plasma current I_p (introduced in Sec. 1.1) heats the plasma due to its finite conductivity. Nevertheless this *Ohmic heating* is not efficient to achieved the relevant temperatures and it is not available in stellarators where no plasma current is driven. The high temperatures are achieved by external heating methods. Here the heating systems relevant for this thesis are introduced:

- *ECRH*: *E*lectron *C*yclotron *R*esonance *H*eating is based on the energy transfer from externally injected electromagnetic waves to the electrons in the plasma. This happens at positions where the wave is resonant with the gyro-motion of the electrons, i.e. the wave frequency matches a harmonic of the electron cyclotron frequency $\omega_c = eB/m_e$. e and m_e are the electron charge and mass, respectively.

  AUG is equipped with eight gyrotrons operating at 140 GHz for heating at the second harmonic of ω_c. Together, they deliver up to 6 MW power [53]. TJ-II is equipped with two gyrotrons operating at 53.2 GHz also for heating at the second harmonic of ω_c, with 300 kW heating power each [54].

- *NBI*: *N*eutral *B*eam *I*njection is based on the energy transfer by energetic neutral atoms to the plasma. A beam of neutral particles is accelerated and sent into the plasma. The neutral atoms of the beam get ionized by collisions with the plasma particles and get confined by the magnetic field. Afterwards, energy is transferred to the plasma by collisions with electrons and ions.

  The NBI system in AUG is composed by two injectors with four sources each, providing a maximum heating power of 20 MW [53]. TJ-II has two injectors with a heating power of up to 1 MW each [55].

3.4 Relevant diagnostics

AUG and TJ-II are equipped with several diagnostics that measure physical quantities required for the plasma operation and physical investigations. In this section, the diagnostics used in this thesis for measurements of plasma density n, electron and ion temperatures (T_e and T_i) and ion velocity are introduced. The Doppler reflectometry which is the main diagnostic used for the turbulence investigations will be discussed in detail in Ch. 4.

- *Thomson Scattering* uses the incoherent scattering of a laser off electrons for measuring their density and temperature. The scattered radiation is measured locally along the laser trajectory. The scattered power is proportional to n and the spectral Doppler broadening to T_e. There are two systems installed on AUG, one for measuring the core and one for the edge. The core system works with 16 lines of sight and a time resolution of 3 ms, whereas the edge system has 11 lines of sight and 8 ms time resolution [56]. TJ-II has a high resolution system with 160 lines of sight, but with a single pulse per discharge [57].

- *Interferometry* provides a line average electron density ($\bar{n}$) measurement. It uses the phase difference between a laser passing through the plasma and a reference one. Due to the density dependence of the refraction index (cf. Eq. 4.4), the phase difference provides the average electron density along the laser path (for more details on the wave propagation in plasmas refer to Sec. 4.1).

  In AUG, 6 interferometer channels are installed. They provide line average densities along different lines of sight [58]. In this thesis the core (H-1) and edge (H-5) channels are used. TJ-II has a single channel interferometer passing through the magnetic axis [59].

- *Standard reflectometry* uses a microwave beam injected perpendicularly to the flux surfaces. The probing frequency is such that the wave is reflected at the cutoff position where the refractive index drops to zero (cf. Sec. 4.1). From a scan of the probing frequency and the phase comparison between the injected and reflected wave, the density profile is computed [60]. TJ-II has a reflectometer using X-mode polarization in a frequency range of 25–50 GHz [61].

- *Electron cyclotron emission (ECE)* provides localized electron temperature (T_e) measurements. Electrons in their gyro-motion emit bremsstrahlung radiation at harmonics of ω_c. For an optically thick plasma, the intensity of the radiation is proportional to T_e according to Planck's radiation formula. Moreover, the measurements can be spatially localized by mapping ω_c to the radial direction considering the $1/R$ dependence of the magnetic field. AUG has an ECE system with 60 frequency channels at the second harmonic of ω_c, corresponding to 60 radial positions [62].

- *Charge exchange recombination spectroscopy (CXRS)* relies on the charge exchange reactions between NBI atoms and impurity ions in the plasma. After the charge exchange reaction, the impurity is in an exited state. It decays and emits photons at specific frequencies. The intensity of the radiation provides a measurement of the impurity density. The velocity of the impurities induces a Doppler shift of the spectral line, and the thermal motion a broadening. Thus, the velocity and temperature of the impurities are obtained from spectroscopic measurements. The thermal equilibration between main ions and impurities on the 100 μs scale allows to assume the ion temperature T_i equal to that of the impurities [63].

  From the CXRS data, the radial electric field E_r can be computed using the radial force balance equation for ions. It can be obtained by taking the cross-product of Eq. 1.3 with $\mathbf{B}$. For a toroidal geometry one obtains

$$E_r = \frac{\nabla p_i}{n_i q_i} - v_{i,\mathrm{pol}} B_{\mathrm{tor}} + v_{i,\mathrm{tor}} B_{\mathrm{pol}}, \tag{3.2}$$

  where $v_{i,\mathrm{tor}}$ and $v_{i,\mathrm{pol}}$ are the components of the ion velocity in toroidal and poloidal directions, respectively.

  AUG has a core and an edge CRXS system measuring at the mid-plane during NBI heated phases or during short NBI blips. The core system has toroidal lines of sights that provide measurements of the toroidal velocity [64].

- *Lithium beam emission spectroscopy* uses a beam of energetic lithium atoms injected into the plasma. The lithium atoms are excited by collisions in the plasma, and then decay emitting photons at frequencies characteristic of the atomic transitions. In particular, the intensity of the transition 2p→2s (670.8 nm) is measured on different lines of sight. Using a forward model, the plasma density is deduced at the edge and in the scrape-off layer. Details on the AUG lithium beam diagnostic are given in Ref. [65].

Chapter 4

Doppler reflectometry

Doppler reflectometry is an established diagnostic technique used for the characterization of density turbulence and plasma flows in magnetic confinement fusion experiments. It uses an obliquely injected microwave beam which is backscattered by density fluctuations. This technique has been used first on the W7-AS stellarator [66]. The capabilities of Doppler reflectometry to provide $k_\perp$ resolved information on the fluctuation level and perpendicular velocity of the density fluctuations have been shown in experiments [67] and simulations [18]. Nowadays there are Doppler reflectometry systems installed on several fusion machines around the world [14, 30, 68, 69, 70]. They have provided experimental data relevant for studies of turbulence and plasma dynamics. For some examples see Ref. [71, 72, 73].

The radial structure of the density turbulence has been investigated by using two probing waves launched simultaneously from the same antenna [15, 16]. This technique is called radial correlation Doppler reflectometry and provides an estimate of the radial correlation length L_r of the density turbulence.

Doppler reflectometry is the main experimental technique used in this thesis for the study of turbulence in fusion plasmas. In this chapter, the waves in magnetized plasmas relevant for the diagnostic are introduced. Afterwards the physical mechanism of the diagnostic is reviewed. At the end, the Doppler reflectometer system installed on the ASDEX Upgrade tokamak and on the TJ-II stellarator are presented.

4.1 Wave propagation in magnetized plasmas

In magnetized plasmas, electrons and ions interact with the electromagnetic fields and with the background magnetic field $\mathbf{B}$, allowing for a large variety of wave phenomena [74]. In this section, only the electromagnetic waves relevant for Doppler reflectometry are introduced.

The wave propagation is determined by the refractive index N which relates wavenumber k and the frequency ω of the wave through the dispersion relation

$$k = \frac{\omega}{c} N = k_0 N, \tag{4.1}$$

where c is the speed of light and $k_0 = \omega/c$ is the vacuum wavenumber. Waves propagate for positive N and are reflected when the cutoff condition $N = 0$ is fulfilled.

For the high frequencies in the GHz range used in Doppler reflectometry, the plasma response to the electromagnetic field is defined only by the electrons. Ions are much heavier, hence they do not respond to the electromagnetic field on the short time scale defined by the frequency of the wave. Moreover, despite the high temperatures of fusion plasmas the thermal velocity of electrons is smaller than the phase velocity of the wave; $v_{\mathrm{th}} \ll \omega/k$. This justifies neglecting thermal effects in the so-called *cold plasma approximation*. Furthermore relativistic effects are also neglected because the electron temperature is substantially below the electron rest mass, $T_e \ll 511$ keV.

Two quantities determine the plasma response to the electromagnetic waves under consideration: The electron plasma frequency ω_p defines the characteristic time scale at which plasmas respond to electromagnetic fields,

$$\omega_p = \sqrt{\frac{ne^2}{\epsilon_0 m_e}}, \tag{4.2}$$

where ϵ_0 is the vacuum permittivity, e and m_e are the electron charge and mass, respectively. The electron cyclotron frequency ω_c is the frequency of electrons in their gyro-motion,

$$\omega_c = \frac{eB}{m_e}. \tag{4.3}$$

For propagation perpendicular to the background magnetic field ($\mathbf{k} \perp \mathbf{B}$) the polarization of the wave, given by the direction of the electric field, defines two propagation modes. The ordinary (O) mode with a polarization parallel to $\mathbf{B}$ and the extraordinary (X) mode with a polarization perpendicular to $\mathbf{B}$.

The O-mode refractive index is

$$N_O^2 = \left(1 - \frac{\omega_p^2}{\omega^2}\right) = \left(1 - \frac{n}{n_c}\right), \tag{4.4}$$

with the cutoff density

$$n_c = \frac{\omega^2 \epsilon_0 m}{e^2}. \tag{4.5}$$

This is the density required to match the cutoff condition given by $\omega = \omega_p$.

The X-mode dispersion relation is

$$N_X^2 = \left(1 - \frac{\omega_p^2}{\omega^2} \frac{\omega^2 - \omega_p^2}{\omega^2 - \omega_p^2 - \omega_c^2}\right) \tag{4.6}$$

with the cutoff condition fulfilled for $\omega = \frac{1}{2}\left(\sqrt{\omega_c^2 + 4\omega_p^2} + \omega_c\right)$.

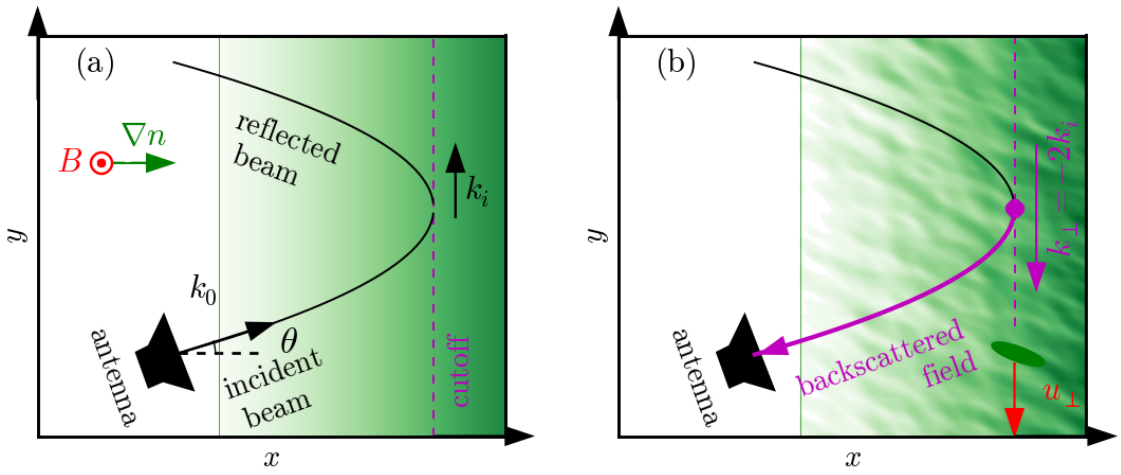

FIGURE 4.1: Schematics showing the physical mechanism of Doppler reflectometry in slab geometry. (a) The probing microwave beam propagates in a plasma without turbulence. The beam bends due to the plasma density increase and is reflected at the cutoff layer. (b) The density fluctuations produce scattering at the cutoff layer satisfying the Bragg's condition. The backscattered radiation is collected by the emitting antenna.

4.2 Physical mechanism

In this section the physical mechanism relevant for Doppler reflectometry is presented. For the sake of simplicity, the slab case is used here. The slab geometry is commonly used in several fields of fusion research, in particular it is often used for Doppler reflectometry modelling [18, 19, 21]. Furthermore, most of the modelling presented in chapters 5, 6 and 7 is done in this geometry.

The slab geometry is depicted in Fig. 4.1a, where the green color represents the plasma density n which grows with x. The plasma-vacuum boundary is indicated with a green line. The background magnetic field and density gradient directions are indicated in the upper-left corner of the figure. The slab geometry is used as a local approximation to fusion plasmas provided that the x, y and z directions are related to the radial, perpendicular and magnetic field directions, respectively.

In Doppler reflectometry a microwave beam is sent into the plasma by an emission/reception antenna located outside the plasma. In Fig. 4.1 the antenna is depicted in black in the lower left corner. The center of the microwave beam is indicated with a black ray. The launching direction defines an angle of incidence θ with respect to the normal of the plasma boundary as depicted in the figure. The probing frequency of the beam f_0 defines the vacuum wavenumber $k_0 = 2\pi f_0/c$ outside the plasma where the refractive index N is 1. The beam enters the plasma and propagates to regions with higher plasma density n and smaller N. As a consequence the beam bends and is reflected outwards at the so-called cutoff layer (magenta line in the figure) where N is minimum. Consequently, the wavenumber decreases and reaches a minimum k_i at the cutoff where it is purely perpendicular to the density gradient. Moreover the electric field of the wave is amplified at the cutoff [75].

The density fluctuations interact with the probing beam and produce scattering along the beam path. However, the maximum of the electric field at the cutoff makes the diagnostic mainly sensitive to the scattering in this region, thus Doppler reflectometry provides spatially well localized measurements of the density fluctuations. Furthermore, the use of the same antenna for emission and reception, makes the diagnostic mostly sensitive to the backscattering from the density fluctuations with perpendicular wavenumber ($k_\perp$) fulfilling Bragg's condition at $k_\perp = -2k_i$, where k_i is the wavenumber of the incident microwave beam [14]. The backscattered wave propagates from the cutoff back to the antenna where it is detected as the reflectometer signal V. The propagation back to the antenna is depicted by a magenta ray in Fig. 4.1b. For typical experimental conditions $k_\perp$ is in the range of several cm^{-1}.

For the slab geometry, the $k_\perp$ of the fluctuations satisfying Bragg's condition is given by

$$k_\perp = 2k_0 \sin\theta. \tag{4.7}$$

For a general configuration including the real plasma geometry and density and magnetic field profiles, $k_\perp$ and the cutoff position are obtained using ray tracing techniques [76]. The trajectory and local wavevector of the ray are computed from a WKB approximation of the wave equations in the cold plasma approximation. The implementation of the ray tracing for AUG and TJ-II will be discussed later in this chapter.

If a linear interaction of the wave with the density fluctuations is assumed, the diagnostic response is said to be *linear*. This condition is fulfilled for small turbulence level, e.g. in the plasma core. In this case the backscattered power P is proportional to the $k_\perp$ resolved turbulence level [14],

$$P \propto \delta n_{\mathrm{rms}}^2 h_\perp^2(k_\perp), \tag{4.8}$$

where $h_\perp(k_\perp)$ is the $k_\perp$ spectrum and δn_{rms} is the density turbulence level. For high turbulence levels, *non-linear* effects may produce significant deviations from Eq. 4.8. The detailed response of P to the turbulence level δn_{rms} and $k_\perp$ spectrum is called *power response*, and is one of the main modelling topics of this thesis studied in detail in Ch. 5 and 6.

The motion of the density fluctuations with a velocity $\mathbf{u}$ induces a Doppler shift in the frequency of $f_D = \omega_D/(2\pi)$ in the backscattered wave. The Doppler shift depends on $\mathbf{u}$ and the scattered wavenumber $\mathbf{k}_s$ according to

$$\omega_D = \mathbf{u}\cdot\mathbf{k}_s = \cancel{u_r k_r} + u_\perp k_\perp + \cancel{u_\parallel k_\parallel}. \tag{4.9}$$

The dot product is written in the radial, perpendicular and parallel components corresponding to the x-, y-, and z-coordinates of the slab case, respectively. The radial term is neglected with respect to the perpendicular one because in the confined region $u_r \ll u_\perp$ and because $k_r \approx 0$ at the cutoff. The parallel term is neglected because the antenna is perpendicularly aligned with respect to the magnetic field such that $k_\parallel \ll k_\perp$. Thus the Doppler shift is produced by the perpendicular velocity $u_\perp$ of the desity fluctuations as

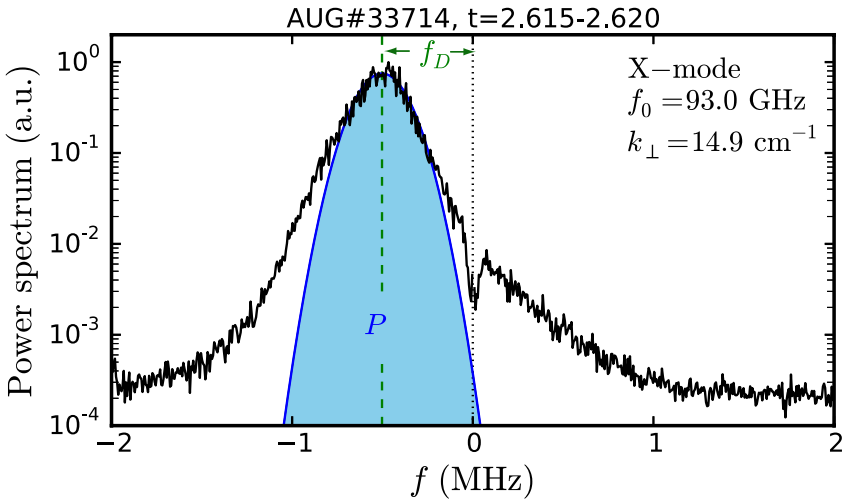

FIGURE 4.2: Power spectrum of the reflectometer signal measured in the ASDEX Upgrade tokamak. The backscattered power P and Doppler shift f_D are indicated.

indicated in Fig. 4.1b with a red arrow. $u_\perp$ is obtained from the Doppler shift through

$$u_\perp = \frac{2\pi f_D}{k_\perp}. \tag{4.10}$$

The perpendicular velocity $u_\perp$ corresponds to the $E \times B$ velocity and the phase velocity (cf. Eq. 2.3). It has been confirmed in several experiments [14, 77, 78] that the phase velocity is small compared to the $E \times B$ velocity in the plasma edge, $v_{\text{ph}} \ll v_{E\times B}$. Hence neglecting v_{ph} allows to calculate the radial electric field as $E_r \approx u_\perp B$. Nevertheless, there are experimental conditions typically in the plasma core in which a non-negligible phase velocity has been measured [79, 80].

The Doppler reflectometry signal V is obtained using the heterodyne detection technique [81]. It removes the fast oscillation of the probing frequency and provides a *complex signal*. A sample power spectrum is shown in Fig. 4.3. It is computed as $|\hat{V}|^2$ where $\hat{\cdot}$ denotes the Fourier transform. The spectrum is two side because V is complex, with the frequency axis f giving the difference with the probing frequency f_0. A peak, named Doppler peak, is observed. The area below it gives the backscattered power P and its position the Doppler frequency f_D. A Gaussian fit to the Doppler peak is shown in blue, P and f_D are indicated for the fit in the figure.

4.2.1 Correlation measurements

The radial structure of the density turbulence is investigated by using two Doppler reflectometry channels with the technique known as radial correlation Doppler reflectometry [15]. In this case two beams with different probing frequency are launched simultaneously into the plasma using the same antenna. They are called *reference* and *hopping* probing channels, and are represented with two rays in Fig. 4.3. Due to the different probing frequencies the cutoff layer of the channels is displaced with respect to each other defining a (radial) separation Δx.

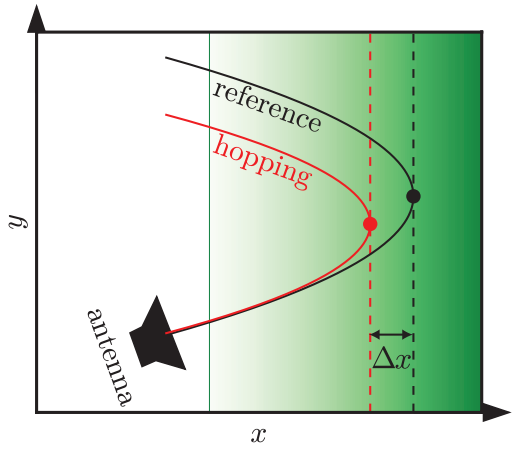

FIGURE 4.3: Schematics showing the two probing channels used for radial correlation Doppler reflectometry. Different probing frequencies produces a Δx separation of the cutoff layers.

The correlation of the density fluctuations δn between the two probing positions is estimated from the cross-correlation function of the backscattered signals,

$$C(\tau) = \frac{\int \mathrm{d}t \, (V_{\mathrm{ref}}(t) - \langle V_{\mathrm{ref}} \rangle)(V_{\mathrm{hop}}(t+\tau) - \langle V_{\mathrm{hop}} \rangle)^*}{\sqrt{\int \mathrm{d}t \, |V_{\mathrm{ref}}(t) - \langle V_{\mathrm{ref}} \rangle|^2 \quad \int \mathrm{d}t \, |V_{\mathrm{hop}}(t) - \langle V_{\mathrm{hop}} \rangle|^2}}, \tag{4.11}$$

where τ is the time delay, * stands for the complex conjugate and $\langle\,\rangle$ for the average. $V_{\mathrm{ref/hop}}$ is the signal of the reference/hopping channel, respectively. By scanning the probing frequency of the hopping channel the correlation is measured for different Δx or radial separations. Further details on this experimental technique will be given in Ch. 7 where it is applied to simulated data. Furthermore, an innovative analysis technique of the correlation data will be presented. It can provide information on the 2D structure of the turbulence, in particular the mean tilt angle of the turbulent structures.

Diagnostic effects related to the $k_\perp$ selectivity and non-linearities have been observed in experiments [15, 16], simulations [19] and theory [21]. These effects are relevant topics of this thesis and will be investigated in simulations (cf. Ch. 7) and experiments (cf. Ch. 8).

4.2.2 Spatial and spectral resolution

Due to the probing wavelength in the mm range and the probing beam width w, the main contribution to the Doppler reflectometer signal comes from an extended scattering region located at the cutoff. In Fig. 4.4a the beam is depicted by the grey envelope of the ray and the scattering region is indicated in magenta. The extension of the scattering region along the cutoff is approximately w, and δr in the x-direction as indicated in the figure.

The radial resolution of the Doppler reflectometry measurements is defined by δr. Its exact value depends on λ_0 and the detailed plasma geometry, density and magnetic

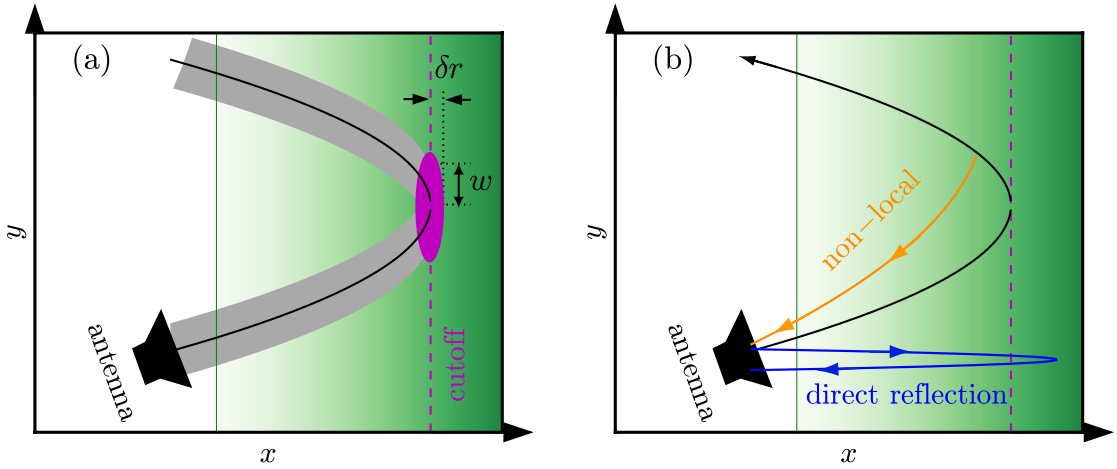

FIGURE 4.4: (a) Schematics showing the extended scattering region at the cutoff. The extension along the x-direction defines the radial resolution δr, and the extension along the cutoff w is related to the spectral resolution of the diagnostic. (b) Schematics showing the direct reflection and non-local scattering. They can be responsible for extra contributions to the Doppler reflectometer signal.

field profiles. It can be roughly estimated with [82]

$$\delta r = 0.5 L_{N^2}^{1/3} \lambda_0^{2/3}, \tag{4.12}$$

where $L_{N^2} = (dN^2/dr)^{-1}$ is the scale length of the squared refractive index.

The width of the scattering region along the cutoff defines the spectral resolution Δk, which can be regarded as the accuracy of the $k_\perp$ selected by the diagnostic. The spectral resolution can be estimated with [14]

$$\Delta k = \frac{2}{w}\sqrt{1 + \left(\frac{w^2 k_0}{R_{\text{eff}}}\right)^2}. \tag{4.13}$$

The pre-factor $2/w$ is obtained for the slab case and non-divergent beams, whereas the square root includes corrections due to the curvature of the cutoff layer and beam front accounted for by the effective radius of curvature R_{eff}. See Ref. [14] for more details.

The exact determination of the spectral and radial resolution is not trivial. Detailed studies combining ray and beam tracing with two-dimensional full-wave simulations have shown complex dependencies of Δk and δr on the experimental parameters [82].

4.2.3 Other contributions to the Doppler reflectometry signal

There can be extra contributions to the Doppler reflectometer signal different to the backscattering previously discussed. The direct reflection and the non-local scattering are introduced here. Their impact in the data analysis will be discussed in simulations (Sec. 7.2) and experiments (Sec. 8.1).

Direct reflections of the probing beam can be collected by the antenna. This is depicted in Fig. 4.4b by a blue ray which is reflected back to the antenna. This direct reflection contribution is often called $m = 0$ contribution in the literature [14]. Contrary to the backscattering contribution, the direct reflection is not Doppler shifted and its spectrum is symmetric around zero frequency.

Scattering along the beam path may occur and may further contribute to the Doppler reflectometer signal. An example of this process is schematically shown in Fig. 4.4b, where the scattering of the reflected beam is collected by the antenna as indicated with the orange ray. These contributions are called *non-local scattering* [21]. Although they do not contribute strongly to the power of the signal P, they can be relevant for the correlation analysis.

4.3 Doppler reflectometer systems

In this section the Doppler refelctometry systems on the ASDEX Upgrade tokamak and the TJ-II stellarator are presented.

4.3.1 ASDEX Upgrade Doppler reflectometers

In this thesis the data of the steerable mirror system in sector 11 of the ASDEX Upgrade tokamak are used. The system is bi-static, meaning that two nearby antennas and two transmission lines are separately used for emission and reception. Two oversized waveguides transmit the probing and backscattered waves between the in-vessel focusing elements and the emission/detection electronics located outside. The beams are formed by two horn antennas, two plane mirrors and one ellipsoidal mirror. The in-vessel components have been optimized for probing frequencies in the W-band (75–105 GHz) and have been aligned to measure perpendicularly to the magnetic field [83]. The orientation of the ellipsoidal mirror is controlled by a piezo actuator. It allows to change the angle of incidence of the beam in the plasma during the discharges. The in-vessel components are shown schematically on the ASDEX Upgrade cross-section in Fig. 4.5.

One W-band (75–105 GHz) reflectometer has been in operation since the installation of the system in 2011. Since 2014 an extra W-band and 2 V-band (50–75 GHz) reflectometers similar to the systems described in Ref. [84] have also been installed. If operated in parallel, the reflectometers are coupled to the oversized waveguides with wire grid polarisers, which set the polarization either to O- or X-mode. By combining the frequency bands and the polarization, a broad range of plasma densities can be investigated. The beam size in the plasma is about 2.8 and 1.9 cm for O- and X-mode, respectively. For typical plasma conditions, the spectral resolution is around 2.1 and 2.3 cm^{-1} for O- and X-mode, respectively [17].

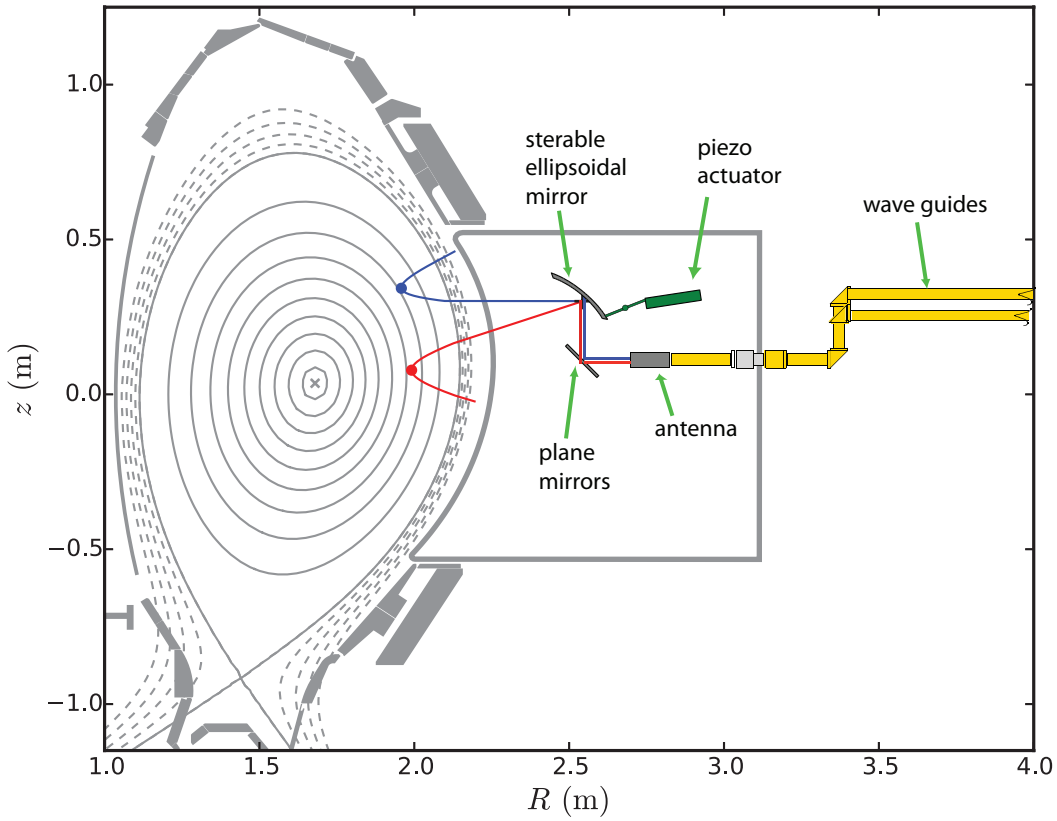

FIGURE 4.5: Cross-section of the ASDEX Upgrade tokamak. The in-vessel components of the reflectometer system are shown. Two sample rays corresponding to different mirror angles are depicted in red and blue. The measurement positions are indicated with circles.

Two sample rays for different mirror angles are depicted by blue and red lines in Fig. 4.5. The circles indicate the cutoff obtained corresponding to the minimum of the refraction index along the ray trajectory. The ray trajectory, cutoff position and $k_\perp$ are computed using TORBEAM [76]. This is the standard code used for wave propagation in the ASDEX Upgrade tokamak. The experimental measurements of the ASDEX Upgrade reflectometers will be presented and analysed in Sec. 8.1 and Ch. 9.

4.3.2 TJ-II Doppler reflectometers

The TJ-II Doppler reflectometer system is located at the toroidal angle of 67.1° in the port C6, the position is indicated in top view in Fig. 4.6a. The system has been aligned for measuring on the plane *perpendicular* to the magnetic field. Fig. 4.6a indicates the direction of the magnetic field at the designed position and the perpendicular plane, with $R_\perp$ the coordinate along it.

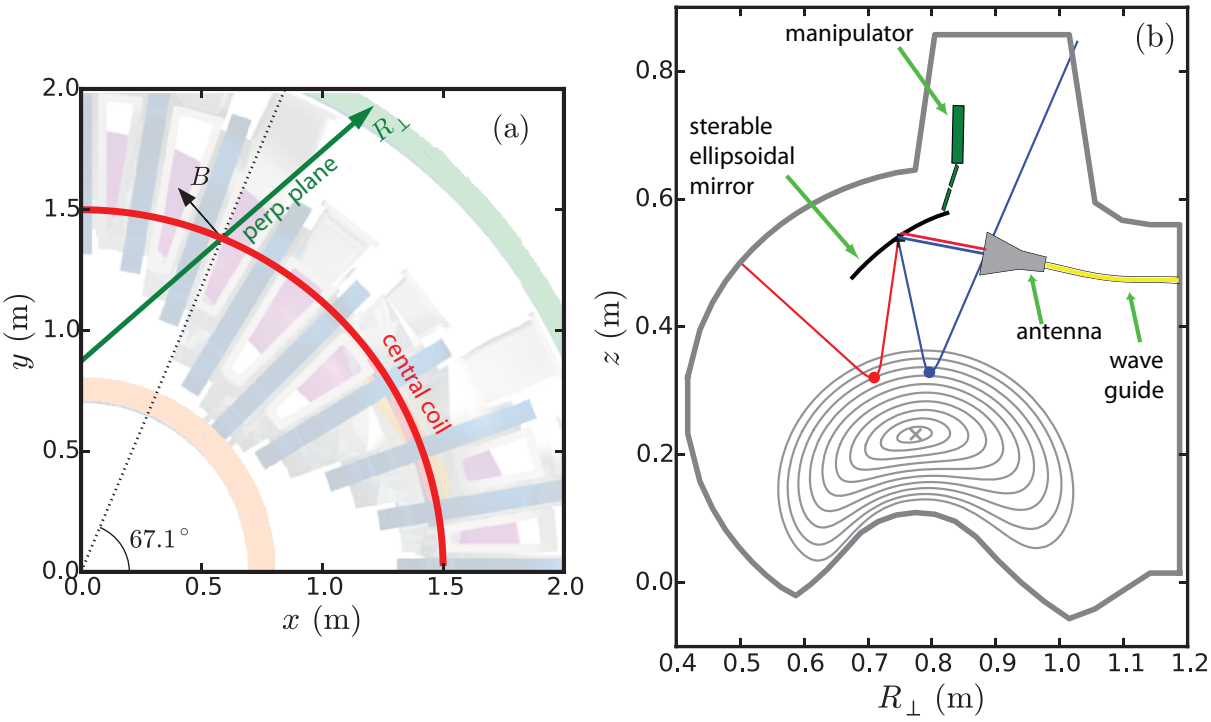

FIGURE 4.6: (a) Schematic top view of TJ-II. The magnetic field at the Doppler reflectometry measurement position and the perpendicular plane are depicted. The coordinate $R_\perp$ is indicated. (b) Cross-section of TJ-II on the plane perpendicular to the magnetic field. The in-vessel components of the reflectometer system are shown. Two sample rays are shown in red and blue, and the respective measurement positions are depicted by circles.

The system is mono-static, with a common antenna and transmission line for emission and reception. A fundamental waveguide transmits the probing and backscatted waves between the in-vessel focusing elements and the emission/detection electronics located outside. The probing beam is achieved by a choked-corrugated antenna coupled at the end of the waveguide and one ellipsoidal mirror. The system possesses a mirror manipulator which modifies the angle of incidence of the beam in the plasma on a shot-to-shot basis. The antenna and mirror have been optimized for probing frequencies in the Q-band (33–50 GHz) [26, 69]. The in-vessel components are schematically shown on the perpendicular cross-section of TJ-II in Fig. 4.6b. Two Q-band channels probing in X-mode polarization have been in operation since the installation of the system in 2009.

Two sample ray trajectories for different mirror angles are depicted by red and blue lines in Fig. 4.6. The measurement positions are depicted by circles. The trajectories are computed with TRUBA [85], which is the standard ray tracing code used for TJ-II wave propagation. The beam size in the plasma is about 2.5 cm and the spectral resolution is around 2.1 cm^{-1} [26, 69]. The experimental measurements of the TJ-II reflectometers will be presented and analysed in Ch. 8.2.

Chapter 5

Modelling of Doppler reflectometry

The modelling of Doppler reflectometry requires the description of the wave propagation in plasmas with realistic geometry and including density fluctuations related to the turbulence. Thus solutions to Maxwell equations where the plasma is included through the current density are required. The general problem is simplified as a result of the strong magnetic field $\mathbf{B}$ characteristic of magnetic confinement fusion devices. The fast dynamics along magnetic field lines smooths out fluctuations such that invariance along the magnetic field direction can be assumed. In the slab geometry (cf. Sec. 4.2) where the magnetic field is taken along the z-axis, this condition implies $\partial_z = 0$ and reduces the problem to two dimensions in the (x, y)-plane. Furthermore O- and X-mode polarizations can be treated separately. Note that for the Doppler reflectometry case only wave propagation perpendicular to $\mathbf{B}$ is relevant.

Despite the mentioned simplifications, modelling of the Doppler reflectometry remains challenging. In this chapter different simulation methods and tools are reviewed. The methods will be applied in Ch. 6 and 7 for investigating the diagnostic response.

5.1 Born approximation and linearity

It has already been established from theory and simulations that the density fluctuation amplitude plays an important role in the diagnostic response [18, 19, 86]. In the limit of small and large turbulence levels the Doppler reflectometer operates in the so-called linear and non-linear regime, respectively. The linearity of the response has a large impact on the measurements of $k_\perp$ spectra and correlation lengths.

To investigate the linearity of the response, the O-mode case is considered first. The wave propagation at frequency $\omega_0 = ck_0$ is described by

$$\left[\nabla^2 + k_0^2\left(1 - \frac{n}{n_c}\right)\right] E = 0, \tag{5.1}$$

where the electric field of the wave E is purely along the z-direction, the frequency ω_0 enters through the cutoff density n_c, and n is the local plasma density. The latter

accounts for both, background density n_0 and density fluctuations δn,

$$n = n_0 + \delta n. \tag{5.2}$$

Solving Eq. 5.1 is challenging given the complex geometry of fusion plasmas, as well as the stochastic nature and multiplicity of scales of the turbulence.

For most of the experimental conditions (excluding the scrape-off layer), the plasma fluctuations are smaller than the background density, i.e. $\delta n < n_0$. Given that the cutoff density is of the order of the background density at the cutoff, the last condition is translated into $\delta n < n_c$. Using Eq. 5.2 in the dispersion relation obtained from Eq. 5.1 gives

$$1 - \frac{n}{n_c} = 1 - \frac{n_0}{n_c} - \frac{\delta n}{n_c}.$$

The last term is of the order $\epsilon = \delta n/n_c < 1$. This allows for a perturbative approach to the scattering problem, where ϵ also accounts for the strength of perturbations on the electric field produced by the density fluctuations [87].

The electric field can be expanded in terms of ϵ:

$$E = E_0 + E_1(\epsilon) + E_2(\epsilon^2) + E_3(\epsilon^3) + ... \tag{5.3}$$

Replacing n and E by their expansions in Eq. 5.1 one obtains

$$\left[\nabla^2 + k_0^2\left(1 - \frac{n_0}{n_c} - \frac{\delta n}{n_c}(\epsilon)\right)\right](E_0 + \ E_1(\epsilon) + E_2(\epsilon^2) + E_3(\epsilon^3) + ...) = 0.$$

The lowest orders are:

$$\epsilon^0: \quad \left[\nabla^2 + k_0^2\left(1 - \frac{n_0}{n_c}\right)\right] E_0 = 0, \tag{5.4}$$

$$\epsilon^1: \quad \left[\nabla^2 + k_0^2\left(1 - \frac{n_0}{n_c}\right)\right] E_1 = k_0^2 \frac{\delta n}{n_c} E_0, \tag{5.5}$$

$$\epsilon^2: \quad \left[\nabla^2 + k_0^2\left(1 - \frac{n_0}{n_c}\right)\right] E_2 = k_0^2 \frac{\delta n}{n_c} E_1, \tag{5.6}$$

$$\vdots$$

The zeroth order equation describes the wave propagation of the unperturbed electric field E_0 in the background density and is equivalent to Eq. 5.1 without turbulence, i.e. $n = n_0$. In the first order equation 5.5, the term $\delta n E_0$ on the r.h.s. indicates that the unperturbed beam is scattered by density fluctuations producing the first order perturbed field E_1. This corresponds to a single scattering process. The second order equation 5.6 gives correspondingly the scattering of E_1 by density fluctuations as the source of E_2, and implies a double scattering process. The set of Eqs. 5.4–5.6 describes a multiple scattering process common to scattering and perturbation theories in physics, e.g. as the higher-order Born approximation Dyson series in quantum mechanics [88].

For *small* turbulence levels, it is sufficient to consider only the first order approximation of Eq. 5.5 which corresponds to the linear scattering theory also known as the Born approximation [89]. This condition is fulfilled in the core region of fusion plasmas where the turbulence level is small, $\delta n/n_0 \sim 0.1$ %. It has been shown [90] that the reflectometer signal V_1 in Born approximation is

$$V_1 \propto \frac{k_0^2}{n_c} \int \mathrm{d}\mathbf{x}\, E_0^2(\mathbf{x}) \delta n(\mathbf{x}), \tag{5.7}$$

where E_0 is the electric field of the beam emitted by the antenna, as if there was no turbulence. The last equation shows that the scattering of the incoming beam by density fluctuations is the source of the backscattered signal. Note that V_1 scales with the fluctuation level δn, hence the linear backscattered power P scales as δn^2 as expected from the linear ansatz of Eq. 4.8. It is also important to note that $E_0^2(\mathbf{x})$ weighs the contribution of the density fluctuations to the signal in Eq. 5.7, hence it is often called the *weighting function* W.

The range of validity of the linear theory has been analytically studied for conventional reflectometry [91]. For a Gaussian turbulence spectrum and slab geometry the following linearity criterion has been proposed

$$\gamma = \left(\frac{\delta n_{\mathrm{rms}}}{n_c}\right)^2 \frac{G^2 (2\pi)^2 L^{\mathrm{ref}} \mathrm{L}_x}{\lambda_0^2} \ln\left(\frac{L^{\mathrm{ref}}}{L_x}\right) \ll 1, \tag{5.8}$$

where $L^{\mathrm{ref}} = (\mathrm{d}N^2/\mathrm{d}x)^{-1}$ is the scale length of the squared refractive index, L_x is the radial correlation length of the turbulence, and γ is the non-linearity coefficient. G is an enhancement factor accounting for the polarisation [91],

$$G = \begin{cases} 1 & \text{for O} - \text{mode} \\ \frac{(\omega_0^2 - 2\omega_p^2)(\omega_0^2 - \omega_c^2) + \omega_p^4}{(\omega_0^2 - \omega_p^2 - \omega_c^2)^2} & \text{for X} - \text{mode.} \end{cases} \tag{5.9}$$

For $\gamma \geq 1$ non-linear effects are expected [17, 19].

Despite the abundant literature on the topic, there are still open issues regarding the linearity of Doppler reflectometry measurements. The question of whether Eq. 5.8 can be applied for the Doppler case has not been tackled yet. Furthermore Eq. 5.6 predicts a double scattering regime with $P \propto \delta n^4$, as well as higher order regimes are foreseen by higher order contributions. The effect of these higher order contributions was not yet studied. In Ch. 6 these contributions are investigated and their importance for Doppler reflectometry is proved.

5.2 Physical optics model

The physical optics (PO) model was originally developed for studying the scattering of waves by rough surfaces [92]. It has been applied in different fields as oceanology [93],

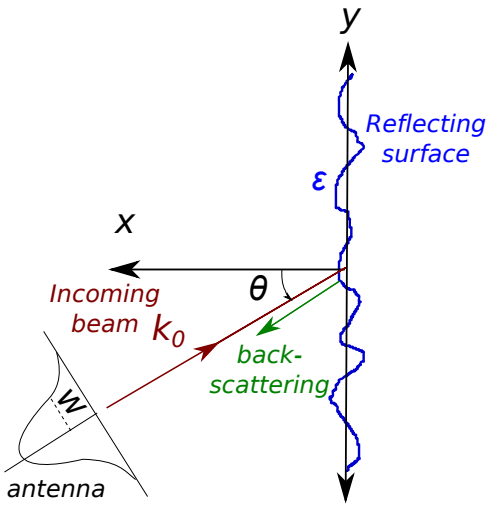

FIGURE 5.1: Schematics of the physical optics model geometry. A corrugated reflecting surface (blue) along the y-axis is characterized by the displacement $\varepsilon(y)$ in the x-direction. An incoming paraxial Gaussian beam with wavenumber k_0 is scattered at the surface. The angle of incidence with respect to the x-axis is θ and the beam size is w.

geology [94], and meteorology [95], i.e., where random surfaces are characterized by their scattering properties. The physical optics model was applied for the first time for Doppler reflectometry modelling in [96], based on the idea of a roughness of the cutoff layer due to density turbulence in fusion plasmas. Although it was early introduced as a simple modelling tool only, it will be shown in the next chapter that it can recover relevant effects of Doppler reflectometry. Moreover, due to its mathematical simplicity and numerical efficiency, it contributes substantially to the understanding of the scattering physics behind the diagnostic response.

The geometry to be considered is shown schematically in Fig. 5.1. The *original model* [96] assumes a corrugated reflecting surface along the y-direction characterized by $\varepsilon(y)$, which gives its displacement in x-direction from the mean surface. This rough surface scatters an incoming paraxial Gaussian beam with wavenumber k_0 and an incidence angle θ. Invariance along the z-axis is assumed. The physical optics model provides the electric field backscattered at the antenna which is taken as the reflectometer signal:

$$V = \left[\int \mathrm{d}y \, \exp\left(-\frac{y^2\cos^2\theta}{w^2} + i2k_0 y\sin\theta\right)\exp(-i2k_0\varepsilon\cos\theta)(\varepsilon'\sin\theta - \cos\theta)\right] \times \left[\int \mathrm{d}y \, \exp\left(-\frac{y^2}{w^2}\right)\right]^{-1}, \tag{5.10}$$

where w is the beam size at the surface and $\varepsilon' = \mathrm{d}\varepsilon/\mathrm{d}y$. The backscattered electric field is normalized to the reflected electric field from a smooth surface at perpendicular incidence. V is equivalent to the scattering coefficient in Ref. [96].

The physical optics model is applied to Doppler reflectometry under slab approximation (see Sec. 4.2) and assuming that ε is related to the the density fluctuations at the cut-off layer. Since the turbulence evolves slowly in time (μs) compared with the probing wave time scale (ns), the turbulence can be assumed static with respect to the wave propagation. Therefore Eq. 5.10 can be computed at each time t for different turbulence realizations $\varepsilon(y,t)$, which results in a time signal for the backscattered electric field $V(t)$. Given that the reflectometer signal is proportional to the backscattered electric field in the antenna, $V(t)$ from Eq. 5.10 can be taken as the reflectometer signal and can be analysed as in the experiment. Although only the slab case is considered here, the physical optics model can be extended to more general geometries [97].

Equation 5.10 is deduced by solving the Helmholtz integral in the far field and by applying the Kirchhoff approximation [92]. The latter assumes the corrugation to be locally flat, neglecting the local curvature of ε, which requires the corrugation amplitude $|\varepsilon|$ to be small compared to the vacuum wavelength λ_0, $|\epsilon| \ll \lambda_0$. This condition imposes a limitation on the application of the model regarding the turbulence level. Nevertheless, the original theory has been extended [98, 99] in order to include the local curvature, providing a more general theory.

The extensions to the Kirchhoff approximation presented in Ref. [98] have been adapted to the Doppler reflectometry case within this thesis (see Appendix A of Ref. [86]). There, the backscattered electric field is given as an expansion in the momentum transfer. The first order in the expansion recovers the original model of Eq. 5.10 [86]. The second order provides the *extended model*

$$V = \cos\theta \left[\int \mathrm{d}y\, \exp\left(-\frac{y^2\cos^2\theta}{w^2} + i2k_0 y\sin\theta\right) \exp\left(-i2k_0\varepsilon\cos\theta\right)\exp(-\varepsilon'\tan\theta)\right.$$
$$\left.\times \exp\left(-\frac{i(1+\tan^2\theta)\varepsilon''}{2k_0\cos\theta} - \frac{(\varepsilon'\tan\theta)^2}{2}\right)\right] \left[\int \mathrm{d}y\, \exp\left(-\frac{y^2}{w^2}\right)\right]^{-1}. \tag{5.11}$$

Note that while the first two exponentials appear also in the original model and the third one can be reduced to the term $\varepsilon'\sin\theta - \cos\theta$, the last exponential includes a further correction considering the curvature through $\varepsilon'' = \mathrm{d}^2\varepsilon/\mathrm{d}y^2$.

The zeroth order in the expansion provides the *effective model*

$$V = \cos\left[\theta \int \mathrm{d}y\, \exp\left(-\frac{y^2\cos^2\theta}{w^2} + i2k_0 y\sin\theta\right)\exp(-2ik_0\varepsilon\cos\theta)\right]$$
$$\times \left[\int \mathrm{d}y\, \exp\left(-\frac{y^2}{w^2}\right)\right]^{-1}. \tag{5.12}$$

It is of interest for the the analytical calculations of Sec. 6.2.4 given its mathematical simplicity. See appendix A of Ref. [86] for more details on the derivation of the two introduced models.

In Sec. 6.2.4, the results of the original, extended and effective models will be compared in order to establish the validity range of the physical optics in its application to Doppler reflectometry studies.

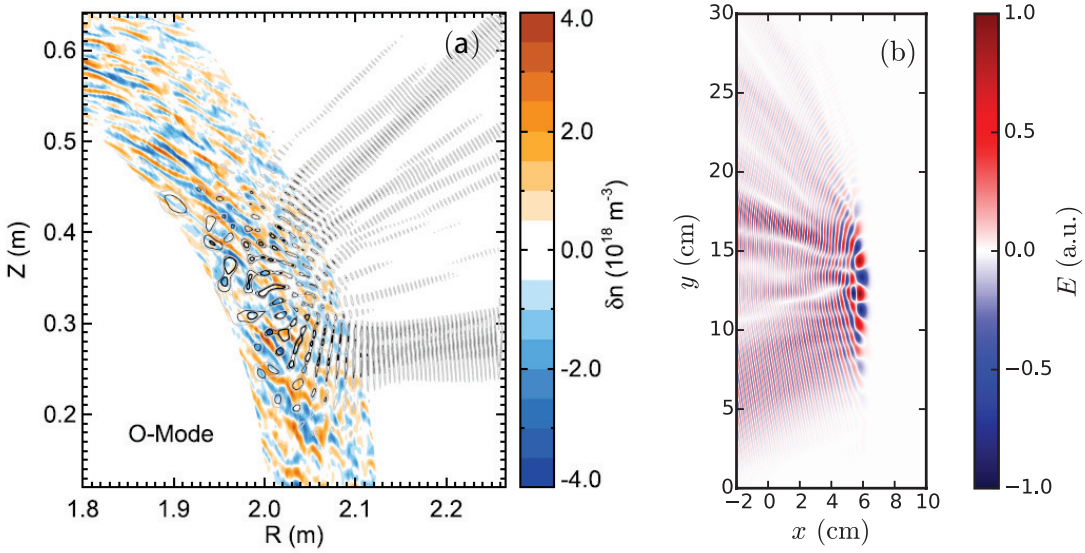

FIGURE 5.2: (a) Electric field contour (black) and density fluctuation (color-coded) obtained in a 2DFW simulation of the ASDEX Upgrade tokamak (adapted from Ref. [17]). (b) Electric field contour obtained with 2DFW simulations in slab geometry using the code presented in [18, 19].

5.3 Two-dimensional full-wave simulations

Two-dimensional full-wave (2DFW) simulations provide a numerical solution to the Maxwell equations in cold magnetized plasmas. Invariance is assumed along the background magnetic field $\mathbf{B}$, hence the equations are solved on the perpendicular plane. The 2D geometry separates O- and X-mode polarization into two different sets of equations relating the components of the electric and magnetic field. These systems are solved by different numerical schemes.

Two-dimensional full-wave simulations are considered nowadays the best modelling tool for fluctuation reflectometry because they contain all the relevant wave physics, and do not make assumptions regarding neither the linearity of the diagnostic response nor the geometry of the system. These simulations have been successfully applied to realistic experimental conditions and using turbulence from gyrokinetic codes, recovering the effects observed in the experiments [17, 100, 101]. Nevertheless, since 2DFW simulations are computationally demanding, systematic studies are rather limited. Sample results of 2DFW simulations in the ASDEX Upgrade tokamak are shown in Fig. 5.2a [17].

In this work the 2DFW code presented in Refs. [18, 19] is used in Secs. 6.3 and 7.2 for modelling the Doppler reflectometry response in the slab geometry. The code uses a rectangular computational domain which is surrounded by a *perfectly matched layer* for avoiding non-physical boundary effects. The plasma density including fluctuations and the background magnetic field are defined on the grid. A mono-static antenna is simulated at the left side of the simulation domain. The beam propagation is simulated for a static turbulence realization, and the reflectometer signal V is obtained by weighting the electric field at the antenna. A sample contour plot of the electric field simulated in the slab geometry with the code under discussion is shown in Fig. 5.2b.

Chapter 6

Power response modelling

In order to measure $k_\perp$ spectra and radial correlation lengths reliably using Doppler reflectometry, a linear diagnostic response is required. However, this is not always the case for typical experimental conditions. In this chapter, the power response of Doppler reflectometry is studied in detail. Specifically deviations from the linear behaviour (Eq. 4.8) and their effects on $k_\perp$ spectrum measurements are studied.

First, a 2D Gaussian synthetic k spectrum of the turbulence is studied. The power response is investigated using the physical optics (PO) model, in particular an enhanced power response regime is found, understood and characterized. In order to validate the results with a more reliable model, the power response is also studied with two-dimensional full-wave (2DFW) simulations in slab geometry for experimentally relevant parameters in Sec. 6.3. The same effects are obtained which confirms the PO analysis. In Sec. 6.4, a more realistic case regarding plasma geometry and $k_\perp$ spectrum is considered [101]. Applications of the developed tools to experimental data analysis are also discussed. Parts of the results from this chapter have been published in Refs. [86] and [102].

6.1 Synthetic Gaussian turbulence

From theory [23, 24, 25] and simulations [10, 27, 28] the turbulence is expected to have a wavenumber spectrum characterized by a decay of the spectral intensity with k. Furthermore, due to the different processes in the plasma, elongation and tilting of turbulent structures are also expected [29] (cf. Sec. 2.1). Gaussian k spectra have often been used in theory [21, 91] and simulations [18, 19] of Doppler reflectometry. They exhibit a spectral decay and are particularly suitable for analytical calculations.

For the modelling purposes of this work 2D Gaussian, elongated and tilted wavenumber spectra are used. The absolute value of the k spectra used here is given by

$$|h(k_x,k_y)| = \frac{\ell_{\min}\ell_{\max}}{8\pi}\exp\left[-\frac{(k_x\cos\beta - k_y\sin\beta)^2\ell_{\max}^2 + (k_x\sin\beta + k_y\cos\beta)^2\ell_{\min}^2}{8}\right], \tag{6.1}$$

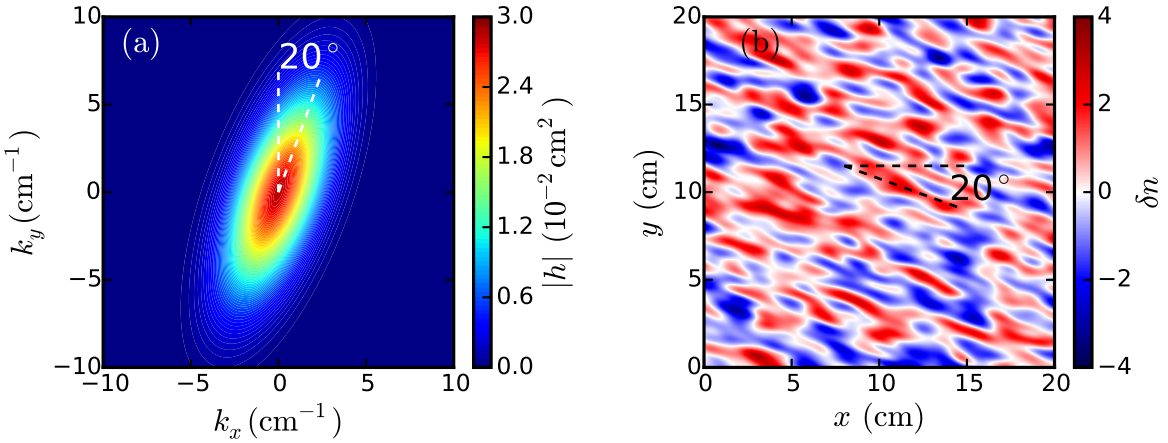

FIGURE 6.1: (a) 2D wavenumber spectrum $h(k_x, k_y)$ and (b) a sample of the turbulent field $\delta n(x, y)$. Elongation and tilting of the spectrum and turbulent structures are observed.

where β is the tilt angle of the spectrum with respect to the k_y-axis, and $\ell_{\max}$ and $\ell_{\min}$ define the minor and major spectral widths, respectively. The complex phase of the spectra will be discussed below. Apart from including elongation and tilting the Gaussian shape provides well defined statistical properties. This type of spectrum will also be used in radial correlation Doppler reflectometry modelling in Ch. 7. In this chapter, $\ell_{\max} = 1.40$ cm, $\ell_{\min} = 0.51$ cm and $\beta = 20°$ are used. The contour plot of $|h|$ is shown in Fig. 6.1a, where the elongation and the tilting can be recognized.

The density fluctuations or turbulent field $\delta n(x, y)$ is the inverse Fourier transform of $h(k_x, k_y)$:

$$\delta n(x, y) = \iint \mathrm{d}k_x\, \mathrm{d}k_y\, h(k_x, k_y) e^{ik_x x + ik_y y}. \tag{6.2}$$

For the analytical calculations all the integrals are performed over the range $(-\infty, \infty)$. For numerical applications the turbulent field $\delta n(x, y)$ is computed by 2D fast Fourier transform of $h(k_x, k_y)$ over a finite domain after including random complex phases,

$$h(k_x, k_y) = |h(k_x, k_y)| e^{i\phi(k_x, k_y)}, \qquad \phi \in [-\pi, \pi] \text{ random}. \tag{6.3}$$

The resulting turbulent field is dimensionless and has a rms of 1. In the following the turbulence amplitudes will be renormalized in order to include the turbulence level and the proper physical dimensions.

A sample contour plot of the turbulent field is shown in Fig. 6.1b for the wavenumber spectrum given in Fig. 6.1a, where random, elongated and tilted structures can be observed. In average the turbulent structures are elongated and tilted by $\beta = 20°$ with respect to the x-axis, and the average size along the major and minor axes are $\ell_{\max}$ and $\ell_{\min}$, respectively. In Ch. 7 it will be shown that these two quantities correspond to the widths of the correlation function of the turbulence along the principal axes.

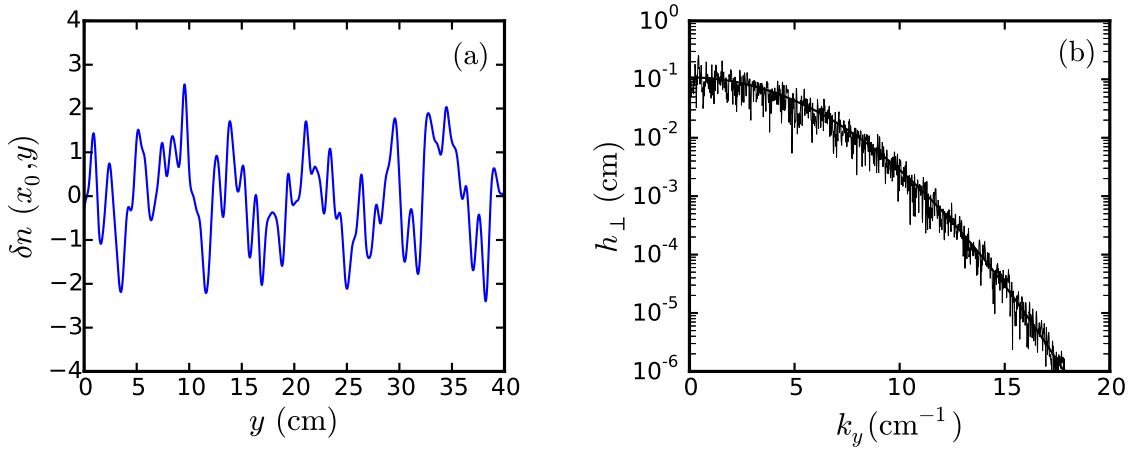

FIGURE 6.2: (a) Sample slice of the turbulence layer $\delta n(x_0, y)$ which is used as input for the PO model and (b) the corresponding perpendicular wavenumber spectrum $h_\perp(k_y)$ of the complete turbulent field. The thicker line depicts the input spectrum from Eq. 6.5.

6.2 Physical optics modelling

In this section the physical optics model (cf. Sec. 6.2) is applied to the power response of a Doppler reflectometer. First the implementation is discussed. Then, the power response is simulated and the effects on the measured $k_\perp$ spectrum are studied. Afterwards the validity range of the PO model is discussed and a multiple scattering interpretation of the power response based on analytical calculations is given.

6.2.1 Numerical implementation

The physical optics model considers the turbulence only at the cut-off layer corresponding to a vertical slice of the turbulent field $\delta n(x_0, y)$. A sample of it is plotted in Fig. 6.2a. Taking the turbulence at a fixed position x_0 in Eq. 6.2, shows that the spectrum of $\delta n(x_0, y)$ can be obtained by integrating h along k_x. Furthermore it corresponds to the $k_\perp$ spectrum of fluctuations along the cutoff layer given by,

$$h_\perp(k_y) = \int \mathrm{d}k_x\, h(k_x, k_y). \tag{6.4}$$

For the Gaussian case the previous equation gives

$$h_\perp(k_y) = \frac{L_y}{\sqrt{8\pi}} \exp(-L_y^2 k_y^2/8), \quad \text{with} \quad L_y = \frac{\ell_{\min}\ell_{\max}}{\sqrt{\ell_{\max}^2 \cos^2\beta + \ell_{\min}^2 \sin^2\beta}} \tag{6.5}$$

the perpendicular correlation length. In Fig. 6.2b the $k_\perp$ spectrum computed from $\delta n(x_0, y)$ is plotted, the thicker line depicts the input $h_\perp$ from Eq. 6.5 with $L_y = 0.54$ cm. Note that L_y is different from $\ell_{\max}$ and $\ell_{\min}$ because the finite tilt angle of the turbulence β.

The integral in Eq. 5.11 is numerically computed (midpoint rule) over the interval $(-7w, 7w)$. ε is chosen to be proportional to the fluctuation amplitude δn at the cut-off

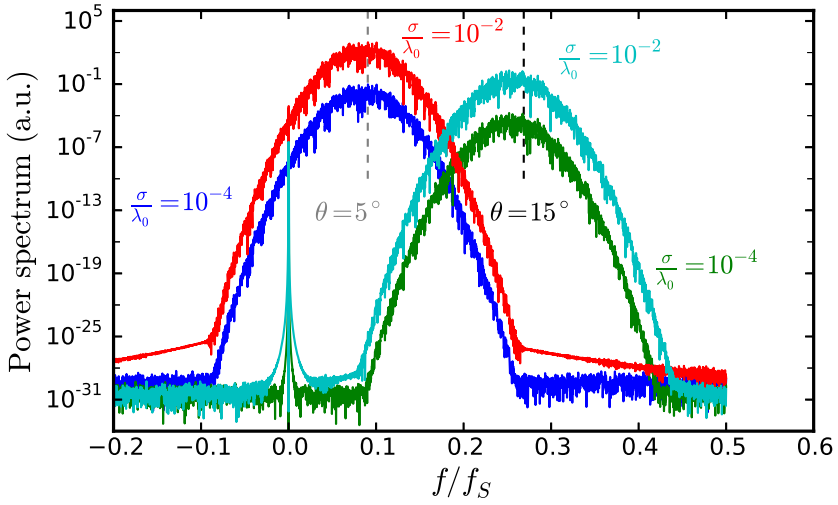

FIGURE 6.3: Power spectra of the backscattered signal simulated using PO for two angles of incidence θ and two turbulence levels σ. The positions of the Doppler peaks depend on the angle of incidence and the intensity depends on the turbulence level.

which is shown in Fig. 6.2a, hence $\varepsilon(y) = \sigma\,\delta n(x_0, y)$. The normalization factor σ sets the rms value of ε and is the control parameter for the turbulence level scans. Note that σ has the unit of a length. In this section a broad σ scan is done in order to study its role in the power response. Afterwards in Sec. 6.3.2, results of PO and 2DFW simulations are compared, and σ is related to the turbulence level and density and magnetic field profiles taking into account the polarization of the probing wave.

The time dependence is included by assuming the turbulence to be *frozen* and to move along the cutoff layer in the y-direction, $\delta n(x_0, y - u_\perp t)$. This is numerically achieved by displacing the turbulence matrix n_d grid points between consecutive time steps, thus the perpendicular velocity of the turbulence is $u_\perp = n_d\,\delta y/\delta t$, with δy the spatial resolution of the grid and δt the time step. Note that δt defines the sampling frequency $f_S = \delta t^{-1}$.

6.2.2 Power response

The power response of the Doppler reflectometer is studied using the extended physical optics model form Eq. 5.11. The complex signal $V(t)$ is computed for two angles of incidence θ and two turbulence levels σ, with $w = 1.66$ cm and $\lambda_0 = 0.318$ cm, corresponding to a probing frequency $f_0 = 94.4$ GHz. Figure 6.3 shows the power spectra of the signal, where the x-axis corresponds to the frequency f normalized to the sampling frequency f_S. Doppler peaks are observed at the Doppler frequency f_D obtained from Eq. 4.7 and indicated with vertical dashed lines. f_D increases with θ because of the higher $k_\perp$ obtained from Eq. 4.7.

The narrow contribution at $f/f_S = 0$ is the direct reflection (cf. Sec. 4.2.3) also predicted by the PO model. For a fixed σ, the Doppler peak intensity decreases with θ because of the smaller spectral intensity at larger $k_\perp$ expected from Eq. 6.5. For fixed θ, the Doppler peak intensity increases as the backscattered power increases with the turbulence level σ.

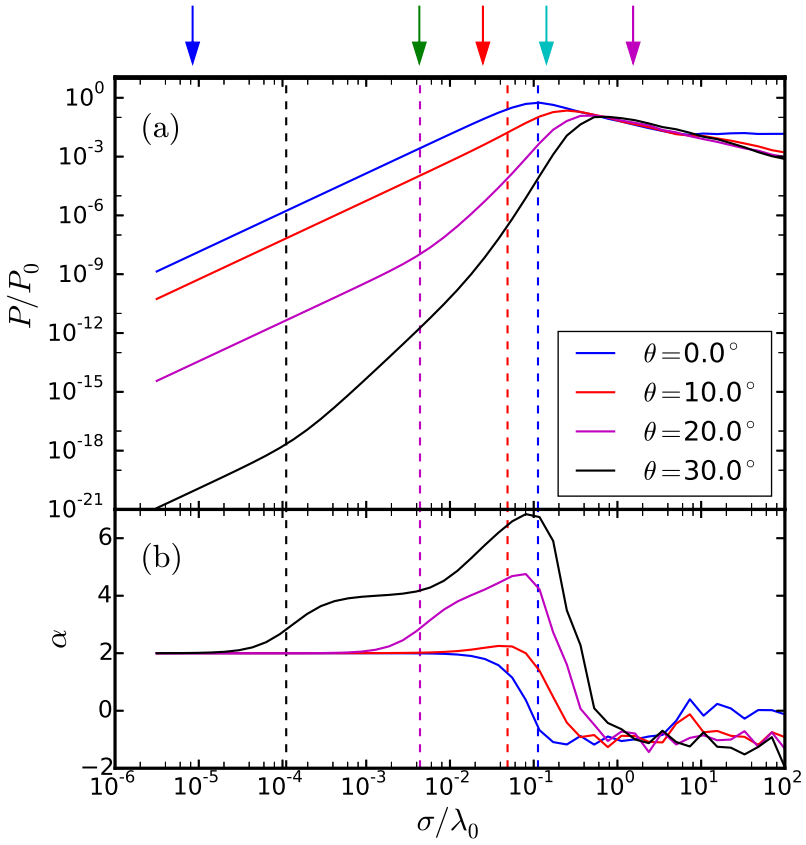

FIGURE 6.4: (a) Backscattered power P/P_0 and (b) scaling exponent α as a function of the turbulence level σ/λ_0. At small σ the response of the diagnostic increases linearly with σ^2 yielding $\alpha = 2$. The critical turbulence level σ_c/λ_0 at which the response becomes non-linear is computed with Eq. 6.12, and is indicated for each angle with dashed lines. The arrows on the top indicate the σ/λ_0 values at which the $k_\perp$ spectra are computed later (cf. Fig. 6.5).

In order to study the linear and non-linear responses of the reflectometer, a scan in both σ and θ has been performed. Figure 6.4a depicts the backscattered power P as a function of the turbulence level σ normalized to the vacuum wavelength (solid lines), the colours represent different angles of incidence θ. Note that due to the normalization of V in Eq. 5.11, the received power is normalized to the probing beam power P_0.

For small σ the power increases proportionally to σ^2 for all θ values. This corresponds to the *linear* regime following the linear ansatz (Eq. 4.8). With increasing σ the power reaches a maximum and then decreases with σ. In this *saturation* regime non-linear physical phenomena such as multiple and non-coherent scattering take place, which explain the decrease of the power despite a turbulence level increase. These two regimes have been already observed and reported in literature [18, 103].

Nevertheless the transition between both regimes is not always clear and appears to depend on θ. For small angles the transition from linear to saturation is immediate ($\theta = 0°$, blue line at $\sigma/\lambda_0 \approx 10^{-1}$). For larger θ, there is an intermediate regime in which the power increases stronger than in the linear regime with σ . Furthermore, the location and extent of this regime depends on θ: for larger angles it starts at smaller σ and ends at larger σ.

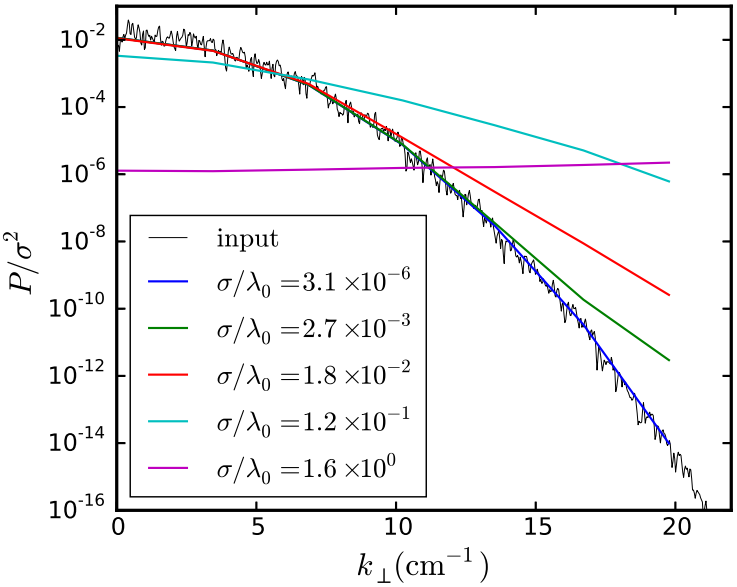

FIGURE 6.5: Input $k_\perp$ spectrum (black) and $k_\perp$ spectra measured using the PO model at different σ. Spectra are normalized to σ^2. A good agreement with the input spectrum is found for small σ (blue line) due to the linear response. For larger σ the spectral power is overestimated (green and red lines) for large $k_\perp$ due to the enhanced power response. For the largest σ value (magenta line), the measured spectrum is flat due to saturation.

The transition can be better analysed by considering the local scaling exponent α defined as $P \sim \sigma^\alpha$. It is computed as $\alpha_i = \ln(P_{i+1}/P_i)/\ln(\sigma_{i+1}/\sigma_i)$ where i indicates the values on the computational grid. Fig. 6.4b shows α as a function of σ/λ_0 for the different values of θ from Fig. 6.4a. It confirms that for low turbulence levels the response is linear with $\alpha = 2$ in agreement with Eq. 4.8. A transition to an *enhanced power response* regime before saturation is observed, which is characterized by an increase of α. The vertical dashed lines indicate analytic calculations of the transition points to be discussed later.

Moreover for large angles, e.g. $\theta = 30°$, there is a σ range where $\alpha \approx 4$. Following the reasoning from Sec. 5.1, one can conclude that the enhanced power response is due to higher order scattering processes. The description in terms of a multiple scattering process will be discussed later (cf. Sec 6.2.4).

6.2.3 Perpendicular wavenumber spectrum measurement

In Fig. 6.5, the $k_\perp$ spectrum is constructed by plotting the backscattered power P as a function of $k_\perp$. The different colours represent various turbulence levels σ, which are also marked by the vertical arrows at the top of Fig. 6.4a. The black line depicts the input $k_\perp$ spectrum computed from the turbulent field δn and corresponding to $h_\perp^2(k_y)$ from Eq. 6.5. Since the input turbulence level is proportional to σ, all spectra have been normalized to σ^2 in order to compare the different cases with the input spectrum. For a low turbulence level (blue line), P gives an accurate measurement of the $k_\perp$ spectrum,

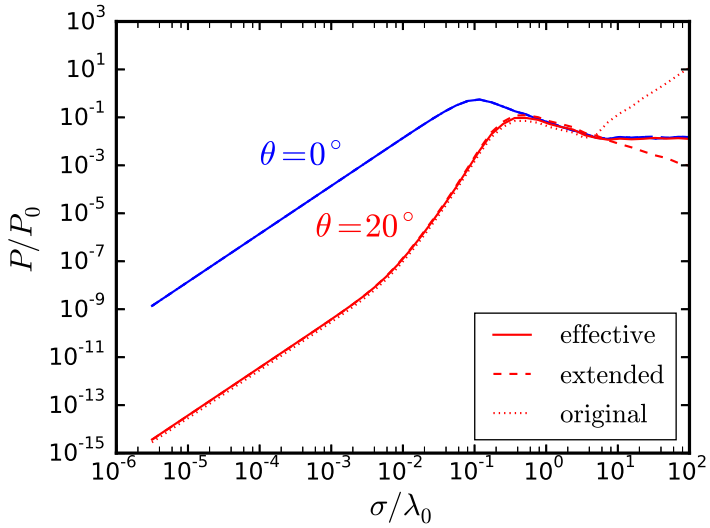

FIGURE 6.6: Backscattered power P/P_0 as a function of the turbulence level σ/λ_0. Extended (dashed), original (dotted) and reduced (solid) models are compared at normal and oblique incidence. All three models agree in the σ range of interest

as expected in the linear regime (Eq. 4.8). When σ increases, the already discussed non-linear response flattens progressively the measured $k_\perp$ spectrum.

For a intermediate turbulence level (green line), the signal at large $k_\perp$ is enhanced by the non-linear response ($\alpha > 2$) and overestimates the spectral power density while the signal at small $k_\perp$ is linear and gives an accurate measurement of the spectrum. In this case the enhanced power response causes the flattening of the spectrum at large $k_\perp$. For a high turbulence level (light blue line) the saturation induces an underestimation of the power for small $k_\perp$, which results in a flattening of the spectrum. For extremely high turbulence levels (magenta line) the response is deeply saturated on the entire $k_\perp$ range and the spectrum is flat.

6.2.4 Perturbative expansion of the physical optics model

In order to achieve a better understanding of the linearity of the power response, a perturbative expansion of the PO model is performed. For the sake of mathematical simplicity the effective model is considered. First, the accuracy of the effective model is assessed by comparing its results to those from the extended and original PO models. These studies reveals also the range of validity of the different model and of the Kirchhoff approximation. The reader should refer to Sec. 5.2 where the different models have been introduced.

σ scans are performed with the original (Eq. 5.10), extended (Eq. 5.11) and effective (Eq. 5.12) models. The results for $\theta = 0°$ (blue) and $\theta = 22.7°$ (red) are shown in Fig. 6.6. All the models agree for perpendicular incidence ($\theta = 0°$). This is trivial, because the first order term in Eq. 5.11 and the second part of the second order term disappear for $\theta = 0°$. For oblique incidence, all the models agree in the linear, non-linear and saturation ranges. For the largest turbulence levels the original model diverges. The effective model saturates and the extended model decreases with the turbulence level.

In summary, although the extended model treats the problem of the scattering from a rough surface more rigorously, the original and effective models are valid in the σ range where the Doppler reflectometry response is studied. Since the effective model of Eq. 5.12 is accurate and can be easily treated analytically, it is used in the following for the estimation of the transition from linear to non-linear regimes.

The effective PO model from Eq. 5.12 without the normalization term is written as:

$$V = \int \mathrm{d}y \, \exp\left(-\frac{y^2 \cos^2\theta}{w^2} + i2k_0 y \sin\theta\right) \exp(-i2k_0 \varepsilon \cos\theta), \tag{6.6}$$

where the first exponential corresponds to a filter function f which sets the diagnostic selectivity at $k_\perp = 2k_0 \sin\theta$. The second exponential in Eq. 6.6 can be Taylor expanded in ε,

$$\begin{aligned} V &= \int \mathrm{d}y f \exp(-i2k_0\varepsilon\cos\theta) \approx \int \mathrm{d}y \, f(1 - i2k_0\varepsilon\cos\theta - 2k_0^2\varepsilon^2\cos^2\theta + ...), \\ &= \underbrace{\int \mathrm{d}y \, f}_{V_0} + \underbrace{(-i2)k_0\cos\theta \int \mathrm{d}y \, f\varepsilon}_{V_1} + \underbrace{(-2)k_0^2\cos^2\theta \int \mathrm{d}y \, f\varepsilon^2}_{V_2} + ... \end{aligned} \tag{6.7}$$

Equation 6.7 is a power series of ε (fluctuation amplitude), and is equivalent to the perturbation expansion considered in Eq. 5.3. The physical optics model has allowed to estimate analytically the relative magnitude of the different contributions in Eq. 6.7. Here the results for the first (V_1) and second order (V_2) contributions are discussed. For details on the derivation referrer to Ref. [86].

The magnitude of the first order term is

$$\overline{|V_1|} \sim 2k_0 \cos\theta \sigma h_\perp(k_\perp). \tag{6.8}$$

It is proportional to the turbulence level σ and the $k_\perp$ spectrum, recovering the linear power response given by Eq. 4.8. If the value of σ is small, V_1 is dominant and the linear regime is obtained. This contribution is understood in terms of a single scattering process because the only contribution to the signal is from $k_\perp$. It is represented schematically on the $k_\perp$ spectrum in Fig. 6.7a, where a black arrow represents the single scattering event giving a contribution $h_\perp(k_\perp)$ only.

The magnitude of the second order term is

$$\overline{|V_2|} \sim 2k_0^2 \cos^2\theta \sigma^2 (h_\perp * h_\perp)(k_\perp), \tag{6.9}$$

Note that it is quadratic in σ and involves the convolution:

$$(h_\perp * h_\perp)(k_\perp) = \int_{-\infty}^{\infty} \mathrm{d}k_1 \, h_\perp(k_1) h_\perp(\underbrace{k_\perp - k_1}_{k_2}). \tag{6.10}$$

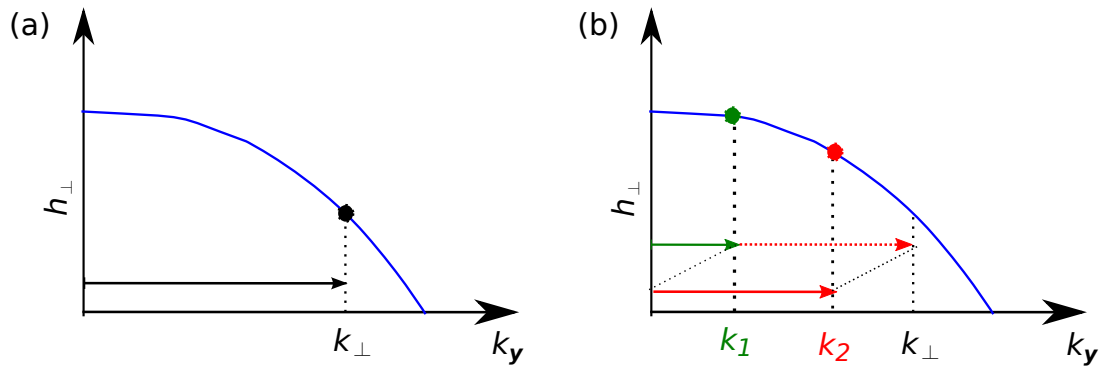

FIGURE 6.7: Schematics of (a) single and (b) double scattering processes represented on the $k_\perp$ spectrum. In (a) a single scattering event at $k_\perp$ (black arrow) indicates a contribution only from $h_\perp(k_\perp)$, while in (b) two scattering events with k_1 and k_2 (green and red arrows) give contributions from different wavenumbers than $k_\perp$.

For intermediate values of σ, V_2 may dominate inducing an enhanced power response characterized by $\alpha = 4$. Moreover based on the convolution from Eq. 6.10, this contribution is understood as a double scattering process at k_1 and k_2 represented in Fig. 6.7b by green and red arrows, respectively. Although Bragg's condition is still fulfilled for the sum $k_1 + k_2 = k_\perp$, the integration in Eq. 6.10 over k_1 implies the contribution of turbulence with multiple k_1 and k_2 to the reflectometer signal. Hence different k_y contributions to the signal degrade the $k_\perp$ selectivity and introduce deviations from Eq. 4.8.

By equating the magnitudes of the linear and quadratic terms, $\overline{|V_1|} = \overline{|V_2|}$, it is possible to estimate a critical σ_c at which non-linear effects set in as

$$\frac{\sigma_c}{\lambda_0} = \frac{1}{2\pi\cos\theta}\frac{h_\perp(k_\perp)}{(h_\perp * h_\perp)(k_\perp)}. \tag{6.11}$$

It gives an estimation of the transition from the linear to either enhanced power response or saturation regimes. The appearance of the $k_\perp$ spectrum shows that the power response depends non-trivially on the spectral shape.

For the Gaussian $k_\perp$ spectrum under study (Eq. 6.5) this expression gives:

$$\frac{\sigma_c}{\lambda_0} = \frac{1}{2\pi\cos\theta\sqrt{2}}\exp\left(-\frac{L_y^2 k_\perp^2}{16}\right) = \frac{1}{2\pi\cos\theta\sqrt{2}}\exp\left(-\frac{L_y^2 k_0^2\sin^2\theta}{4}\right). \tag{6.12}$$

This equation predicts a decrease of σ_c with θ and L_y. In Fig. 6.4 σ_c is plotted as dashed lines together with the simulated data. A good match to the transition from the linear to the non-linear regime is achieved.

In principle there are several regimes characterized by double, triple, etc. scattering processes in which the reflectometer signal scales with σ^4, σ^6, etc. but the range in which they appear is limited. For large σ, if the argument of the second exponential in Eq. 6.6 is larger than one ($|-i2k_0\cos\theta\varepsilon| > 1$), all terms contribute and the series in Eq. 6.7 cannot be truncated any more. In this case saturation is reached. The turbulence level

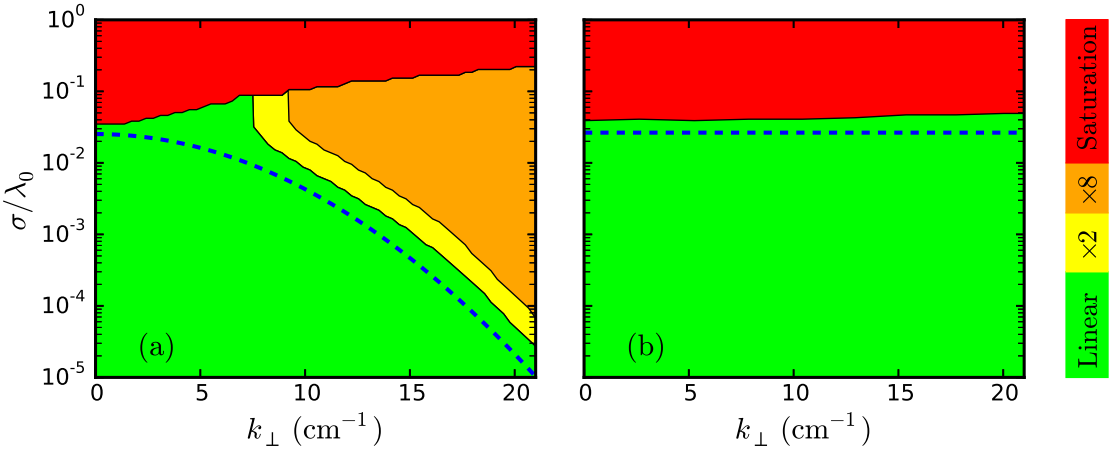

FIGURE 6.8: Power response map for (a) the Gaussian and (b) flat k spectrum cases. The red colour indicates saturation, yellow ×2 and orange ×8 enhanced and green linear. The blue dashed line gives critical turbulence level computed from Eq. 6.12.

for saturation σ_s can be roughly estimated as

$$\frac{\sigma_s}{\lambda_0} = \frac{1}{4\pi \cos\theta}. \tag{6.13}$$

Note that for normal incidence, $\sigma_c \approx \sigma_s$. In this case there is a direct transition from the linear to the saturation regime as in Fig. 6.4, while for oblique incidence transitions to higher order regimes occur between σ_c and σ_s.

6.2.5 Graphical representation of the power response

The transition between the different regimes is smooth. For example, the scaling exponent α in Fig. 6.4b shows a slow increase with σ for the black curve during the transition to the enhanced power response regime. In this work the saturation is defined at the turbulence level where P has a maximum, $\mathrm{d}P/\mathrm{d}\sigma = 0$, because from this point on the measured power does not increase with the turbulence level. Since the enhanced power response yields an overestimation of the spectral intensity, a transition to a *times two* (×2) enhanced response is defined, which is at the turbulence level where P is overestimated by a factor of two with respect to the linear response. A ×8 enhanced response with P eight times overestimated is also regarded [102, 104].

These definitions allow to illustrate the power response dependence on the turbulence level and the probed $k_\perp$. In Fig. 6.8 the linear (green), ×2 (yellow) and ×8 (orange) enhanced and saturation (red) regimes are depicted in the $(k_\perp, \sigma/\lambda_0)$-plane for the Gaussian (a) and a flat $k_\perp$ spectrum (b). The blue dashed line is the critical turbulence level from Eq. 6.11.

For the Gaussian case (Fig. 6.8a), a direct transition from linear to saturation regime is observed at small $k_\perp$. In contrast, a strong enhanced power response appears for intermediate turbulence levels and large $k_\perp$. The transition to enhanced power response shifts to smaller σ when $k_\perp$ increases. On the other hand, the flat $k_\perp$ spectrum case

depicted in Fig. 6.8b is radically different from the Gaussian one. A direct transition from linear to saturation regime is observed for all $k_\perp$ at approximately the same σ. The absence of the enhanced power response in the flat spectrum case explains why it has not been observed in previous works [18, 103], where either a completely or locally flat spectrum was used.

The analytical prediction (blue dashed line) reproduces properly the $k_\perp$ dependence of the transition to a non-linear behaviour for both cases. There is a slight vertical shift of the blue line with respect to the green area boundary. The condition $\overline{|V_1|} = \overline{|V_2|}$ used for the derivation of Eq. 6.11 yields a convention different from the one used to define the regions in the plot. Note that for the flat spectrum case ($L_y \to 0$) Eq. 6.12 gives $\sigma_c \approx \sigma_s$ for all θ, leaving no room for an enhanced power response. Hence, a direct transition from a linear to saturation regime is expected in this case.

In conclusion, the enhanced power response and saturation regimes introduce deviations from the linear diagnostic response of Doppler reflectometry. They are responsible of the flattening of the $k_\perp$ spectra measured at high turbulence levels. Moreover the spectral shape has a strong effect on the Doppler reflectometry power response. In particular, the transition from a linear to a non-linear response can be estimated with Eq. 6.11 which explicitly contains a non-trivial dependence with $h_\perp(k_\perp)$. Furthermore, the diagram presented in Fig. 6.8 is useful for assessing the linearity of the measurements in a broad parameter space. In the experiment σ/λ_0 is fixed by the turbulence level and other experimental parameters. For a given $k_\perp$ range, the diagram provides information on the scattering regime.

6.3 Two-dimensional full-wave simulations

In order to study the existence of enhanced power response regimes in Doppler reflectometry and to validate the analysis based on the PO model, the power response is studied in detail using two-dimensiontal full-wave simulations (2DFW). As mentioned in Sec. 5.3, 2DFW simulations contain all relevant (non-linear) physics and can thus be used to cross-check the results from the previous section.

Simulations of the wave propagation in ordinary (O) and extraordinary (X) mode have been performed in slab geometry. The probing frequencies are $f_0 = 60.2$ and 94.4 GHz, respectively. The background density profile is linear, $n_0 = n_c(x/L)$, with the cutoff for normal incidence located at $L = 5$ cm from the plasma boundary and with a cutoff density of $n_c = 4.5 \cdot 10^{19}$ m^{-3}. An uniform magnetic field with a strength of $B = 2$ T is applied. The beam waist is $w = 3.48$ and 2.22 cm for O- and X-mode, respectively. The turbulent field $\delta n(x, y)$ is normalized and added to the background density. The normalization is chosen to set the required turbulence level given by $\delta n_{\mathrm{rms}}/n_c$. Four values of θ are used such that the resulting $k_\perp$ in between 2 and 15 cm^{-1} is experimentally meaningful. These parameters correspond to typical ASDEX Upgrade conditions.

An example of the electric field contours for O-mode is depicted in Fig. 6.9a–c. The angle of incidence is $\theta = 17.7°$. The different plots correspond to various $\delta n_{\mathrm{rms}}/n_c$, indicated in the bottom left of each plot. For a low turbulence level (Fig. 6.9a) incoming and reflected beams are observed, also a regular electric field pattern is obtained at the

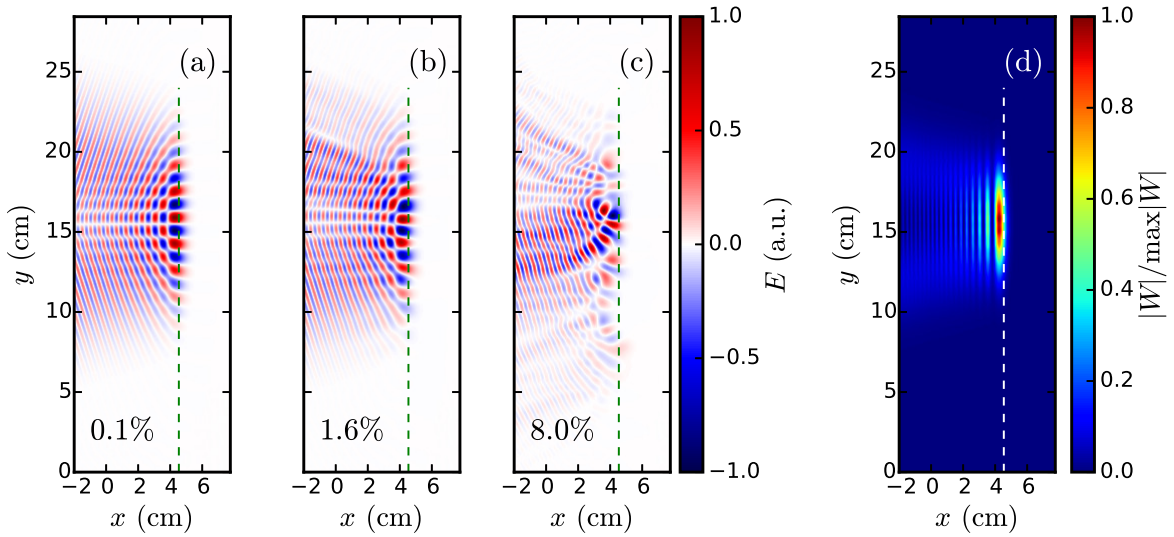

FIGURE 6.9: Electric field contours for 2DFW O-mode simulations with an incidence angle $\theta = 17.7°$ and different turbulence levels $\delta n/n_c = 0.1$ % (a), 1.6 % (b) and 8.0 % (c). (d) Absolute value of the weighting function normalized to its maximum value in the simulation domain. The nominal cutoff is indicated by a dashed line in all cases. The strongest contribution at the cutoff layer position indicates a good localization of the scattering there.

cutoff. The propagation of the beam is barely affected by the turbulence. For a higher turbulence level (Fig. 6.9b and c) an interaction with the turbulence is noticeable; random structures appear in the cutoff, also both incoming and reflected beams are perturbed. In Fig. 6.9d the corresponding weighting function W is shown, which corresponds to the squared electric field without turbulence averaged within a microwave period. The strongest contribution can be observed at the cutoff (there is a slight displacement which is discussed in Appendix A), whereas weaker contributions appear in other regions. It indicates that most of the contributions to the backscattered power are well localized at the cutoff layer.

This setup is used in the following systematic scans of both, turbulence level and incidence angle, and will be later compared to the PO results. Furthermore, in Sec. 7.2 the radial correlation Doppler reflectometry measurements will be modelled using the same configuration.

6.3.1 Power response

A scan of the turbulence level has been performed for different angles of incidence and both polarizations. Fig. 6.10a and b show the backscattered power P as a function of the turbulence level $\delta n_{\mathrm{rms}}/n_c$ for O- and X-mode, respectively. The points depict the 2DFW results and the solid lines show the PO results which are discussed later. The scaling exponent α (cf. Sec. 6.2.2) is correspondingly plotted in Fig. 6.10c and d. The upper axes show the non-linearity parameter from Eq. 5.8.

For low turbulence level (0.1 %) a linear response can be observed especially for the O-mode polarization and for small θ in X-mode polarization. For larger turbulence level

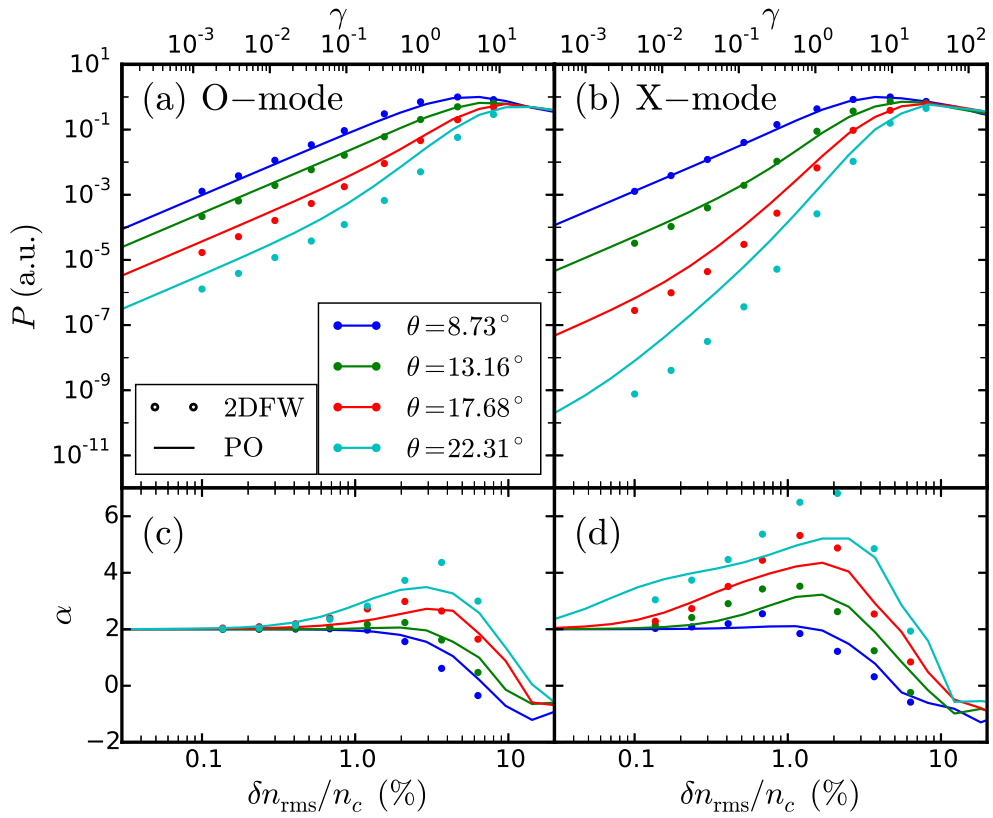

FIGURE 6.10: Backscattered power P for (a) O- and (b) X-mode polarizations, and scaling exponent α for (c) O- and (d) X-mode as a function of the turbulence level for different angles. 2DFW data are plotted with points and PO results with solid lines.

(1.0 %) a larger growth of the power with $\delta n_{\rm rms}/n_c$ is evident for large values of θ and especially for X-mode polarization. This indicates an enhanced power response. For the largest turbulence level (8.0 %) the power saturates. The occurrence of $\alpha > 2$ for turbulence levels between the linear and saturation regimes confirms the existence of the enhanced power response regime in 2DFW simulations of Doppler reflectometry.

The 2DFW results are in qualitative agreement with those obtained from PO. Hence the same interpretation in terms of multiple scattering processes seems to be valid in general for Doppler reflectometry. In particular, α values of up to 6 may be explained by double and triple scattering events.

6.3.2 Comparison with physical optics

The main contribution to the Doppler reflectometer signal is expected to be originated from a well localized region around the cutoff due to the minimization of the refractive index there. This is confirmed for the case under study by the dominance of the weighting function at the cutoff in Fig. 6.9d. Since the interactions away from the cutoff can be neglected, the application of physical optics to Doppler reflectometry modelling is justified. It is important to remark that although the weaker contributions away from the cutoff are not relevant for the power response, they may be important for radial

correlation length studies, where signal contributions of very low amplitude can still give strong correlations [21].

In order to compare results from the physical optics model and 2DFW simulations, the density fluctuation field δn used as input for the 2DFW simulations has to be translated into the corrugation ε in the PO model. In the Born approximation (Eq. 5.7) and the linear contribution of physical optics model (V_1 in Eq. 6.7), the turbulence is *weighted* by a function related to the beam and integrated over a certain domain. Therefore, in order to make both equations analogous $\varepsilon \propto \delta n$ is chosen, which means using the density fluctuations δn as the corrugation in the physical optics model with a proper normalization.

Accordingly, a normalization factor N linking the turbulence level in the PO model and the 2DFW simulations is defined as,

$$\frac{\delta n_{\mathrm{rms}}}{n_c} = N\sigma. \tag{6.14}$$

This normalization factor must account for the density gradient, magnetic field and the wave polarization, which are not included in the PO model. It is possible to estimate N by matching the σ_s for normal incidence (Eq. 6.13) with $\gamma = 1$ from the conventional reflectometry linearity criterion (Eq. 5.8). This yields

$$N = \sqrt{\frac{4}{G^2 L^{\mathrm{ref}} L_x \ln(L^{\mathrm{ref}}/L_x)}}. \tag{6.15}$$

Furthermore the non-linearity parameter can be written in terms of σ as:

$$\gamma = \left(\frac{4\pi\sigma}{\lambda_0}\right)^2. \tag{6.16}$$

For O-mode, the squared refractive index (cf. Eq. 3.8) is linear in the plasma density, therefore $L^{\mathrm{ref,O}} = (\nabla n_0/n_0)^{-1} = 5$ cm. For X-mode, the magnetic field has to be taken into account (cf. Eq. 3.10). The squared refractive index is numerically computed and from its gradient at the cut-off $L^{\mathrm{ref,X}} = 2.5$ cm is obtained. The enhancement factor for X-mode (cf. Eq. 5.9) computed at the cut-off is $G_{\mathrm{X}} \approx 4.9$.

The same f_0, w and θ as for the 2DFW simulations are used for PO calculations. Note that the difference between O- and X-mode is included through the different f_0, w, G and L^{ref}. Using the normalization given in Eq. 6.14, the PO data are plotted with continuous lines together with 2DFW results (points) in Fig. 6.10. The qualitative agreement in terms of the occurrence of the different regimes is evident.

It is remarkable that the difference between O- and X-mode is reproduced by the PO model only by the choice of the probing frequency f_0. Equation 6.11 indicates that the linearity depends mainly on $k_\perp$ and the specific $k_\perp$ spectrum. Therefore the large difference observed between both polarizations is mainly due to the intrinsically smaller $k_\perp$ of the O-mode. Thus if O- and X-mode measurements are compared at the same angle of incidence, the O-mode response is expected to be more linear, whereas this large

difference in diagnostic response is not expected if they are compared at the same $k_\perp$. Nevertheless the enhancement factor G in Eq. 6.15 makes the O-mode more linear than the X-mode even when comparing at the same $k_\perp$.

The agreement of the two models for O- and X-mode in Fig. 6.10 at $\theta = 8.73^\circ$ (close to normal incidence) suggests that the normalization factor N from Eq. 6.15 is appropriate, thus PO may be used for quantitative estimations in Doppler reflectometry. However, here only one scenario with a specific radial correlation length of the turbulence L_x, and density and magnetic field profiles has been studied. Further studies are required in order to validate this normalization factor, in particular for the case of shallow density gradients where the PO model may fail [100].

In the pure linear regime at low turbulence level, the two models do not agree completely. Indeed, the 2DFW simulations underestimate the spectral intensity at large $k_\perp$ due to a sensitivity loss inherent to the wave propagation. This effect, known as *scattering efficiency* [86, 102], is discussed in detail in Appendix A. It should be noted that the impact of the scattering efficiency on the $k_\perp$ spectrum measurements is small compared to that of non-linearities.

The scaling exponent α has comparable values and peaks at a similar turbulence level value for both models, although the PO gives a maximum α smaller than the 2DFW simulations. Nevertheless, it is remarkable that the PO model can reproduce indeed most of the features of the 2DFW power response regarding the linearity in the broad parameter space under study. These studies show that PO can be used as a tool for estimating the linearity of real Doppler reflectometry measurements. In particular the representation given in Fig. 6.8 will be shown to be of special interest for experimental data analysis in the following section.

6.4 Application to Kolmogorov-type turbulence and realistic plasma geometry

It is also important to assess the impact of the enhanced power response and saturation in a more realistic case, regarding both, $k_\perp$ spectrum and plasma geometry. In this section the power response from more realistic 2DFW simulations is compared with the previous modelling. The application of the main results and developed methods to experimental data analysis is also discussed.

In Ref. [101], the wave propagation for a previously installed W-band X-mode Doppler reflectometer [105] on the ASDEX Upgrade tokamak was simulated using a 2DFW code. The plasma geometry and density profile are obtained from the equilibrium reconstruction and multi-diagnostics profile measurements for discharge #22009, respectively. The real geometry of the magnetic field is included in the code. An isotropic synthetic density turbulence is included. Its $k_\perp$ spectrum is Kolmogorov-like, flat up to 3.0 cm^{-1} followed by a spectral decay with a spectral index of -4.0. More details on the experiments and simulations can be found in Ref. [101].

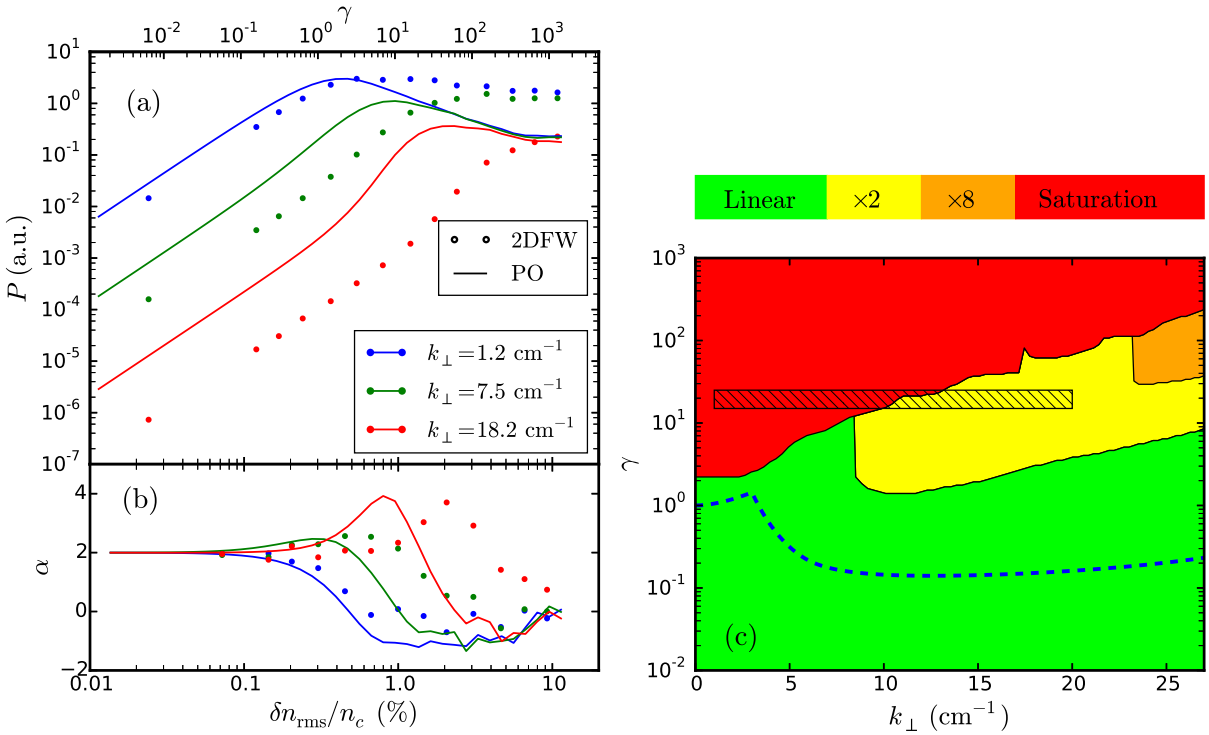

FIGURE 6.11: (a) Power and (b) scaling exponent as a function of the turbulence level for 2DFW data (points) for the ASDEX Upgrade case and a Kolmogorov-type $k_\perp$ spectrum [101]. The solid lines depict PO results. (c) Power response map for the Kolmogorov-type spectrum. The red colour indicates saturation, yellow $\times 2$ and orange $\times 8$ enhanced and green linear. The dashed line indicates the critical turbulence level obtained from Eq. 6.11. The hatched are indicates the parameter space where the experimental measurements presented in Ref. [101] were performed.

A scan of the turbulence level has been performed in Ref. [101] (see Fig. 15 of the reference). The resulting backscattered power P and the scaling exponent α are presented in Figs. 6.11a and b, respectively. 2DFW data are depicted by points and PO data are presented by solid lines. The colours represent three $k_\perp$ values and the upper axis the non-linearity coefficient γ. A similar behaviour as for the Gaussian case is observed: For small $k_\perp$ values (blue points) the transition from linear to saturation regime is direct, α is 2 for small γ and drops for $\gamma > 1$. Whereas for large $k_\perp$ (red points) an enhanced power response is obtained as indicated by $\alpha \approx 4$ at $\gamma \approx 40$. This confirms the existence and importance of enhanced power response for Doppler reflectometry measurements in more realistic conditions. The vertical offset between PO and 2DFW data is related to the scattering efficiency and is discussed in detail in Appendix A. The PO model recovers qualitatively the power response regarding the appearance of the different regimes, e.g. the maximum α for each $k_\perp$ series is approximately recovered. The comparison of 2DFW and PO results in Figs. 6.11a and b confirms the suitability of PO to describe approximately the linearity of a Doppler reflectometer in realistic cases.

The power response for the Kolmogorov-type $k_\perp$ spectrum is studied using the PO model and presented on the $(k_\perp, \gamma)$-plane in Fig. 6.11b (see Sec. 6.2.5). The linear

(green), ×2 (yellow) and ×8 (orange) enhanced and saturation (red) regimes are depicted. The boundaries of the regimes are different from the Gaussian and flat spectrum case presented in Fig. 6.8. For low enough γ the response is linear for all $k_\perp$. The enhanced power appears for γ around 10 and large $k_\perp$. The critical level obtained from Eq. 6.11 is plotted with a dashed blue line. Although it does not match accurately the linear boundary, it also predicts a linear response for all $k_\perp$ at small γ and an enhanced power response at intermediate γ and large $k_\perp$. The difference between Gaussian, flat, and Kolmogorov-type cases shows that the spectral shape plays an important role in determining the linearity of the response.

The hatched region in Fig. 6.11b indicates where the X-mode experimental measurements presented in the Ref. [101] were performed. The response is saturated below $k_\perp \approx 10$ cm^{-1} and enhanced above. This is in agreement with the simulated and measured $k_\perp$ spectra therein, where a flat spectrum (saturation) and an underestimated spectral index (enhanced power) were observed below and above $k_\perp \approx 10$ cm^{-1}, respectively. A similar assessment of the linearity of O- and X-mode Doppler reflectometry measurements at the ASDEX Upgrade tokamak has been performed in Ref. [104]. The results of this chapter will be consider for the discussion of the linearity of the experimental measurements presented in Ch. 8.

Summary

The power response of Doppler reflectometry has been investigated using the physical optics model. In addition to the known linear and saturation regimes, an enhanced power response regime has been found for the first time. It is characterized by a growth of the backscattered power with the turbulence level faster than in the linear regime. The enhanced power response contributes to the non-linear flattening of the measured $k_\perp$ spectra, in particular at large $k_\perp$. The enhanced power response has been also observed in two-dimensional full-wave simulations for both, a Gaussian $k_\perp$ spectrum in slab geometry and a Kolmogorov-type $k_\perp$ spectrum in realistic plasma geometries.

A graphical representation of the power response dependence with the turbulence level and $k_\perp$ has been proposed (cf. Figs. 6.8 and 6.11c). It was shown that the shape of the $k_\perp$ spectrum plays a key role in determining the occurrence of the different regimes. Moreover this representation has been used to assess the linearity of experimental measurements.

A perturbative expansion of the physical optics has been performed. It was shown that the enhanced power response is produced by multiple scattering events. Furthermore, these results allow to extend the conventional reflectometry linearity criterion from Eq. 5.8 to include the Doppler reflectometry case:

$$\left(\frac{\delta n_{\mathrm{rms}}}{n_c}\right)^2 \frac{G^2(2\pi)^2 L^{\mathrm{ref}} L_x}{\lambda_0^2} \ln\left(\frac{L^{\mathrm{ref}}}{L_x}\right) \left[\frac{(h_\perp * h_\perp)(k_\perp)}{h_\perp(k_\perp)}\right]^2 \ll 1. \tag{6.17}$$

This equation allows to estimate the linearity of the experimental measurements accounting for $k_\perp$ and the spectral shape through $h_\perp(k_\perp)$.

Chapter 7

Modelling of radial correlation Doppler reflectometry

Radial correlation Doppler reflectometry, already introduced in Sec. 4.2.1, is an experimental technique which can provide information on the radial structure of turbulent density fluctuations. In this chapter, the technique is studied in detail. Diagnostic effects are investigated by means of two-dimensional full-wave simulations (2DFW) and a linear analysis based on the Born approximation. Furthermore, an innovative analysis technique is developed, which provides a measurement of the tilt angle of the turbulent structures (cf. Sec. 2.2).

First, the characterization of a turbulent field by correlation techniques assuming a point measurement is discussed in Sec. 7.1. It is shown how the correlation length in radial and perpendicular directions, and the tilt of the turbulent structures can be recovered. Afterwards, the complex diagnostic response is investigated with 2DFW simulations in Sec. 7.2. The filter effect of the diagnostic is investigated based on the Born approximation in Sec. 7.3. The impact of the temporal decorrelation of the turbulence is analytically studied in Sec. 7.4. Finally, a realistic turbulent field obtained from gyrokinetic simulations [17] is investigated in Sec. 7.5.

7.1 Turbulence characterization: Point measurement

In this section, a method to characterize the correlation function of a turbulent field is discussed. It uses a local and exact measurement of the field in slab geometry (cf. Sec. 4.2). The method is applied to the characterization of turbulent fields with a 2D Gaussian wavenumber spectra given by Eq. 6.1. The application of the method to reflectometer signals including further diagnostic effects and to more realistic k spectra is discussed in the following sections.

A point measurement assumes the reflectometer signal probing at (x, y) to be proportional to the density fluctuation amplitude at the measurement position,

$$V(x, y) = \delta n(x, y). \tag{7.1}$$

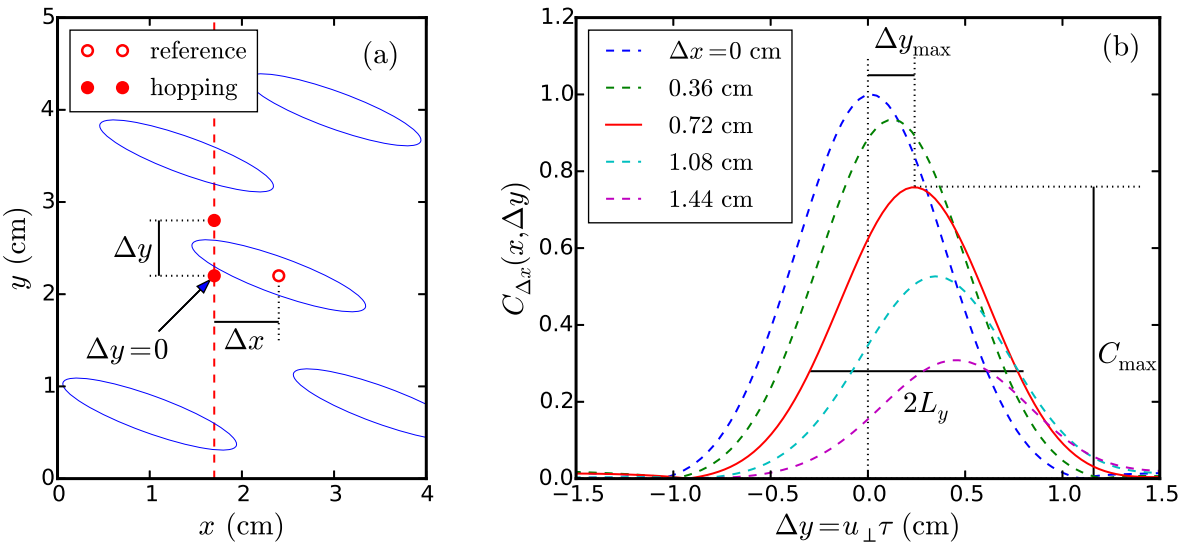

FIGURE 7.1: (a) Schematics showing the measurement positions of the reference and hopping channels on a turbulent field. Δx and Δy are depicted. (b) Cross-correlation function $C_{\Delta x}(x, \Delta y)$ for different separations Δx. The definitions of $C_{\max}$, L_y and $\Delta y_{\max}$ are illustrated.

The turbulence advection by plasma flows and its intrinsic dynamics results in a time dependence of the reflectometer signal V. In the following, the intrinsic dynamics of the turbulence is neglected in the so-called *frozen approximation*, where the fluctuations are assumed *frozen* in the plasma frame. The motion of the turbulence in the y-direction with velocity $u_\perp$ (cf. Eq. 2.3) provides the equivalence $y = u_\perp t$. The effect of the intrinsic dynamics in the following analysis will be discussed in Sec. 7.4.

7.1.1 Correlation function

The point measurement approximation of Eq. 7.1 is replaced in the *cross-correlation function* of Eq. 4.11. The following expression is obtained for the reference and hopping channels probing at x and $x + \Delta x$, respectively:

$$C_{\Delta x}(x, \Delta y) = \int \mathrm{d}y \, \delta n^*(x, y) \delta n(x + \Delta x, y + \Delta y), \tag{7.2}$$

where * stands for the complex conjugate. The turbulent field has a zero mean value and is normalized such that the denominator of Eq. 4.11 is not required. Given the frozen approximation the time delay τ of the cross-correlation is translated into $\Delta y = u_\perp \tau$. The measurement positions of the channels and Δx and Δy are illustrated on a schematic turbulent field in Fig. 7.1a. The turbulent structures are depicted by blue ellipses.

The cross-correlation function of the signals (Eq. 7.2) is computed for the synthetic turbulent field discussed in Sec. 6.1 at an arbitrary x position. In Fig. 7.1b the results are plotted for different separations of the channels Δx in different colors. In all cases a peak is observed. Its amplitude decreases and its position moves to positive Δy when Δx increases. The correlation function is characterized with its maximum $C_{\max}$, $1/e$-

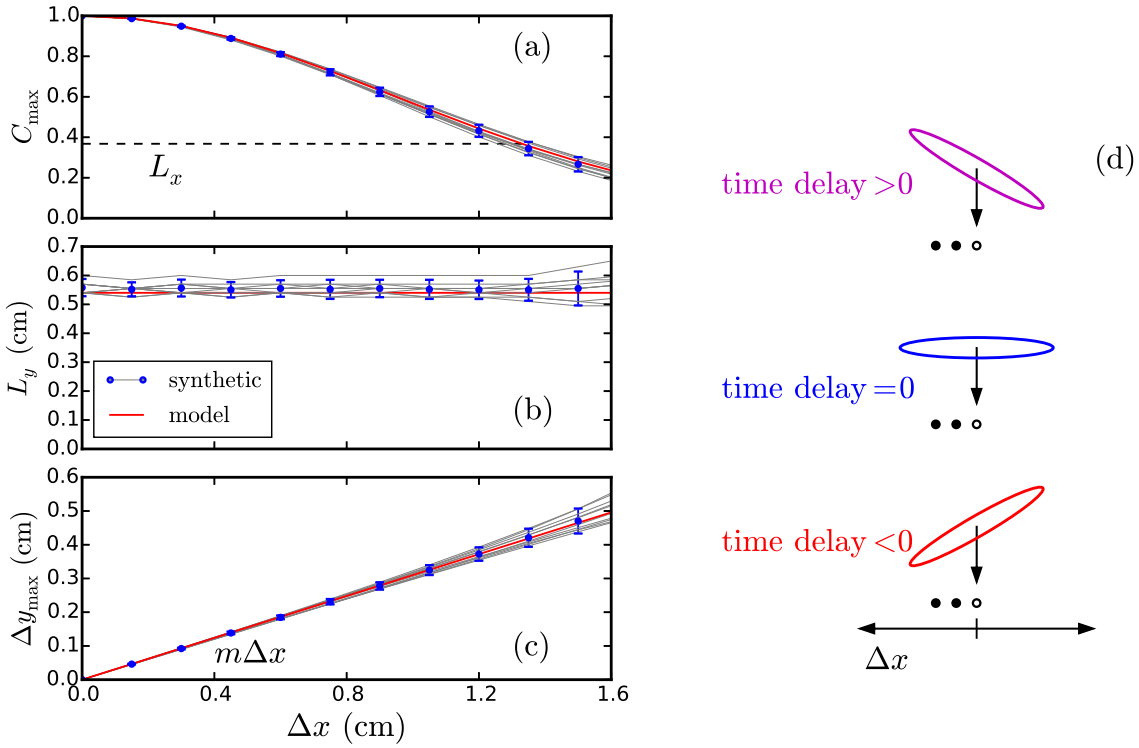

FIGURE 7.2: (a–c) Maximum $C_{\max}$, $1/e$-half-width L_y and position of the maximum $\Delta y_{\max}$ of the cross-correlation as a function of the separation Δx. L_x and m are indicated. The thin grey lines depict the results for several x values and the blue symbols their mean. The red lines depict the analytical results from Eq. 7.6-7.9. (d) Schematics illustrating the effect of the tilt angle of the structure on the time delay.

half-width L_y and position of the maximum $\Delta y_{\max}$. The three quantities are indicated on Fig. 7.1b for the $\Delta x = 0.72$ cm curve in red. It is important to remark that $\tau_{\max} = \Delta y_{\max}/u_\perp$ is time delay between the signals.

In Figs. 7.2a–c the dependence on Δx of the properties of the correlation function is shown in detail. The thin grey lines depict the results at different reference positions x and the blue symbols the average of them with the error bars indicating the standard deviation. The red line depicts the analytical prediction which will be discussed later. The maximum of the correlation $C_{\max}$ decays with Δx due to the spatial decorrelation of the turbulence in the x (radial) direction, therefore the $1/e$-decay length is defined as the correlation length L_x. The width of the correlation function is independent of the radial separation and its value is the correlation length in the y (perpendicular) direction L_y.

The position of the maximum $\Delta y_{\max}$ or equivalently the time delay, shows a linear behaviour $\Delta y_{\max} = m\Delta x$ characterized with a slope m, which is related to the tilt angle of the turbulent structures. This is schematically shown in Fig 7.2d where three structures with different tilt angles are displayed. The measurement points are depicted by black circles, the empty one indicates the reference. A clockwise tilted structure (purple) is seen earlier by the reference channel, resulting in a positive time delay that

increases with Δx, and gives a positive slope m. On the contrary, a counter-clockwise tilted structure (red) is seen later by the reference channel giving a negative time delay and m value. If the structure is not tilted and therefore aligned with the measurement points, the time delay and m are zero.

Since Eq. 7.2 depends explicitly on the reference position x, it gives a local measurement of the correlation function. This is illustrated by the grey lines in Fig. 7.2a–c which differ slightly for different x. Nevertheless, for statistically uniform turbulence, the correlation function is expected to be independent of x. For the synthetic turbulence, the finiteness of the computational domain induces fluctuations of $C_{\Delta x}(x, \Delta y)$ which can be treated as statistical uncertainties on L_x, m, and L_y.

For the following analytical calculations it is suitable to integrate Eq. 7.2 over x. The results do not change given the statistical uniformity of the turbulence, and it is convenient because the *2D correlation function* of the turbulent field is obtained:

$$C_{\Delta x}(\Delta y) = \iint \mathrm{d}x\,\mathrm{d}y\,\delta n^*(x,y)\delta n(x+\Delta x, y+\Delta y). \tag{7.3}$$

Inserting Eq. 6.2 into 7.3 yields the correlation function of the k spectrum:

$$C_{\Delta x}(\Delta y) = \iint \mathrm{d}k_x\,\mathrm{d}k_y\,|h(k_x,k_y)|^2 e^{ik_x\Delta x + ik_y\Delta y}, \tag{7.4}$$

which corresponds to the inverse Fourier transform of $|h|^2$. The previous result allows to link quantitatively the characteristics of the correlation function to the 2D k spectrum of the turbulence. This is done in detail for 2D Gaussian wavenumber spectra in the next subsection and for a Kolmogorov-type spectrum in Sec. 7.4.2.

7.1.2 Two-dimensional Gaussian k spectrum case

The correlation function of the Gaussian wavenumber spectrum in Eq. 6.1 is computed using Eq. 7.4. In this case a 2D Gaussian correlation function is obtained,

$$C_{\Delta x}(\Delta y) = \exp\left[-\frac{(\Delta x\cos\beta - \Delta y\sin\beta)^2}{\ell_{\max}^2} - \frac{(\Delta x\sin\beta + \Delta y\cos\beta)^2}{\ell_{\min}^2}\right]. \tag{7.5}$$

In Fig. 7.3a the $1/e$-contour of the correlation function is shown. It can be considered as the shape of the average turbulent structure, which is elongated and tilted by an angle β with respect to the x-direction. The correlation lengths along the major, $\ell_{\max}$, and minor, $\ell_{\min}$, axes are indicated.

It is useful to rewrite Eq. 7.5 as

$$C_{\Delta x}(\Delta y) = \overbrace{\exp\left[-\frac{(\Delta x)^2}{L_x^2}\right]}^{C_{\max}} \exp\left[-\frac{(\Delta y - \overbrace{m\Delta x}^{\Delta y_{\max}})^2}{L_y^2}\right], \tag{7.6}$$

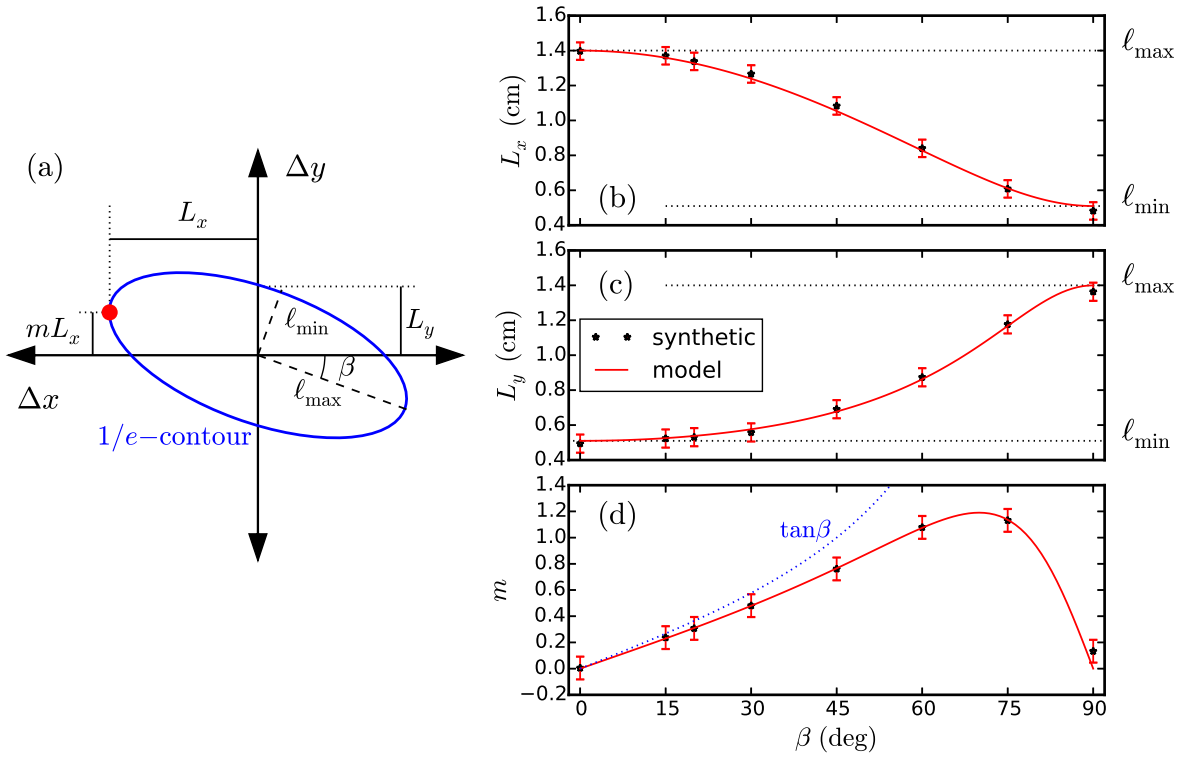

FIGURE 7.3: (a) $1/e$-contour of the correlation function Eq. 7.5. $\ell_{\max}$, $\ell_{\min}$, β and the quantities given in Eqs. 7.7–7.9 are indicated. (b–d) L_x, L_y and m as a function of the tilt angle β. The values obtained from synthetic turbulence (points) are in agreement with the results of Eqs. 7.7–7.9 (solid line).

where

$$L_x = \ell_{\max} \cos\beta \left[1 + \frac{\ell_{\min}^2}{\ell_{\max}^2} \tan^2\beta\right]^{1/2}, \tag{7.7}$$

$$L_y = \frac{\ell_{\min}}{\cos\beta} \left[1 + \frac{\ell_{\min}^2}{\ell_{\max}^2} \tan^2\beta\right]^{1/2}, \tag{7.8}$$

$$m = \tan\beta \left[\frac{1 - (\ell_{\min}/\ell_{\max})^2}{1 + (\ell_{\min}/\ell_{\max})^2 \tan^2\beta}\right]. \tag{7.9}$$

The geometrical meaning of L_x, L_y, and m is shown in Fig. 7.3a. L_x gives half the maximum width of the structure in the x-direction marked by the red point. The vertical position of this point is mL_x and depends on the tilt angle. The half width in y-direction on the axis is given by L_y.

For every Δx, Eq. 7.6 gives a Gaussian peak with amplitude $C_{\max}$, width L_y, and centred at $\Delta y_{\max}$, which is in agreement with the cross-correlation function depicted in Fig. 7.1b. Furthermore, the Δx dependence of $C_{\max}$, L_y, and $\Delta y_{\max}$ depicted by red

lines in Figs. 7.2a–c matches the average synthetic data (blue points), proving that the results of Eq. 7.2 and 7.3 are equivalent.

In order to confirm the dependence of L_x, L_y, and m on the turbulence parameters given in Eqs. 7.7–7.9, a scan of the tilt angle β has been performed. The values of L_x, L_y and m obtained from the synthetic turbulence are depicted by points in Figs. 7.3b–d, respectively. The results from the analytical expressions of Eqs. 7.7–7.9 are depicted by solid lines. L_x evolves from $\ell_{\max}$ at $\beta = 0°$ to $\ell_{\min}$ at $\beta = 90°$, corresponding to a change from horizontally to vertically aligned structures. L_y exhibits the opposite behaviour with a transition from $\ell_{\min}$ to $\ell_{\max}$. For small β, m increases as the structure's major axis misaligns with respect to the x-axis, whereas for β close to 90°, m decreases as the structure's minor axis aligns with the x-axis. As a result of these behaviours m has a maximum around 70°. Figs. 7.3b–d show good agreement between the results from the synthetic turbulence and the analytical model from Eqs. 7.7–7.9 for the three quantities. The system of equations 7.7 to 7.9 can be inverted for obtaining $\ell_{\max}$, $\ell_{\min}$, and β from the measurements of L_x, L_y, and m.

Since m increases with the tilt angle in a broad β range, it can be used to estimate directly the tilt angle. The bracket term in Eq. 7.9 can be approximated by 1 for elongated structures ($\ell_{\min}/\ell_{\max} < 1$) and angles far from 90° obtaining

$$m \approx \tan\beta. \tag{7.10}$$

This approximation is depicted in Fig. 7.3d by a dashed blue line. It agrees well with the exact solution for β up to 30°, therefore the tilt angle is precisely obtained from $\beta = \tan^{-1} m$. For β between 30° and 55°, $\tan\beta$ is above the exact solution hence the tilt angle is underestimated. The range of validity of the approximation increases with the elongation. Eq. 7.10 allows to calculate the tilt angle directly from m, assuming elongated structures with a finite tilt angle with respect to the cutoff. This approximation is useful because the diagnostic effects have an impact on the L_x and L_y measurements that make the inversion of Eqs. 7.7–7.9 problematic.

7.1.3 Ray propagation effect

For oblique angles of incidence, the radial scan pertaining to a radial correlation measurement results in a perpendicular displacement of the measurement position. Fig. 7.4a depicts rays for different probing frequencies in slab geometry. The measurement positions are indicated with circles. The change in the radial position Δx induces a perpendicular displacement Δy_{ray} of the measurement position. For a small cutoff separation the measurement points are aligned along a straight line defining an angle Θ_{ray} with respect to the x-axis which fulfils

$$\Delta y_{\text{ray}} = \tan(\Theta_{\text{ray}})\Delta x. \tag{7.11}$$

The geometrical definition of Θ_{ray} is shown in the zoomed Fig.7.4b. The upper and right axes indicated Δx and Δy_{ray}, respectively. Θ_{ray} can be computed from ray tracing data.

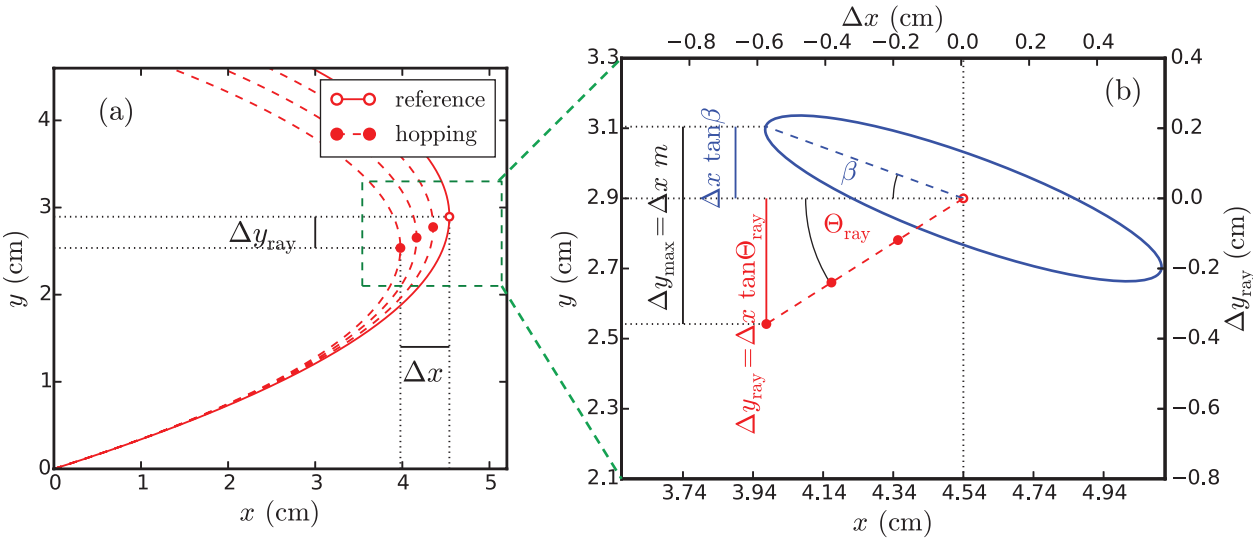

FIGURE 7.4: (a) Rays of the reference frequency and three hopping frequencies for O-mode and linear density profile, $\theta = 17.7°$. The measurement positions are indicated with circles. Δx and Δy_{ray} are depicted for one case. (b) Zoom showing schematically the effect of the vertical displacement of the measurement positions on the Δy_{max} measurement. Refer to the text for more details.

Equations 7.2 and 7.3 assume that both Doppler channels are measuring at the same y-position. This is valid only for normal incidence where there is no perpendicular displacement of the measurement positions. However, for Doppler reflectometry the perpendicular displacement of the measurement points introduces an extra contribution to Δy_{max} and therefore to m. This extra contribution results from geometrical considerations as shown in Fig. 7.4b. The measurement points are depicted by red points and the turbulent structure is shown with the blue contour. The measurement Δy_{max} (indicated with a black line) is the sum of the ray tracing contribution $\Delta y_{\mathrm{ray}} = \Delta x \tan\Theta_{\mathrm{ray}}$ (red line) and of the structure tilt contribution $\Delta x \tan\beta$ (blue line). Therefore

$$m = \tan\beta + \tan\Theta_{\mathrm{ray}}. \tag{7.12}$$

Concluding, it is important to consider the perpendicular displacement of the measurement positions, which has an impact on Δy_{ray} (hence on the time delay τ_{max}) and m.

The geometrical considerations summarized in Eq. 7.12 are the basis of the tilt angle measurement method. In Chs. 8 and 9 the tilt angle will be determined from the analysis of experimental time delays τ_{max}, $u_{\perp}$, and Θ_{ray} in the ASDEX Upgrade tokamak and the TJ-II stellarator. Eq. 7.12 will be adapted to the sign conventions of time delay and angle used there. Diagnostic effects on this measurement are investigated in the following sections. In particular, the impact of the temporal decorrelation of the turbulence is discussed in Sec. 7.4.

7.2 Two-dimensional full-wave simulations

In order to investigate the influence of plasma-wave interactions in the correlation measurements and to asses if the characterization method presented in the previous section can be applied to Doppler reflectometry signals, radial correlation Doppler reflectometry measurements are modelled with 2DFW simulations. The same configuration as for the power response studies (cf. Sec. 6.3) is used with 60.2 and 94.4 GHz as reference frequencies. The hopping channel signal is obtained by repeating the simulations with lower frequencies in the range 60.2–47.8 and 94.4–83.4 GHz for O- and X-mode, respectively. The turbulent field with a 2D Gaussian spectrum is the same of Sec. 6.1. Five turbulence levels within the same range as in the power response studies were used. Aiming for a better $k_\perp$ overlap between O- and X-mode, $\theta = 5.6°$ is also simulated for X-mode. In order to minimize statistical fluctuations the number of samples was increased to 5920.

7.2.1 Linear case

From the power response studies (cf. Fig. 6.10) it is known that for $\delta n_{\mathrm{rms}}/n_c = 0.1$ % the reflectometer response is linear for both polarizations, excluding the X-mode at $\theta = 22.31°$ where a slight enhanced power response is observed. This linear case allows to study the diagnostic response excluding any non-linear effect.

The cross-correlation function of the complex signals is calculated. Only its absolute value is considered, since the complex phase contains information on the Doppler frequency irrelevant for the correlation analysis. The quantities $C_{\max}$, L_y and $\Delta y_{\max}$ are computed. Figs. 7.5a–c shows the O-mode results (points) as a function of Δx for different angles of incidence θ. The dashed lines will be explained later. The correlation decays with the radial separation, but the decay is strongly affected by the angle of incidence. A similar effect has been already observed in Ref. [19] and was attributed to non-local scattering [21]. The width of the cross-correlation L_y is independent of Δx for small values and shows a slight dependence with θ. $\Delta y_{\max}$ shows a linear behaviour with the radial separation for small Δx as observed previously. The slope m increases with θ as expected from the perpendicular displacement effect already discussed (cf. Sec. 7.1.3).

For large Δx and small θ (blue and green data), the correlation decay seems to be slower than what is expected for a Gaussian decay depicted by the dashed lines. This effect is related to non-local scattering, where scattering along the beam path contributes to the reflectometer signal (cf. Sec. 4.3). This results in a higher correlation compared to what one would expect for the cutoff [21]. This effect explains also the deviations of $\Delta y_{\max}$ from the expected linear behaviour, because the scattering from different regions along the probing beam do not have a well defined time delay like the contribution from the cutoff.

A Gaussian fit $C_{\max} = \exp[-(\Delta x/L_x)^2]$ is done weighting the data with $1/C_{\max}^2$. Since points with low correlation are less important, this procedure filters out non-local scattering effects and focuses the analysis to the cutoff contribution. Furthermore, it is also convenient because for low correlation levels, the cross-correlation and therefore the extracted quantities are strongly affected by the statistical fluctuations. A detailed study of non-local scattering effects would require increased statistics in the simulations. L_y

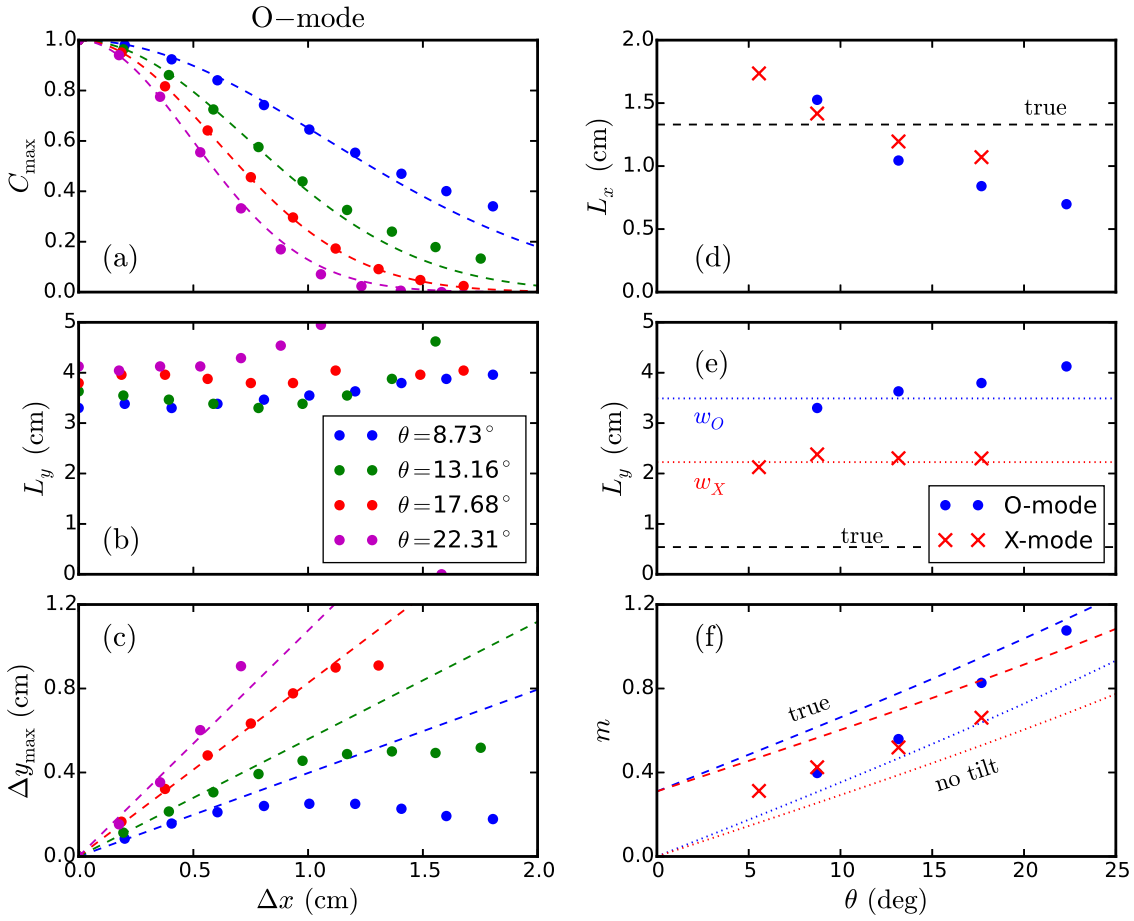

FIGURE 7.5: (a–c) Correlation parameters C_{max}, L_y and Δy_{max} obtained from 2DFW simulations in the linear regime. The colours represent different angles of incidence θ. (d–f) L_x, L_y and m obtained from O- and X-mode 2DFW data. Refer to the text for more details.

is taken from its value at $\Delta x = 0$. Δy_{max} is fitted with a linear function using only the first few points which behave linearly and are not affected by the non-local scattering.

L_x, L_y and m are obtained from the fitting process described above. The results as a function of θ are shown in Figs. 7.5d–f. Additionally, data from X-mode simulations are included. L_x decreases with the angle of incidence for both polarizations in Fig. 7.5d. A similar trend has been observed previously in simulations [19] and experiments [16]. L_x is slightly overestimated for small θ compared to the true value marked with a dashed line in the plot, and is underestimated for large θ. It has been found that the $k_\perp$ variation produced by the probing frequency scan induces decorrelation of the signals for large θ. This effect is discussed in detail in Appendix B. The decorrelation effect is strong in the performed simulations and is responsible, to a large extent, for the L_x reduction with θ reported here. This prevents a detailed study of the non-local scattering which may induce an overestimation of L_x for small θ and a convergence to the true value for large θ [21]. In the presented simulations, the correlation length L_x can be estimated from the data at small θ (not affected by the decorrelation effect) with an error of 10 and 20 % for O- and X-mode, respectively.

For both polarizations, L_y is strongly overestimated compared to the true value indicated with a black dashed line in Fig. 7.5e. L_y exhibits a slight dependence on θ for the O-mode data. Note that the obtained values match well the beam size w indicated with dotted lines for each polarization. Therefore in the simulations presented, the width of the cross-correlation gives the beam size rather than the perpendicular correlation length L_y.

The 2DFW data for both polarizations in Fig. 7.5f underestimate m compared to the point measurement depicted by dashed lines and computed with Eq. 7.12 ($\beta = 20°$). Nevertheless the dependence with θ is similar, which shows that the m change is due to the perpendicular displacement effect. Note that m is larger than the point measurement for the case without tilting ($\beta = 0$) depicted by dotted lines. This means that a non-zero tilt with the correct sign is recovered from the simulations. The tilt angle obtained from the simulated data using Eq. 7.12 is $\beta \approx 10°$, which has the correct sign but underestimates the true value by 50 %.

In summary, the radial correlation length L_x can be estimated (10–20 % error) from the simulated data at small θ for which the impact of decorrelation effect discussed in Appendix B is negligible. The width of the cross-correlation gives an estimation of the beam size and not of the perpendicular correlation length L_y. The time delay and the slope m behave as predicted by the perpendicular displacement discussed in Sec. 7.1.3. The tilt angle of the turbulence can be extracted from the simulated data with the correct sign, although the value is underestimated. These simulations have shown the applicability of the developed analysis techniques to Doppler reflectometer signals in the linear regime. The role of the radial and spectral resolutions on the linear measurements will be investigated in the next section, which will allow to understand better the effects observed in these simulations. Moreover the conditions required for a more accurate characterization will also be discussed.

7.2.2 Non-linear case

The previous correlation analysis is repeated for the turbulence level scan. L_x, L_y and m are obtained from $C_{\max}$, width and $\Delta y_{\max}$ as for the linear case. The results are shown in Fig. 7.6 as a function of the turbulence level for different angles of incidence depicted by different colours. O- and X-mode results are plotted in the left and right columns, respectively. The upper axis shows the non-linearity parameter γ (cf. Eq. 5.8). L_x decreases with the turbulence level in the non-linear regime ($\gamma = 0.1$–10), for all angles of incidence and both polarizations. In the saturation regime ($\gamma \approx 10$), L_x does not depend on the angle of incidence and is underestimated compared to the true value indicated with the dashed line. L_y does not change appreciably with the turbulence level. For increasing turbulence level between $\gamma = 0.1$–1, m decreases as the reflectometer starts operating in the non-linear regimes. This effect is stronger for X-mode since it runs first into non-linear operation (cf. Ch. 6). For the highest turbulence level in the saturation regime m shows an erratic behaviour.

The decrease of the correlation with the turbulence level (Figs. 7.6a and d) is explained by the multiple scattering processes responsible for the non-linear effects dis-

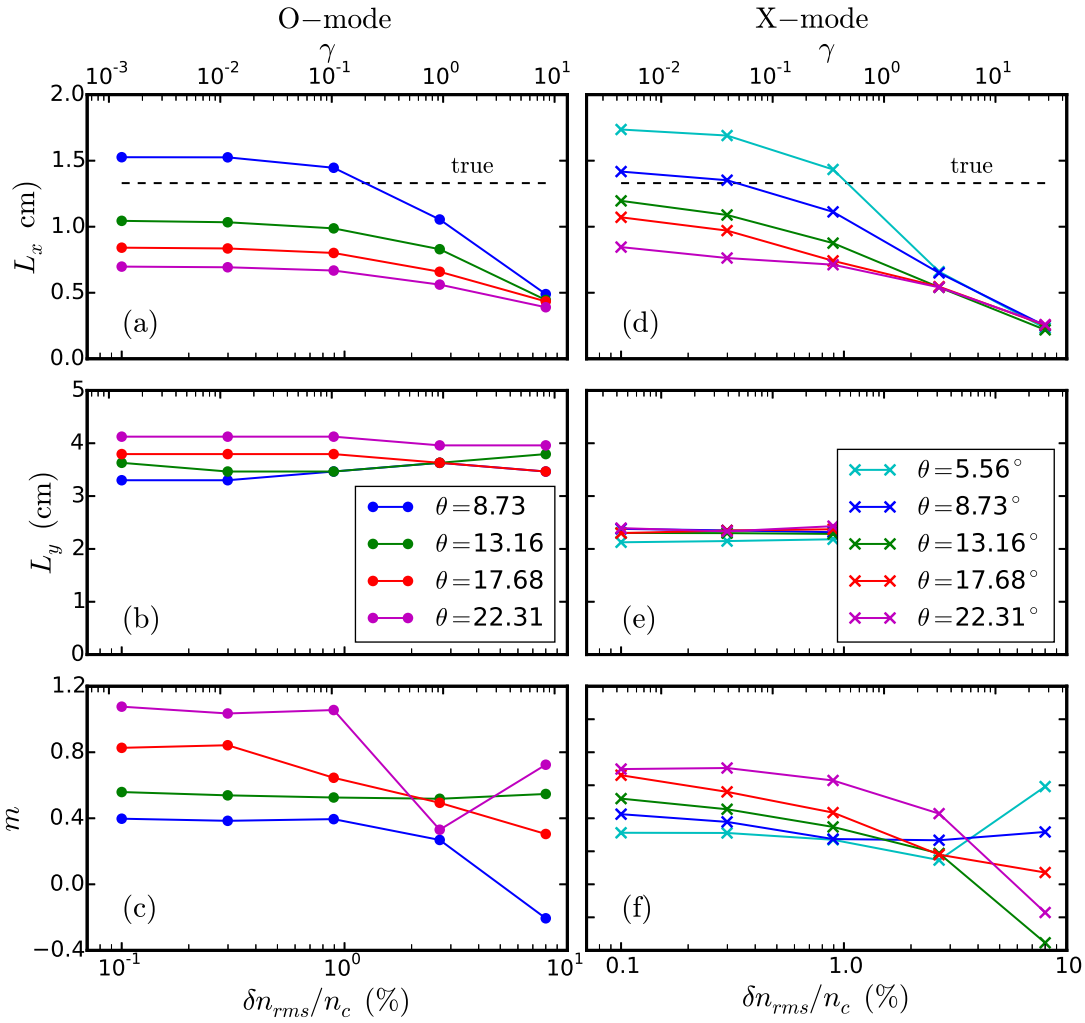

FIGURE 7.6: Turbulence parameters L_x, L_y and m as a function of the turbulence level obtained from O- (a–c) and X-mode (d–f) 2DFW data. The colours depict different angles of incidence.

cussed in Sec. 6.2.4. In the linear regime, the reflectometer signal is produced by scattering events at $k_\perp$. This contribution is well correlated for both reflectometer channels. However, for large turbulence levels, multiple scattering events at wavenumbers different from $k_\perp$ contribute to the reflectometer signal (see Fig. 6.7). These multiple contributions are poorly correlated.

The strong effects of non-linearities on L_x and m limit the direct application of the characterization method when the diagnostic response is non-linear. The method could be still applied if non-linear effects are assessed with 2DFW simulations. Nevertheless, this must be done in detail for the specific experimental conditions, because the linearity of the response depends strongly on the k spectrum and differs from the Gaussian case.

7.3 Diagnostic filter effect

The filter effect of the diagnostic in k space is considered. This allows to understand better the linear simulations presented in the previous section, to predict the diagnostic response for more general cases, and to identify conditions for which the characterization of the turbulence with radial correlation Doppler reflectometry is accurate.

The Doppler reflectometer is studied using the Born approximation from Eq. 5.7. For the sake of simplicity, here E_0^2 or equivalently the weighting function W is approximated with a Gaussian filter function f given by

$$E_0^2(x,y) \approx f(x,y) = \exp\left[-\frac{x^2}{(\delta r)^2} - \frac{2y^2}{w^2} - ik_\perp y\right]. \tag{7.13}$$

The width in the x- and y-directions is defined by the radial resolution δr and the beam width $w = 2/\Delta k$, respectively. The complex phase gives the Bragg condition at $k_\perp$. In Fourier space the filter function is

$$\widehat{f}^{-1}(k_x,k_y) = \exp\left[-\frac{k_x^2(\delta r)^2}{4}\right]\exp\left[-\frac{(k_y-k_\perp)^2}{2(\Delta k)^2}\right], \tag{7.14}$$

where $\widehat{\cdot}^{-1}$ stands for the inverse Fourier transform. It corresponds to a 2D filter centred at $k_x = 0$ and $k_y = k_\perp$ and is analogous to the filter function f introduced for the physical optics model in Sec. 6.2.4.

Equation 7.13 is a reasonable approximation given the maximization of E_0 at the cutoff discussed in Sec. 6.3. It will be shown that it recovers some of the effects observed in 2DFW simulations and experiments. Furthermore, it is useful for the understanding and assessment of the impact of the radial and spectral resolution on the characterization method discussed in Sec. 7.1. Nevertheless, quantitative predictions should be taken carefully considering the approximations done and the absence of non-local scattering effects [21].

Using the Born approximation (Eq. 5.7) with the filter function (Eq. 7.13), the Doppler signal probing at the position (x,y) is

$$V(x,y) = \iint \mathrm{d}x'\mathrm{d}y'\, \delta n(x+x', y+y') f(x',y'). \tag{7.15}$$

This expression considers the integration over the scattering volume, therefore it is a generalization of the point measurement of Eq. 7.1. Writing δn in terms of the k spectrum from Eq. 6.2, Eq. 7.15 becomes:

$$\begin{aligned} V(x,y) &= \iiiint \mathrm{d}x'\mathrm{d}y'\,\mathrm{d}k_x\mathrm{d}k_y\, h(k_x,k_y) e^{ik_x(x+x')+ik_y(y+y')} f(x',y'), \\ &= \iint \mathrm{d}k_x\mathrm{d}k_y\, h(k_x,k_y)\widehat{f}^{-1}(k_x,k_y) e^{ik_x x + ik_y y}. \end{aligned} \tag{7.16}$$

In the last step the signal is given by the turbulent field filtered in k-space. This indicates the filtering role of the Doppler reflectometer.

The cross-correlation of the Doppler reflectometer signals is

$$\widetilde{C}_{\Delta x}(\Delta y) = \iint \mathrm{d}x\,\mathrm{d}y\, V^*(x,y)V(x+\Delta x, y+\Delta y),$$

where the tilde stands for the fact that the filtered signals are used as input. In the last equation the statistical uniformity of the turbulence has been used as it has been done to obtain Eq. 7.3. Inserting Eq. 7.16 in the last expression yields the correlation function

$$\widetilde{C}_{\Delta x}(\Delta y) = \iint \mathrm{d}k_x \mathrm{d}k_y\, |h(k_x,k_y)|^2 |\widehat{f}^{-1}(k_x,k_y)|^2 e^{ik_x\Delta x + ik_y \Delta y}. \tag{7.17}$$

It corresponds to the inverse Fourier transform of the filtered k spectrum. This is different from the point measurement case of Eq. 7.4 where no filter is included.

For the 2D Gaussian spectrum of Eq. 6.1, the integral in Eq. 7.17 is solved analytically obtaining

$$|\widetilde{C}_{\Delta x}(\Delta y)| = \exp\left[-\frac{(\Delta x)^2}{\widetilde{L}_x^2} - \frac{(\Delta y - \widetilde{m}\Delta x)^2}{\widetilde{L}_y^2}\right]. \tag{7.18}$$

The absolute value is taken because the k_y-filter gives a complex phase without further physical information. The tilded quantities are:

$$\widetilde{L}_x = L_x\sqrt{1+\frac{2(\delta r)^2}{L_x^2}}, \tag{7.19}$$

$$\widetilde{L}_y = \sqrt{L_y^2 + \frac{4}{(\Delta k)^2} + \frac{2m^2(\delta r)^2}{1+2(\delta r)^2/L_x^2}}, \tag{7.20}$$

$$\widetilde{m} = m\left(1+\frac{2(\delta r)^2}{L_x^2}\right)^{-1}. \tag{7.21}$$

The measured radial correlation length $\widetilde{L}_x$ is overestimated by a factor $\sqrt{1+2(\delta r)^2/L_x^2}$. If the radial resolution is small compared to the radial correlation length, $\delta r \ll L_x$, this effect is small and the true L_x is recovered. This is in agreement with the linear 2DFW results from Fig. 7.5d at small θ, where a slight overestimation of L_x is observed. It is important to note that no dependence on $k_\perp$ is obtained for the Gaussian case. The decrease of the measured L_x with θ observed in the simulations is not reproduced by the filter effect and is explained in Appendix B.

The measured width of the correlation $\widetilde{L}_y$ is overestimated by the spectral and radial resolution through the second and third term in Eq. 7.20, respectively. For a good spectral resolution ($L_y\Delta k \ll 1$), the second term dominates and the width of the correlation is rather given by the beam width, $\widetilde{L}_y \approx 2/\Delta k = w$. This is the case of the 2DFW simulations shown in Fig. 7.5e.

The slope $\widetilde{m}$ in Eq. 7.21 underestimates m due to the radial resolution by a factor $(1+2(\delta r)^2/L_x^2)^{-1}$. Nevertheless, for $\delta r \ll L_x$ this effect is also negligible. There is also no $k_\perp$ dependence for the Gaussian case. The filter effect recovers the underestimation of m and hence of the tilt angle β obtained from the 2DFW results by taking $\delta r \approx 0.8$ cm. Note that the ray propagation effect can be considered by adding $\tan\Theta_{\mathrm{ray}}$ at the r.h.s. of Eq. 7.21.

The filtering effect of the Doppler reflectometry does affect the quantities used for the 2D characterization of the turbulence. The measured radial correlation lengths and time delays can be affected by the radial resolution, nevertheless for favourable experimental conditions ($\delta r \ll L_x$) the effect is negligible, thus the radial correlation length and tilt angle can be measured. The width of the correlation is mostly given by the beam width, hence the estimation of the perpendicular correlation length is problematic.

7.4 Temporal decorrelation effect

Up to now, frozen turbulence has been assumed in the characterization method presented in Sec. 7.1 and has been used in the 2DFW simulations and the filtering effect discussed in the previous sections. This is a valid assumption if the structures do not change appreciably while they propagate through the scattering region. This condition can be fulfilled depending on the turbulence decorrelation time τ_d and the plasma flow $u_\perp$. Here, the effect of the decorrelation time is considered. A correction to the characterization method accounting for the decorrelation time is given.

The cross-correlation function for a given radial separation Δx and considering the decorrelation time of the turbulence is

$$C_{\Delta x}(\tau) = C_{\max} \exp\left[-\frac{(u_\perp \tau - \Delta y_{\max})^2}{w^2}\right] \exp\left(-\frac{\tau^2}{\tau_d^2}\right) \tag{7.22}$$

The first two terms correspond to the frozen turbulence case as in Eq. 7.6, where $C_{\max}$ and $\Delta y_{\max}$ are defined by the 2D structure of the turbulence. The beam width w is taken instead of L_y because of the filtering effect discussed previously. The last term includes a Gaussian correlation function in time [106].

$C_{\Delta x}(\tau)$ has been plotted in Fig. 7.7 for $w = 4.0$ cm, $u_\perp = 1$ km/s, $\Delta y_{\max} = 1.0$ cm. Colours indicate different τ_d values. The blue line for $\tau_d \to \infty$ shows a peak centred at $\tau_{\max} = \Delta y_{\max}/u_\perp = 10$ μs as in the frozen turbulence case. As τ_d decreases the peak becomes narrower and moves closer to $\tau = 0$, implying a reduction of the measured time delay $\tau_{\max}$. This effect is small for $\tau_d = 119$ μs (green line) with a time delay 10 % smaller than the one of the frozen case. The effect is strong for $\tau_d = 13$ μs (light blue line) with a time delay 90 % smaller than the one of the frozen case. The maximum of the correlation is not strongly affected, even for small τ_d.

It can be shown that the maximum of $C_{\Delta x}(\tau)$ is at

$$\tau_{\max} = \frac{\Delta y_{\max}}{u_\perp}\left(1 + \frac{w^2}{u_\perp^2 \tau_d^2}\right)^{-1} = \frac{\Delta y_{\max}}{u_\perp} F_d. \tag{7.23}$$

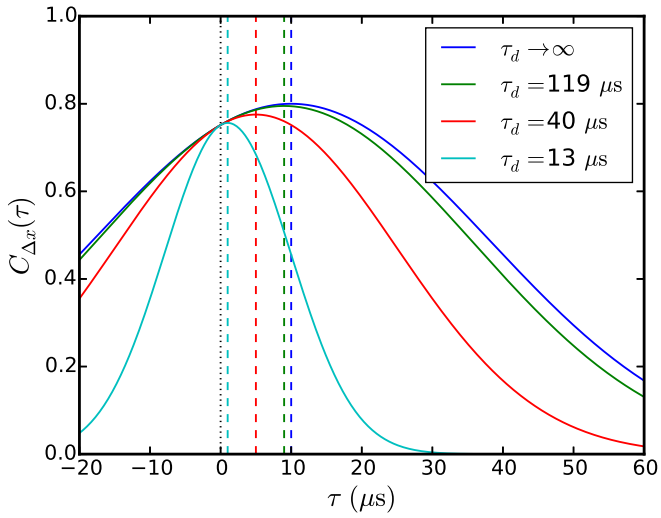

FIGURE 7.7: Cross-correlation function from Eq. 7.22 for different τ_d values. The blue curve corresponds to the frozen turbulence case.

The first term gives the time delay expected from the frozen turbulence case, and the second term is a correction factor F_d related to the temporal decorrelation that reduces the measured time delay. It is relevant for $\tau_d \leq w/u_\perp$.

The time delay reduction leads to an underestimation of m. This effect can be included in Eq. 7.12 with the correction factor F_d as follows:

$$m = F_d \left[\tan(\beta) + \tan(\Theta_{\text{ray}})\right]. \tag{7.24}$$

In the experiments, the impact of the decorrelation time can be assessed by comparing the passing time $w/u_\perp$ with τ_d measurements or expected values [106, 107]. For large plasma velocities the passing time is substantially smaller than τ_d and the decorrelation time effect has no impact, whereas for small velocities the passing time is comparable to or larger than τ_d and the correction factor F_d is necessary. The impact of the temporal decorrelation on the experimental measurements will be investigated in Chs. 8 and 9. Eq. 7.24 will be used for the tilt angle measurement and Eq. 7.23 for estimations of the correction factor and decorrelation time.

7.5 Realistic wavenumber spectrum

Gaussian k spectra have often been used in theory [21] and simulations [19] of radial correlation Doppler reflectometry. Their properties make them suitable for analytical calculations, as it has been shown in the previous sections and in Ch. 6. Nevertheless, more realistic Kolmogorov-type spectra should be also considered (cf. Sec. 2.1). It is important to assess how the spectral shape impacts the correlation measurements and what other effects may appear when non-Gaussian spectra are considered. In this section the turbulence from a gyrokinetic simulation of the ASDEX Upgrade tokamak plasma is studied. The 2D k spectrum is computed and characterized with the method presented in Sec. 7.1. Then, the diagnostic effects are investigated with the filter effect from Sec. 7.3.

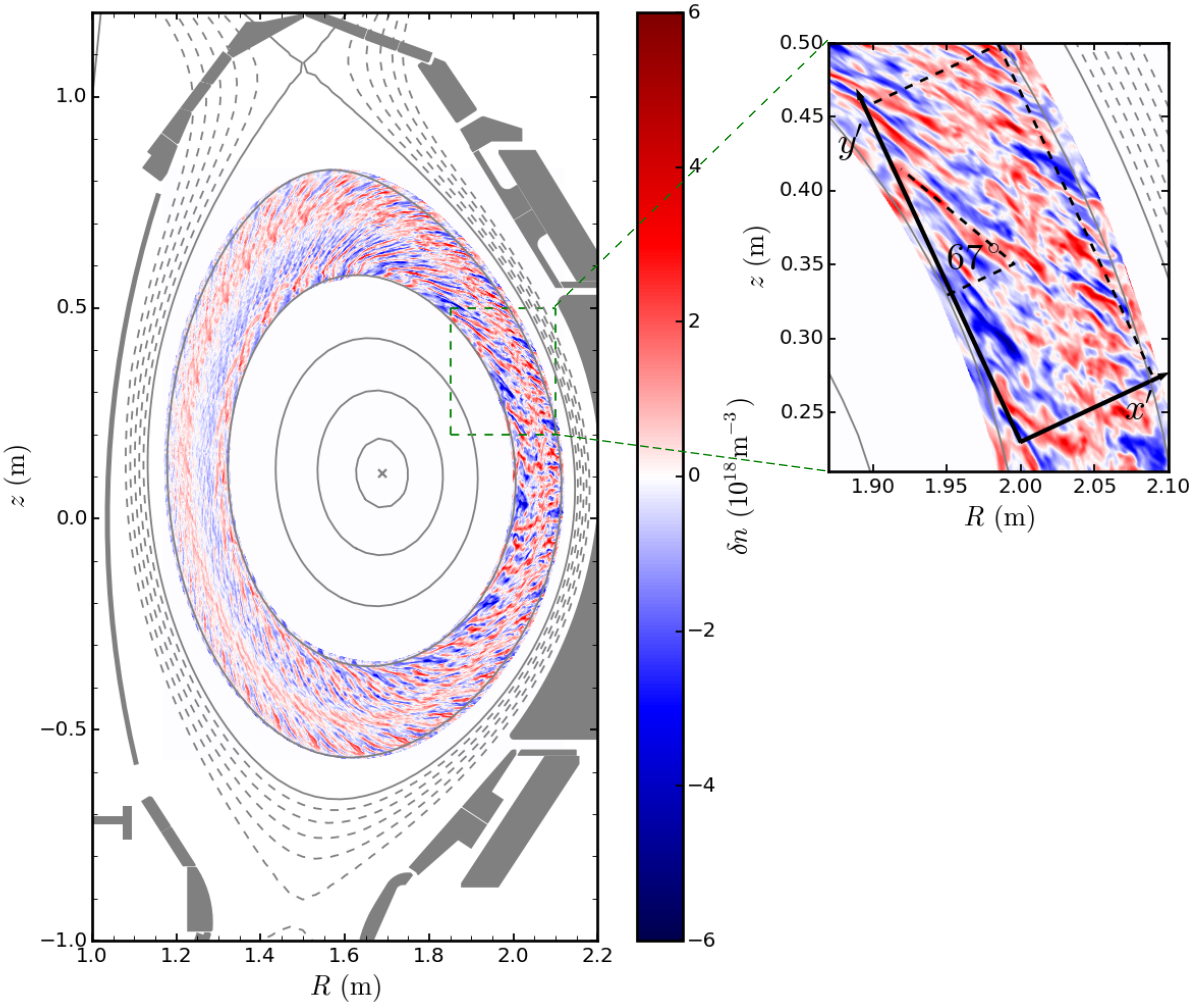

FIGURE 7.8: Contour plot of the density fluctuations on the cross-section of the ASDEX Upgrade tokamak. A zoom to the region of interest is also shown. The turbulence is computed byt he gyrokinetic code GENE [17, 41].

7.5.1 Gyrokinetic turbulence and 2D k spectrum

The gyrokinetic simulations for the plasma conditions in Ref. [17] are studied. The reference discharge is AUG#31260, a L-mode in USN configuration with 1 MW NBI and 0.45 MW ECRH power. The core average density is $5.5{\times}10^{19}$ m^{-3}. The density fluctuations are obtained from non-linear GENE [28, 41] simulations, local to the flux surface at $\rho = 0.8$. The turbulence is ITG driven for large scales $k_\perp \rho_s < 1$. More details on the discharge and the simulations can be found in Ref. [17].

The poloidal cross-section of the ASDEX Upgrade tokamak together with a sample contour plot of the density fluctuations is shown in Fig. 7.8. The turbulent field located between the flux surfaces $\rho = 0.75$ and 0.95 shows an asymmetry between the high and low field side. The fluctuation level is higher on the low field side (bad curvature) reflecting the ballooning character of the turbulence. Elongated turbulent structures are observed, their size and tilt changes along the flux surface reflecting the locality of the turbulence.

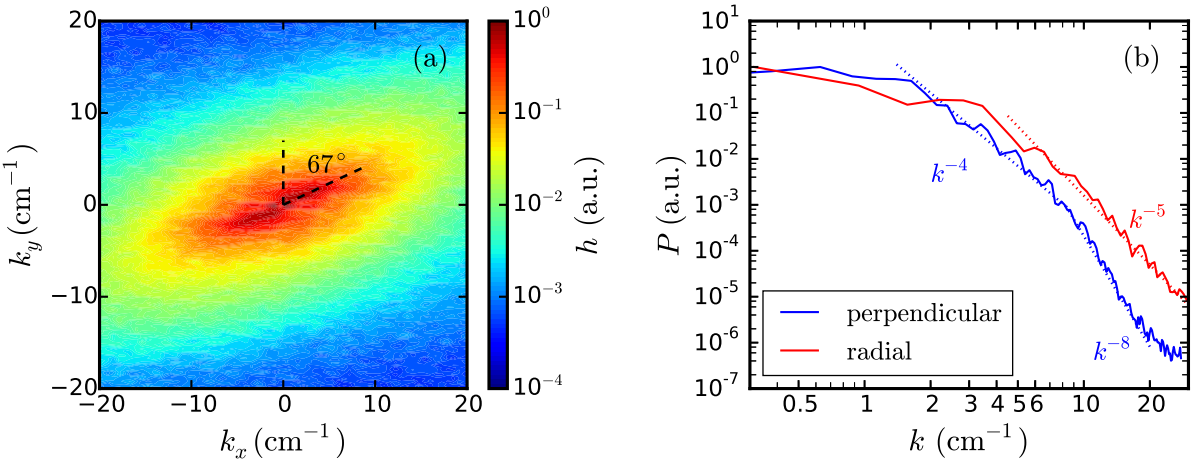

FIGURE 7.9: (a) Contour plot of the k spectrum computed from GENE data. (b) Perpendicular and radial k power spectra. Power laws in different k ranges are indicated.

The analysis in this section is focused on the region where the steerable Doppler reflectometer system measures (cf. Sec. 4.2.2). This region is indicated with a dashed square in Fig. 7.8 and magnified on the right side of the figure. Elongated and tilted structures show a tilt angle with respect to the normal to the flux surface of about 67° as indicated in the zoomed area.

In order to compute the 2D k spectrum a local coordinate system (x', y') is defined with the x'-axis perpendicularly aligned to the flux surfaces. The new coordinate system and the analysis domain are depicted by arrows and a dashed box in the zoom in Fig. 7.8. The 2D k spectrum is obtained by computing the Fourier transform of the density fluctuations in this new coordinate system.

The contour plot of the k spectrum averaged over 20 samples is shown in Fig. 7.9a. Elongation and a tilt of 67° with respect to the vertical axis are observed, similarly to the synthetic Gaussian case in Fig. 6.1a. The radial and perpendicular wavenumber spectra are computed by taking the spectral power $|h|^2$ at $k_y = 0$ and $k_x = 0$, respectively. The results are plotted in Fig. 7.9b, where a Kolomorov-type spectrum of density fluctuations is obtained for both cases. The perpendicular wavenumber spectrum is flat up to approximately 2 cm^{-1}. Afterwards it is characterized by power laws with spectral indices of about -4 and -8 in regions separated by a knee at about 8 cm^{-1}. The radial wavenumber spectrum is almost flat up to approximately 4 cm^{-1} and then it is characterized by a spectral index of -5.

It has to be remarked that tilt angles obtained in local simulations do not consider radial shear of the plasma parameters, which is a relevant ingredient in the tilt angle generation mechanism [38]. A comparison of the tilt angle with experimental measurements requires global gyrokinetic simulations which do account for these effects.

7.5.2 Correlation function

The correlation function is computed from the 2D k spectrum using Eq. 7.4. The contour plot of $C_{\Delta x}(\Delta y)$ is shown in Fig. 7.10a, where a main structure centred at the origin is

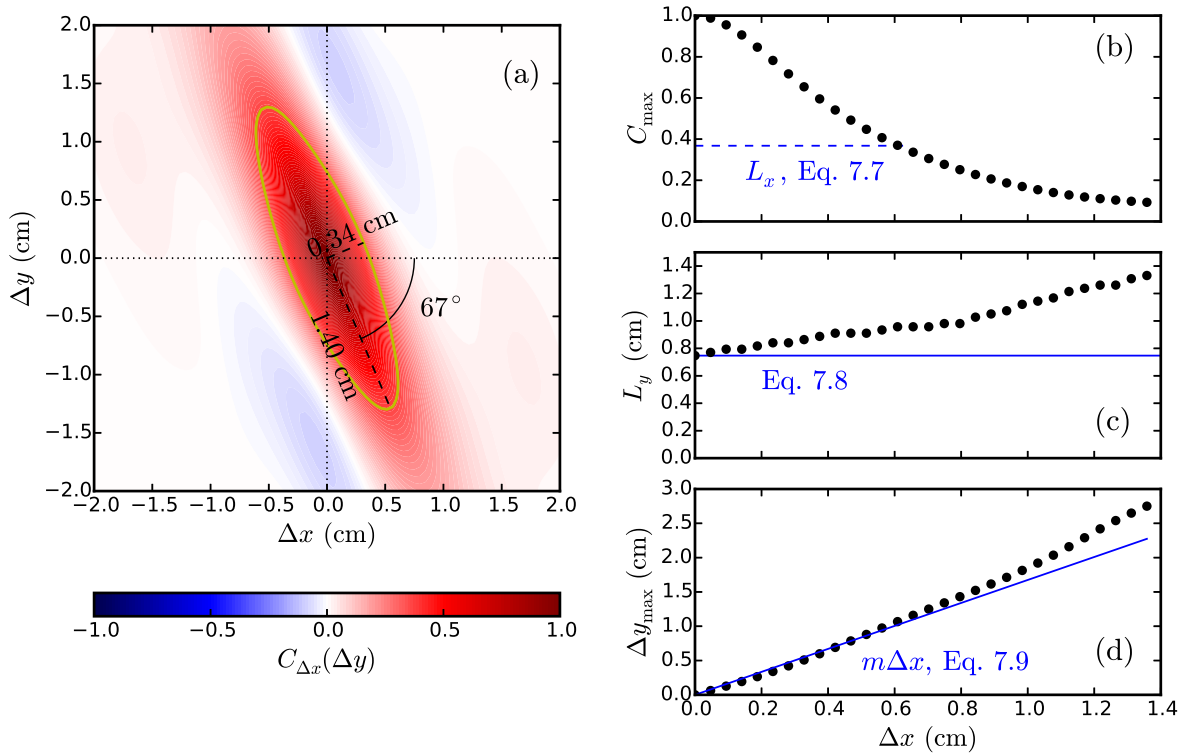

FIGURE 7.10: (a) 2D correlation function of the turbulent field. (b) $C_{\max}$, (c) L_y and (d) $\Delta y_{\max}$ as a function of Δx. Predictions of Eqs. 7.7–7.9 are depicted in blue.

obtained. Its elongation and tilt are in agreement with the structures zoomed in Fig. 7.8. The $1/e$-contour depicted by the yellow line is approximately an ellipse characterized with $\ell_{\max} = 1.40$ cm, $\ell_{\min} = 0.32$ cm and $\beta = 67°$. The three quantities are indicated in Fig. 7.10a.

The turbulent field is characterized using the method presented in Sec. 7.1. $C_{\max}$, L_y and $\Delta y_{\max}$ are computed from $C_{\Delta x}(\Delta y)$ at different Δx, which corresponds to vertical cuts in Fig. 7.10a. $C_{\max}$, L_y and $\Delta y_{\max}$ are plotted with points as a function of Δx in Figs. 7.10b–d. The maximum of the correlation decreases similarly to the Gaussian case for small Δx. The radial correlation length L_x computed with Eq. 7.7 is depicted by the dashed blue line in Fig. 7.10b. It matches the $1/e$-decay length. Nevertheless contrary to the Gaussian case, there is a slowly decaying tail for large Δx. This is due only to the spectral shape and not to diagnostic effects which have not been considered yet. L_y in Fig. 7.10c is not constant contrary to the Gaussian case, instead it increases with Δx. Nevertheless L_y computed from Eq. 7.8 depicted by a blue line matches the value at $\Delta x = 0$. $\Delta y_{\max}$ in Fig. 7.10d depends linearly on Δx. The solid blue line depicts $m\Delta x$ with m computed from Eq. 7.9. A good agreement is obtained for small Δx.

$C_{\max}$, L_y and $\Delta y_{\max}$ are well described by the model proposed in Sec. 7.1.2, also for a Kolmogorov-type k spectrum. The characterization method presented in Sec. 7.1 can be applied to more realistic turbulence in the point measurement case.

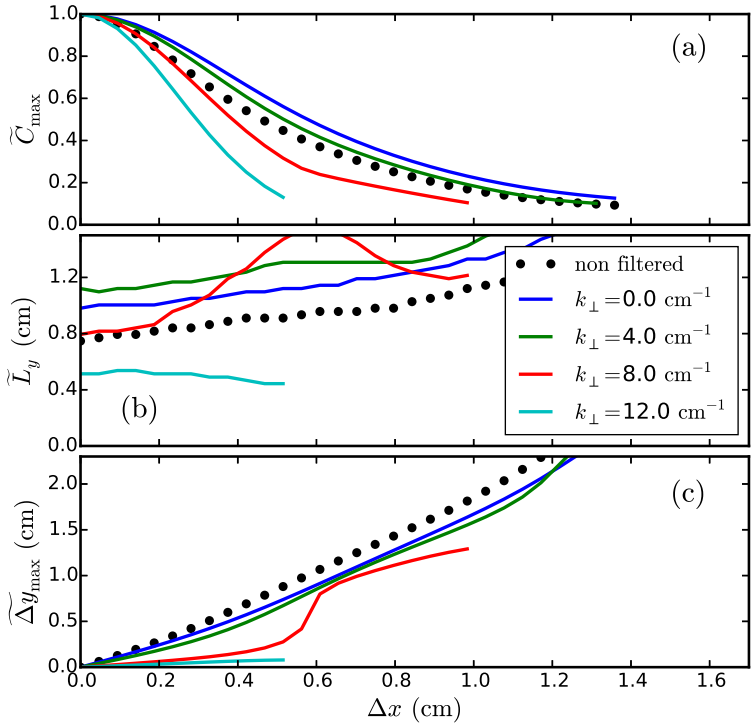

FIGURE 7.11: (a) $\widetilde{C}_{\max}$, (b) $\widetilde{L}_y$ and (c) $\widetilde{\Delta y}_{\max}$ as a function of Δx obtained from the filtered correlation function. The colours depict different $k_\perp$ values. The non-filtered (point measurement) results are shown with black symbols.

7.5.3 Diagnostic filter effect

It has been shown for the Gaussian case in Sec. 7.2, that diagnostic effects can have an important impact on correlation measurements and therefore on the proposed characterization method. A complete study for realistic k spectra would require systematic 2DFW simulations in order to include non-linearities, non-local scattering and k filtering. Nevertheless, here only the filtering effect discussed in Sec. 7.3 is considered. Further studies with 2DFW simulations are left for future work.

The filter effect of the Doppler reflectometer is included through Eqs. 7.14 and 7.17. The values for the radial and spectral resolutions are 0.2 cm and 3.5 cm^{-1}, respectively. The filtered correlation function for different $k_\perp$ values is computed and $\widetilde{C}_{\max}$, $\widetilde{L}_y$ and $\widetilde{\Delta y}_{\max}$ are obtained. The results are plotted in Figs. 7.11a–c where the colours correspond to different $k_\perp$ values. The black points depict the non-filtered (point measurement) case already shown in Fig. 7.10b–d.

In Fig. 7.11a, $C_{\max}$ decays faster for larger $k_\perp$. This effect, absent in the Gaussian case, is due to the filter effect combined with the spectral shape. It is important to remark that despite of the qualitative similarities, this behaviour is not caused by non-local scattering [21] or the decorrelation effect discussed in Appendix B. Moreover for small $k_\perp$, the correlation decays slightly slower compare to the point measurement because of the finite radial resolution. It should be noted that the radial correlation length is well recovered for the measurements at small $k_\perp$. This effect can explain the reduction

of the radial correlation length with $k_\perp$ measured in the ASDEX Upgrade tokamak (cf. Sec. 8.1.3) and the TJ-II stellarator (cf. Ref. [16]).

For small $k_\perp$, $\widetilde{L}_y$ in Fig. 7.11b follows the point like measurements, but overestimate the value due to the beam waist contribution (cf. Eq. 7.20). For larger $k_\perp$, $\widetilde{L}_y$ decreases and shows a different behaviour with Δx. In Fig. 7.11c, $\Delta y_{\max}$ increases linearly for small Δx in all cases. The slope obtained at small $k_\perp$ (blue and green lines) recovers the value of the point like measurement related to the tilt angle of the turbulence. Nevertheless, the slope decreases with $k_\perp$ obtaining values close to zero for the higher $k_\perp$ (light blue line). This effect was also absent in the Gaussian case.

In summary, the filter effect of the Doppler reflectometer has an impact on the correlation measurements. In particular, a $k_\perp$ dependence of L_x and m appears for Kolmogorov-type turbulence. Although L_x and m are underestimated for large $k_\perp$, the values obtained at small $k_\perp$ yield to a good estimation of the the radial correlation length and tilt angle. This effect has not been investigated yet in the literature where only Gaussian turbulence has been considered [19, 21]. The difference between the Gaussian and the Kolmogorov-type case, show that the spectral shape plays an important role in the diagnostic response. This deserves further investigations.

Summary

A new analysis technique of the time delay of the cross-correlation function $\tau_{\max}$, velocity $u_\perp$ and the geometry of the measurement positions has been proposed (cf. Sec. 7.1). It can be used to measure the tilt angle of elongated turbulent structures. The effect of the temporal decorrelation of the turbulence has been investigated. It has been shown that for small velocities, $u_\perp \leq w/\tau_d$, the measured time delays are underestimated with respect to the frozen turbulence case. This effect can be assessed and accounted in the analysis with a correction factor F_d (cf. Sec. 7.4). The analysis technique developed will be applied in Chs. 8 and 9, where the tilt angle will be measured in the experiments.

The diagnostic response has been considered using two-dimensional full-wave simulations and a linear analysis based on the Born approximation. It has been found that in the linear diagnostic regime, the radial correlation length and the tilt angle can be estimated. The impact of the finite radial resolution of the diagnostic has been studied, it is relevant when the radial resolution is comparable or bigger than the radial correlation length. The non-linear diagnostic response has a strong impact on the correlation measurements, hence estimations of the radial correlation length and tilt angle are problematic when a strong linear diagnostic response is involved.

It has been found that the spectral shape plays an important role in the diagnostic response. For a realistic Kolmogorov-type turbulence, the filter effect of the Doppler reflectometer induces a reduction of the measured radial correlation length and tilt angle with $k_\perp$. This result is used for the interpretation of experimental data in Sec. 8.1.3.

Chapter 8

Turbulence characterization in ASDEX Upgrade and TJ-II plasmas

The density turbulence in the ASDEX Upgrade tokamak and the TJ-II stellarator is characterized in detail using Doppler reflectometry. The $k_\perp$ spectrum, $u_\perp$ profile and radial correlation length L_r are experimentally investigated. The purpose of these studies is two-fold. On the one hand the experimental data are analysed based on the modelling presented in Ch. 6 and 7. The impact of the diagnostic effects and the accuracy of the measurements are discussed. On the other hand, specific physical aspects of the turbulence are discussed. In particular, the effect on the turbulence structure of different driving forces and the turbulence regulation by sheared flows (cf. Ch. 2) is discussed.

The application of the analysis techniques developed in Secs. 7.1.3 and 7.3.2 to experimental data is discussed in detail. As a result, the mean tilt angle of the turbulent structures is measured in the confined region for the first time in both machines. This is a proof of principle of the tilt angle measurement method which is one of the major contributions of this thesis. The tilt angle measurement in TJ-II is compared to results from gyrokinetic simulations.

L-mode plasmas in the ASDEX Upgrade tokamak and the TJ-II stellarator are experimentally investigated in Sec. 8.1 and 8.2, respectively. A discussion summarizing the results in both machines and conclusions are presented in Sec. 8.3.

8.1 Measurements on ASDEX Upgrade

In this section, the density turbulence is investigated with Doppler reflectometry in the ASDEX Upgrade tokamak (AUG) in a medium density L-mode discharge . The recently installed W- and V-band reflectometers (cf. Sec. 4.3.1), together with the steerable mirror [83] have made possible detailed $k_\perp$ spectra and radial correlation studies. In Sec. 8.1.1 the discharge under investigation is described. In Sec. 8.1.2 a detailed experimental study of $k_\perp$ spectra and $u_\perp$ profile is presented. Doppler reflectometry measurements with O- and X-mode polarizations are compared. In Sec. 8.1.3 a detailed study of the diagnostic effects on the radial correlation length L_r is carried out and the new measurement technique of the tilt angle of turbulent structures is applied.

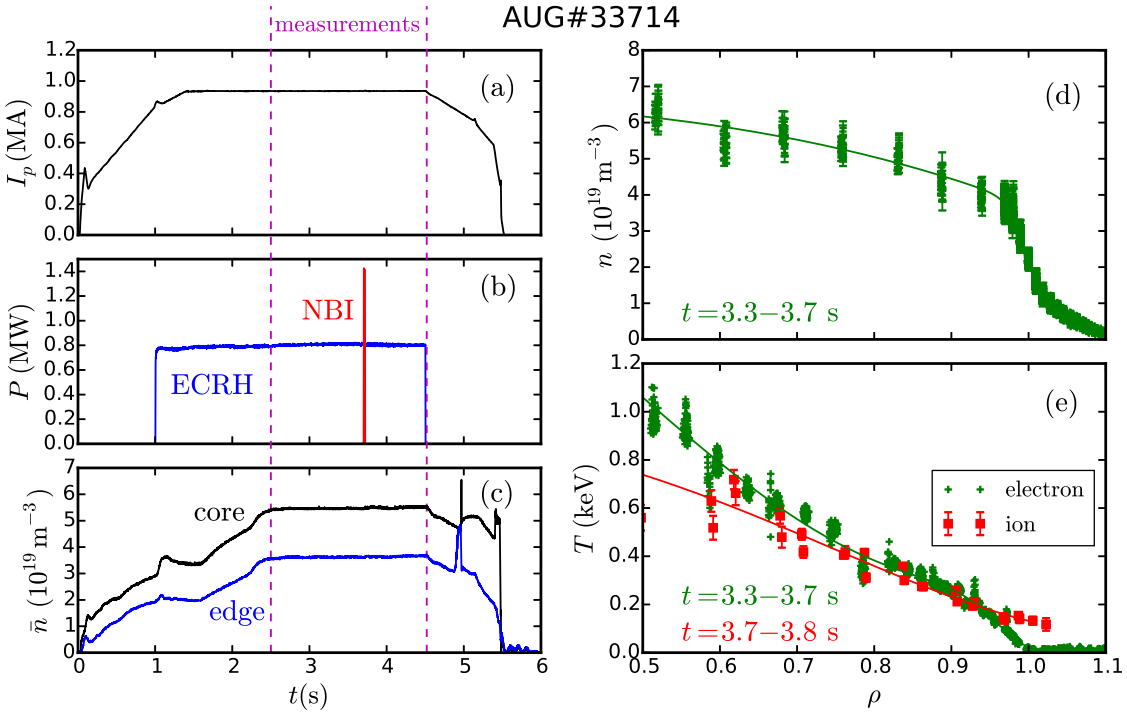

FIGURE 8.1: Time traces of (a) the plasma current, (b) auxiliary heating power and (c) plasma density for the reference discharge #33714. The phase of constant density used for the reflectometry measurements is indicated with magenta lines. (d) Density and (e) temperature profiles during the measurement phase. Measured data are depicted by symbols and the respective fits with solid lines.

8.1.1 Discharges

Dedicated experiments have been performed on the ASDEX Upgrade tokamak for the turbulence characterization using Doppler reflectometry. ECRH heated L-mode plasmas with medium density have been investigated. The density has been chosen in order optimize the radial range measured by the Doppler reflectometers. The upper single null (USN) configuration has been used in order to avoid a transition into the H-mode because of the higher L-H power threshold for this configuration [108].

The time traces of the plasma current, heating power and line average density of the reference discharge #33714 are shown in Figs. 8.1a–c. A constant 0.8 MW of ECR heating power on axis is applied to the plasma. The core and edge line average densities are stationary between t =2.5 and 4.5 s. The reflectometry measurements are performed during this time window as indicated at the top of the figure. A NBI blip is applied for CXRS measurements. Four comparable discharges (#33714–17) have been performed to allow for a complete reflectometer parameter scan.

The density and temperature profiles in the measurement phase are shown in Figs. 8.1d and e, respectively. The plasma density obtained from Thomson scattering and lithium beam diagnostics is shown in Fig. 8.1d with symbols. The solid line depicts the fit to the density profile which will be used later for ray tracing calculations with TORBEAM. The electron temperature depicted by green plus symbols in Fig. 8.1e is obtained from

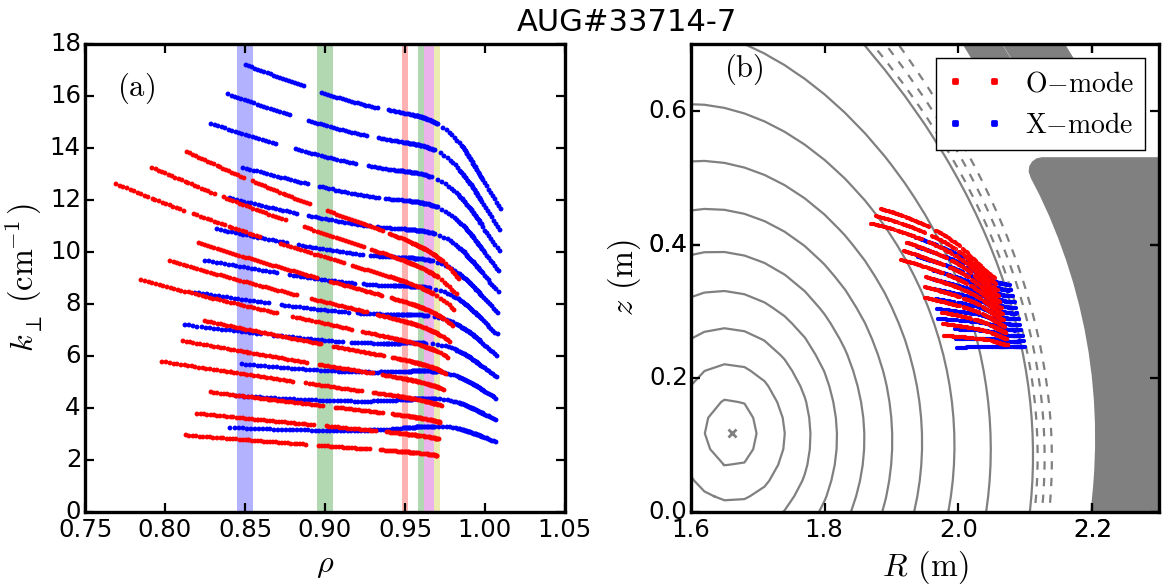

FIGURE 8.2: (a) Probed $k_\perp$ values as a function of the measured radial position ρ. (b) Measurement position on the poloidal AUG cross-section. O- and X-mode are plotted with red and blue symbols, respectively.

Thomson scattering and ECE measurements. The ion temperature (red squares) is obtained from the CXRS measurements. In both cases the solid line depicts the fit to the data. The density and temperature profiles are stationary during the measurement phase and are similar for the four discharges.

8.1.2 Measurement of $k_\perp$ spectra and $u_\perp$ profile

The two V-band (50–75 GHz) reflectometers have been used in O-mode polarization, and the W-band (75–103 GHz) in X-mode polarization. For more details on the reflectometer configuration refer to Sec. 4.3.1. In this section only the data of one W- and one V-band channel is considered for $k_\perp$ spectra and $u_\perp$ profile measurements. The second V-band channel will be considered later in Sec. 8.1.3 for correlation measurements. The probing frequency has been stepped rapidly (5 ms per frequency). A broad scan of the angle of incidence (12 values) and probing frequencies (120 frequencies per angle of incidence) has been performed during the measurement phase of the four discharges (cf. Figs. 8.1a–c). The frequency patterns have been specially designed in order to cover a large radial region and to have an overlap of the O- and X-mode measurements.

The scattering position and the probed $k_\perp$ are computed using TORBEAM with the fit to the density profile shown in Fig. 8.1d. The probed $k_\perp$ is plotted as a function of the radial position ρ in Fig. 8.2a. O- and X-mode data are depicted by red and blue symbols, respectively. For each polarization 12 rows of points are distinguished. Each of them corresponds to one angle of incidence, and the constitutive points to the different probing frequencies. The coloured areas illustrate the radial windows where the $k_\perp$ spectra are computed later. Both polarizations overlap radially in the range $\rho \approx 0.87$–0.97. The measurements overlap also in $k_\perp$, while the specific range depends on ρ. The X-mode

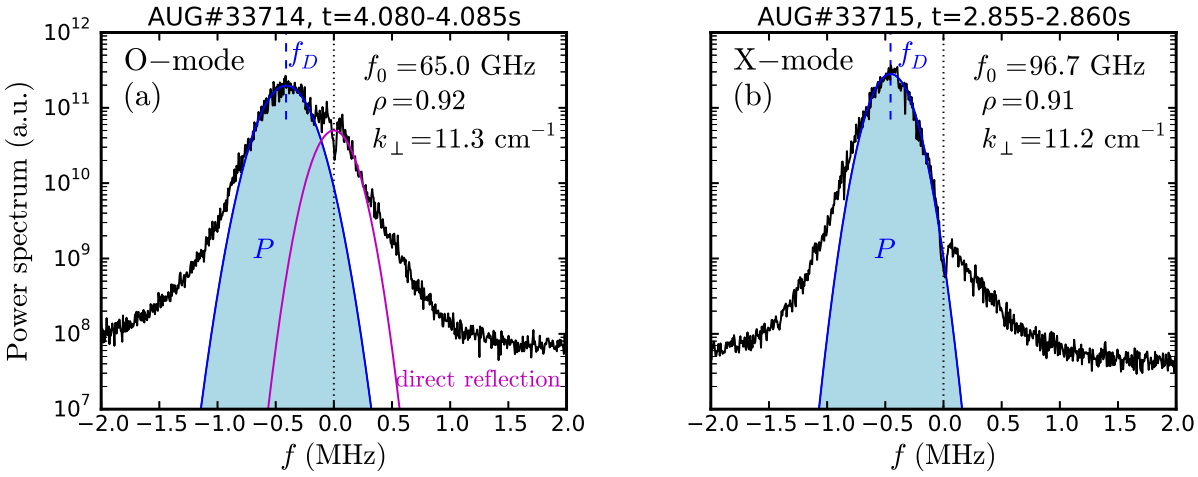

FIGURE 8.3: Power spectra of the (a) O- and (b) X-mode reflectometer signal measured at similar radial positions and $k_\perp$. The fit to the Doppler peak is shown with a blue line. The O-mode exhibits a zero-order reflection.

probes at higher $k_\perp$ (up to 16 cm^{-1}) due to the higher probing k_0. Fig. 8.2b shows the O- and X-mode measurement positions on the AUG cross-section, which overlap spatially.

For each probing frequency and angle of incidence, the power spectrum of the reflectometer signal is computed as described in Sec. 4.2. Example spectra measured in O- and X-mode polarization at similar ρ and $k_\perp$ values are depicted in Figs. 8.3a and b, respectively. The blue and magenta lines are the fits to be explained below. Both spectra show a Doppler peak (blue) at approximately 0.45 MHz, however the O-mode spectrum exhibits also a contribution at zero frequency (magenta). It corresponds to the direct reflection discussed in Sec. 4.2.2 which contains information different to the backscattering at the cutoff, and that can corrupt the analysis if it is not properly treated. The direct reflection is excluded from the analysis by fitting separately the Doppler peak and the direct reflection contribution with Gaussian functions as depicted in Fig. 8.3a. The X-mode spectrum shows no direct reflection contribution and is fitted with a single peak as shown in Fig. 8.3b. The backscattered power P and the Doppler shift f_D are obtained from the Gaussian fit to the Doppler peak in both cases. The optimization of the antenna and mirrors for frequencies in the W-band [83] explains the better quality of the X-mode spectrum.

The $k_\perp$ spectra at different radial positions are computed by taking P as a function of $k_\perp$ for narrow radial windows, plotted with different colours in Fig. 8.4 for (a) O- and (b) X-mode data. The different spectra have been vertically offset for visualization purposes. A spectral decay with $k_\perp$ is observed for all cases. In general the O-mode spectra decay faster than the X-mode spectra, and a faster decay for large $k_\perp$ is observed. Separate power laws have been fitted to the spectra for small and large $k_\perp$. The results are depicted by solid lines and the spectral indices are indicated in the figure. The dispersion of the X-mode data at $\rho = 0.85$ and 0.9 (blue and green data) makes the fit difficult, thus in these cases the fits are just meant as a guide to the eye.

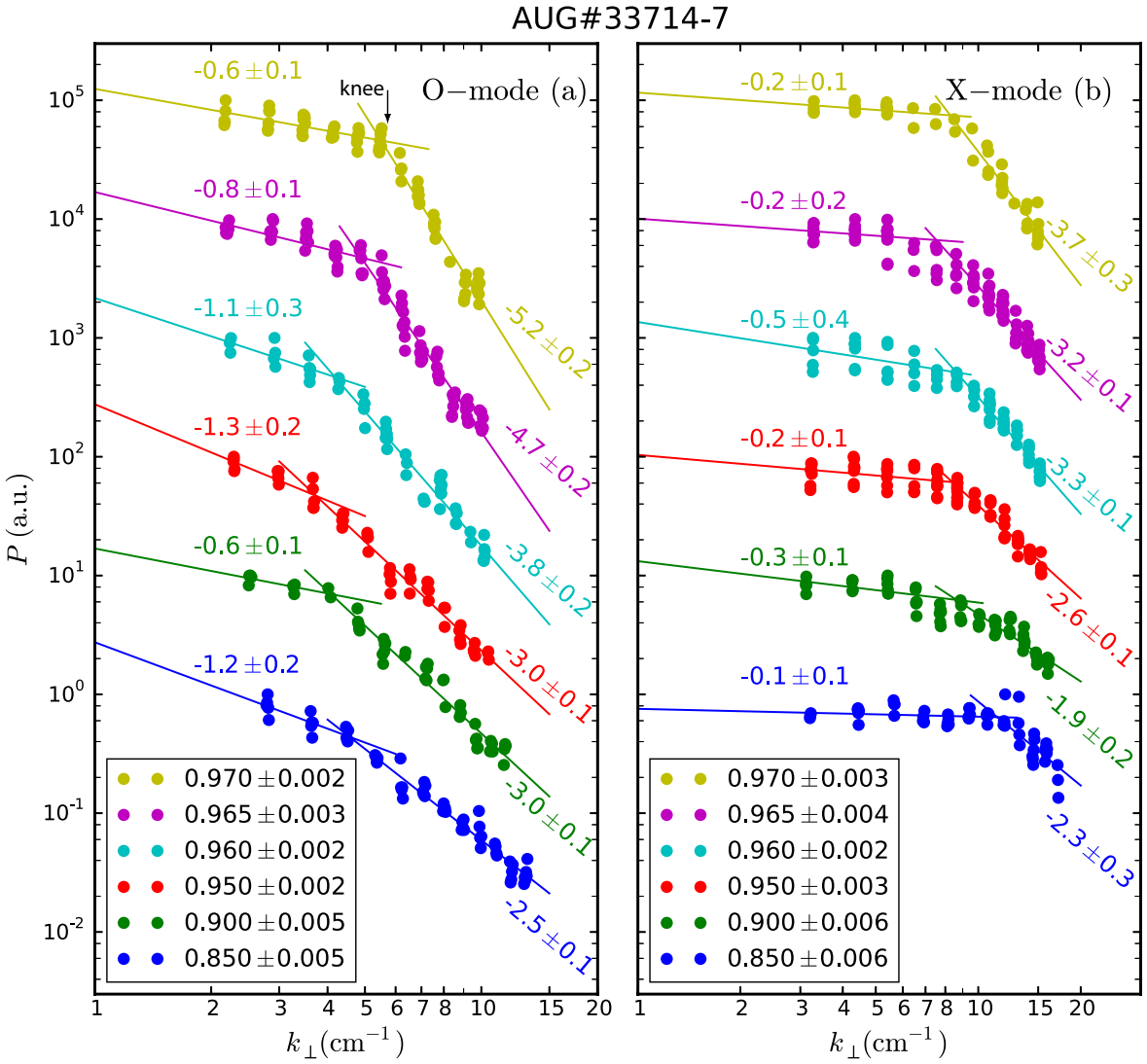

FIGURE 8.4: $k_\perp$ spectra at different radial positions (ρ ranges are indicated in the legend) obtained with (a) O-mode and (b) X-mode polarization. The spectra are vertically shifted for better visibility. Power law fits are depicted by solid lines, and the spectral indices are indicated.

A progressive steepening of the spectra in the high $k_\perp$ range is observed for increasing ρ. For O-mode polarization, the spectral index increases slightly between $\rho = 0.85$ and 0.95 from -2.5 to -3.0, then it increases rapidly between $\rho = 0.95$ and 0.97 from -3.0 to -5.2. For X-mode data, the the spectral index increases from -1.9 to -3.7 in the entire measured range. The wavenumber separating the regions with different power laws suggests the presence of a knee in the spectra. For the O-mode the knee is located at around 4 cm^{-1} for $\rho \lesssim 0.95$. It moves to higher $k_\perp$ as ρ increases reaching a value of about 6 cm^{-1} for the outermost measurement positions. For the X-mode the knee is at higher $k_\perp$ for all cases.

In Ch. 6 it has been discussed that non-linear diagnostic effects may occur as the turbulence level increases, and that they can lead to a flattening of the measured $k_\perp$ spectrum. Since the turbulence level is expected to increase towards the plasma edge, a

transition to the non-linear regime would cause a flattening of the measured spectra as ρ increases. In contrast, the O-mode data shows a strong spectral steepening towards the plasma edge. This suggest a linear diagnostic response and a radial variation of the real $k_\perp$ spectrum.

The O-mode spectral indices are in all cases more pronounced than the X-mode ones. The smallness of the X-mode spectral indices indicates a non-linear diagnostic response as discussed in Sec. 6. The approximately flat spectra observed up to 8 cm^{-1} suggest a power response closed to the saturation regime, while the smaller spectral indices in the high $k_\perp$ range indicate an enhanced power response, cf. Fig.6.11c. The observations on the linearity of the O-mode and non-linearity of the X-mode measurements are supported by studies done for similar experimental conditions and presented in Ref. [17, 104]. In the following, the O-mode spectra are interpreted in terms of physics, while the X-mode spectral shape is most likely influenced by diagnostic effects.

The small change of the O-mode spectra measured between $\rho = 0.85$ and 0.95 indicates similar turbulence characteristics in this radial range. The further steepening of the spectra at $\rho > 0.95$ may indicate a change of the turbulence drive or a non-linear saturation mechanism. This change will be further discussed in this section after considering the turbulence level profile and the turbulence driving terms.

The spectra knees are in the range $k_\perp \rho_i = 0.26$–0.4 which is rather low compared to the typical observation of $k_\perp \rho_i \approx 1$ [17, 30]. For the innermost measurements, the spectral indices are comparable to those obtained in Ref. [30] (-3.5 and -3.0) in a similar $k_\perp \rho_i$ range. In previous measurements at AUG reported in Ref. [17], a spectral knee at around 8 cm^{-1} and spectral indices of -2.2 and -7.2 were measured in the $\rho = 0.80$–0.85 range. The knee obtained here is at lower values and the spectral indices are shallower. Nevertheless it should be noted that the plasma investigated in Ref. [17] had lower ECR and additional NBI heating, thus a different turbulence driving or non-linear saturation mechanism may lead to a different $k_\perp$ spectrum. Further investigations with gyrokinetic simulations may provide a better understanding of the measured $k_\perp$ spectra and the radial evolution observed. This is left for future work.

The relative variations of the turbulence level $\delta n^2_{\mathrm{rms}}$ can be estimated from the backscattered power P measured in the linear regime according to Eq. 4.8. The radial profile of P is plotted in Fig. 8.5b as an estimation of the turbulence level. The O-mode measurements in a low (2.5–3.8 cm^{-1} red circles) and high (7.0–9.0 cm^{-1} red crosses) $k_\perp$ range are depicted. The last set of data is lower due to the spectral drop-off. X-mode data in the low $k_\perp$ range have been also included (blue symbols) in order to have edge measurements. It should be noted that due to the non-linear diagnostic response of the X-mode measurements, the turbulence level cannot be accurately obtained from the X-mode data. Although trends in P may still be an indication of turbulence level changes, quantitative estimations based on X-mode data should be taken carefully. The normalized gradients of ion temperature $\nabla T_i/T_i$ and density $\nabla n/n$ are plotted on top with a magenta dashed and green solid lines, respectively. The $u_\perp$ profiles (cf. Eq. 4.10) obtained for the same sets of data are shown in Fig. 8.5c. The plasma density and ion temperature profiles have been included in Fig. 8.5a for comparison.

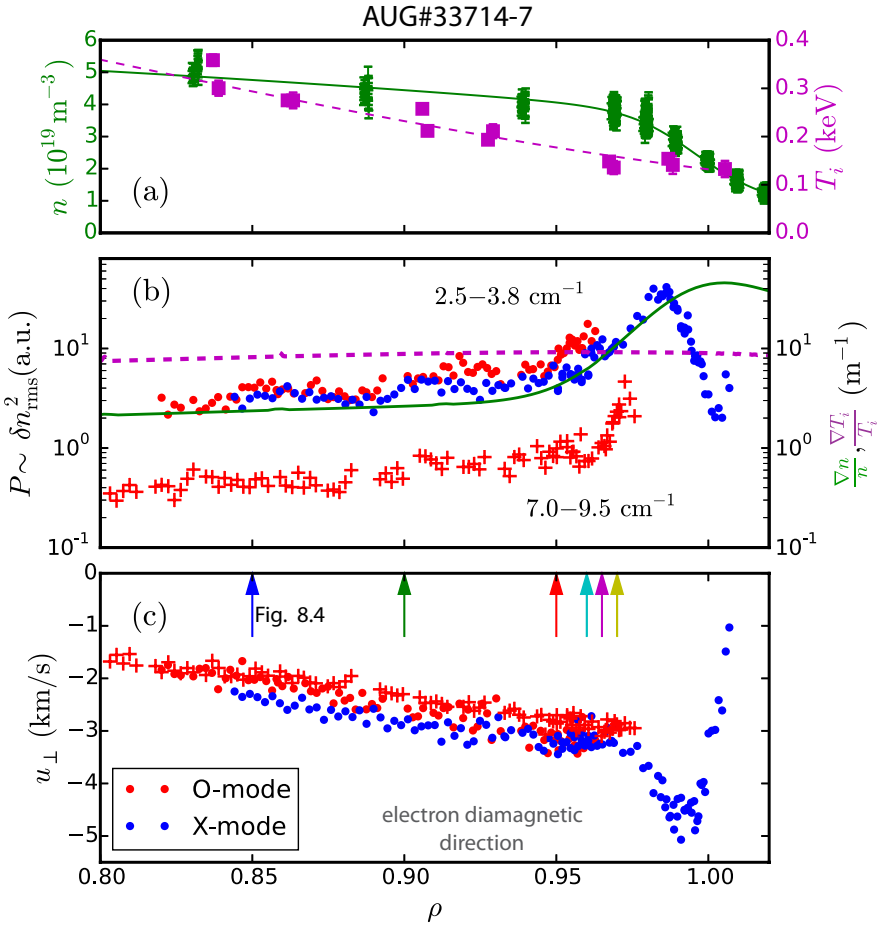

FIGURE 8.5: (a) Plasma density and ion temperature, (b) turbulence level and (c) velocity profiles. The turbulence level is estimated from the backscattered power P. Refer to the text for more details.

The turbulence level in Fig. 8.5b shows a slow increase in the range $\rho = 0.80$–0.96, and a faster one in $\rho = 0.96$–0.98. O- and X-mode data show a similar behaviour, nevertheless X-mode data increases slower probably due to the non-linear diagnostic saturation discussed previously. The turbulence level peaks at $\rho \approx 0.98$ and then decreases drastically. $u_\perp$ in Fig. 8.5c is about -2 km/s for the innermost positions and becomes more negative (-3 km/s) at $\rho = 0.97$. At $\rho > 0.97$, a well is observed in which the velocity drops to -4.5 km/s. This radial range corresponds to the shear region observed in AUG L-mode discharges [68, 109]. A correspondence between turbulence level and $u_\perp$ shear is observed in Fig. 8.5b and c. The turbulence level increases in the range where the $u_\perp$ shear is small ($\rho < 0.97$), and saturates where the $u_\perp$ shear is strong ($\rho \approx 0.98$). This may be an indication of turbulence decorrelation by sheared flows as discussed in Sec. 2.3.

From the normalized gradients $\nabla T_i/T_i$ and $\nabla n/n$, depicted in Fig. 8.5b, two radial regions can be defined. A first region at $\rho \lesssim 0.96$ with $\nabla T_i/T_i > \nabla n/n$, and a second one at $\rho \gtrsim 0.96$ with $\nabla T_i/T_i < \nabla n/n$. Note that the turbulence level follows approximately the dominant normalized gradient, reproducing approximately the slight turbulence level increase below $\rho \approx 0.96$ and the strong one above. The density gradient is dominant in the edge region, suggesting a electromagnetic drift-wave (EDW) dominated turbulence

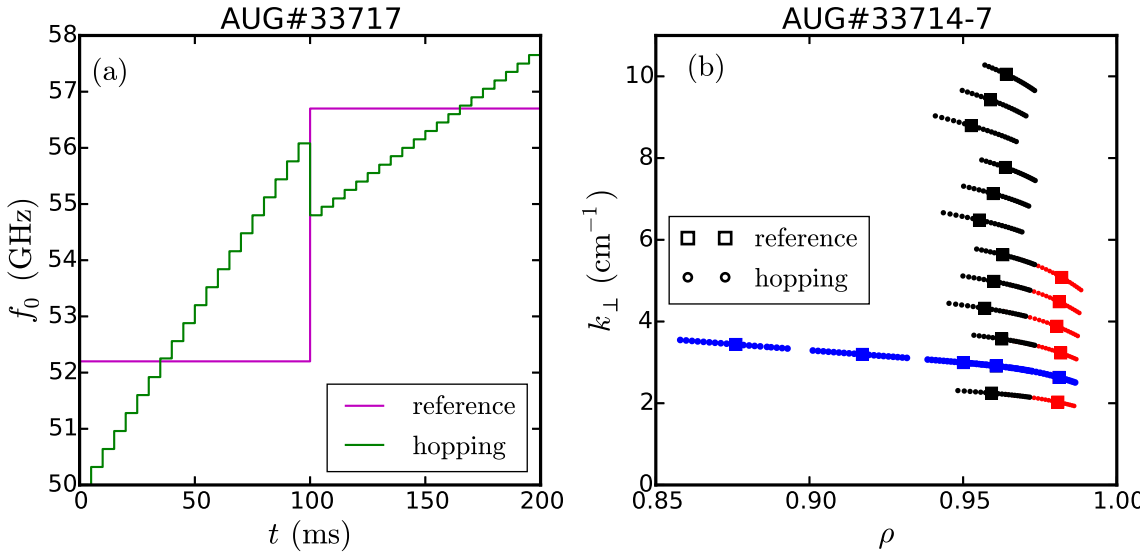

FIGURE 8.6: (a) Example frequency pattern used for the correlation measurements. The reference and hopping channel probing frequencies are depicted. (b) $k_\perp$ as a function of the measured radial position ρ for the O-mode. Reference and hopping channels are indicated. Data in red and black are used for $k_\perp$ scans, while data in blue for a radial scan.

regime [43, 44, 45]. In the core region, where the temperature gradient is dominant ITG and TEM dominated turbulence is expected [44].

The radial evolution of the $k_\perp$ spectra in Fig. 8.4a supports the previous observations. The radial positions at which the $k_\perp$ spectra shown in Fig. 8.4a have been measured are indicated with vertical arrows in Fig. 8.5c. The spectra measured in the first region, blue and green data in Fig. 8.4a, are similar despite of the large radial difference between the measurement positions. The steepening of the $k_\perp$ spectra is observed precisely at the transition between both regions. The substantial differences in the spectral indices and knee position between $\rho = 0.85$ and 0.97 may indicate different driving and nonlinear saturation mechanisms of the turbulence. A detailed gyrokinetic stability analysis would be necessary in order to determine precisely the dominant micro-instabilities in the different radial regions. These detail comparisons are left for future investigations.

8.1.3 Correlation measurements

Detailed correlation measurements have been performed for the same set of discharges discussed in Sec. 8.1.1. The measurements are performed with the two V-band systems with O-mode polarization. One V-band channel (reference channel) probed 6 frequencies, with 100 ms each. During this time, the other V-band channel (hopping channel) probed 20 nearby frequencies. A sample of the frequency patterns showing two reference channel frequencies is presented in Fig. 8.6a. The frequency patterns have been optimized according to the density profile. The hopping channel frequency steps are large in the edge region (low probing frequencies) because of the steep gradient of the density profile, whereas they are smaller towards the plasma core (high probing frequencies) because of the shallow gradients there.

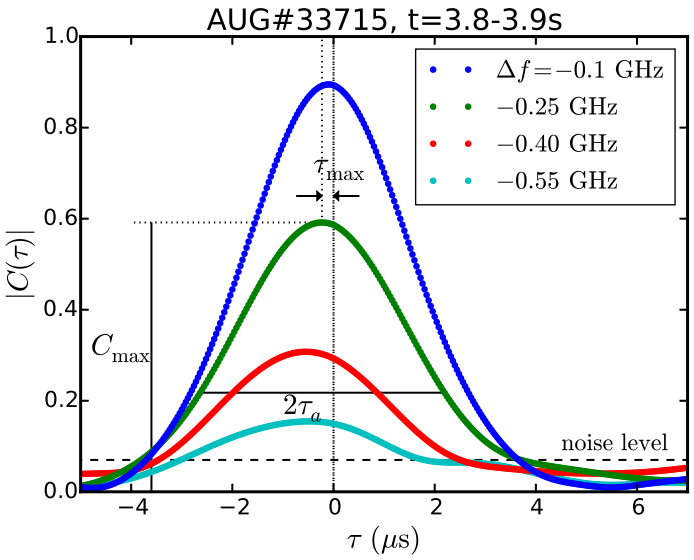

FIGURE 8.7: Cross-correlation function of the O-mode reflectometer signals for different probing frequency separations Δf. The reference channel probing frequency is 58.9 GHz, corresponding to $\rho = 0.955$ and $k_\perp = 6.5$ cm^{-1}. The definition of $C_{\max}$, $\tau_{\max}$ and τ_a is illustrated for the green data.

The analysis of the cross-correlation assumes only backscattering contributions, hence the direct reflection contribution observed in Fig. 8.3a has to be suppressed. This is done by filtering out the direct reflection contribution of the spectra before computing the cross-correlation function. Although a broad scan of the reference channel probing frequency and angle of incidence has been done, here only cases are discussed where the Doppler peak is dominant and the correlation quality is good. Further details on the filtering process are given in Appendix C.

The probed parameter space $k_\perp(\rho)$ computed with TORBEAM is depicted in Fig. 8.6b. Each reference channel data point depicted by a square is accompanied by several hopping channel data points indicated by circles. A $k_\perp$ scan is performed for $\rho \approx 0.96$ and 0.98 as depicted by the black and red symbols, respectively. Also a radial variation of the reference position at approximately fixed $k_\perp \approx 3$ cm^{-1} is performed (blue symbols).

Cross-correlation function

The cross-correlation function $C(\tau)$ of the reference and hopping channels is computed with Eq. 4.11. Since the reflectometer signal V is complex (cf. Sec. 4.2), $C(\tau)$ is also a complex quantity. In the following analysis only $|C(\tau)|$ is considered, the complex phase gives no further information for the correlation analysis. Representative cases of the cross-correlation are shown in Fig. 8.7. The reference channel is probing at $\rho = 0.955$ and $k_\perp = 6.5$ cm^{-1}. The colours depict different values of the probing frequency difference $\Delta f = f_{0,\text{hopping}} - f_{0,\text{reference}}$. The maximum of $|C(\tau)|$ decreases and shifts towards negative τ for increasing Δf. For the following analysis, the maximum of the correlation $C_{\max}$, time delay at the maximum $\tau_{\max}$ and width τ_a (obtained at $C_{\max}/e$) are defined as indicated for the green data in Fig. 8.7. The behaviour of the cross-correlation function is similar to the one observed for the synthetic turbulence shown in Fig. 7.1 and discussed in Sec. 7.1. The reader is referred to that section where a detailed analysis of

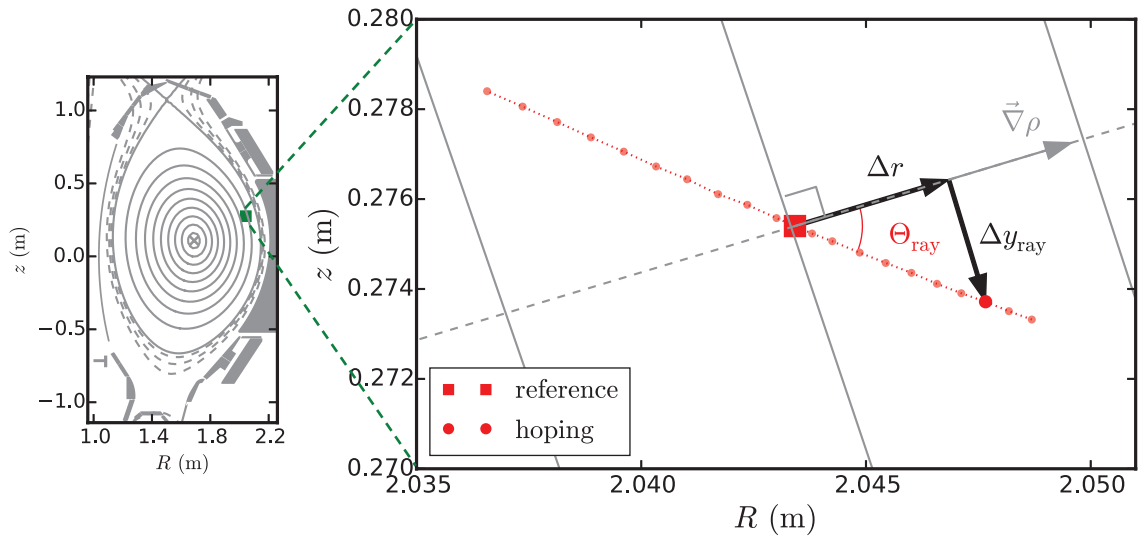

FIGURE 8.8: Measurement positions on the cross-section of the ASDEX Upgrade tokamak. The region of interest is zoomed in. The distance between hopping and reference measurement positions is decomposed in a radial Δr and perpendicular Δy_{ray} separation. Δr is taken along the gradient of the magnetic flux $\nabla\rho$. The geometrical definition of Θ_{ray} is also depicted.

the cross-correlation function is presented.

Radial and perpendicular separation

The measurement positions of the reference and hopping channels define a radial Δr and perpendicular Δy_{ray} separation, both required for the correlation analysis presented in Sec. 7.1. The geometrical definition of the separations for the slab case has been discussed in Sec. 7.1.3 and depicted in Fig. 7.4. Here the definition of the radial and perpendicular separation in a general geometry is shown in Fig. 8.8 for the AUG case. The measurement positions of the reference and hopping channels are shown in the zoomed region of interest. The grey solid lines depict the flux surfaces.

The local gradient $\nabla\rho$ at the reference measurement position defines the radial direction. This is indicated with a dashed grey line in the plot, which is locally perpendicular to the flux surface. The distance between the reference and hopping measurement positions is decomposed into a vector parallel and perpendicular to $\nabla\rho$, their magnitude defines Δr and Δy_{ray}, respectively. The vector decomposition is shown in the figure for one measurement position of the hopping channel. Δr pointing outwards is defined positive and Δy_{ray} pointing in the clockwise direction is defined negative. The same definition and conventions will be used in Sec. 8.2 for the TJ-II correlation analysis.

All measurement positions in Fig. 8.8 lie on a straight line which defines an angle Θ_{ray} with respect to the radial direction, as indicated in the figure. The angle is obtained from:

$$\tan\Theta_{\mathrm{ray}} = \frac{\Delta y_{\mathrm{ray}}}{\Delta r}.$$

A clockwise Θ_{ray} is defined negative as the case depicted.

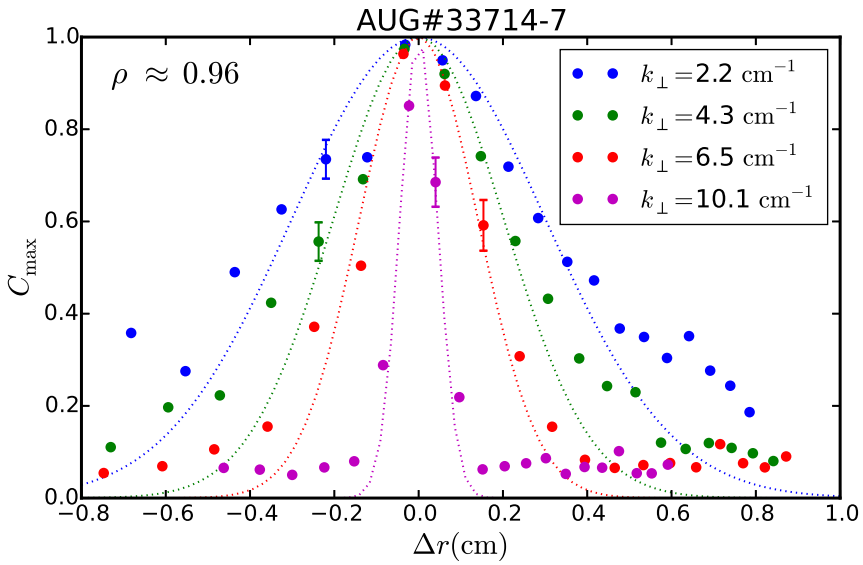

FIGURE 8.9: Maximum of the correlation function $C_{\max}$ as a function of the radial separation. Sample error bars are shown. The different colours depict different $k_\perp$ and the dashed line the Gaussian fit to the data.

Since the calculation of Δr and Δy_{ray} depends on the measurement positions obtained from ray tracing, a reliable density profile is required for an accurate determination of the mentioned quantities. Attention should be paid to the density gradient at the scattering position, to which Δr and Δy_{ray} are especially sensitive.

Radial correlation length

In this section the behaviour of $C_{\max}$ as a function of Δr is studied experimentally. The effect of $k_\perp$ in the experimental measurements is investigated in detail and the results are compared with the modelling presented in Ch. 7. The radial correlation length L_r of the turbulence is estimated from the experimental measurements. The impact of the diagnostic effects and the accuracy of the measurement are discussed.

In Fig. 8.9 the maximum of the cross-correlation function $C_{\max}$ is shown as a function of the radial separation Δr. The results for $\rho \approx 0.96$ and different $k_\perp$ values are depicted by different colours. The dataset corresponds to the one presented in Fig. 8.6 in black. The points depict the experimental data and the dashed lines a Gaussian fit that will be discussed later. A symmetric decay of the correlation with the radial separation is observed. The correlation drops faster for large $k_\perp$. Moreover, a slowly decaying tail is observed for small $k_\perp$, this effect is particularly strong for $k_\perp = 2.2$ cm^{-1} at large positive Δr.

The data are in qualitative agreement with the correlation results of the Kolmogorov-like $k_\perp$ spectrum shown in Fig. 7.11a. There, a faster decay of the correlation for large $k_\perp$ and a slow decaying tail for small $k_\perp$ result from the filtering effect of the diagnostic. A similar effect on the TJ-II measurements has been reported in Ref. [16]. Since the $k_\perp$ spectrum is Kolmogorov-like (cf. Fig. 8.4), both the faster decay for large $k_\perp$ and

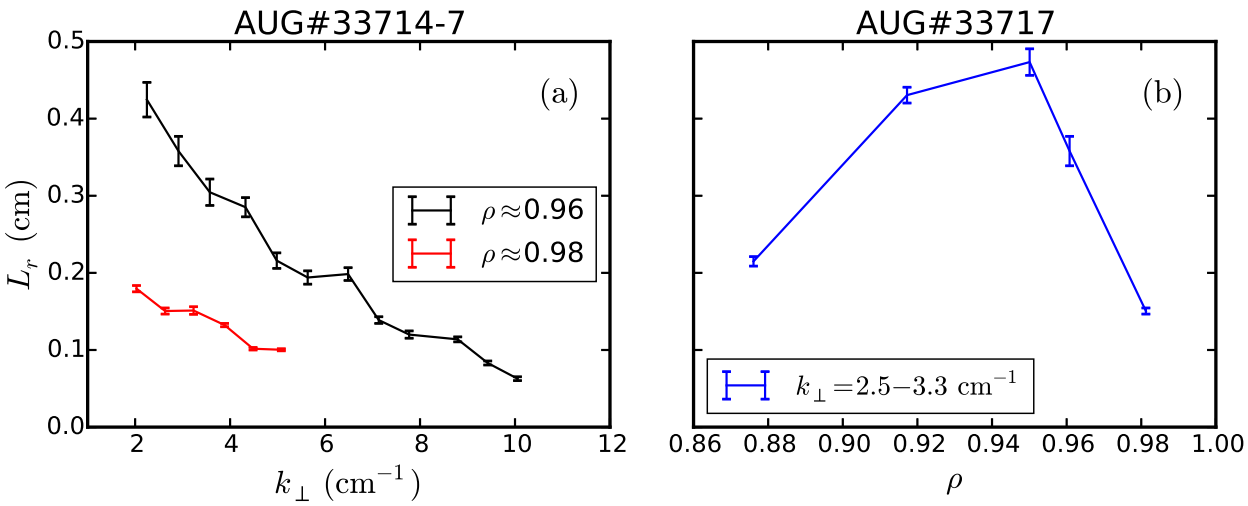

FIGURE 8.10: Measured radial correlation length (a) as a function of $k_\perp$ at two radial positions, and (b) as function of ρ for measurements with $k_\perp$ in the range 2.5–3.3 cm^{-1}.

the deviations from Gaussian in Fig. 8.9 are likely to be caused to some extent by the filter effect of the diagnostic. The non-local scattering may have an impact on the data, specially in the slowly decaying tail. The relevance of this effect will be discussed later in this section.

The Gaussian fit depicted in Fig. 8.9 by dotted lines is computed by weighing each data point with $1/C_{\max}^2$. The fits show a $k_\perp$ dependence of the correlation despite of the slowly decaying tail. This fitting method has also been applied in the analysis of simulated data in Ch. 7. In this way, the fit focuses the analysis on the data with small Δr which reduces the impact of the slowly decaying tail in the analysis. This is justified for the Kolmogorov like $k_\perp$ spectrum case studied in Sec. 7.5. There the radial correlation length is defined by the $C_{\max}$ drop for small Δr, which is followed by the slowly decaying tail. The fit can also reduce the contributions of non-local scattering to the correlation that manifest as a slowly decaying tail (cf. Fig. 7.5a).

The radial correlation length L_r is extracted from the Gaussian fit to the data $C_{\max} = \exp -(\Delta r/L_r)$. The results are plotted as a function of $k_\perp$ in Fig. 8.10a at $\rho \approx 0.96$ and 0.98 in black and red, respectively. The cases shown in Fig. 8.9 are included in the black series. L_r decreases with $k_\perp$ for both radial positions. The values at $\rho \approx 0.98$ are smaller than at $\rho \approx 0.96$. Hence, despite of the $k_\perp$ related diagnostic effect a reduction of the radial correlation length for the outermost measurement position is confirmed.

The non-local scattering may produce an overestimation of L_r due to the scattering along the beam path. Nevertheless this effect is reduced for large $k_\perp$, thus a convergence to the real correlation length is expected at large $k_\perp$ for a Gaussian $k_\perp$ spectrum [21]. Figure 8.10a shows no convergence of L_r as expected from non-local scattering. If L_r converges for $k_\perp$ larger than the measured range, the convergence value would be smaller than 0.05 cm. This is a non-realistic value for the radial correlation length, which is expected to be of the order of (sub-)centimetres [15, 110]. Although non-local scattering contributions cannot be discarded, they are not likely to produce the L_r reduction with $k_\perp$ and have a small impact on the measurements.

The decrease of L_r with $k_\perp$ is likely due to the diagnostic filtering effect discussed in Sec. 7.5.3 and shown in Fig. 7.11a. In this case the best estimation of the radial correlation length is the given by the measurements at small $k_\perp$. For the measurements shown in Fig. 8.10a the correlation length can be estimated to be $L_r^{\text{true}} \approx 0.4$ cm and $L_r^{\text{true}} \approx 0.2$ cm for the black and red series, respectively.

The radial evolution of L_r is investigated by considering the measurements at small and approximately constant $k_\perp$. The probed parameters correspond to the blue data in Fig. 8.6. The results are depicted in Fig. 8.10b as a function of ρ. The radial correlation length increases from 0.2 to 0.45 cm at $\rho \approx 0.95$, then decreases reaching 0.2 cm at $\rho \approx 0.98$. Note that the two different behaviours corresponds approximately to the two regions presumably with different turbulence driving mechanisms discussed in Sec. 8.1.2. The small L_r of the outermost measurement, already in the shear region, may be related to the turbulence regulation by sheared flows (cf. Sec. 2.3). Alternatively, the reduction of L_r may also be justified with the mixing length argument which predicts $L_r \propto \delta n_{\text{rms}} (\nabla n/n)^{-1}$ [22], thus the steepening of the density profile towards the plasma edge can account to some extent for the observation. The reduction of L_r at $\rho > 0.95$ coincides with the shift of the spectral knee towards larger $k_\perp$ observed in Fig. 8.4a. Since a wider spectrum corresponds to a longer correlation length, the reduction of the radial size of the turbulent structures is accompanied by a reduction of their perpendicular size.

Tilt angle measurement

The time delay of the cross-correlation function is investigated experimentally. The results are analysed based on the modelling presented in Secs. 7.1.3 and 7.4, where the time delays have been related to the tilt angle β and the perpendicular velocity of the turbulent structures. The tilt angle is measured for the first time in the AUG confined region. The impact of the diagnostic effects is discussed.

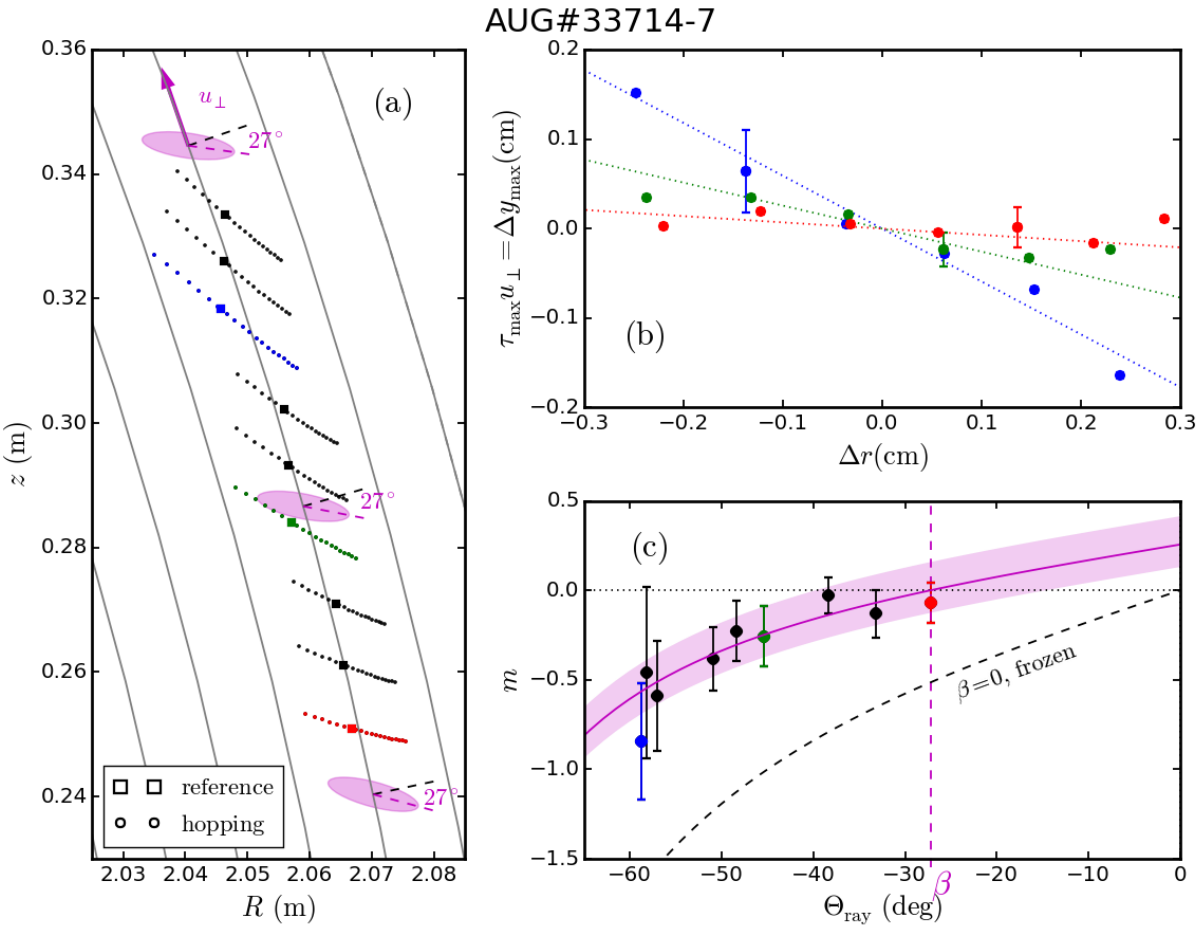

FIGURE 8.11: (a) Detail of the measurement positions on the AUG cross-section. Turbulent structures are schematically depicted, the tilt angle and propagation velocity are indicated. (b) Perpendicular displacement $\Delta y_{max} = \tau_{max} u_\perp$ computed from the time delay of the cross-correlation function vs. the radial separation. Selected cases measured at $\rho \approx 0.96$ are shown. The dashed lines depict linear fits to the data. (c) Slope m as a function of Θ_{ray}; the fit to the data with Eq. 7.12 is depicted by a magenta line. The tilt angle β is indicated.

In the following, the measurements at $\rho \approx 0.96$ corresponding to the black data in Fig. 8.6 are analysed. The measurement positions of the reference and hopping channel are shown on the AUG cross-section in Fig. 8.11a. The region of interest is shown in detail. The nine sets of points stand for different angles of incidence. Due to the different angle of incidence of the probing beam, the point sets have a different alignment with respect to the radial direction. The lowermost points are better aligned with the radial direction compared to the uppermost. Thus, the angle Θ_{ray} defined by the measurement positions with respect to the radial direction is scanned between -27 and $-60°$, from the lower to the upper measurements. Turbulent structures are schematically depicted.

The time delay τ_{max} at the maximum of the cross-correlation function has been computed and multiplied by $u_\perp = 3.0$ km/s in order to obtain the perpendicular displacement $\Delta y_{max} = \tau_{max} u_\perp$. Sample results of Δy_{max} as function of Δr are shown in Fig. 8.11b, the three cases correspond to the measurement positions depicted in Fig. 8.11a by the

same colours. Data points obtained with high correlation and hence a well defined time delay are considered. Positive $\tau_{\max}$ values mean that the signal features are detected first by the reference channel. A linear dependence is observed for the three cases. Linear functions are fitted to the data and are depicted by dashed lines in Fig. 8.11b. The fits have a different slope m for the three cases shown.

The tilt and the propagation direction of the structures depicted in Fig. 8.11a are consistent with the time delays presented in Fig. 8.11b. The structure is approximately aligned with the red measurement positions, therefore it is seen almost simultaneously by the reference and hopping channel (small time delays). Whereas the structure is miss-aligned with respect to the blue measurement positions, hence it is "seen" first by the hopping channel (negative time delay) for positive Δr while it propagates upwards. The tilt angle indicated in the figure is calculated next.

The slope m obtained from the fits (Fig. 8.11b) is plotted as a function of Θ_{ray} in Fig. 8.11c. The blue, green and red data points correspond to the cases shown in Figs. 8.11a and b. Despite the dispersion the data show a clear trend; $|m|$ increases with $|\Theta_{\text{ray}}|$. It has been shown in Sec. 7.1.3 that m can be described with Eq. 7.12 under the frozen turbulence approximation. The prediction of Eq. 7.12 for zero tilt ($\beta = 0$) is depicted in Fig. 8.11c by a dashed black line. The experimental data show a similar behaviour and are vertically shifted due to the tilt angle of the turbulence. Nevertheless the increase of $|m|$ with $|\Theta_{\text{ray}}|$ is slightly slower compared to the frozen turbulence prediction, thus the data cannot be satisfactorily described by Eq. 7.12. One has to include the effect of the decorrelation time of the turbulence discussed in Sec. 7.4. This effect reduces the measured time delays with respect to the frozen turbulence expectation, and can be accounted with a correction factor F_d included in Eq. 7.24. The data in Fig. 8.11c has been fitted with Eq. 7.24 with the tilt angle β and the correction factor F_d as free parameters. The fit is depicted by the magenta solid line in the figure. The good quality of the fit shows that the time delays are explained by the tilt of the turbulent structures as discussed in Secs. 7.1.3 and 7.4. The tilt angle and correction factor are

$$\beta = (-27 \pm 12)^\circ, \qquad F_d = 0.5 \pm 0.2. \tag{8.1}$$

The tilt angle is indicated in the plot as the value of Θ_{ray} at the intersection with the $m = 0$ axis, at which the structure is aligned with the measurement points. The resulting tilt of the structures is schematically depicted in Fig. 8.11a.

The relevance of the decorrelation time of the turbulence τ_d is assessed by comparing it with the passing time of the structures in front of the probing beam. Taking a beam width of 2.0 cm, the passing time is $w/u_\perp \approx 7$ μs. In AUG, the decorrelation time τ_d has been investigated using a poloidal correlation reflectometry diagnostic recently installed [106, 107]. For ECRH discharges as the one under study, τ_d is of the order of 10 μs [107]. Since the passing time is only slightly shorter than τ_d, a correction factor $F_d \approx 0.6$ according to Eq. 7.23 is still needed. This value is comparable with the experimental one (Eq. 8.1), which supports the modelling of the τ_d effect presented in Sec. 7.4. It should be remark that poloidal correlation reflectometry diagnostic measures at smaller wavenumbers ($k_\perp < 2$ cm^{-1}) compared with Doppler reflectometry. Therefore the decorrelation time which may vary with $k_\perp$ gives only a rough estimation of F_d.

The impact of other diagnostic effects on the tilt angle measurement has been discussed in Ch. 7. In particular, the non-linear diagnostic response and the filter effect have been considered. Here, non-linear effects are excluded based on the analysis of the $k_\perp$ spectra presented in Sec. 8.1.2, where the linearity of the O-mode measurements has been justified. The k filtering of the Doppler reflectometer may lead to an underestimation of m and therefore of the tilt angle, especially for large $k_\perp$. The fact that all the measured data are above the $\beta = 0$ line indicates that the same direction of the tilt is recovered for all cases. However, the data for large $|\Theta_{\text{ray}}|$ corresponding to large $k_\perp$ are closer the the $\beta = 0$ line. This may indicate an underestimation of m for large $k_\perp$ similar to the one observed in Fig. 7.11c. A decrease of the tilt along the perpendicular direction could also explain this underestimation, nevertheless since the measurements span only a small poloidal section of AUG, the turbulence characteristics are not expected to change significantly and the assumption of a constant tilt is well justified. Finally, a precise numerical assessment of the filter effect would require an accurate knowledge of the weighting function for the specific experimental conditions. This is left for future studies.

Concluding, the analysis techniques developed in Secs. 7.1.3 and 7.4 can be applied to the experimental data, and the mean tilt angle of the turbulent structures can be experimentally measured. A further insight on the physical meaning of the measured tilt angle (Eq. 8.1) would require a detailed modelling of the plasma under study. In Ch. 9 the tilt angle measurement will be used to investigate changes of the turbulence regime in plasmas with either dominant electron or dominant ion heating.

8.2 TJ-II measurements

A detailed experimental study of the density turbulence in L-mode TJ-II plasmas using Doppler reflectometry is presented in this section. In Sec. 8.2.1 the discharges under investigation are introduced and in Sec. 8.2.2 $k_\perp$ spectra and $u_\perp$ profiles are measured and analysed. In Sec. 8.2.3 correlation measurements are presented. First, a radial scan of the correlation length is done and second, the tilt angle measurement is carried on for the first time in TJ-II. In Sec. 8.2.4, the tilt results are compared with linear global gyrokinetic simulations. In Sec. 8.2.5 a two-point correlation technique is presented.

8.2.1 Discharges

Dedicated experiments for the characterization of turbulence with Doppler reflectometry have been performed in TJ-II. ECR heated L-mode plasmas with low density have been investigated. The standard magnetic configuration has been used. Two series of comparable discharges are analysed; the *series 1* includes the discharges #42754-65, and the *series 2* #43459-91. The series 1 has been used for $k_\perp$ spectra and $u_\perp$ measurements. The results will be shown in the following section. The series 2 has been used for correlation measurements and will be discussed in Sec. 8.2.3.

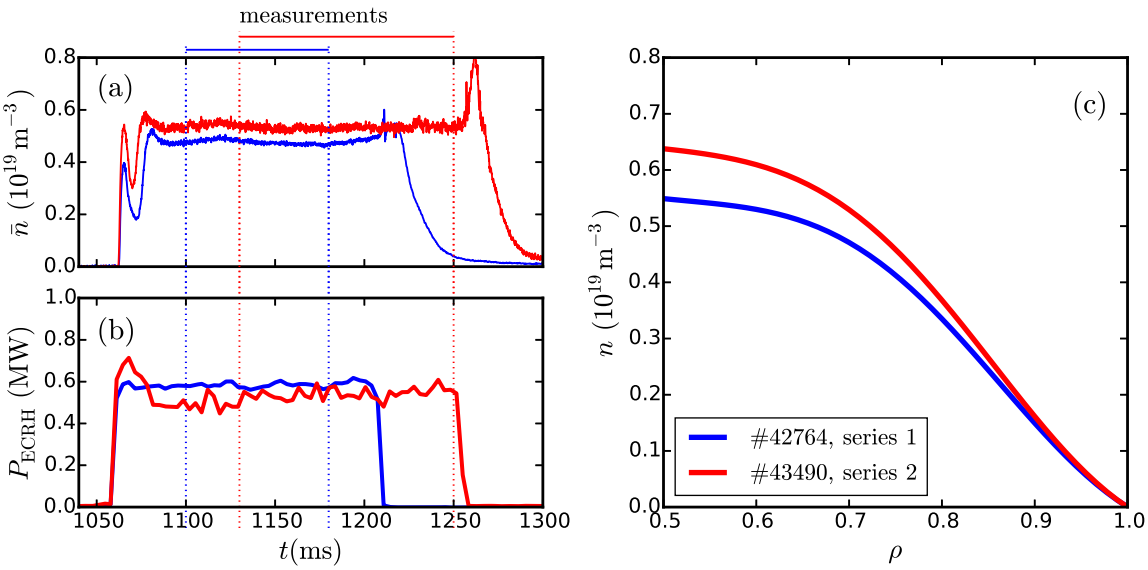

FIGURE 8.12: (a) Line average plasma density and (b) ECRH power time traces of representative discharges of series 1 and 2. (c) Density profiles during the measurement phases obtained from a multi-diagnostics statistical analysis [111].

The line average density and ECRH power time traces for representative discharges of the series are shown in Figs. 8.12a and b. Similar plasma conditions were targeted for both sets of experiments. Nevertheless the two series were performed on different days, thus the wall condition was not the same and a slightly higher density was obtained for the second series. The line average density is below the critical density of 0.6×10^{19} m^{-3} for both cases, which ensures the electron root confinement regime [112]. The plasma density is stable between 1100–1200 ms for the series 1 and between 1100–1250 ms for the series 2. The reflectometry measurements are performed during these time windows as indicated at the top of Fig. 8.12a.

The density profile during the measurement phases has been computed by statistical analysis of Thomson scattering, interferometry and AM reflectometer data [111]. The profiles for both series are shown in Fig. 8.12c. The profile for the series 1 is slightly lower compared to the one of the series 2. These profiles will be used as input for ray tracing calculations with the TRUBA code.

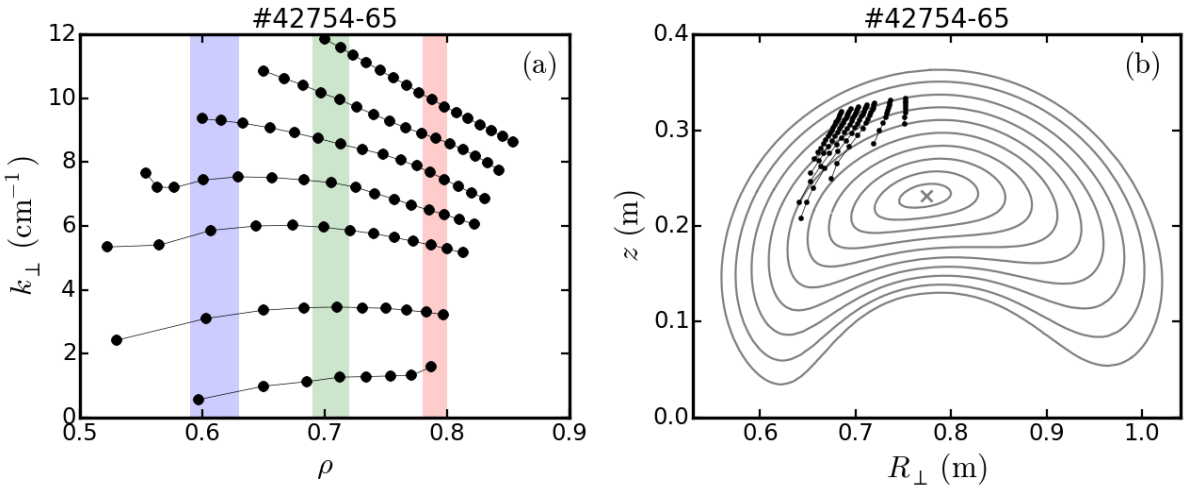

FIGURE 8.13: (a) Probed $k_\perp$ as a function of the measured radial position ρ. The shadowed areas correspond to the radial ranges where the $k_\perp$ spectra are computed. (b) Measurement positions on the perpendicular cross-section of TJ-II. The gray lines depict the flux surfaces.

8.2.2 Measurements of $k_\perp$ spectra and $u_\perp$ profile

Detailed measurements have been performed with the two Q-band (33–50 GHz) X-mode Doppler reflectometer channels. For more details on the reflectometer configuration refer to Sec. 4.3.2. Fine probing frequency and angle of incidence scans have been performed for discharges of the series 1. Seven angles of incidence have been used, with 16 probing frequencies (5 ms each) in the range 33.0–40.5 GHz per angle. The angle of incidence has been scanned on a shot to shot basis. The probed $k_\perp$ and radial position ρ obtained with the TRUBA code are plotted in Fig. 8.13a. Data points connected with lines correspond to the same angle of incidence. The radial range measured is $\rho = 0.50$–0.85 and $k_\perp$ is between 1 and 12 cm^{-1}. The measurement positions on the perpendicular cross-section of TJ-II are shown in Fig. 8.13b. A poloidally extended region in the upper left side is measured.

The power spectrum of the reflectometer signal is computed for each probing frequency and angle of incidence. A sample power spectrum is shown in Fig. 8.14a. A Doppler peak at -0.44 MHz is obtained. No contribution from direct reflection is observed. That is the case for all the measurements on TJ-II discussed in this thesis. Direct reflections may be important under other plasma conditions with smaller turbulence level, as it is the case for NBI heated plasmas or close to the shear layer where turbulence is suppressed [32]. The blue line depicts the Gaussian fit to the Doppler peak. The backscattered power P and Doppler shift f_D are obtained from fit.

The $k_\perp$ spectra are calculated taking P as a function of $k_\perp$ for the different radial windows depicted by coloured areas in Fig. 8.13a. The results for three radial positions are plotted in Fig. 8.14 with different colours. A vertical shift between the different cases has been included for visualization purposes. A spectral fall-off with $k_\perp$ is observed for the three cases. It is faster for large $k_\perp$. For a numerical comparison, the spectra have been fitted with power laws in the small and large $k_\perp$ ranges. The fits are depicted by solid lines and the spectral indices are indicated in the figure. Similar spectral indices

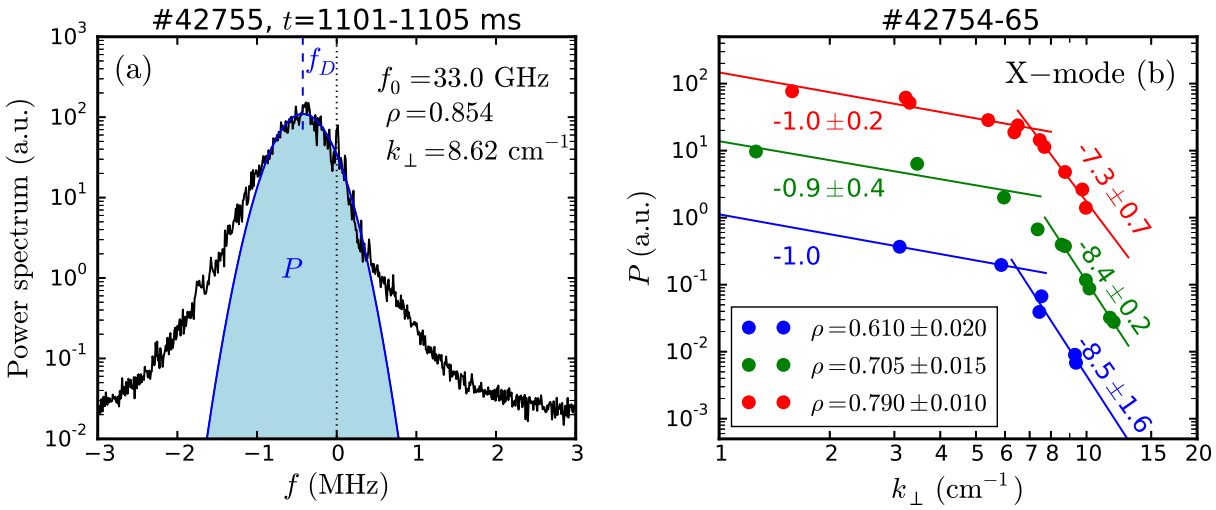

FIGURE 8.14: (a) Sample power spectrum measured in TJ-II. The fit to the Doppler peak is depicted by a blue solid line. No zero-order reflection is observed. (b) $k_\perp$ spectra at different radial positions measured in X-mode polarization. Similar spectra are obtained at different radial positions.

are obtained in the three measured radial positions. For low and high $k_\perp$ the spectral index is about -1.0 and -8.0, respectively. The two ranges are separated by a knee at approximately $k_\perp \approx 7$ cm^{-1}. The spectral indices in the low $k_\perp$ range are similar to those measured in AUG, while the ones in the high $k_\perp$ range are more pronounced, and the spectral knee is located at larger $k_\perp$ (cf. Fig. 8.4a.)

The similarity between the outer and inner most spectra (blue and red cases in Fig. 8.14) suggest that the diagnostic response is linear in the measured range. Given that the turbulence level is expected to increase towards the plasma edge, non-linear effects would produce a flatennig of the $k_\perp$ spectra (cf. Ch. 6) in the outermost measurement positions. This non-linear effect has been reported in Ref. [16], where smaller spectral indices were measured in the large $k_\perp$ range for outer measurement positions. On the contrary, the measurements presented here show no spectral flattening and spectral indices comparable to those obtained in the linear regime in Ref. [16]. Therefore strong non-linear scattering regimes in the measured range can be discarded.

The similarity of the spectra also suggests that the driving and saturation mechanisms of the turbulence are the same in the measured radial range. The obtained spectral indices are comparable to those reported in Ref. [16] for similar ECRH plasmas, though the reported knee position at $k_\perp \approx 5$ cm^{-1} is slightly smaller. The spectral indices in NBI heated plasmas reported in Ref. [31, 32] are more pronounced and the spectral knee appears at larger $k_\perp \approx 8.4$ cm^{-1}.

The relative changes of the turbulence level profile have been estimated from P according to Eq. 4.8. The radial profile for $k_\perp \approx 6$ cm^{-1} has been plotted in Fig. 8.15b as a proxy of the turbulence level δn_{rms}. This approximation is justified by the linear diagnostic response discussed previously and by the approximately constant $k_\perp$ that avoids changes of P related to the spectral fall-off. The turbulence level increases towards the edge by approximately one order of magnitude. The growth follows roughly the normalized gradient of the plasma density $\nabla n/n$, which is indicated in the Fig. 8.15b with

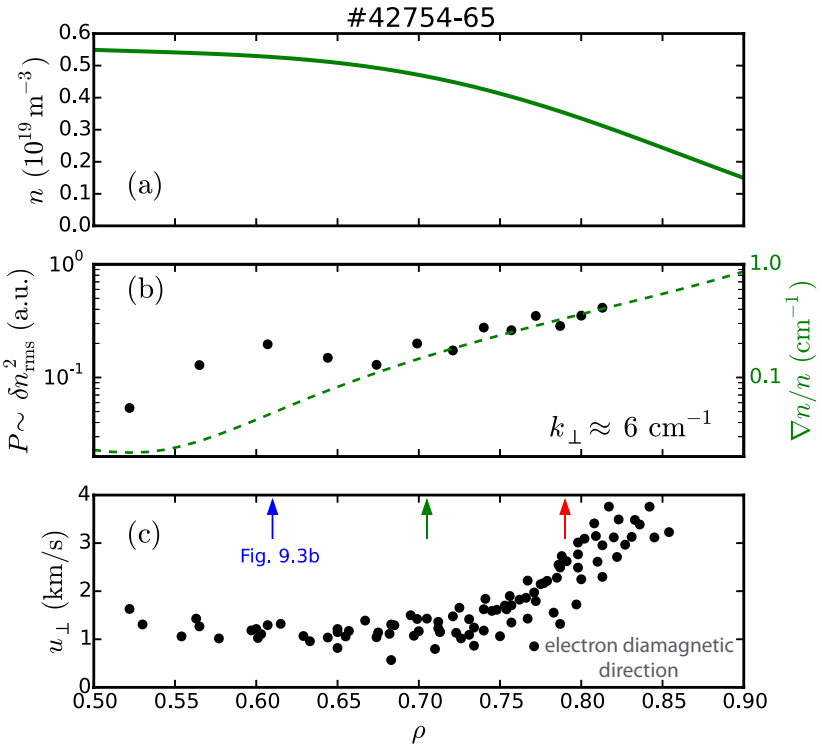

FIGURE 8.15: (a) Density, (b) turbulence level and (c) $u_\perp$ profiles for the series 1. The turbulence level is estimated from P measured at $k_\perp \approx 6.0$ cm^{-1}.

a dashed green line. The density profile has been included in Fig. 8.15a for comparison. The perpendicular velocity $u_\perp$ has been computed from f_D according to Eq. 4.10. The results for the complete parameter scan are shown in Fig. 8.15c. $u_\perp$ has an approximately constant value of 1 km/s between $\rho = 0.5$ and 0.7, then increases towards the edge reaching values of about 3.5 km/s at $\rho \approx 0.82$.

Although a region of velocity shear is observed between $\rho = 0.75$ and 0.85, there is no reduction of the turbulence level. Moreover, no significant differences in the spectral shape have been observed in the $k_\perp$ spectra measured at the positions indicated with arrows in Fig. 8.15c. The turbulence regulation by sheared flows mechanism (cf. Sec. 2.3) is not observed in the fluctuation level, or at least does not play a significant role. However, it should be noted that the velocity shear in electron root confined plasmas is small compared to other types of plasma in TJ-II. A turbulence reduction correlated to the velocity shear has been observed for densities close to the threshold density [113] and in H-mode plasmas [32]. Similar effects have also been observed in other stellarators at the transition between electron and ion root regimes [114].

8.2.3 Correlation measurements

Detailed correlation measurements have been performed in TJ-II for discharges of the series 2 discussed in Sec. 8.2.1. The two Q-band X-mode Doppler reflectometer channels have been used; for more details refer to Sec. 4.3.2. The probing frequency of one channel (reference) has been scanned slowly, 60 ms per frequency. During this time the other

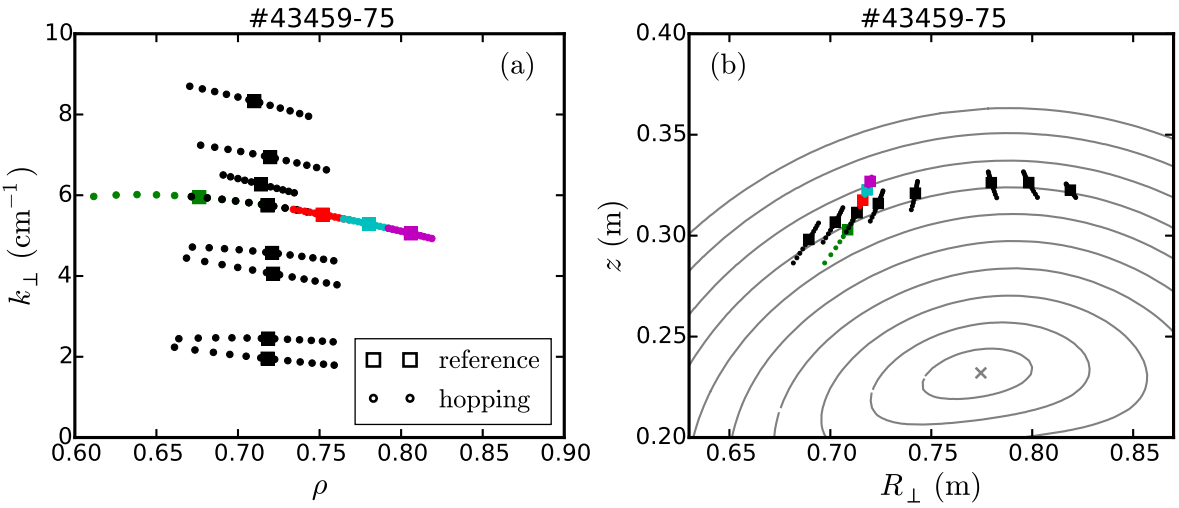

FIGURE 8.16: (a) Probed $k_\perp$ as a function of the radial position ρ used for correlation studies. (b) Measurement positions on the perpendicular cross-section of TJ-II. Multi-colour data points are used for correlation measurements at several radial positions. Black data points will be used for the tilt angle measurement.

channel (hopping) probed 12 nearby frequencies, 6 above and 6 below with 5 ms per frequency. The mirror position has been changed on a shot to shot basis. The probing frequencies and the mirror angle have been specifically designed for a radial position and a $k_\perp$ scan.

The probed ρ and $k_\perp$ range of the reference and hopping channels are shown in Fig. 8.16a. The measurement positions on the perpendicular cross-section of TJ-II are presented in Fig. 8.16b. The multi-colour data points correspond to a radial scan of the reference channel measurement position with a fixed mirror angle. The position varies between $\rho = 0.67$ and 0.81 and $k_\perp$ in the range 5 to 6 cm^{-1}, with a slight increase towards the core. The black data points correspond to a scan of the mirror angle. The probing frequencies have been adjusted in order to compensate the radial displacement of the measurement position when scanning $k_\perp$, such that the reference channel probes at $\rho = 0.72$ for all cases.

For the following correlation analysis the radial Δr and perpendicular Δy_{ray} separations are obtained from the ray tracing data as it has been illustrated in Fig. 8.8 for the ASDEX Upgrade case. The cross-correlation function of reference and hopping channel signals has been computed. The maximum of the correlation $C_{\max}$, time delay at the maximum $\tau_{\max}$ and width τ_a are obtained. This procedure has been explained in detail for ASDEX Upgrade analysis in Sec. 8.1.3 and has been illustrated in Fig. 8.7. Given that no direct reflection has been observed in the TJ-II power spectra (cf. Fig. 8.14a), no filtering in frequency is required before the cross-correlation function calculation. This is contrary to the O-mode measurements in the ASDEX Upgrade shown in Fig. 8.3a and discussed in the Appendix C.

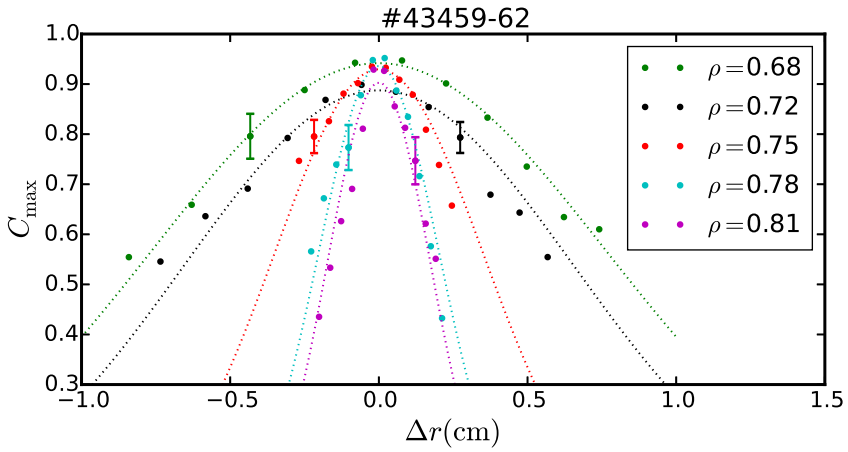

FIGURE 8.17: Maximum of the cross-correlation as a function of Δr. Data for different radial positions of the reference channel are shown. $k_\perp$ is approximately 5.5 cm^{-1} for all cases. Gaussian fits to the data are depicted by dotted lines.

Radial correlation length

The maximum of the cross-correlation $C_{\max}$ has been plotted as a function of the radial separation Δr in Fig. 8.17. The colours depict different radial positions of the reference channel. The probed parameter space is included in the multicolour data points of Fig. 8.16. A decay of the correlation with the radial separation is observed. The decay is faster for outer measurement positions. The dotted lines in the figure corresponds to Gaussian fits as explained for the AUG case, cf. Sec. 8.1.3. The comparison of the data with the fits reveals an asymmetry of the positive and negative Δr branches of the correlation. This effect is strongest for the $\rho = 0.72$ case in black, where the correlation decays faster for positive Δr. This asymmetries will by further discussed next.

It has been shown in Sec. 7.4 that the filter effect of the diagnostic together with a Kolmogorov type turbulence induces a $k_\perp$ dependence of the measured L_r. This effect has been confirmed in Sec. 8.1.3 for AUG data and in Ref. [16] for TJ-II. Thus L_r obtained from the fit in Fig. 8.17 are underestimated by the $k_\perp$ effect. Nevertheless, the measurements at different radial positions can be compared in order to investigate relative changes because the probed $k_\perp$ and the spectrum are approximately constant. L_r obtained from the (symmetric) fits are plotted in red in Fig. 8.18a as a function of ρ. A strong decrease of the radial correlation length towards the plasma edge is observed.

A strong decrease of the measured correlation length has been observed at the transition from the linear to the non-linear regime in two-dimensional full-wave simulations (cf. Figs. 7.6a and d, and Ref. [19]). Nevertheless for the experimental conditions here, a linear diagnostic response has been evidenced in the $k_\perp$ spectra studies in Sec. 8.2.2. Furthermore there is only a modest increase in the turbulence level in the range $\rho = 0.68$–0.78 (see Fig. 8.15b) which cannot account for such a strong decrease of L_r. It is concluded that the decrease observed in Fig. 8.18a is not due to a non-linear diagnostic response and corresponds to a real reduction of the L_r towards the plasma edge.

The reduction of L_r is in line with the reduction of the density gradient scale length $L_n = (\nabla n/n)^{-1}$, which has been re-scaled and depicted by a green dashed line in

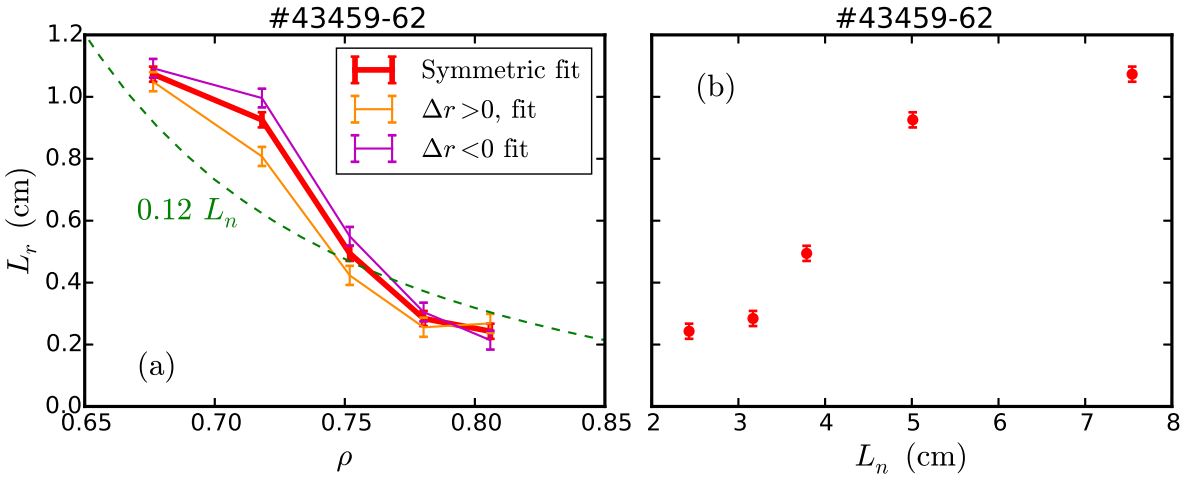

FIGURE 8.18: (a) Radial correlation length L_r measured at $k_\perp \approx 5.5$ cm^{-1} as a function of the radial position ρ. Results from the symmetric fit are depicted by red, and fits of positive and negative Δr by yellow and magenta, respectively. (b) L_r as a function of the density gradient scale length L_n.

Fig. 8.18a. The scaling of L_r with L_n is observed in Fig. 8.18b. A similar scaling has been observed for ECRH plasmas in Ref. [16], where L_n was varied by changing the plasma density and magnetic configuration. Here a similar behaviour has been obtained when the radial variation of L_n is considered. Alternatively, the increase of the $u_\perp$ shear towards the plasma edge may indicate that turbulence regulation by sheared flows is responsible of the L_r reduction (cf. Sec. 2.3). Nevertheless neither a turbulence level reduction nor an effect on the $k_\perp$ spectra has been observed in Sec. 8.2.2.

The asymmetries observed in Fig. 8.17 are further investigated by fitting the positive and negative Δr wings separately. L_r obtained for positive and negative Δr are depicted in Fig. 8.18a by orange and magenta lines, respectively. The inner and outermost measurement positions show similar values for both fits, indicating symmetric $C_{\max}(\Delta r)$. Whereas an asymmetry is observed for intermediate radial positions in the L_r gradient region. The longer correlation length is measured towards the core ($\Delta r < 0$) precisely in the direction in which L_r increases. From these two observations the asymmetry of the correlation function can be explained by the L_r gradient. If L_r has a strong gradient (as at $\rho = 0.75$), the hopping channel measures in regions with different L_r when probing at positive and negative Δr. Thus $\Delta r < 0$ measures at a smaller ρ having larger L_r, while $\Delta r > 0$ measures at larger ρ providing a smaller L_r.

It is proposed that a strong L_r radial gradient induces asymmetries in the correlation. It should be noted that, magnetic islands close to the measurement positions can also produce asymmetries [115]. Nevertheless, in the presented experiments, no strong impact of magnetic islands is expected because of the absence of low order rational surfaces in the measured region, and no signatures of the magnetic islands in the Doppler peaks has been observed as the ones reported in Ref. [116].

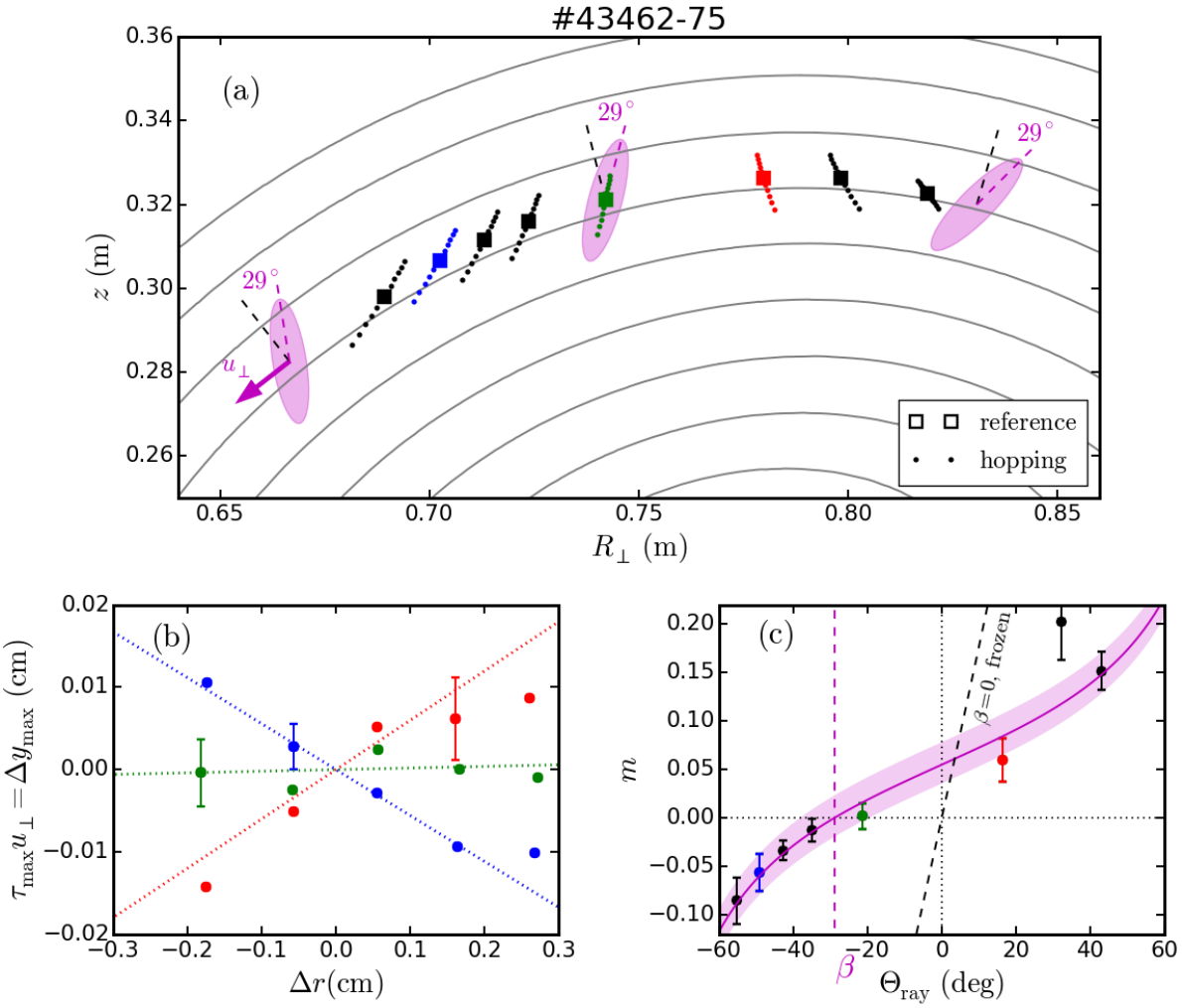

FIGURE 8.19: (a) Measurement positions at $\rho = 0.72$ on the perpendicular cross-section of TJ-II. Turbulent structures are schematically depicted, the tilt angle and propagation velocity are indicated. (b) Perpendicular displacement $\Delta y_{max} = \tau_{max} u_\perp$. Results for three angles of incidence are presented (see colours in *a*). Linear fits are indicated with a dotted lines. (c) Slope m as a function of Θ_{ray}. The fit of the data with Eq. 7.24 is depicted by the purple line, the tilt angle β is indicated.

Tilt angle measurements

The time delay of the cross-correlation function and the tilt angle of the turbulent structures are studied in detail for the measurements at $\rho = 0.72$ (black points in Fig. 8.16). The measurement positions of the reference and hopping channel are shown in detail on the perpendicular cross-section of TJ-II in Fig. 8.19.a. The eight sets of points correspond to different angles of incidence, hence the measurement positions are perpendicularly displaced. The blue measurement points define a negative angle Θ_{ray} (clockwise) with respect to the radial direction, while the red ones define a positive one (counterclockwise). The scan of the angle of incidence provides a broad Θ_{ray} scan between -60 and $40°$. Turbulent structures are artistically depicted.

The time delay $\tau_{\max}$ at the maximum of the cross-correlation is multiplied with the local perpendicular velocity $u_\perp$. The perpendicular displacement $\Delta y_{\max} = u_\perp \tau_{\max}$ is plotted as a function of Δr in Fig. 8.19b. Only points obtained with high correlation and hence a well defined time delay are considered. The colours correspond to the three angles of incidence coloured in Fig. 8.19a. Linear fits to the data are depicted by dotted lines. The slope m is different for the three cases, and an opposite sign is observed for the red and blue data.

The tilt angle and propagation velocity depicted in Fig. 8.19a are qualitatively consistent with the time delays of Fig. 8.19b. Turbulent structures aligned with the green measurement points provide a small time delay for this case. Moreover due to the misalignment of the structures with respect to the blue (red) measurement points, the structures are "seen" first (later) by the hopping channel for positive Δr, resulting in a negative (positive) time delay.

The slope m is plotted as a function of Θ_{ray} in Fig. 8.19c. The blue, green and red data points correspond to the cases presented in Fig. 8.19b. A clear dependence of m on Θ_{ray} is observed. In Sec. 7.1.3 it has been shown that under the frozen turbulence approximation, m is related to the tilt angle of the turbulent structures β through Eq. 7.12. The prediction of Eq. 7.12 for $\beta = 0$ is depicted in Fig. 8.19c by a dashed black line. The comparison of the $\beta = 0$ line with the experimental data shows that m is substantially small compared to the frozen turbulence expectation. The smallness of m would require the unlikely alignment of the turbulent structures with the measurement points for all the angles of incidence depicted in Fig. 8.19a if frozen turbulence is assumed. Moreover, the passing time of the structures in front of the beam is estimated as $w/u_\perp \approx 2$ cm/(1.5 km/s) = 13 μs, which is comparable to typical values for the decorrelation time of the turbulence τ_d [106]. The last two observations indicate that the frozen turbulence approximation is not valid for the present case.

The effect of the decorrelation time of the turbulence on the time delays has been discussed in Sec. 7.4. It has been shown there that the temporal decorrelation of the turbulence decreases the measured time delays by a correction factor F_d. This leads to an underestimation of m which is accounted for by Eq. 7.24. The data of Fig. 8.19b have been fitted using Eq. 7.24 assuming a constant tilt angle β. The validity of this assumption will be discussed later. F_d and β are free parameters obtained from the fit. The purple solid line in Fig. 8.19c depicts the fit obtained. It is remarkable that the fit recovers accurately the Θ_{ray} dependence of m. The good agreement between the experimental data and the fit shows that, although the decorrelation time of the turbulence has a strong impact on the time delays, Eq. 7.24 reproduces the experimental data and allows to compute the tilt angle of the turbulent structures. The tilt angle and factor are,

$$\beta = (-29 \pm 9)^\circ, \qquad F_d = (9.9 \pm 0.9) \times 10^{-2}. \tag{8.2}$$

The tilt angle is indicated in Fig. 8.19c as Θ_{ray} value at the interception with the $m = 0$ axis, corresponding approximately to the data in green. The tilt depicted in Fig. 8.19a corresponds to the value experimentally obtained. The above result is the first measurement of the turbulent structure tilt in the confinement region of TJ-II

Using Eq. 7.23, the decorrelation time of the turbulence can be estimated from F_d, $w = 2.0$ cm and $u_\perp = 1.5$ km/s to

$$\tau_d = \frac{w}{u_\perp} \left(F_d^{-1} - 1 \right)^{-1/2} \approx 4\,\mu\text{s}. \tag{8.3}$$

It should be noted that Eq. 7.23 has been derived for turbulence with a Gaussian correlation function in both space and time. Hence this result is only a rough but the first experimental estimation of τ_d done in TJ-II.

8.2.4 Comparison with linear gyrokinetic simulations

Given the uniqueness of the tilt angle measurement method, its accuracy and the validity cannot be assessed by comparison with other diagnostics currently installed on TJ-II. In this section, results of linear global gyrokinetic simulations of the code EUTERPE [47, 48, 117] are qualitatively compared with the experimental results. The similarities observed between measurements and simulations give confidence in the experimental measurements as well as in the simulation code.

An accurate description of the fully developed turbulence requires non-linear simulations including non-linear coupling between different modes. Nevertheless some features of the turbulence are defined mainly by the linear drive and the most unstable modes [28, 118, 119], and therefore can be investigated with linear simulations. Non-linear gyrokinetic simulations of TJ-II plasmas will be available for the first time in the near future, and will make possible a numerical comparison with the experimental measurements.

Global linear simulations for a similar discharge (#42759) of TJ-II have been performed using EUTERPE [120, 121]. Simulations are electrostatic with kinetic electrons. Collisions are not considered. The contour plot of the density and electric potential fluctuations are shown on the perpendicular cross-section of TJ-II in Figs. 8.20a and b, respectively. The measurement positions of the previous analysis are depicted by green circles. In both cases, the fluctuations are stronger in the upper right region of the plasma, where the more unstable modes are located. In this region well defined elongated structures with a slight negative tilt are observed, consistent with the tilt obtained experimentally. The structures in the density and electrostatic fluctuations are similar, though they are better defined for the electrostatic potential at the measurement positions. The zooms to the measurement region show that the structure tilt does not change appreciably along the flux surface. Moreover, the structure tilt is similar to the one deduced from the measurements and depicted by ellipses. The constant tilt assumed for the fit of the experimental data and the obtained tilt angle are reasonable and comparable to the simulation results. The similarities observed give confidence in the measurement method. A stronger statement on the accuracy of the tilt angle measurement and the τ_d estimation would be possible in the near future when non-linear global simulations of TJ-II become available.

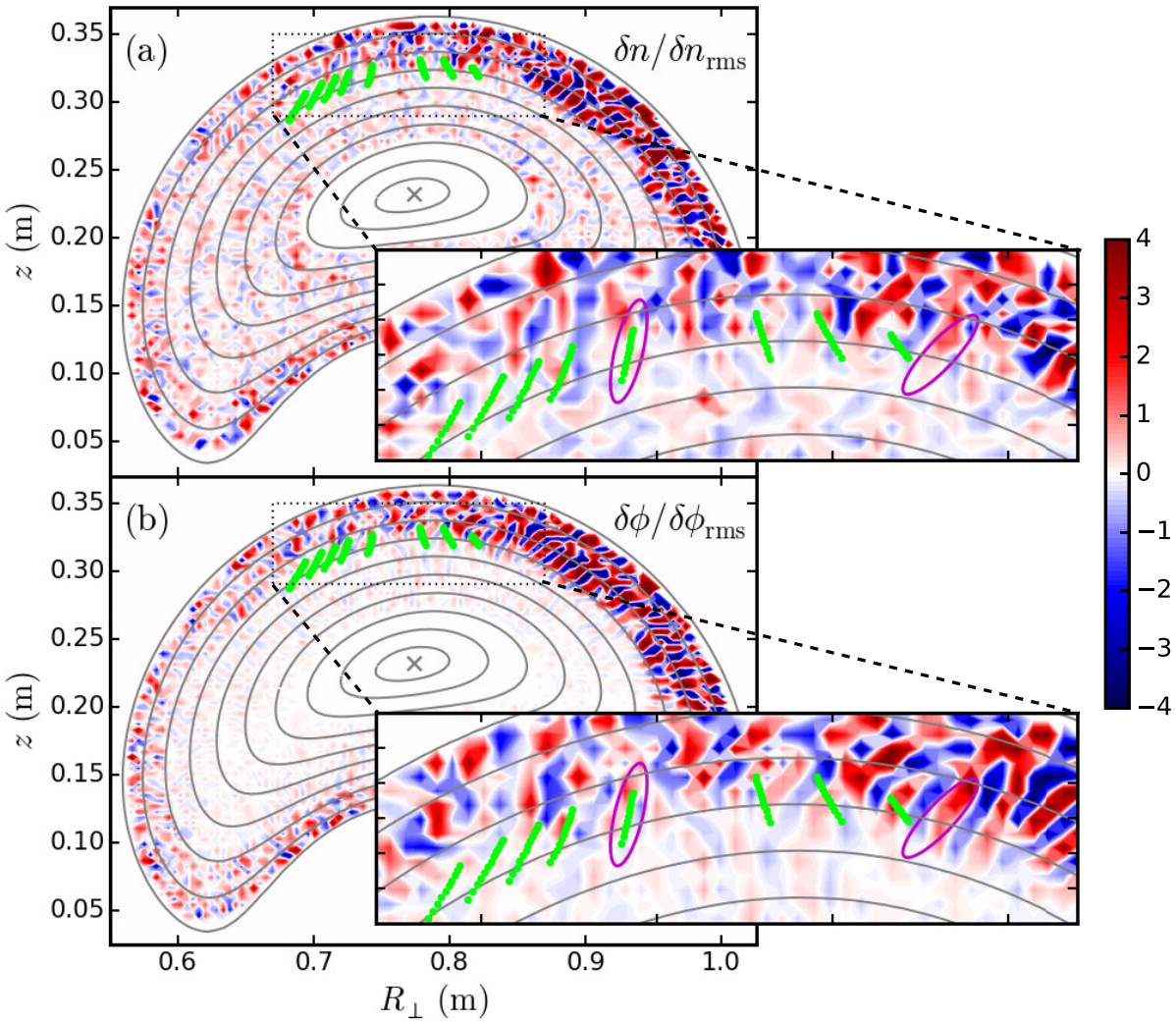

FIGURE 8.20: (a) Density and (b) electric potential fluctuations obtained from linear global gyrokinetic simulations [120, 121] on the perpendicular cross-section of TJ-II. The measurement positions for the tilt angle determination are depicted by green points. The inserts show a zoom to the region measured in the experiments.

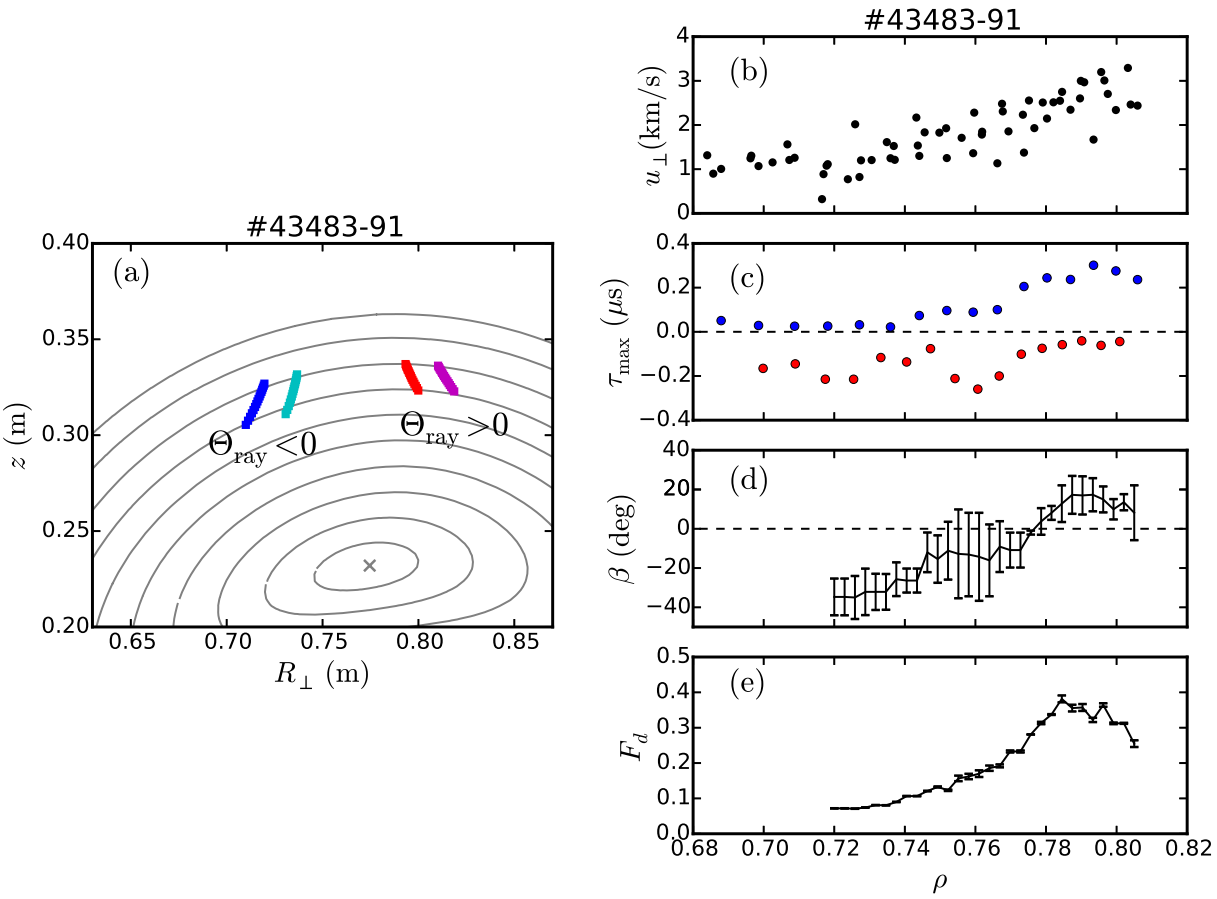

FIGURE 8.21: (a) Measurement positions on the perpendicular cross-section of TJ-II. Radial profiles of (b) $u_\perp$, (c) time delay of the cross correlation τ_{max}, (d) tilt angle of the turbulence β and (e) correction factor F_d. Refer to the text for more details.

8.2.5 Two-point correlation radial scan

The radial profile of the tilt angle has been investigated by two-point correlation measurements. A fine scan of the reference channel probing frequency in the range 33–39 GHz has been performed. In contrast to the frequency patterns previously used in this chapter (cf. Fig. 8.6a) which had several Δf values, here the frequency difference with the hopping channel was fixed at 500 MHz obtaining only one Δf per probing frequency. Four angles of incidence, two with $\Theta_{ray} < 0$ and two with $\Theta_{ray} > 0$, have been used. The measurement positions on the perpendicular cross-section of TJ-II are depicted in Fig. 8.21a. Only the reference channel is shown.

The time delay τ_{max} profiles for two angles of incidence (blue and red measurements in Fig. 8.21a) are shown in Fig. 8.21c. Note that the data sets have an opposite sign due to the opposite Θ_{ray} leading to a different alignment with the turbulent structures. For the outermost positions around $\rho = 0.8$, the magnitude of τ_{max} is larger for the blue than for the red data. This indicates a better alignment of the turbulent structure with the measurement points depicted by red, obtaining a positive tilt angle. In contrast, for the inner positions around $\rho = 0.72$, τ_{max} is larger for the red data indicating a better alignment with the blue measurement points and hence negative tilt angle.

The slope is computed as $m = \tau_{\max} u_\perp / \Delta r$ for each radial position and angle of incidence. The tilt angle β and correction factor F_d are obtained by fitting the data of the four angles of incidence in different radial windows with Eq. 7.24. The results are shown in Figs. 8.21d and e, respectively. As expected from the time delay comparison, there is a change of the tilt angle from approximately -30 to 20° from the innermost to the outermost measurement positions. F_d increases towards the plasma edge.

At $\rho = 0.72$, the tilt angle and the correction factor agree with the values obtained in the previous detailed measurements (cf. Eq. 8.2), which underlines the fact that a two-point correlation scan can provide radially resolved information on β and F_d. The increase of the correction factor is consistent with the $u_\perp$ increase towards the plasma edge observed in Fig. 8.21b. A faster structure propagation means that the decorrelation time of the turbulence has a smaller impact on the time delays, thus the correction factor approaches one (cf. Eq. 7.23). The tilt angle increase towards the edge is consistent with the $u_\perp$ shear direction as depicted schematically in Fig. 2.5. Moreover the L_r decrease (cf. Fig. 8.18a) correlate with the $u_\perp$ shear increase towards the plasma edge. These observations may be an indication of the turbulence regulation by sheared flows.

8.3 Discussion and summary

A similar characterization of the turbulent density fluctuations using Doppler reflectometry has been performed in L-mode plasmas at the ASDEX Upgrade tokamak and the TJ-II stellarator. In this section the main results from both machines are summarized and discussed together.

A radially resolved study of wavenumber spectra has been performed. In the AUG case, the $k_\perp$ spectra measured with O- and X-mode polarization in the range $\rho = 0.85$ to 0.97 have been compared. The more pronounced spectral indices obtained with the O-mode and the steepening of the spectra towards the plasma edge despite of the turbulence level increase, support the linearity of the O-mode measurements. In the TJ-II case, $k_\perp$ spectra have been measured with X-mode polarization in the range $\rho = 0.61$ to 0.79. The small spectral shape variation despite of the turbulence level increase towards the plasma edge and the large spectral indices indicate the linearity of the measurements.

The linearity of the measurements can be explained from the non-linearity parameter γ of Eq. 5.8, particularly by its $G^2/\lambda_0^2 (= G^2 f_0^2/c^2)$ dependence. For the AUG case, the X-mode measures more in the non-linear regime because of the enhancement factor $G_X \approx 5$ and the higher probing frequencies (75–103 GHz). For the O-mode, $G_O = 1$ and the lower probing frequencies (50–75 GHz) provide a more linear measurement. In the TJ-II case, although the enhancement factor is $G_X \approx 5$, the lower probing frequencies (33–50 GHz) push the measurements towards the linear response. Moreover, a small turbulence level is expected in the measured radial range.

A radial evolution of the $k_\perp$ spectra has been observed in AUG. Regarding the O-mode measurements, the position of the spectral knee changes from 4 to 6 cm^{-1} and the spectra index in the large $k_\perp$ range from -2.5 to -5.2. It has been suggested that the changes of the $k_\perp$ spectra are related to a change of driving mechanism and non-linear saturation of the turbulence towards the plasma edge. In TJ-II, no significant radial

variation of the spectra is observed. The spectral knee is at 7 cm^{-1} and the spectral index in the large $k_\perp$ range is about -8.0.

The turbulence level and velocity $u_\perp$ profiles have been investigated. In both machines, a turbulence level increase towards the plasma edge has been observed. In addition, a turbulence level decrease in the $u_\perp$ shear region is observed at the edge ($\rho = 0.98$) of AUG. No turbulence reduction related to the $u_\perp$ shearing is evidenced in TJ-II. In the AUG case, the analysis of the turbulence level and the comparison to the normalized density and ion temperature gradients, suggest a change in the turbulence driving mechanism towards the plasma edge, in agreement with the $k_\perp$ spectra observations.

Detailed radial correlation measurements have been performed in both machines. A decreases of the measured radial correlation length L_r with $k_\perp$ has been observed in AUG. The diagnostic filtering effect and the Kolmogorov-like nature of the turbulence (cf. Sec. 7.5.3) can explain this behaviour which has also been reported in TJ-II measurements [16]. The radial variation of L_r has been investigated. In AUG, L_r increase towards the plasma edge for $\rho < 0.95$ and then drops. This could correspond either to the change of the turbulence character already discussed, or to a $u_\perp$ shear effect. In TJ-II, L_r drops rapidly towards the plasma edge. A explanation in terms of a L_n scaling or a $u_\perp$ shear effect has been proposed.

The time delay of the cross-correlation function has been experimentally investigated. The data analysis technique presented in Secs. 7.1.3 and 7.4 has been applied and the tilt angle of the turbulent structures has been measured in both machines. The effect of the temporal decorrelation of the turbulence has been accounted for with a correction factor F_d (cf. Eq. 7.24). The impact of the temporal decorrelation is strong in the TJ-II measurements; due to the small velocity ($u_\perp = 1.5$ km/s) the time delays are strongly underestimated ($F_d = 0.099$) with respect to the frozen turbulence prediction. In the AUG measurements, the larger velocity ($u_\perp = 3$ km/s) makes the frozen turbulence approximation more suitable, though a small correction ($F_d = 0.5$) is still needed. The correction factor in AUG is consistent with the one obtained with Eq. 7.23 from the decorrelation time τ_d predictions [107]. $\tau_d \approx 4$ μs has been estimated in TJ-II from the the experimental data.

The tilt angle obtained in TJ-II is comparable to the results of a global linear gyrokinetic simulation. Moreover a two-point correlation technique has provided a radial profile of the tilt angle. A change of the tilt angle from -30 to 20° consistent with the $u_\perp$ shear direction has been observed, however no turbulence level reduction is evidenced.

The application of the analysis techniques developed (cf. Sec. 7.1.3 and 7.4) to the experimental data presented here, constitutes the tilt angle measurement method. This is one of the most important contributions of this thesis. In the next chapter, the tilt angle measurements will be compared to gyrokinetic simulation results and related to the dominant micro-instabilities for different plasma conditions in AUG.

Chapter 9

Tilt angle measurements in predominantly ECR and NBI heated plasmas

The tilt angle of the turbulent structures is a quantity predicted by theories [122, 123] and gyrokinetic simulations [38, 124], which can provide information on the turbulence interaction with sheared flows and the type of the dominant micro-instabilities, e.g. ITG and TEM instabilities. The new tilting measurement method using Doppler reflectometry opens the possibility of investigating experimentally the tilt angle and comparing it with theory an simulation results, in benefit of a better understanding of core turbulence in fusion plasmas

In this chapter the tilt measurement method is applied to a low density L-mode discharge of the ASDEX Upgrade tokamak (AUG). Two phases are considered, one with NBI heating only and another with additional ECRH. The resulting dominant ion and dominant electron heating are intended to induce an ITG and TEM dominated turbulence regimes, respectively. The experimental setup is presented in Sec. 9.1. The $u_\perp$ profiles are discussed in Sec. 9.2. The tilt angle measurement is presented in Sec. 9.3, where a tilt difference between both phases is obtained. In Sec. 9.4, the character of the turbulence is assessed with a linear gyrokinetic stability analysis, and the tilt angle measurements are qualitatively compared with gyrokinetic simulation results.

9.1 Discharge and diagnostic setup

The dedicated discharge #34930 has been performed for the turbulence tilt angle determination using Doppler correlation measurements. A low density L-mode plasma in lower single null (LSN) configuration is investigated. The time traces of the plasma currect, ECRH and NBI heating power, and line average density are shown in Figs. 9.1a–d. A constant low NBI power is applied, which is accompanied by blips for CXRS measurements. On axis ECRH is applied during the second half of the discharge. Two phases are considered: one labelled "NBI phase" with NBI heating only, and another labelled

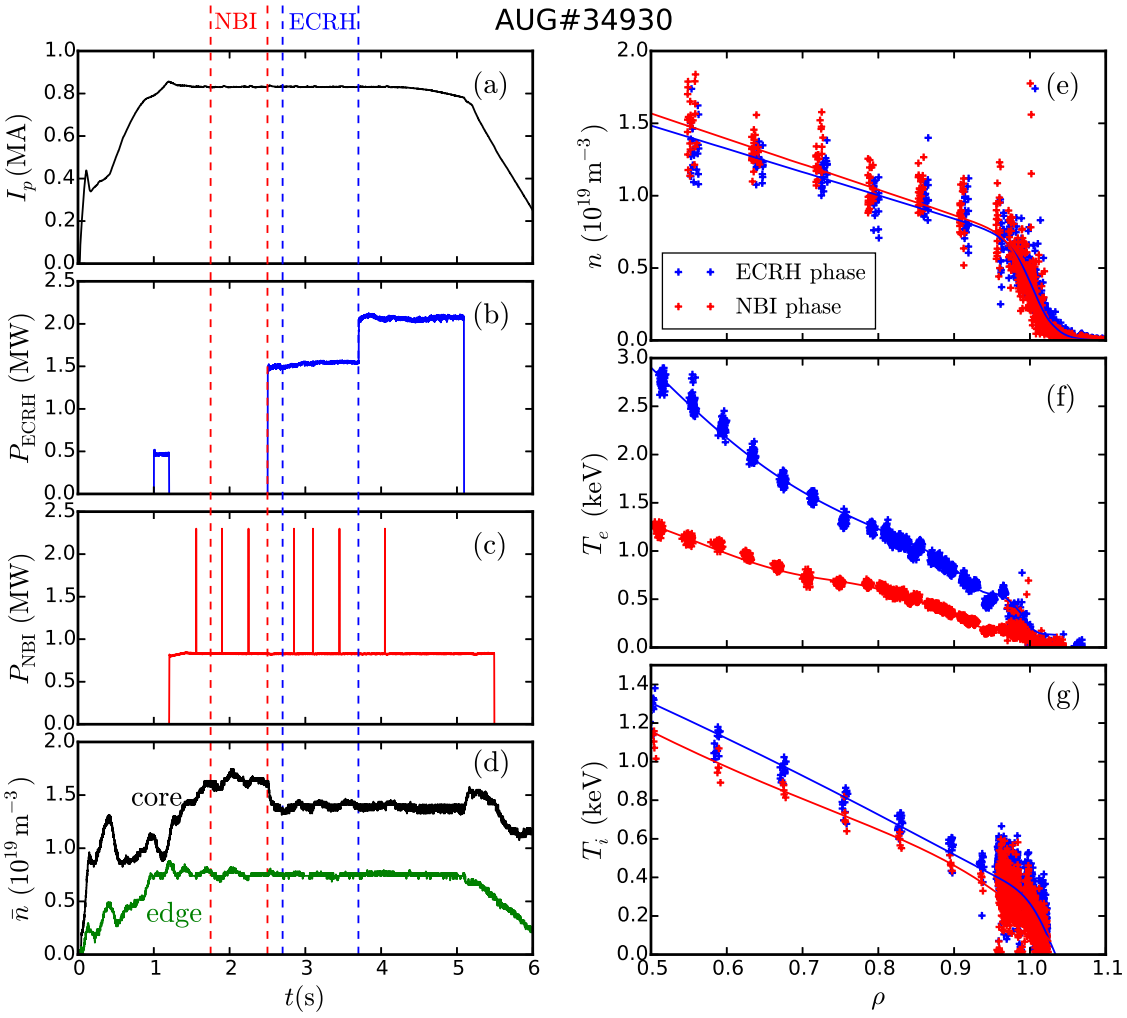

FIGURE 9.1: Time traces of the (a) plasma current, (b) ECRH and (c) NBI heating power, and (d) line averaged plasma density for AUG#34930. The duration of the NBI and ECRH phases is indicated on the top. (e) Plasma density, (f) electron and (g) ion temperature profiles for both phases.

"ECRH phase" with additional 1.5 MW of ECRH. The time windows of the phases are indicated on top of Fig. 9.1a.

The plasma density, electron and ion temperature profiles during the two phases are shown in Figs. 9.1e–g. The plasma density in (e) is obtained from Thomson scattering and lithium beam diagnostic. The solid lines depict the fits which will be used for ray tracing calculations with TORBEAM [76]. A similar density profile is obtained for both phases. The electron temperature profiles in (f) are obtained from Thomson scattering and ECE measurements. The additional electron heating results in a higher electron temperature for the ECRH phase. The ion temperature in (g) obtained from CXRS is rather similar for both phases. Although the NBI ion heating is the same for both phases, the electron-ion collisional heat transfer increases slightly the ion temperature for the ECRH phase. The NBI is kept on also during the ECRH phase in order to induce a high

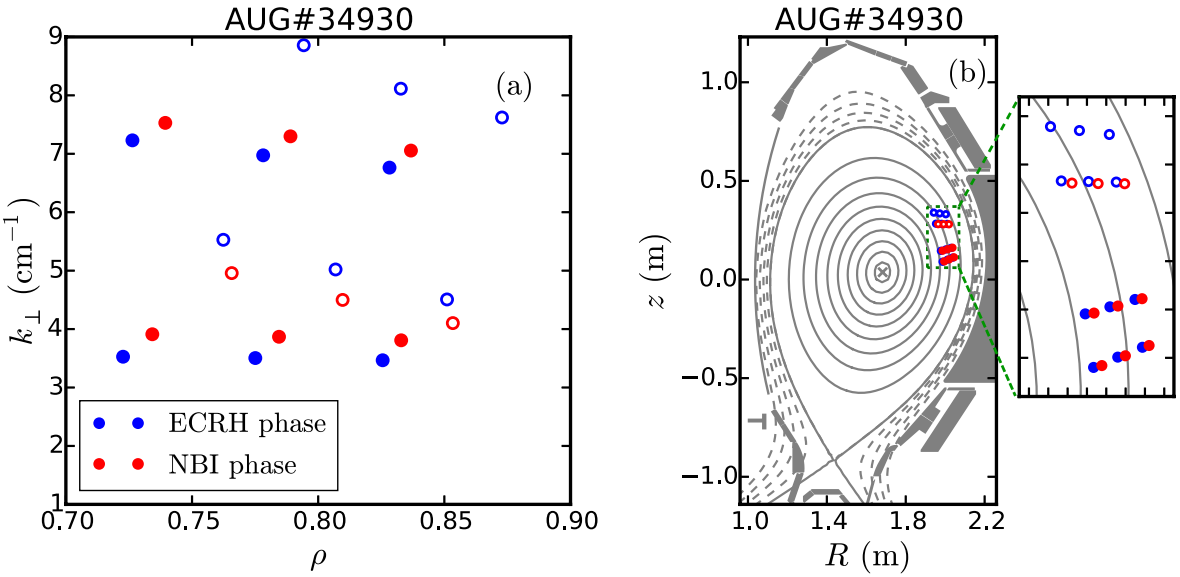

FIGURE 9.2: (a) Probed $k_\perp$ as a function of the radial position ρ. (b) Measurement position on the poloidal AUG cross-section. Empty and filled symbols depict upwards and downwards angles of incidence. Only the reference channel is shown.

$u_\perp$. This allows to apply the tilting angle measurement method avoiding corrections due to the decorrelation time of the turbulence (cf. Sec. 7.4).

To measure this low-density plasma, correlation measurements have been performed with two V-band channels (50–75 GHz) probing in X-mode polarization. The reference channel probes three frequencies (50 ms each), and the hopping channel probes 10 frequencies around the reference one with 5 ms per frequency. The same frequency patterns is used with three and four mirror angles for the NBI and ECRH phase, respectively. Angles with the mirror pointing up- and downwards have been selected.

The probed parameter space $(\rho, k_\perp)$ and the measurement positions on the AUG cross-section are shown in Fig. 9.2. The empty symbols depict the data for the mirror pointing upwards. A radial overlap of up- and down-pointing measurements is achieved between $\rho = 0.75$ and 0.85. The probed $(\rho, k_\perp)$ range is similar for both scenarios given the similarity of density profiles, cf. Fig. 9.1e.

9.2 Measurement of $u_\perp$ profile

The $u_\perp$ profiles have been computed from the Doppler shift according to Eq. 4.10. The results for both phases are shown in Fig. 9.3. The convention for the mirror pointing up- (empty symbols) and downwards (filled symbols) is kept. Large perpendicular velocities are obtained for both phases. The ECRH phase has an approximately constant velocity of about 6 km/s. The NBI phase has a larger velocity, it is about 7 km/s at $\rho = 0.9$ and increases to 10 km/s at $\rho = 0.7$. A scatter of the $u_\perp$ Doppler reflectometry data is observed. The measurements obtained with the mirror pointing upwards (empty circles) are about 1 km/s smaller than the measurements pointing downwards (filled circles) obtained closer to the mid-plane.

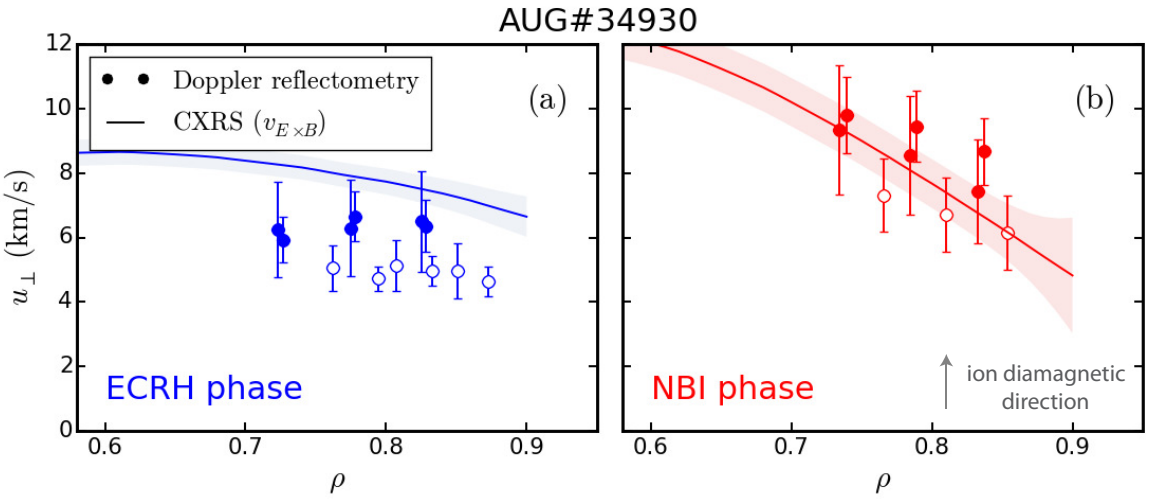

FIGURE 9.3: $u_\perp$ profile for the (a) ECRH and (b) NBI phases. The Doppler reflectometry measurements are shown as circles, where the empty and filled symbols depict the data obtained with the mirror pointing up- and downward, respectively. CXRS measurements are shown with lines.

The $E \times B$ velocity, $v_{E\times B} = E_r/B$, is computed from the radial electric field E_r obtained from CXRS measurements (cf. Eq. 3.2) [125]. The results are depicted by lines together with the Doppler reflectometry data in Fig. 9.3. It should be remarked that CXRS measurements do not contain phase velocity contributions, whereas the Doppler reflectometry measurements do. In the ECRH phase, the velocities measured with Doppler reflectometry are smaller than CXRS data, indicating a phase velocity in the electron diamagnetic direction. In the NBI phase, there is a better agreement between Doppler reflectometry and CXRS measurements indicating a small phase velocity. Nevertheless, the Doppler reflectometry measurements depicted with full symbols are slightly higher than those of CXRS also taken close to the mid-plane. This suggest a phase velocity in the ion diamagnetic direction.

The $u_\perp$ differences between upper and mid-plane measurement positions can be due to the phase velocity, fine diagnostic effects or even due to real $u_\perp$ poloidal asymmetries. A multi-diagnostic investigation of this differences is currently ongoing, but it is out of the scope of this work. For the following analysis, the local $u_\perp$ obtained from Doppler reflectometry measurements is used. The differences are accounted for with the error bars.

9.3 Tilt angle determination

In this section the tilt angle of the turbulent structures is measured with the method presented in Sec. 7.1 and applied in Secs. 8.1.3 and 8.2.3. The reader should refer to these sections for more details.

The time delay $\tau_{\max}$ of the cross-correlation function and the perpendicular displacement $\Delta y_{\max} = u_\perp \tau_{\max}$ are computed. $\Delta y_{\max}$ as function of Δr is shown in Figs. 9.4b

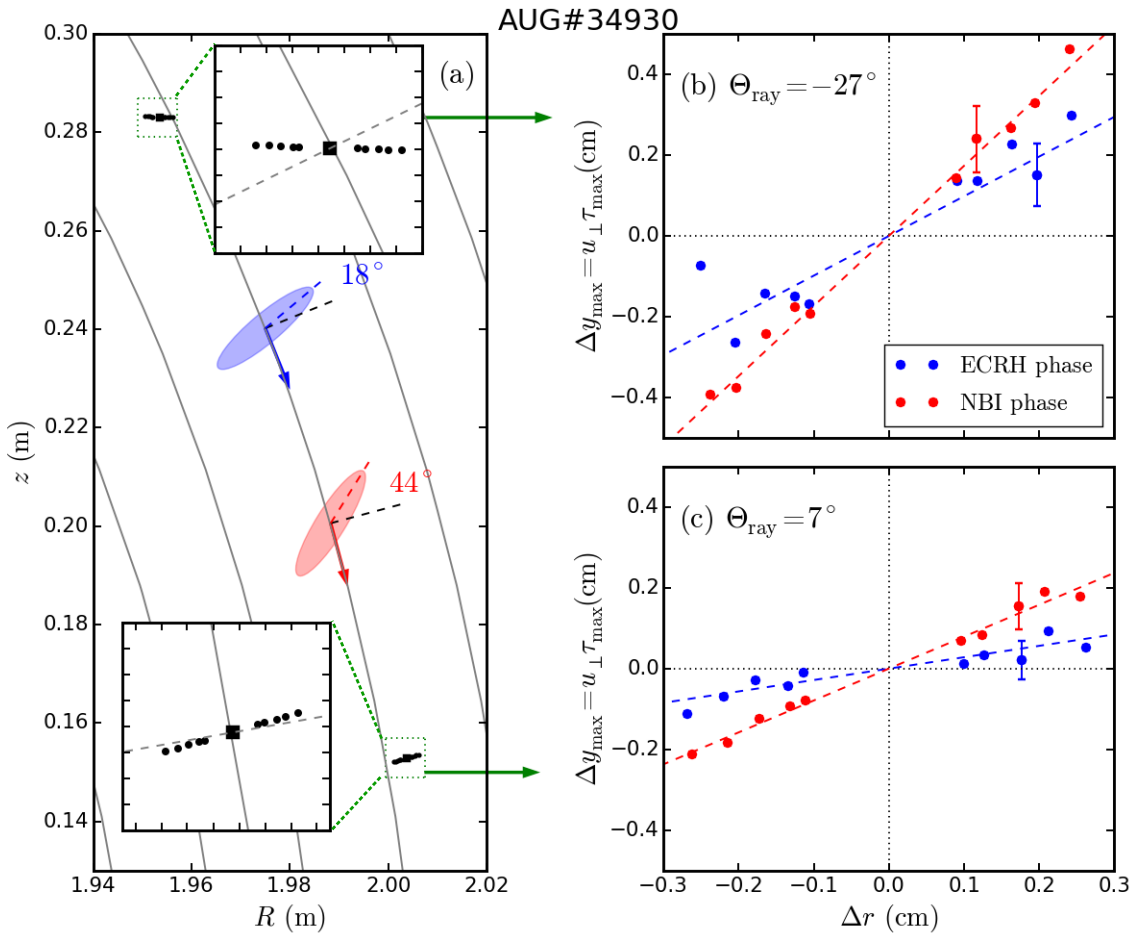

FIGURE 9.4: (a) Measurement positions for two angles of incidence are shown on the AUG cross-section. The reference and hopping channels are depicted by squares and circles, respectively. Structures are artistically depicted. (b–c) $\Delta y_{\max} = u_{\perp}\tau_{\max}$ as a function of Δr for the two cases depicted in (a). A different slope is obtained for ECRH and NBI phases.

and c. The results for the ECRH and NBI phases are depicted by blue and red symbols, respectively. The two plots correspond to the measurement positions indicated on the AUG cross-section in Fig. 9.4a. Due to the different angles of incidence used for the upper and lower case, the measurement positions are differently aligned with respect to the radial direction. Θ_{ray} is -27 and $7°$ for the upper and lower measurements, respectively.

A linear behaviour of $\Delta y_{\max}$ with Δr is observed in Figs. 9.4b and c. The dashed lines are the linear fits to the data. For each measurement position, a different slope is obtained for the ECRH and NBI phases indicating a different tilt angle of the turbulence. Note that the difference is similar for both measurement positions. The larger slope obtained in the NBI phase implies a stronger structure tilt compared to the ECRH phase. For both phases, the time delays in (b) are larger than those in (c). This is due to the different alignment of the measurement position.

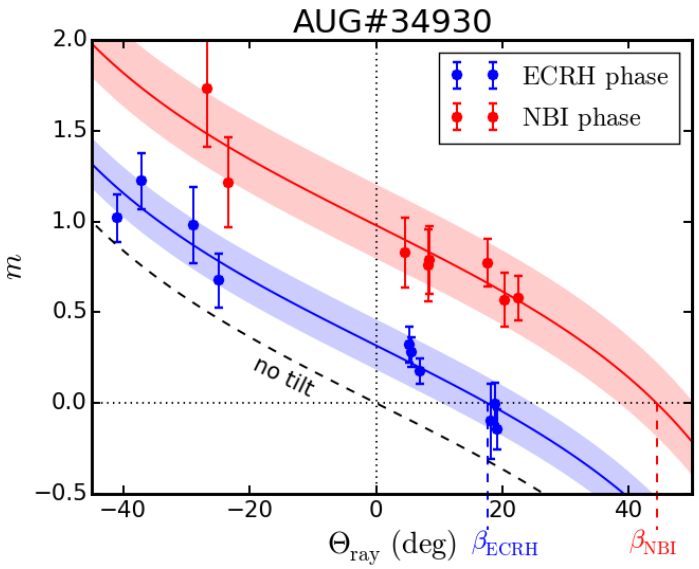

FIGURE 9.5: m as a function of Θ_{ray} for the ECRH and NBI phases. The solid lines depict the fit to the data using Eq. 7.12.

The slope m from all the measurements in the range $\rho = 0.70$–0.84 is plotted as a function of Θ_{ray} in Fig. 9.5. The data of both phases show a similar trend with Θ_{ray} as the one predicted by Eq. 7.12 for $\beta = 0$ and depicted by a dashed black line. The signs of the equation have been adapted to the conventions used here. The vertical offset between both series indicates a difference in the tilt angle. In this case no correction factor F_d is required because of the large $u_\perp$ (cf. Sec. 7.4), hence the data is fitted with Eq. 7.12. The fits are shown with solid lines. A good agreement suggests that the time delays are explained by the tilt of the turbulent structures. The dispersion of the data could be due either to a radial or a poloidal change of the tilt, nevertheless within the error bars the constant tilt is reasonable. The tilt angles are

$$\beta_{\text{ECRH}} = (18 \pm 7)^\circ, \tag{9.1}$$

$$\beta_{\text{NBI}} = (44 \pm 6)^\circ, \tag{9.2}$$

These values are indicated in the figure by the intersection of the fit with the Θ_{ray}-axis. The error bars are illustrated as shadowed areas around the fit. A significant difference of the tilt angle between both phases is obtained. This will be related to different types of turbulence in the next section. Structures with the corresponding tilt are schematically depicted in Fig. 9.4a.

Given the large value of $u_\perp$, no correction factor F_d accounting for the decorrelation time effect is required (cf. Sec. 7.4). The passing time of the structures is about $w/u_\perp \approx 3$ and 2 μs for the ECRH and NBI phases, respectively. This is smaller than the decorrelation time $\tau_d \approx 9$ μs measured with the poloidal correlation refletometry diagnostic recently installed on AUG [106, 107]. The frozen turbulence approximation is suitable for this case.

The radial correlation length L_r is estimated from the measurements at $k_\perp \approx 4\,\mathrm{cm}^{-1}$ using a Gaussian fit. For the ECRH and NBI phases L_r is about 0.5 and 0.6 cm, respectively. That is larger than the radial resolution which is of the order of 0.2 cm. Therefore no strong underestimation of the tilt angle due to the finite radial resolution is expected.

The difference of the $u_\perp$ shear observed in Fig. 9.3 is qualitatively consistent with the tilt angle difference obtained experimentally. On the one hand, the $u_\perp$ gradient in the NBI phase may tilt the structures positively by the mechanism depicted schematically in Fig. 2.5a. On the other hand, the structure tilt may contribute to the toroidal velocity through the Reynolds [36, 39], and hence to $u_\perp$. A strong statement on the relevance of such contributions would require a detailed momentum transport study which is out of the scope of this thesis.

9.4 Linear gyrokinetic modelling

The dominant electron and ion heating used in the ECRH and NBI phases, respectively, can induce different turbulence regimes. It has been observed in simulations [38] and analytical models [123] that the global linear unstable modes have defined tilt angles, which change for the different types of micro-instabilities, e.g. TEM and ITG modes. In this section, the measured tilt angles are related to the dominant instabilities. Moreover, the use of the tilt angle measurement as an important element to compare with gyrokinetic simulations is discussed.

The dominant electron heating during the ECRH phase increases T_e (Fig. 9.1f), obtaining a stronger $\nabla T_e/T_e$ which is a driving term for the TEM instability. Therefore the additional electron heating during the ECRH phase may induce a more TEM dominated turbulence with respect to the NBI phase with smaller $\nabla T_e/T_e$. The character of the turbulence depends non-trivially on the equilibrium and the detailed plasma parameter profiles and gradients. It can be investigated using gyrokinetic simulations. Although global non-linear simulations provide the most complete description available of the turbulence, local linear simulations are often used to assess the linear stability of the turbulent modes [17, 79, 101, 126].

The two phases have been investigated with linear local simulations using the gyrokinetic code GKW [46, 126]. The experimental density and temperature profiles have been used as an input for the code. A linear stability analysis has been performed at $\rho = 0.7$ and 0.8, corresponding to the radial range of interest. The simulation provides the growth rate γ and the frequency ω_r of the most unstable mode with wavenumber k_y in the simulations grid. For the measurement positions under consideration, k_y is aligned with the perpendicular direction and metric corrections are unnecessary, therefore the perpendicular wavenumber is directly obtained as $k_\perp = k_y$.

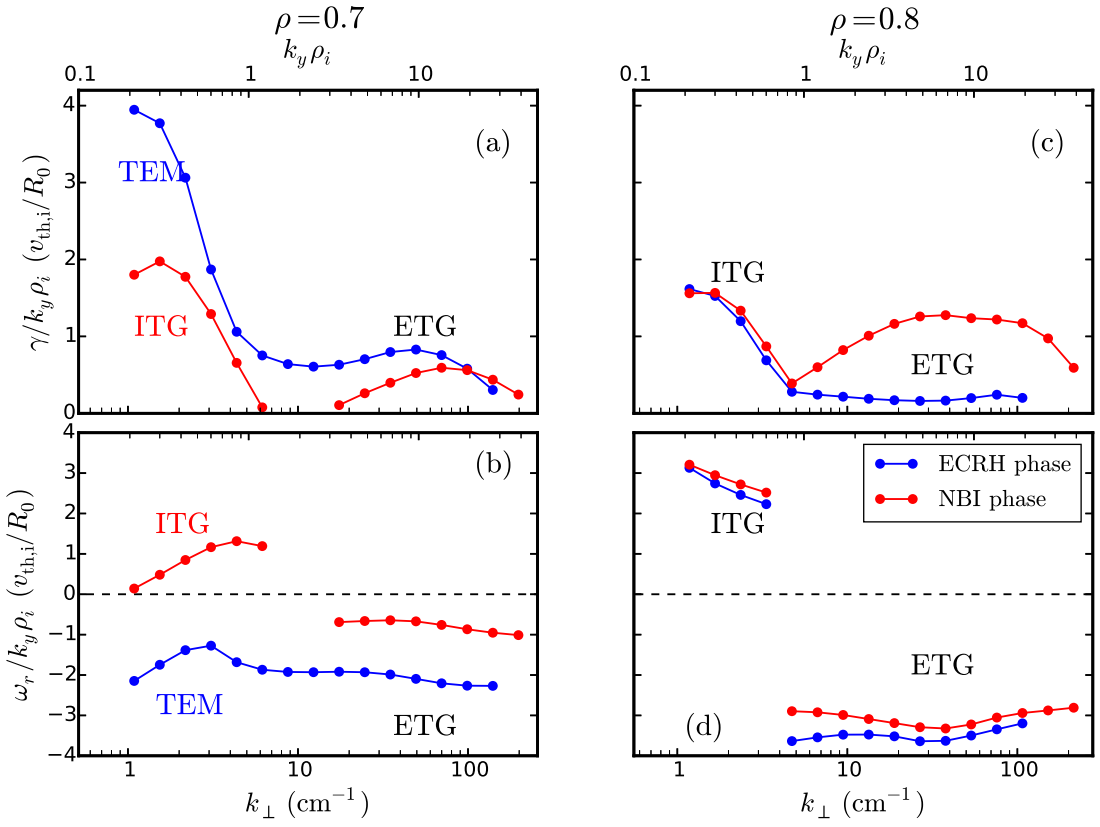

FIGURE 9.6: Results of the linear stability analysis performed with the gyrokinetic code GKW [46, 126]. The normalized growth rate γ (a,c) and mode frequency ω_r (b,d) are presented as a function of $k_\perp$. The results for $\rho = 0.7$ and 0.8 are shown on the left and right sides, respectively.

The results of the linear stability analysis are presented in Fig. 9.6. The left column shows data for $\rho = 0.7$ and the right one for $\rho = 0.8$. The ECRH and NBI phases are depicted by blue and red symbols, respectively. γ and ω_r are normalized with $k_y\rho_i$ and are given in $v_{\mathrm{th,i}}/R_0$ units, where ρ_i is the ion Larmor radius, $v_{\mathrm{th,i}}$ is the ion thermal velocity and R_0 is the major radius. This normalization and units are typically used in gyrokinetic studies [36, 126]. The upper and lower axes depict $k_y\rho_i$ and $k_\perp$, respectively.

For $\rho = 0.7$ in the range $k_y\rho_i < 1$, the unstable modes have a negative frequency (electron diamagnetic direction) for the ECRH phase indicating TEM modes. Whereas for the NBI phase the frequency is positive (ion diamagnetic direction) indicating ITG modes. For $\rho = 0.8$, the unstable modes in the range $k_y\rho_i < 0.7$ have a positive frequency indicating ITG modes for both phases. In the large $k_y\rho_i$ range, the unstable modes with negative frequency for all cases correspond to ETG modes. Their $k_\perp$ range is not relevant for Doppler reflectometry measurements probing up to $k_\perp = 10$ cm^{-1}. Furthermore, no effect of ETG modes at large wavenumber ($k_\perp\rho_i \approx 3$) has been observed in density fluctuation measurements [30]. Summarizing, the NBI phase is linearly ITG dominated in the radial range of interest, whereas the ECRH phase exhibits a mix character between TEM and ITG unstable modes. Moreover, the phase velocity discussed from the comparison of $u_\perp$ from Doppler reflectometry with $v_{E\times B}$ from CXRS (cf.

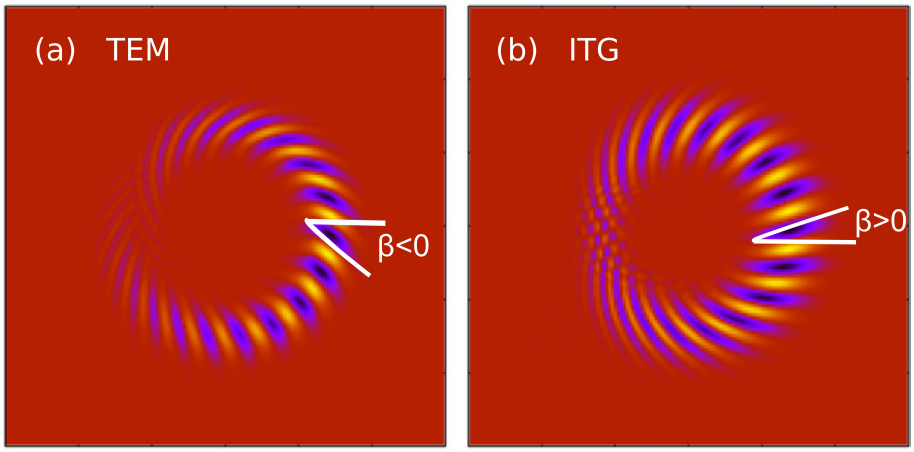

FIGURE 9.7: Structure of the global mode for (a) TEM and (b) ITG turbulence (adapted from Ref. [38]).

Sec. 9.2), supports the identification of the NBI and ECRH phases with dominant ITG and more TEM dominated turbulence regimes, respectively.

The TEM and ITG linear modes have an opposite tilt angle. This difference has been found using analytical expressions and in global linear gyrokinetic simulations [38]. The mode structure for TEM and ITG turbulence obtained in the Ref. [38] is shown in Fig. 9.7a and b, respectively. Elongated and tilted structures are observed in both cases. The tilt at the mid-plane, indicated in the figure, has a different sign for ITG (positive) and TEM (negative) modes. The tilt angle difference of 26° (cf. Eqs. 9.1 and 9.2) observed in the experiment agree qualitatively with these results. The NBI phase is ITG turbulence dominated, hence a positive and large tilt angle is expected. Moreover the in ECRH phase one expects a mixture of TEM and ITG modes, thus the mode structure would be a combination of structures with positive and negative tilts that averages to a small tilt angle value.

The joint analysis of the tilt angle measurements, linear stability and $u_\perp$ profiles has shown the utility of the developed technique for physical studies in fusion plasmas. Moreover, the measurement of tilt angle might be used as a signature of the dominant turbulence regime. Nevertheless, a stronger statement on identification of the turbulence regime using the tilt angle measurement requires quantitative comparisons with non-linear global simulations for the specific conditions of the experiment. These simulations are challenging and are left for future investigations.

Summary

The method developed to measure the tilt angle has been applied to a discharge using different heating methods in the ASDEX Upgrade tokamak. Measurements have been performed in the range $\rho = 0.70 - 0.84$ for phases with either dominant ion or electron heating. A tilt angle difference of 26° has been obtained between both phases. The tilt change is in qualitative agreement with a transition from an ITG dominated to a

ITG/TEM mixed turbulence regime. The dominant micro-instabilities for the specific plasma conditions have been confirmed with linear gyrokinetic simulations.

For the large velocities involved of $u_\perp \geq 6$ km/s, the temporal decorrelation of the turbulence has no impact on the measured time delays. Therefore no correction factor F_d is needed for the tilt angle determination according to the analysis presented in Sec. 7.4.

The sensitivity of the tilt angle measurement to different plasma conditions and the qualitative agreement with theoretical predictions show that the tilt angle is an useful quantity for comparisons of experimental measurements with theory and gyrokinetic simulations. Thus the measurement technique developed and applied in this thesis provides a valuable tool for detailed turbulence studies in the future.

Chapter 10

Conclusions and outlook

Turbulence is a relevant phenomenon in magnetic confinement experiments because it contributes to the transport of energy and particles in fusion plasmas. Therefore, a better understanding of the turbulence dynamics and the related transport is required for optimizations of the experimental devices and future reactors. In the last years, a large progress has been made towards the understanding of turbulence; theoretical predictions and gyrokinetic simulations have become available. However, a more detailed experimental characterization of the turbulence is required for comparison and validation of physical models and simulation codes. Doppler relfectometry is one of the experimental techniques used for density turbulence investigations in fusion plasmas. It uses the scattering of microwaves off density fluctuations to provide measurements of the perpendicular velocity $u_\perp$, perpendicular wavenumber ($k_\perp$) spectrum and radial correlation length (L_r) of the density turbulence.

In this thesis, the Doppler reflectometry technique has been deeply investigated and applied to the detailed characterization of density turbulence in fusion plasmas. The complex diagnostic response has been investigated by modelling the wave propagation and scattering processes relevant for the technique. Experimental measurement have been performed in L-mode plasmas at the ASDEX Upgrade tokamak (AUG) and the TJ-II stellarator. The experimental data have been analysed based on the modelling results, which have made possible a more accurate and complete characterization of the turbulence in both machines.

The linearity of the diagnostic response has been investigated in detail with the physical optics model and two-dimensional full-wave simulations. An enhanced power response regime has been found and characterized for the first time. This regime and the saturation regime have been found responsible of the flattening of the $k_\perp$ spectra, which is measured when a non-linear diagnostic response is involved. The physical optics model has been used for a characterization of the power response in a broad range of turbulence level and $k_\perp$, and for different types of wavenumber spectra. This analysis has shown that the power response depends strongly on the spectral shape and has been useful to asses the linearity of experimental measurements. Furthermore, a perturbative expansion of the physical optics model has shown that the enhanced power response is produced by multiple scattering events.

Radial correlation Doppler reflectometry has been modelled using two-dimensional full-wave simulations and a linear analysis based on the Born approximation. The effect of the spectral and radial resolution on the diagnostic response has been investigated. It has been found that the spectral shape of the turbulence has an impact on the correlation measurements. In particular, the filter effect of the diagnostic and the Kolmogorov-like nature of the wavenumber spectrum introduce a instrumental $k_\perp$ dependence of the measured radial correlation length L_r. This effect explains the decrease of L_r with $k_\perp$ measured in AUG and reported for TJ-II [16].

The density turbulence has been characterised in L-mode plasmas in AUG and TJ-II. In AUG, a radial evolution of the $k_\perp$ spectra has been observed in the range $\rho = 0.85$ to 0.97. The spectral index at large $k_\perp$ increases from -2.5 to -5.2 and the position of the spectral knee shifts from $k_\perp = 4$ to 6 cm^{-1}. Moreover a radial variation of the radial correlation length L_r has been observed. The radial profiles of density and temperature normalized gradient, together with the radial changes observed in $k_\perp$ spectra and L_r suggest a change of the turbulence regime towards the plasma edge. In TJ-II, the $k_\perp$ spectra in the range $\rho = 0.61$–0.79 have a spectral index of about -8 and a knee at $k_\perp = 7$ cm^{-1}, and show no radial evolution. A strong decrease of L_r towards the plasma edge has been observed. Possible explanations are either a scaling with the density gradient length L_n or an effect of the $u_\perp$ shear, which can lead to decorrelation of the turbulent structures i.e. to a reduction of L_r according to standard theories.

A new method for the measurement of the mean tilt angle of the turbulent structures has been developed. It is based on the analysis of the time delay of the cross-correlation between Doppler reflectometry channels, which measure at positions radially and perpendicularly displaced. Diagnostic effects have been considered with two-dimensional full-wave simulations and a linear analysis. It has been found that for a linear diagnostic response and for a radial resolution smaller than L_r, the method gives a good estimation of the tilt angle. The impact of the temporal decorrelation of the turbulence on the method has been investigated. The relevant quantities to asses such impact are the decorrelation time of the turbulence τ_d and the passing time of the structures in front of the probing beam $w/u_\perp$, with w the beam width. If the passing time is shorter than the decorrelation time, $w/u_\perp < \tau_d$, there is no impact and the method can be directly applied. This is the case for large plasma velocities ($u_\perp > w/\tau_d$), whereas for small ones ($u_\perp \leq w/\tau_d$) the temporal decorrelation of the turbulence reduces the measured time delays. This effect has been accounted for with a correction factor F_d.

The tilt angle measurement method has been applied for the first time to fusion plasmas in AUG and TJ-II. The experimentally measured time delays correspond to the modelling predictions and allow to obtain the tilt angle. The effect of the decorrelation time of the turbulence has been experimentally confirmed; for $u_\perp \approx 1.5$ km/s the effect is strong and the time delays are reduced by factor 10, for $u_\perp \approx 3$ km/s time delays are reduced by a factor 2, and for $u_\perp > 5$ km/s no time delay reduction has been observed. Even in cases when the decorrelation time has a strong impact, the tilt angle can be obtained using the correction factor F_d.

The tilt angle measured in TJ-II is comparable to the one obtained in global linear gyrokinetic simulations. Furthermore, a two-point correlation technique has been used to obtain a radial profile of the tilt angle. A change from -30 to 20° has been observed, which is consistent with the the $u_\perp$ shear effect on the turbulence expected from theories. In AUG, the tilt angle has been measured in low density L-mode plasmas during phases with dominant ion and electron heating. A change of the tilt angle has been observed between both phases. Linear gyrokinetic simulations have confirmed a transition from an ITG to a more TEM dominated turbulence regime. Moreover the tilt angle difference is in qualitative agreement with predictions for ITG and TEM dominated turbulence.

This thesis represents a major step towards a better understanding of Doppler reflectometry and towards a more advanced characterization of turbulence in fusion plasmas. The detailed study of the power response and of the correlation measurements have highlighted diagnostic properties and effects important for a more complete and accurate characterization of the turbulence. In particular, the finding of the enhanced power response regime has contributed to a better understanding of the measured $k_\perp$ spectra. The tilt angle measurement method, proposed and applied here, has provided unique measurements of this type in the confinement region of fusion plasmas. It has been shown that the tilt angle is an useful quantity for studies of the turbulence dynamics, and which can be compared with physical models and gyrokinetic simulations. This method can be applied for systematic experimental investigations in AUG and TJ-II, and also in other fusion experiments where Doppler reflectometry is available. The methods developed in this thesis will potentially contribute to a better understanding of the turbulence in fusion plasmas in the near future.

Outlook

During the development of this thesis, topics that deserve further investigation have been identified. Regarding the Doppler reflectometry modelling: (i) The correlation measurements for Kolmogorov-like turbulence can be investigated with two-dimensional full-wave simulations. The study of non-linearities and non-local scattering for this case would complement the linear analysis presented here and the literature on the topic. (ii) It has been shown that the physical optics model reproduces the linearity of Doppler reflectometry. Further studies of the weighting function and its inclusion into the model could deliver a "2D physical optics model". This may simulate more accurately and efficiently Doppler reflectometry taking into account multiple and non-local scattering processes.

Regarding the experimental measurements presented here, the AUG and TJ-II discharges characterized experimentally can be further investigated with global non-linear gyrokinetic simulations. This would allow to study more accurately specific effects that have been reported in the thesis. Some of them are listed: (i) the radial evolution of $k_\perp$ spectra and L_r as a consequence of the turbulence regime change in AUG. (ii) The radial evolution of L_r and the tilt angle as a consequence of the velocity shear in TJ-II. (iii) The tilt angle change as a signature of the transition between ITG and TEM dominated turbulence regimes in AUG.

In this thesis, poloidal asymmetries in the plasma flow in AUG have been reported for the first time (cf. Sec. 9.2). Similar asymmetries have been already observed in other fusion experiments and have been related to contributions of turbulence to plasma flows [127]. These observations deserve further experimental investigations, which could be the starting point of new turbulence studies in the ASDEX Upgrade tokamak.

Bibliography

[1] E. Teller. *Fusion: Magnetic confinement*, volume 1, Academic Press, New York, 1981.

[2] V. D. Shafranov. "The initial period in the history of nuclear fusion research at the Kurchatov Institute." *Physics-Uspekhi*, **44**(8):835, 2001.

[3] F. Birol *et al.* *Energy and Climate Change - World Outlook Special Report.* International Energy Agency (IEA), 2015. Available at `http://www.iea.org/publications/freepublications/publication/weo-2015-special-report-2015-energy-and-climate-change.html`.

[4] F. Birol *et al.* *Key World Energy Statistics 2017.* International Energy Agency (IEA), 2017. Available at `https://www.iea.org/publications/freepublications/publication/key-world-energy-statistics.html`.

[5] J. D. Lawson. "Some Criteria for a Power Producing Thermonuclear Reactor." *Proceedings of the Physical Society. Section B*, **70**(1):6, 1957.

[6] J. Nuckolls, L. Wood, A. Thiessem *et al.* "Laser Compression of Matter to Super-High Densities: Thermonuclear (CTR) Applications." *Nature*, **239**(139):4941, 1972.

[7] I. Milch. *50 Jahre Max-Planck-Institut für Plasmaphysik : Forschung für die Energie der Zukunft*, Max-Planck-Institut für Plasmaphysik (IPP), Garching / Greifswald, 2010.

[8] F. L. Hinton and R. D. Hazeltine. "Theory of plasma transport in toroidal confinement systems." *Reviews of Modern Physics*, **48**:239, 1976.

[9] A. J. Wootton, B. A. Carreras, H. Matsumoto *et al.* "Fluctuations and anomalous transport in tokamaks." *Physics of Fluids B: Plasma Physics*, **2**(12):2879, 1990.

[10] P. C. Liewer. "Measurements of microturbulence in tokamaks and comparisons with theories of turbulence and anomalous transport." *Nuclear Fusion*, **25**(5):543, 1985.

[11] A. J. Brizard and T. S. Hahm. "Foundations of nonlinear gyrokinetic theory." *Reviews of Modern Physics*, **79**:421, 2007.

[12] X. Garbet, Y. Idomura, L. Villard *et al.* "Gyrokinetic simulations of turbulent transport." *Nuclear Fusion*, **50**(4):043002, 2010.

[13] U. Stroth, A. B. Navarro, G. Conway *et al.* "Experimental turbulence studies for gyro-kinetic code validation using advanced microwave diagnostics." *Nuclear Fusion*, **55**(8):083027, 2015.

[14] M. Hirsch, E. Holzhauer, J. Baldzuhn *et al.* "Doppler reflectometry for the investigation of propagating density perturbations." *Plasma Physics and Controlled Fusion*, **43**(12):1641, 2001.

[15] J. Schirmer, G. D. Conway, E. Holzhauer *et al.* "Radial correlation length measurements on ASDEX Upgrade using correlation Doppler reflectometry." *Plasma Physics and Controlled Fusion*, **49**(7):1019, 2007.

[16] F. Fernández-Marina, T. Estrada and E. Blanco. "Turbulence radial correlation length measurements using Doppler reflectometry in TJ-II." *Nuclear Fusion*, **54**(7):072001, 2014.

[17] T. Happel, T. Görler, P. Hennequin *et al.* "Comparison of detailed experimental wavenumber spectra with gyrokinetic simulation aided by two-dimensional full-wave simulations." *Plasma Physics and Controlled Fusion*, **59**(5):054009, 2017.

[18] E. Blanco and T. Estrada. "Study of Doppler reflectometry capability to determine the perpendicular velocity and the k-spectrum of the density fluctuations using a 2D full-wave code." *Plasma Physics and Controlled Fusion*, **50**(9):095011, 2008.

[19] E. Blanco and T. Estrada. "Two-dimensional full-wave simulations of radial correlation Doppler reflectometry in linear and non-linear regimes." *Plasma Physics and Controlled Fusion*, **55**(12):125006, 2013.

[20] E. Z. Gusakov and A. Y. Popov. "Two-dimensional non-linear theory of radial correlation reflectometry." *Plasma Physics and Controlled Fusion*, **46**(9):1393, 2004.

[21] E. Gusakov, M. Irzak and A. Popov. "Radial correlation reflectometry at oblique probing wave incidence (linear scattering theory predictions)." *Plasma Physics and Controlled Fusion*, **56**(2):025009, 2014.

[22] U. Stroth. *Plasmaphysik: Phänomene, Grundlagen, Anwendungen*, Vieweg+Teubner Verlag, Wiesbaden, 2011.

[23] A. N. Kolmogorov. "Dissipation of Energy in the Locally Isotropic Turbulence." *Proceedings of the Royal Society of London A: Mathematical, Physical and Engineering Sciences*, **434**(1890):15, 1991.

[24] R. H. Kraichnan. "Inertial Ranges in Two-Dimensional Turbulence." *The Physics of Fluids*, **10**(7):1417, 1967.

[25] R. H. Kraichnan. "Inertial-range transfer in two- and three-dimensional turbulence." *Journal of Fluid Mechanics*, **47**(3):525–535, 1971.

[26] T. Happel. "Doppler reflectometry in the TJ-II Stellarator: Design of an Optimized Doppler Reflectometer and its Application to Turbulence and Radial Electric Field Studies." Ph.D. thesis, Universidad Carlos III de Madrid, Spain, 2010.

[27] P. W. Terry, A. F. Almagri, G. Fiksel *et al.* "Dissipation range turbulent cascades in plasmas." *Physics of Plasmas*, **19**(5):055906, 2012.

[28] T. Görler and F. Jenko. "Multiscale features of density and frequency spectra from nonlinear gyrokinetics." *Physics of Plasmas*, **15**(10):102508, 2008.

[29] N. Fedorczak, P. Ghendrih, P. Hennequin *et al.* "Dynamics of tilted eddies in a transversal flow at the edge of tokamak plasmas and the consequences for L–H transition." *Plasma Physics and Controlled Fusion*, **55**(12):124024, 2013.

[30] P. Hennequin, C. Honoré, A. Truc *et al.* "Doppler backscattering system for measuring fluctuations and their perpendicular velocity on Tore Supra." *Review of Scientific Instruments*, **75**(10):3881, 2004.

[31] T. Estrada, E. Ascasíbar, E. Blanco *et al.* "Spatial, temporal and spectral structure of the turbulence–flow interaction at the L–H transition." *Plasma Physics and Controlled Fusion*, **54**(12):124024, 2012.

[32] T. Happel, T. Estrada, E. Blanco *et al.* "Scale-selective turbulence reduction in H-mode plasmas in the TJ-II stellarator." *Physics of Plasmas*, **18**(10):102302, 2011.

[33] U. Stroth, P. Manz and M. Ramisch. "On the interaction of turbulence and flows in toroidal plasmas." *Plasma Physics and Controlled Fusion*, **53**(2):024006, 2011.

[34] H. Biglari, P. H. Diamond and P. W. Terry. "Influence of sheared poloidal rotation on edge turbulence." *Physics of Fluids B: Plasma Physics*, **2**(1):1, 1990.

[35] P. H. Diamond and Y. Kim. "Theory of mean poloidal flow generation by turbulence." *Physics of Fluids B: Plasma Physics*, **3**(7):1626, 1991.

[36] C. Angioni, R. M. McDermott, F. J. Casson *et al.* "Intrinsic Toroidal Rotation, Density Peaking, and Turbulence Regimes in the Core of Tokamak Plasmas." *Physical Review Letters*, **107**:215003, 2011.

[37] P. H. Diamond, S.-I. Itoh, K. Itoh *et al.* "Zonal flows in plasma - a review." *Plasma Physics and Controlled Fusion*, **47**(5):R35, 2005.

[38] Y. Camenen, Y. Idomura, S. Jolliet *et al.* "Consequences of profile shearing on toroidal momentum transport." *Nuclear Fusion*, **51**(7):073039, 2011.

[39] R. McDermott, C. Angioni, G. Conway *et al.* "Core intrinsic rotation behaviour in ASDEX Upgrade ohmic L-mode plasmas." *Nuclear Fusion*, **54**(4):043009, 2014.

[40] P. N. Guzdar, L. Chen, W. M. Tang *et al.* "Ion-temperature-gradient instability in toroidal plasmas." *The Physics of Fluids*, **26**(3):673, 1983.

[41] F. Jenko, W. Dorland, M. Kotschenreuther *et al.* "Electron temperature gradient driven turbulence." *Physics of Plasmas*, **7**(5):1904, 2000.

[42] J. Weiland, A. Jarmén and H. Nordman. "Diffusive particle and heat pinch effects in toroidal plasmas." *Nuclear Fusion*, **29**(10):1810, 1989.

[43] B. D. Scott. "The nonlinear drift wave instability and its role in tokamak edge turbulence." *New Journal of Physics*, **4**(1):52, 2002.

[44] B. D. Scott. "Computation of electromagnetic turbulence and anomalous transport mechanisms in tokamak plasmas." *Plasma Physics and Controlled Fusion*, **45**(12A):A385, 2003.

[45] B. D. Scott. "Tokamak edge turbulence: background theory and computation." *Plasma Physics and Controlled Fusion*, **49**(7):S25, 2007.

[46] A. Peeters, Y. Camenen, F. Casson *et al.* "The nonlinear gyro-kinetic flux tube code GKW." *Computer Physics Communications*, **180**(12):2650, 2009.

[47] G. Jost, T. M. Tran, W. A. Cooper *et al.* "Global linear gyrokinetic simulations in quasi-symmetric configurations." *Physics of Plasmas*, **8**(7):3321, 2001.

[48] V. Kornilov, R. Kleiber and R. Hatzky. "Gyrokinetic global electrostatic ion-temperature-gradient modes in finite β equilibria of Wendelstein 7-X." *Nuclear Fusion*, **45**(4):238, 2005.

[49] M. J. Pueschel, D. Told, P. W. Terry *et al.* "Magnetic Reconnection Turbulence in Strong Guide Fields: Basic Properties and Application to Coronal Heating." *The Astrophysical Journal Supplement Series*, **213**(2):30, 2014.

[50] D. Told, F. Jenko, J. M. TenBarge *et al.* "Multiscale Nature of the Dissipation Range in Gyrokinetic Simulations of Alfvénic Turbulence." *Physical Review Letters*, **115**:025003, 2015.

[51] A. Herrmann and O. Gruber. "Chapter 1: ASDEX Upgrade - Introduction and Overview." *Fusion Science and Technology*, **44**(3):569, 2003.

[52] C. Alejaldre, J. J. A. Gozalo, J. B. Perez *et al.* "TJ-II Project: A Flexible Heliac Stellarator." *Fusion Technology*, **17**(1):131, 1990.

[53] B. Streibl, P. T. Lang, F. Leuterer *et al.* "Chapter 2: Machine Design, Fueling, and Heating in ASDEX Upgrade." *Fusion Science and Technology*, **44**(3):578, 2003.

[54] A. Fernández, J. de la Fuente, D. Ganuza *et al.* "Performance of the TJ-II ECRH system with the new -80kV 50A high voltage power supply." *Fusion Engineering and Design*, **84**(2):772, 2009.

[55] M. Liniers, J. Damba, J. Guasp *et al.* "Beam transmission dependence on beam parameters for TJ-II Neutral Beam Injectors." *Fusion Engineering and Design*, **123**:259, 2017.

[56] H. Murmann, S. Götsch, H. Röhr *et al.* "The Thomson scattering systems of the ASDEX Upgrade tokamak." *Review of Scientific Instruments*, **63**(10):4941, 1992.

[57] C. J. Barth, F. J. Pijper, H. J. v. d. Meiden *et al.* "High-resolution multiposition Thomson scattering for the TJ-II stellarator." *Review of Scientific Instruments*, **70**(1):763, 1999.

[58] A. Mlynek, G. Schramm, H. Eixenberger *et al.* "Design of a digital multiradian phase detector and its application in fusion plasma interferometry." *Review of Scientific Instruments*, **81**(3):033507, 2010.

[59] H. Lamela, P. Acedo and J. Irby. "Laser interferometric experiments for the TJ-II stellarator electron-density measurements." *Review of Scientific Instruments*, **72**(1):96, 2001.

[60] C. Laviron, A. J. H. Donné, M. E. Manso *et al.* "Reflectometry techniques for density profile measurements on fusion plasmas." *Plasma Physics and Controlled Fusion*, **38**(7):905, 1996.

[61] T. Estrada, J. Sánchez, B. van Milligen *et al.* "Density profile measurements by AM reflectometry in TJ-II." *Plasma Physics and Controlled Fusion*, **43**(11):1535, 2001.

[62] S. K. Rathgeber, L. Barrera, T. Eich *et al.* "Estimation of edge electron temperature profiles via forward modelling of the electron cyclotron radiation transport at ASDEX Upgrade." *Plasma Physics and Controlled Fusion*, **55**(2):025004, 2013.

[63] M. Cavedon. "The role of the radial electric field in the development of the edge transport barrier in the ASDEX Upgrade tokamak." Ph.D. thesis, Technische Universität München, 2016.

[64] R. M. McDermott, A. Lebschy, B. Geiger *et al.* "Extensions to the charge exchange recombination spectroscopy diagnostic suite at ASDEX Upgrade." *Review of Scientific Instruments*, **88**(7):073508, 2017.

[65] R. Fischer, E. Wolfrum, J. Schweinzer *et al.* "Probabilistic lithium beam data analysis." *Plasma Physics and Controlled Fusion*, **50**(8):085009, 2008.

[66] M. Hirsch, E. Holzhauer, J. Baldzuhn *et al.* "Doppler Reflectometry for the Investigation of poloidally propagating Density Perturbations." *Proc. 4th International Reflectometry Workshop (Cadarache, France)*, 1999.

[67] X. L. Zou. "Poloidal Rotation Measurement in Tore Supra by Oblique Reflectometry." *Proc. 4th International Reflectometry Workshop (Cadarache, France)*, 1999.

[68] G. D. Conway, J. Schirmer, S. Klenge *et al.* "Plasma rotation profile measurements using Doppler reflectometry." *Plasma Physics and Controlled Fusion*, **46**(6):951, 2004.

[69] T. Happel, T. Estrada, E. Blanco *et al.* "Doppler reflectometer system in the stellarator TJ-II." *Review of Scientific Instruments*, **80**(7):073502, 2009.

[70] J. C. Hillesheim, W. A. Peebles, T. L. Rhodes *et al.* "A multichannel, frequency-modulated, tunable Doppler backscattering and reflectometry system." *Review of Scientific Instruments*, **80**(8):083507, 2009.

[71] P. Hennequin, C. Honoré, A. Truc *et al.* "Fluctuation spectra and velocity profile from Doppler backscattering on Tore Supra." *Nuclear Fusion*, **46**(9):S771, 2006.

[72] T. Happel, P. Manz, F. Ryter *et al.* "Turbulence intermittency linked to the weakly coherent mode in ASDEX Upgrade I-mode plasmas." *Nuclear Fusion*, **56**(6):064004, 2016.

[73] G. D. Conway, C. Angioni, F. Ryter *et al.* "Mean and Oscillating Plasma Flows and Turbulence Interactions across the L-H Confinement Transition." *Physical Review Letters*, **106**:065001, 2011.

[74] V. Ginzburg. *The Propagation of Electromagnetic Waves in Plasmas*, Pergammon Press, Oxford, UK, 1970.

[75] R. B. White and F. F. Chen. "Amplification and absorption of electromagnetic waves in overdense plasmas." *Plasma Physics*, **16**(7):565, 1974.

[76] E. Poli, A. Peeters and G. Pereverzev. "TORBEAM, a beam tracing code for electron-cyclotron waves in tokamak plasmas." *Computer Physics Communications*, **136**(1):90, 2001.

[77] T. Estrada, T. Happel, L. Eliseev *et al.* "Sheared flows and transition to improved confinement regime in the TJ-II stellarator." *Plasma Physics and Controlled Fusion*, **51**(12):124015, 2009.

[78] E. Viezzer, T. Pütterich, G. Conway *et al.* "High-accuracy characterization of the edge radial electric field at ASDEX Upgrade." *Nuclear Fusion*, **53**(5):053005, 2013.

[79] T. Happel, A. Bañón Navarro, G. D. Conway *et al.* "Core turbulence behavior moving from ion-temperature-gradient regime towards trapped-electron-mode regime in the ASDEX Upgrade tokamak and comparison with gyrokinetic simulation." *Physics of Plasmas*, **22**(3):032503, 2015.

[80] G. Conway, C. Angioni, R. Dux *et al.* "Observations on core turbulence transitions in ASDEX Upgrade using Doppler reflectometry." *Nuclear Fusion*, **46**(9):S799, 2006.

[81] H. J. Hartfuss, T. Geist and M. Hirsch. "Heterodyne methods in millimetre wave plasma diagnostics with applications to ECE, interferometry and reflectometry." *Plasma Physics and Controlled Fusion*, **39**(11):1693, 1997.

[82] G. D. Conway, C. Lechte, A. Fochi *et al.* "Assessment of Doppler reflectometry accuracy using full-wave codes with comparison to beam-tracing and analytic expressions." *Proc. 12th International Reflectometry Workshop (Jülich, Germany)*, 2015.

[83] T. Happel, G. D. Conway, W. Kasparek *et al.* "Design of a New Doppler Reflectometer Frontend for the ASDEX Upgrade Tokamak." *Proc. 10th International Reflectometry Workshop (Padual, Italy)*, 2011.

[84] R. Sabot, P. Hennequin and L. Colas. "Fluctuation Measurements and Their Link with Transport on Tore Supra." *Fusion Science and Technology*, **56**(3):1253, 2009.

[85] F. Castejón, A. Cappa, M. Tereshchenko *et al.* "Computation of EBW heating in the TJ-II stellarator." *Nuclear Fusion*, **48**(7):075011, 2008.

[86] J. R. Pinzón, T. Happel, E. Blanco *et al.* "Enhanced Doppler reflectometry power response: physical optics and 2D full wave modelling." *Plasma Physics and Controlled Fusion*, **59**(3):035005, 2017.

[87] F. C. Karal and J. B. Keller. "Elastic, Electromagnetic, and Other Waves in a Random Medium." *Journal of Mathematical Physics*, **5**(4):537, 1964.

[88] J. J. Sakurai. *Modern Quantum Mechanics*, The Benjamin/Cummings Publishing Company, Inc, Menlo Park, CA, 1985.

[89] M. Born. "Zur Quantenmechanik der Stoßvorgänge." *Zeitschrift fur Physik*, **37**:863, 1926.

[90] A. D. Piliya and A. Y. Popov. "On application of the reciprocity theorem to calculation of a microwave radiation signal in inhomogeneous hot magnetized plasmas." *Plasma Physics and Controlled Fusion*, **44**(5):467, 2002.

[91] E. Z. Gusakov and A. Y. Popov. "Non-linear theory of fluctuation reflectometry." *Plasma Physics and Controlled Fusion*, **44**(11):2327, 2002.

[92] P. Beckmann and A. Spizzichino. *The scattering of electromagnetic waves from rough surfaces*. International series of monographs on electromagnetic waves, Pergamon Press, Oxford, UK, 1963.

[93] I. S. Robinson. *Measuring the Ocean from Space: The Principles and Methods of Satellite Oceanography*, Springer, Heidelberg, Germany, 2004.

[94] L. Wang and J. J. Qu. "Satellite remote sensing applications for surface soil moisture monitoring: A review." *Frontiers of Earth Science in China*, **3**(2):237, 2009.

[95] J. Röttger. "Reflection and scattering of VHF radar signals from atmospheric refractivity structures." *Radio Science*, **15**(2):259, 1980.

[96] G. D. Conway. "Effects of reflectometer asymmetries on fluctuation measurements." *Plasma Physics and Controlled Fusion*, **41**(1):65, 1999.

[97] A. Ejiri, T. Yamada, Y. Adachi *et al.* "The response of microwave reflectometry under generalized configuration." *Plasma Physics and Controlled Fusion*, **50**(6):065003, 2008.

[98] E. Rodriguez. "Beyond the Kirchhoff approximation." *Radio Science*, **24**(5):681, 1989.

[99] E. Rodríguez. "Beyond the Kirchhoff approximation II electromagnetic scattering." *Radio Science*, **26**(1):121, 1991.

[100] G. D. Conway, B. Kurzan, B. Scott *et al.* "Coupling of turbulence and reflectometer simulation codes and comparison with experiment." *Plasma Physics and Controlled Fusion*, **44**(4):451, 2002.

[101] C. Lechte, G. D. Conway, T. Görler *et al.* "X mode Doppler reflectometry k-spectral measurements in ASDEX Upgrade: experiments and simulations." *Plasma Physics and Controlled Fusion*, **59**(7):075006, 2017.

[102] J. R. Pinzón, T. Happel, E. Blanco *et al.* "Modelling of the power response in Doppler reflectometry." *Proc. 13th International Reflectometry Workshop (Daejeon, Korea)*, 2017.

[103] F. da Silva, S. Heuraux, E. Z. Gusakov *et al.* "A Numerical Study of Forward- and Backscattering Signatures on Doppler-Reflectometry Signals." *IEEE Transactions on Plasma Science*, **38**(9):2144, 2010.

[104] T. Happel, T. Görler, P. Hennequin *et al.* "Understanding of wavenumber spectra measured by Doppler reflectometry through simulation and related estimation of wave-plasma interaction regimes." *Proc. 13th International Reflectometry Workshop (Daejeon, Korea)*, 2017.

[105] C. Tröster. "Development of a flexible Doppler reflectometry system and its application to turbulence characterization in the ASDEX Upgrade tokamak." Ph.D. thesis, Ludwig-Maximilians-Universität, München, Germany, 2008.

[106] D. Prisiazhniuk, A. Krämer-Flecken, G. D. Conway *et al.* "Magnetic field pitch angle and perpendicular velocity measurements from multi-point time-delay estimation of poloidal correlation reflectometry." *Plasma Physics and Controlled Fusion*, **59**(2):025013, 2017.

[107] D. Prisiazhniuk. "Development and application of poloidal correlation reflectometry to study turbulent structures in the ASDEX Upgrade tokamak." Ph.D. thesis, Technische Universität München, Germany, 2017.

[108] F. Ryter, R. Fischer, J. Fuchs *et al.* "I-mode studies at ASDEX Upgrade: L-I and I-H transitions, pedestal and confinement properties." *Nuclear Fusion*, **57**(1):016004, 2017.

[109] J. Schirmer, G. Conway, H. Zohm *et al.* "The radial electric field and its associated shear in the ASDEX Upgrade tokamak." *Nuclear Fusion*, **46**(9):S780, 2006.

[110] T. L. Rhodes, J.-N. Leboeuf, R. D. Sydora *et al.* "Comparison of turbulence measurements from DIII-D low-mode and high-performance plasmas to turbulence simulations and models." *Physics of Plasmas*, **9**(5):2141, 2002.

[111] B. P. van Milligen, T. Estrada, E. Ascasíbar *et al.* "Integrated data analysis at TJ-II: The density profile." *Review of Scientific Instruments*, **82**(7):073503, 2011.

[112] C. Hidalgo, M. Pedrosa, L. Garcia *et al.* "Experimental evidence of coupling between sheared-flow development and an increase in the level of turbulence in the TJ-II stellarator." *Physical Review E*, **70**(6, 2), 2004.

[113] M. A. Pedrosa, C. Hidalgo, E. Calderón *et al.* "Threshold for sheared flow and turbulence development in the TJ-II stellarator." *Plasma Physics and Controlled Fusion*, **47**(6):777, 2005.

[114] U. Stroth, K. Itoh, S.-I. Itoh *et al.* "Internal Transport Barrier Triggered by Neoclassical Transport in W7-AS." *Physical Review Letters*, **86**:5910, 2001.

[115] F. Fernández-Marina, T. Estrada, E. Blanco *et al.* "Radial correlation length across magnetic islands: Simulations and experiments." *Physics of Plasmas*, **24**(7):072513, 2017.

[116] T. Estrada, E. Ascasíbar, E. Blanco *et al.* "Plasma flow, turbulence and magnetic islands in TJ-II." *Nuclear Fusion*, **56**(2):026011, 2016.

[117] E. Sanchez, R. Kleiber, R. Hatzky *et al.* "Linear and Nonlinear Simulations Using the EUTERPE Gyrokinetic Code." *IEEE Transactions on Plasma Science*, **38**(9):2119, 2010.

[118] A. Bañón Navarro, T. Happel, T. Görler *et al.* "Gyrokinetic studies of core turbulence features in ASDEX Upgrade H-mode plasmas." *Physics of Plasmas*, **22**(4):042513, 2015.

[119] D. Told, F. Jenko, T. Görler *et al.* "Characterizing turbulent transport in ASDEX Upgrade L-mode plasmas via nonlinear gyrokinetic simulations." *Physics of Plasmas*, **20**(12):122312, 2013.

[120] E. Sánchez, I. Calvo, J. L. Velasco *et al.* "Simulation of electrostatic instabilities in a heliac configuration." *Proc. 41st EPS Conference on Plasma Physics (Berlin, Germany)*, 2014.

[121] E. Sánchez, P. Monreal, I. Calvo *et al.* "Relaxation of zonal flows in stellarators: influence of the magnetic configuration." *Proc. 42nd EPS Conference on Plasma Physics (Lisbon, Portugal)*, 2015.

[122] R. R. Dominguez and G. M. Staebler. "Anomalous momentum transport from drift wave turbulence." *Physics of Fluids B: Plasma Physics*, **5**(11):3876, 1993.

[123] Y. Kishimoto, J.-Y. Kim, W. Horton *et al.* "Toroidal mode structure in weak and reversed magnetic shear plasmas and its role in the internal transport barrier." *Plasma Physics and Controlled Fusion*, **41**(3A):A663, 1999.

[124] A. G. Peeters, C. Angioni, A. Bottino *et al.* "Toroidal momentum transport." *Plasma Physics and Controlled Fusion*, **48**(12B):B413, 2006.

[125] A. Lebschy, R. McDermott, C. Angioni *et al.* "Measurement of the complete core plasma flow across the LOC–SOC transition at ASDEX Upgrade." *Nuclear Fusion*, **58**(2):026013, 2018.

[126] C. Angioni, R. Bilato, F. Casson *et al.* "Gyrokinetic study of turbulent convection of heavy impurities in tokamak plasmas at comparable ion and electron heat fluxes." *Nuclear Fusion*, **57**(2):022009, 2017.

[127] L. Vermare, P. Hennequin, O. D. Gürcan *et al.* "Poloidal asymmetries of flows in the Tore Supra tokamak." *Physics of Plasmas*, **25**(2):020704, 2018.

[128] E. Gusakov and M. Tyntarev. "The two-dimensional theory of reflectometry diagnostics of plasma fluctuations." *Fusion Engineering and Design*, **34**:501, 1997.

[129] P. M. Morese and H. Feshbach. *Methods of theoretical physics. Part I.* International series in pure and applied physics, McGraw-Hill, New York, 1953.

Appendix A

Scattering efficiency

It has been discussed in Ch. 6 how non-linear effects can produce large deviations of the measured $k_\perp$ spectra with respect to the real one. Nevertheless, small deviations have also been observed in the linear regime, e.g. a slight loss of the reflectometer sensitivity with $k_\perp$ has been observed in Fig. 6.10 and 6.11, and reported in Ref. [18]. This effect, referred to as *scattering efficiency* modifies the measured $k_\perp$ spectra. Hence its understanding and the application of a correction is relevant for detailed studies of the turbulence. In this section the scattering efficiency is studied by comparing in detail the $k_\perp$ spectra obtained in two-dimensional full-wave (2DFW) simulations for a linear response with the input spectrum. A correction formula is proposed and tested.

The 2DFW simulations presented in Sec. 6.3 are extended in order to study the purely linear response. In particular more angles (including normal incidence) and a lower turbulence level (0.01%) for X-mode are included. The $k_\perp$ spectra computed from the 2DFW data in linear regime are plotted with red symbols in Fig. A.1a, where the black line represents the input spectrum (cf. Eq. 6.5). The blue symbols are the corrected data to be explained afterwards. Although the reflectometer is operating in the linear regime, the $k_\perp$ spectrum decays slightly faster than the input spectrum for both O- and X-mode.

In the linear regime, P is proportional to the power spectrum of the turbulence according to Eq. 4.8. However, the beam propagation for different angles of incidence induces an instrumental dependency of the backscattered power on θ (or equivalently $k_\perp$), which causes the scattering efficiency drop. This effect is included with a correction factor A as

$$P \propto \delta n_{rms}^2 A^2(\theta) h_\perp^2(k_\perp). \tag{A.1}$$

From the simulated data $A^2 \propto P/h_\perp^2(k_\perp)$ is computed. The values are normalized to the normal incidence and plotted with symbols as a function of θ in Fig. A.1b. The correction formula for A is depicted by solid lines and will be explained next. A similar decrease of the sensitivity with θ is observed for O- and X-mode.

Although the scattering efficiency has been observed in simulations [18] and has been studied in the literature [128], predictions applicable to experimental data analysis are not available. In the following a correction formula is deduced for O-mode in slab geometry and with a linear density profile. It recovers the trends of the simulations, and

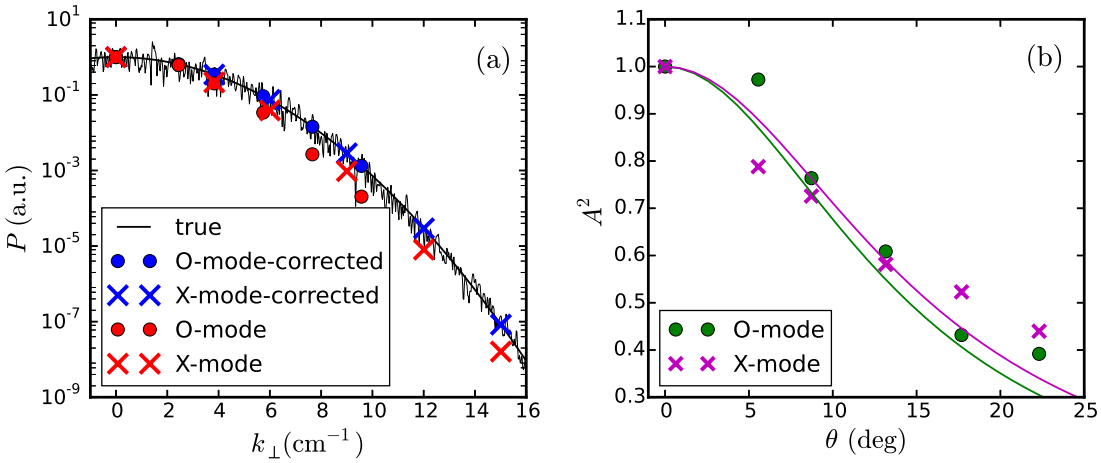

FIGURE A.1: (a) $k_\perp$ spectra obtained with 2DFW simulations in the linear regime (red). The black line depicts the input spectrum. $k_\perp$ spectra corrected with Eq. A.4 are shown in blue. (b) Factor A^2 accounting for the scattering efficiency effect.

allows to understand the role of the basic parameters. Moreover it will be applied to a more realistic case .

First, the unperturbed electric field E_0 is computed by solving Eq. 5.4. For slab geometry, linear density profile and oblique incidence, the x-dependent part of the electric field is given by [75]

$$\frac{\partial^2 E_0}{\partial x^2} + k_0^2 \left(1 - \frac{x}{L} - \sin^2\theta\right) E_0 = 0. \tag{A.2}$$

Using the transformation

$$\zeta = \left(\frac{k_0^2}{L}\right)^{1/3} (L\cos^2\theta - x),$$

the previous equation turns into

$$\frac{\partial^2 E_0}{\partial \zeta^2} + \zeta E_0 = 0.$$

The solution to the previous equation is given by the Airy function. It is depicted in Fig. A.2a for $\theta = 17.7°$. Both coordinates, x and ζ are shown in the lower and upper axes, respectively. The nominal cutoff, at $x = L\cos^2\theta$ or equivalently $\zeta = 0$, is indicated with a green dashed line. E_0^2 oscillates and maximizes close to the cutoff as it was discussed in Sec. 4.2. An absolute maximum is obtained at $\zeta_{\max} \approx 1$ corresponding to $x_{\max} = L\cos^2\theta - (L/k_0^2)^{1/3}$, which is slightly displaced with respect to the nominal cutoff.

The solution shown in Fig. A.2a has an absolute maximum slightly displaced from the nominal cutoff, similarly to the weighting function from Fig. 6.9d. The dominance of the scattering in a narrow region along $x_{\max}$, makes possible a reduction of the problem to one dimension. Shrinking the system to a line along $x_{\max}$, Eq. 5.5 becomes

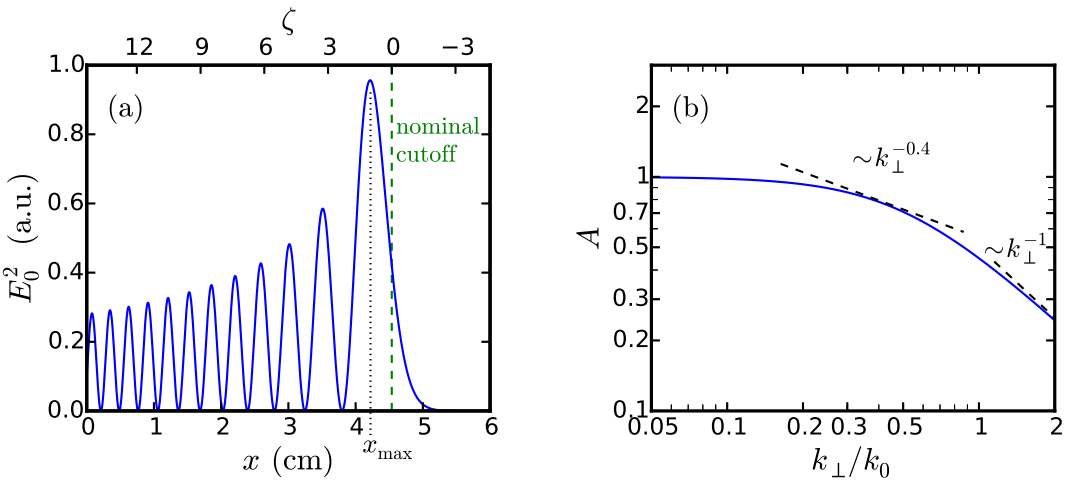

FIGURE A.2: (a) Unperturbed electric field squared obtained from solving Eq. A.2. A maximum is observed close to the nominal cutoff. (b) Scattering efficiency A as a function of $k_\perp/k_0$ computed from Eq. A.3. A drop of the scattering efficiency with $k_\perp$ is observed. Two scalings are indicated in different ranges.

$$(\partial_y^2 + k_{\max}^2)E_1 = k_0^2 \frac{\delta n}{n_c} E_0.$$

where $k_{\max}$ is taken from the dispersion relation at $x_{\max}$ following

$$k_{\max}^2 = k_0^2 \left[1 - \frac{n_0(x_{\max})}{n_c}\right] = k_0^2 \left[1 - \frac{x_{\max}}{L}\right] = k_0^2 \left[\left(\frac{1}{k_0 L}\right)^{2/3} + \sin^2\theta\right].$$

The scattered field can be computed with the Green function for the relevant geometry [129],

$$E_1 \propto \int \mathrm{d}y G_{1\mathrm{D}}(y)\delta n E_0, \quad \text{with} \qquad G_{1\mathrm{D}}(y) = \frac{i e^{ik_{\max}|y|}}{2k_{\max}}.$$

The Green function introduces a $k_{\max}^{-1}$ dependency on the scattered field E_1, which results in a $k_{\max}^{-2}$ dependency on the backscattered power. This dependency provides the scattering efficiency correction factor as $A \sim k_{\max}^{-1}$, which after normalizing for normal incidence gives

$$A = \left[1 + \left(\frac{2\pi L}{\lambda_0}\right)^{2/3} \sin^2\theta\right]^{1/2} = \left[1 + \left(\frac{L}{8k_0^2}\right)^{2/3} k_\perp^2\right]^{1/2}. \tag{A.3}$$

In Fig. A.2 the scattering efficiency A is plotted as a function of $k_\perp/k_0$ for the parameters used in Sec. 6.3. In the limit of large $k_\perp$ the scattering efficiency scales as $k_\perp^{-1}$, hence the measured spectral index for the power could be underestimated by at most 2. In the limit of small $k_\perp$ the scattering efficiency is constant and 1, and in between both limits A scales with a $k_\perp$ exponent in between 0 and 1. Fig. A.2 depicts also a scaling $k_\perp^{-0.4}$ at an intermediate position which has been reported in Ref. [18].

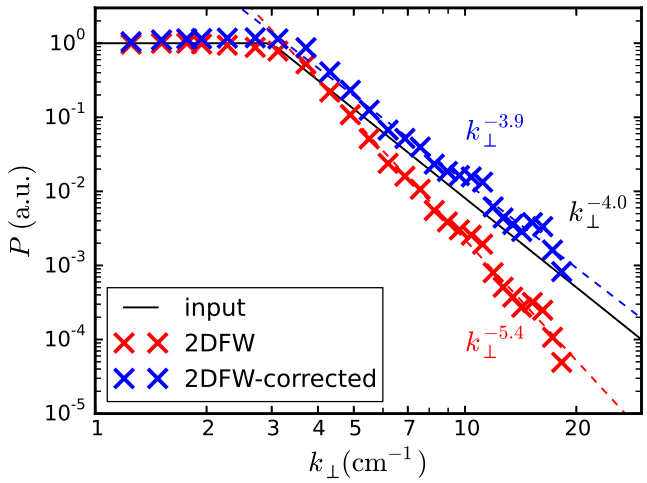

FIGURE A.3: $k_\perp$ spectra for a Kolmogorov type input spectrum [101]. The input spectrum is plotted with a black line and 2DFW data in the linear regime with red symbols. The blue symbols depict 2DFW data corrected with Eq. A.4. Spectral indices for the different case are indicated.

Although the previous calculation is done for O-mode and for a linear density profile, it can applied in general cases by taking the gradient scale length of the squared refractive index L^{ref}. This includes the magnetic field for the X-mode case. Fig. A.1b shows that Eq. A.3 is able to follow approximately the simulated data for O- and X-mode. Furthermore, $k_\perp$ spectra obtained in the linear regime can be corrected for the scattering efficiency with

$$P_{\mathrm{corrected}} = P\left[1 + \left(\frac{L^{\mathrm{ref}}}{8k_0^2}\right)^{2/3} k_\perp^2\right]. \tag{A.4}$$

The corrected $k_\perp$ spectra are presented with blue symbols in Fig. A.1a. A better agreement with the input spectrum is observed for both polarizations.

The scattering efficiency is also observed in the 2DFW simulations with the ASDEX Upgrade geometry and a Kolmogorov-type turbulence presented in Sec. 6.4 [101]. The $k_\perp$ spectrum obtained in the purely linear regime is shown in Fig. A.3 with red symbols. The simulated spectrum recovers the shape of the input spectrum in black, but with a stronger spectral index of -5.4 due to the scattering efficiency effect. The spectrum corrected using Eq. A.4 is shown in the figure with blue symbols. A better agreement with the input spectrum is obtained after applying the correction; the corrected spectral index is -3.9. This shows that the correction factor Eq. A.4 does reproduce the scattering efficiency for realistic plasma geometries and spectral shapes.

The $k_\perp$ spectra, measured for experimental conditions where the response of the Doppler reflectometer is linear, can be corrected with Eq. A.4. The effects here discussed could explain the small discrepancies between the spectral indices obtained in gyrokinetic simulations and with O-mode Doppler reflectometry measurements at the ASDEX Upgrade tokamak [17].

Appendix B

Decorrelation due to $k_\perp$ variation

In the Sec. 7.2 the radial correlation Doppler reflectometry has been investigated using two-dimensional full-wave (2DFW) simulations. There a decrease of the radial correlation length L_x with the angle of incidence θ has been observed (cf. Fig. 7.5a and d). The decorrelation effect responsible is discussed here.

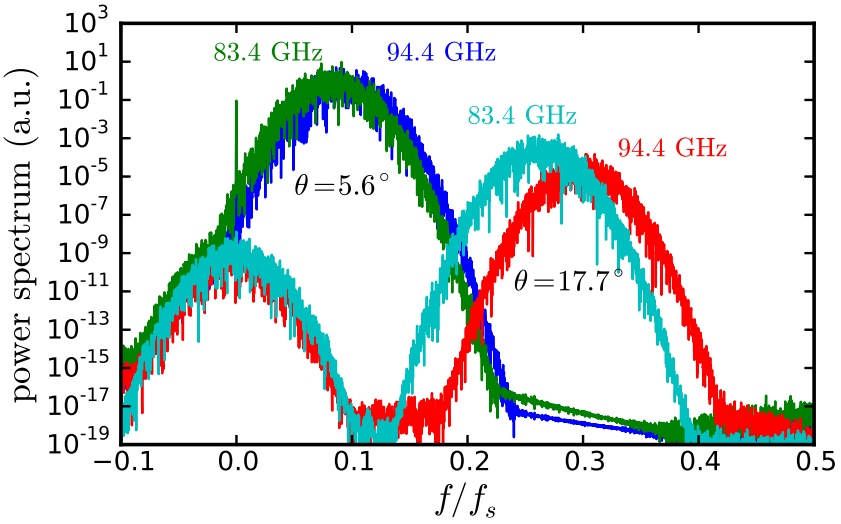

FIGURE B.1: Power spectra obtained from X-mode 2DFW simulations in linear regime. Two angles of incidence and two probing frequencies are presented.

A probing frequency f_0 scan is performed in order to induce a radial separation between the reference and hopping channels. Moreover, $k_\perp$ depends on the probing frequency as it is seen for the slab case in Eq. 4.7 through the k_0 dependency. As a consequence, the f_0 scan results in a change of $k_\perp$ for oblique incidence. This effect is observed in Fig. B.1, where the power spectra of 2DFW signals for two angles of incidence and two probing frequencies are shown. The Doppler peak appears approximately at the same position for $\theta = 5.6°$ and both probing frequencies. However for $\theta = 17.7°$, the Doppler peaks appear at different positions for the two probing frequencies. For all cases a broad peak centred at $f = 0$ is observed. It corresponds to the direct reflection

contribution (cf. Sec. 4.2.3) and is several orders of magnitude below the Doppler peak in these 2DFW simulations.

The difference of the peak position is large compared to its width for $\theta = 17.7°$, hence the overlap of the peaks is partially lost. It means that reference and hopping channels are not measuring at the same $k_\perp$. This causes a decrease of the correlation between the two signals. Since the $k_\perp$ difference increases with the frequency separation, the correlation of the signals decreases with Δx. This is an instrumental effect that is not related to the turbulence. It modifies the decay of $C_{\max}$ with Δx, and therefore the measured L_x.

The simulations presented are performed with a good spectral resolution and a strong density gradient. Accordingly narrow Doppler peaks ($\Delta f < f_D$) are obtained and a broad frequency scan is performed. These conditions make the decorrelation effect particularly strong, which is in line with the observed decrease of L_x with θ in Fig. 7.5a and d. This effect is strong and dominates over other effects on the correlation, e.q. non-local scattering [21].

It should be noted that this effect is not relevant in the experimental measurements presented in Ch. 8 and Ch. 9. The Doppler peaks there are wide rand a small $k_\perp$ variation is induced by the probing frequency scan.

Appendix C

Effect of the direct reflection contribution in the correlation analysis and its filtering

The characterization method of the density turbulence (cf. Sec. 7) using radial correlation Doppler reflectometry assumes backscattering contributions only. Nevertheless, the direct reflection introduced in Sec. 4.2.3 and observed the $k_\perp$ spectrum (cf. Fig. 8.3a) can have an impact in the correlation analysis, which has to mitigated in the case where is relevant. The direct reflection contribution has been filtered out for the correlation analysis in the ASDEX Upgrade tokamak presented in Sec. 8.1 and Ch. 9. Here the effect and the filtering are discussed in detail.

An example where the direct reflection affects the O-mode correlation analysis is discussed. The power spectra obtained for the reference and hopping channel are shown in Fig. C.1a. A Doppler peak at about -400 kHz and a direct reflection contribution around zero frequency are observed. The impact of the contributions for the correlation analysis can be analysed by looking at the cross-spectrum of the signals, $\hat{V_0}\hat{V_1}^*$. The absolute value and complex phase of the cross-spectrum are shown in Fig. C.1b and c, respectively. Backscattering and direct reflection contributions are also observed in the cross-spectrum of the signals.

Although the direct reflection contribution to the power spectra is weak compared with the Doppler peak (Fig. C.1a), it is strong and comparable to the backscattering contribution in the cross-spectrum (Fig. C.1b). This shows that the direct reflection has an impact in the correlation analysis. The complex phase of the cross-spectrum in Fig. C.1c, shows a well defined linear behaviour at the Doppler frequency. Its slope gives the time delay of the backscattering contribution which is related to the tilt of the turbulent structures. Nevertheless, the phase behaves erratically at around zero frequency due to the direct reflection. This can corrupt the time delay analysis of the correlation.

The cross-correlation function of the signals is shown in Fig. C.1d with red points. A mixture of two peaks centred at different τ is obtained. The interference of the direct reflection contribution with the backscattering corrupt the cross-correlation function

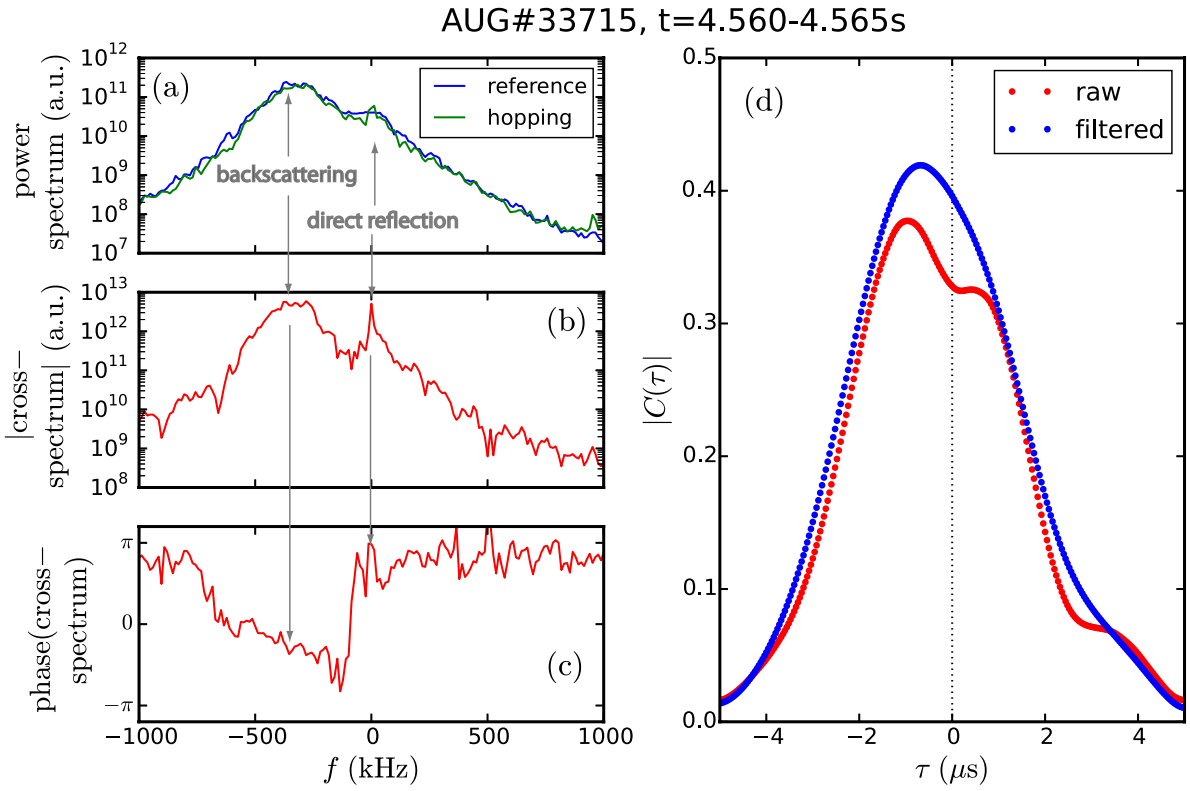

FIGURE C.1: (a) Power spectra of the reference and hopping channels signal. (b) Absolute value and (c) complex phase of the cross-spectrum. (d) Cross-correlation function for the raw signals in red and the band-pass filtered signals in blue.

producing satellite peaks as the one one observed in the figure. The direct reflection contribution is suppressed by filtering, in this case the signals have been pass-filtered in the range of -700 to -200 kHz. The cross-correlation function computed with the filtered signals is depicted by blue symbols in (d). A single peak suitable for the correlation analysis is obtained.

The analysis of the cross-spectrum shows that the direct reflection contribution may have negative impact on the correlation analysis; the maximum $C_{\max}$ and the time delay $\tau_{\max}$ of the cross-correlation can be affected. Nevertheless, this effect can be avoid by filtering the out the direct reflection contributions in the data processing.

The filtering works well when the Doppler peak is dominant (as in the case here discussed) and when the Doppler shift is large. For cases where Doppler peak is sub-dominant and small Doppler shift, the filtering the filtered signal quality is poor and the correlation analysis is problematic.

Acknowledgements

The process of writing this doctoral thesis would not have been possible without the help and support of a large number of people. This process of three and a half years has been a big step forward in my scientific career, but also an important period in my life during which I learnt valuable lessons about life. Here, I would like to thank to all people that contributed directly to the development of this thesis, and also to those that supported me by being part of my life during the last years.

First of all, it is a pleasure to thank Dr. Tim Happel who was my supervisor at the Max-Planck-Institut für Plasmaphysik (IPP). He supported me unconditionally since the very first day of my PhD, and his motivation and interest on my research project encouraged me throughout the entire process. He was always available and had time for discussions, explanations, re-explanations, corrections... Moreover, the fact that he listened to my eccentric ideas and encouraged me to pursue them, was decisive for the completion of this thesis. I appreciate very much Tim's friendly support and commitment. *Danke schön!*

I would like to express my deep gratitude to Prof. Dr. Ulrich Stroth, my academic supervisor at the Technical University of Munich. He was always involved and interested in my research project. Moreover, our regular meetings were important for staying in focus and for bringing this thesis to a good end. I also appreciate the broad discussions led by Uli in the turbulence group that contributed to my understanding on the topics of the thesis.

It was a pleasure to work with Dr. Pascale Hennequin. This experimental thesis would have never been possible without the high quality reflectometry data obtained with her systems. I am thankful for her efforts, commitment and invested time. I always enjoyed working with her in the torus hall and the control room, and also appreciated the enlightening discussions on physics and data analysis. *Merci beaucoup!*

I would like to express my deep gratitude to Dr. Teresa Estrada, who was my supervisor at CIEMAT. The experimental results on the TJ-II stellarator would not have been possible without her support. Furthermore, I profoundly admire her ability to explain complex ideas in a simple and instinctive way. I felt always inspired and motivated when working with her.

I am grateful to Dr. Emilio Blanco, who provided me with the two-dimensional full-wave code. His support on the simulations and our enlightening discussions on wave propagation were crucial for the modelling of Doppler reflectometry presented in this thesis. I always enjoyed and had fun while working with him.

The comparisons of experimental measurements with simulations would not have been possible without the help and support of the gyrokinetic experts. I want to thank Dr. Edilberto Sanchez, Dr. Tobias Görler and Dr. Clemente Angioni, for performing the simulations, for the explanations and discussions, and for their interest in my project. I hope our work leads to some publications in the near future.

I am grateful to the IPP and ASDEX Upgrade teams, including scientific, administrative and technical staff. In particular, I would like to extend my thanks to the reflectometry group; their members (all of them truly reflectometry experts) supported me in specific problems I faced during the thesis. I thank especially to Dr. Garrard Conway for his enlightening discussions and because he introduced me to the physical optics model, one of the key pieces of my work. I would also like to thank to the whole CIEMAT and TJ-II teams for their scientific excellence, as well as for the friendly environment that made me enjoy my stays at CIEMAT.

Of course, my time at IPP would not have been pleasant and funny without my colleagues. Apart of enjoy the daily work with them; we had a good time during conferences, excursions (especially at the *Wiesn* and *Starkbierfest*), weekends... Their friendship has been very valuable for me during this time. A special acknowledgement to my office mates and best German teachers, Michael Griener and Dr. (since yesterday) Felician Mink.

I would like to thank the Erasmus Mundus FUSION-DC program for giving me the opportunity to participate in this international doctoral college. In particular, I would like to thank Prof. José Ramón Martín Solís, who was my academic supervisor at the Universidad Carlos III de Madrid. His support and help in all organizational matters were crucial for my participation in the program.

Last but not least, I would like to thank my friends outside the institute. They just made my life in Munich and Madrid worth. Special acknowledgement to my Socratic friends, my climbing partners, the medicine students community in Munich, the MiO orchestra and many others. I would like to mention Lea Krauß, who has been at my side during the last year and who unconditionally supported me during the hardest time. *Que afortunado soy! Finalmente, un caluroso reconocimiento a mi familia en la lejana Colombia, a mis padres y hermanos, quienes bien saben que sin ellos, nada de esto hubiera sido posible. Gracias!*